

### III

Department of Transport Technology,  
University of Technology,  
Loughborough,  
England.

Von-Karman Institute for Fluid  
Dynamics,  
Rhode St. Genese,  
Brussels.

"On the Response and Interaction with the Flow of Structures  
Immersed in Turbulent Flow Fields."

By:

GEORGE P. SKORDILIS

B.Tech. - Loughborough University.

Postgr. Dipl. V.K.I. - Von-Karman Institute.

Master of Science Thesis

Thesis submitted in fulfillment of the requirements for the award of  
"Master of Science" of the Loughborough University of Technology.

APRIL 1976

Supervisors:

University of Technology  
Loughborough.

1) Professor D. Johns,  
Head of Department of  
Transport Technology.

2) Mr. F.G. Maccabee,  
Lecturer,  
Department of Transport  
Technology.

Von-Karman Institute,  
Brussels.

1) Professor J.J. Ginoux,  
Associate Director.

2) Mr. D. Olivari,  
Lecturer,  
Low Speed Aerodynamics  
Department.

( VOLUMES I AND II )

6 by George P. Skordilis, 1976

ACKNOWLEDGEMENTS

The author would like to thank the Von-Karman Institute for providing the facilities for the present work. Furthermore, the help of many of the Institute's personnel must be acknowledged, specifically: Mr. J. Hauchart of the Low-Speed Laboratory for his help with the experiments and Mr. Jean-Glaude Lobet for his fine photography.

Sincere appreciations and thanks are given to Dr. J. J. Ginoux and Mr. D. Olivari of the Von-Karman Institute for their thorough evaluation and constructive criticism of the present work as well as for their generosity in giving considerable time and effort in aid to this author over such a distance and great personal inconvenience.

Finally, the author can only inadequately convey his gratitude and thanks to his University advisers, Professor D. J. Johns and Mr. F. G. Maccabee; without their support, guidance, encouragements and friendly advice this work would not have been possible.

ABSTRACT.

The present work deals with the response and interaction with the flow of structures immersed in turbulent flow fields.

For ease of reference the work is subdivided in three parts.

In the first part of the work, experiments are described in which the interaction of the flow of the oscillating and rigidly held models - under various conditions - is examined. The experiments were carried out in turbulent flow fields of relatively large scale and high intensity. The second part of the report includes the results of a series of measurements of the fluctuating drag forces on low aspect ratio plates, prisms and cylinders. In the third part of the thesis an attempt is being made to produce a mathematical model of the turbulent flow field in front of the model.

The interaction of the flow-model system is studied experimentally by considering the lateral cross-correlation coefficient, the probability density function of the longitudinal velocity component and the spectrum variation of the longitudinal velocity component in front of the rigidly and free to oscillate models. It is shown that the interaction of the model with the flow results in a reduction of the flow fluctuating kinetic energy when the model oscillates compared with the case when the model is held rigidly.

The experiments being basic in nature no attempt is being made to use complicated models, and the experiments are conducted using simple geometric shapes.

A deeper understanding of the variation of the flow parameters is attempted by considering the variation of the energy level of the

different eddies as they approach the model. The results show that the energy level variation depends on the frequency range considered, the greatest variation in the energy level of the different eddies being present in the stagnation line flow.

The relation between the pressure fluctuations at the stagnation point on a flat plate model and the upstream flow velocity is also examined. It is shown that at low frequencies the pressure spectra are the same as the velocity spectra, measured just in front of the stagnation point. At higher frequencies the pressure spectra fall below the respective velocity spectra.

As a preliminary in considering the dynamic response of bluff bodies immersed in turbulent flow fields, the correlation of the forces along the length and width of the models is looked at. This is achieved by considering the variation of the integral scale of turbulence (in the three directions) as the flow approaches the model, for the following cases:

1. Empty tunnel (reference case)
2. Model held rigidly
3. Model free to oscillate
4. Model externally excited at discrete frequencies and amplitudes.

In the last case the harmonic content of the model oscillations is of primary interest. It is shown that the integral scale of turbulence decreases as the frequency of vibration or amplitude of oscillations increases.

Three turbulent fields were used, one of them being a two-dimensional jet produced from a slit across the wind tunnel working section.

The power spectral density of the force response is com-



## VII

pared with the respective power spectral density of the velocity and it is shown that the concluded aerodynamic admittance has a high frequency decline which usually starts at about  $(fA)/(UL_y)=0.1$ .

## VIII

### TABLE OF CONTENTS

	Page
THESIS ACCESS CONDITIONS FORM.....	I
CERTIFICATE OF ORIGINALITY.....	II
FLYLEAF.....	III
ACKNOWLEDGEMENTS.....	IV
ABSTRACT.....	V
TABLE OF CONTENTS.....	VIII
LIST OF SYMBOLS.....	XV
LIST OF FIGURES.....	XVIII
GENERAL INTRODUCTION.....	XXI

### PART I

#### ON THE FLOW PHENOMENA RELATED TO BLUFF BODIES

##### IMMERSED IN TURBULENT FLOW FIELDS

1. INTRODUCTION.....	3
2. LITERATURE SURVEY AND GENERAL DISCUSSION OF THE PHENOMENON	
2.1 Atmospheric Turbulence.....	8
2.1.1 The Structure of Turbulence.....	8
2.1.2 Probability Density Function of the Horizontal Wind Speed.....	9
2.1.3 Power Spectral Density of the Horizontal Wind Speed.....	10
2.1.4 Spatial Correlations.....	11
2.1.5 Development of the Energy-content of the Different Eddies.....	14
2.1.6 Pressure Fluctuations.....	15

2.2	On the Mechanics of Flow around Bluff Bodies....	16
3.	THEORETICAL CONSIDERATIONS	
3.1	The Probability Distribution of the Longitudinal Velocity Component.....	20
3.2	The One-Dimensional Spectrum.....	22
3.3	The Wavenumber Variation as the Flow Approaches the Model.....	22
4.	GENERATION OF TURBULENCE	
4.1	Baffle Design.....	25
4.2	Baffle Development.....	26
4.3	Final Baffle Design and Verification.....	27
5.	THE STRUCTURE OF THE BAFFLE GENERATED TURBULENCE FIELD	
5.1	General.....	28
5.2	Intensity of Turbulence.....	28
5.3	Scale of Turbulence and Variation of the Turbulent Scale in the Longitudinal Direction.....	28
5.4	The Spectrum of the Longitudinal Velocity Component.....	29
5.5	Probability Density Function of the Longitudinal Velocity Component.....	29
5.6	Space Correlations and Two-Point Cross-Spectrum of the Turbulent Field.....	29
5.7	Spectrum Variation Along the Stagnation Line Flow.....	31
6.	DESCRIPTION OF APPARATUS	
6.1	Model Hardware.....	32
6.2	Method of Model Mounting.....	33
6.2.1	Model Held Rigidly.....	33
6.2.2	Model Free to Oscillate.....	33

6.2.3	Model Excited Externally.....	34
7.	INSTRUMENTATION	
7.1	Wind Tunnel.....	35
7.2	Hot-wire Instrumentation.....	35
7.3	Spectral Analysis System.....	37
7.4	Microphone.....	39
7.5	Probability Density Function Displayer.....	40
7.6	Accuracy of Measurements.....	41
7.6.1	Wall Interference Corrections.....	43
8.	RESULTS AND DISCUSSION	
8.1	Mean Velocity Profiles.....	45
8.2	Intensity Profiles of the Turbulent Fields.....	48
8.3	Integral Scales of Turbulence.....	49
8.4	The Spectrum of the Longitudinal Velocity Component.....	52
8.5	Cross-Spectrum of the Longitudinal Velocity Component.....	54
8.6	Spectrum Variation of the Longitudinal Velocity Component in Front of the Model.....	57
8.7	Probability Density Function of the Longitudinal Velocity Component.....	59
8.8	The Development of the Energy Level of the Eddies as they Approach the Model	
8.8.1	Reasons for the Investigation.....	61
8.8.2	Explanatory Notes on the Experiments and the Plotting of the Graphs.....	63
8.8.3	Discussion of the Resulted Plots.....	67
8.9	The Variation of the Integral Scale of Turbulence in Front of the Model when the Latter is	

Externally Excited.....	72
8.10 Pressure-Velocity Correlation.....	77
9. CONCLUSIONS.....	80

## XII

### VOLUME II

CERTIFICATE OF ORIGINALITY.....	I
FLYLEAF .....	II
TABLE OF CONTENTS .....	III

### PART II

#### ON THE RESPONSE OF BLUFF BODIES IMMERSED IN TURBULENT FLOW FIELDS

10. INTRODUCTION.....	84
11. A REVIEW OF THE GENERAL PROBLEMS PRESENT IN THE INVESTIGATION OF THE RESPONSE OF STRUCTURES TO TURBULENT FLOW FIELDS.....	87
12. THEORETICAL CONSIDERATIONS	
12.1 General Concepts.....	90
12.2 Mechanical Admittance.....	91
12.3 Linearized Theory.....	92
13. DESCRIPTION OF APPARATUS	
13.1 Model Mounting.....	96
13.2 Model-Load Balance Assembly Calibration.....	96
13.3 Extraneous Inputs.....	97
14. INSTRUMENTATION	
14.1 Strain Gauges.....	99
14.2 General Arrangement.....	99
14.3 Comments on the Performance of the Balance.....	100
14.4 Accuracy of Measurements.....	101
15. RESULTS AND DISCUSSION	
15.1 Discussion of the General Experimental Procedure.....	104
15.2 Effect of Frontal Area on Aerodynamic Admittance.....	106

### XIII

15.3	Effect of Aspect Ratio on Aerodynamic Admittance.....	107
15.4	Effect of Turbulence Level on Aerodynamic Admittance.....	107
15.5	Effect of Scale of Turbulence on Aerodynamic Admittance.....	108
15.6	Mean and Fluctuating Drag.....	109
16.	CONCLUSIONS.....	112
17.	RECOMMENDATIONS.....	113

### PART III

#### A MATHEMATICAL MODEL OF THE FLOW SITUATION

##### IN FRONT OF THE MODEL

18.	INTRODUCTION .....	118
19.	FORMULATION.....	123
20.	MODEL PREDICTION.....	127
21.	DISCUSSION OF THE MATHEMATICAL MODEL.....	128
22.	CONCLUSIONS DRAWN ON THE MATHEMATICAL MODEL.....	128
23.	GENERAL CONCLUSIONS.....	130
24.	REFERENCES.....	131

#### APPENDICES

Appendix A.	Joint Probability Density Distribution of the Velocity Fluctuations.....	140
Appendix B.	Hot-Wire Instrumentation	
	B.1 Linearization and Longitudinal Velocity Component Measurements.....	143
	B.2 Frequency Response Considerations.....	144
Appendix C.	Measurement of Frequency-Dependent Cor- relation.....	146

## XIV

Appendix D. Measurements of the Turbulence Kinetic	
Energy Using a Single Hot-Wire .....	148
Appendix E. Calculation of the Mechanical Admittance.....	151
Appendix F. Statistical Reliability of Power-Spectrum	
Measurements.....	152



LIST OF SYMBOLS\*

A	-frontal area of model ( $\text{mm}^2$ )
$ AI ^2$	-aerodynamic admittance
AR	-aspect ratio, $\frac{\text{length}}{\text{width}}$
$C_D$	-drag force coefficient
$C_D(f)$	-frequency dependent drag coefficient
D	-disc diameter or width of model (mm) (See also b)
$\frac{Du}{Dt}$	-total differential
$L_x$	-integral scale of turbulence (x-direction) (mm)
$L_y$	-integral scale of turbulence (y-direction) (mm)
$L_z$	-integral scale of turbulence (z-direction) (mm)
N	-longitudinal force on the model (N)
$\bar{N}$	-mean longitudinal force on the model (N)
P(t)	-forcing function
$R_{ij}(r_1, r_2, r_3) = \frac{\overline{u_{i1} u_{j2}}}{\left\{ \overline{u_{i1}^2} \overline{u_{j2}^2} \right\}^{1/2}}$	-correlation coefficient
$S_{u_1}(f)$	-power spectral density of $u_1$
$S_n(f)$	-power spectral density of n
$S_{u_1 u_2}(f)$	-cross-spectrum of velocities $u_1$ and $u_2$
T	-time (s)
$T_c$	-time constant
Y	-wind tunnel width in the y-direction (mm)
Z	-wind tunnel width in the z-direction (mm)
b	-plate width (mm)
c	-viscous damping of system (Ns/m)
$d_s$	-width of slot of slotted baffle (mm)
$d_{30}$	-diameter of holes of the 30mm holes baffle
$d_{50}$	-diameter of holes of the 50mm holes baffle
$d_i$	-general notation of $d_{30}, d_s, d_{50}$

$e'$	-voltage
$f$	-frequency (Hz)
$k$	-wavenumber ( $m^{-1}$ )
$k_s$	-structural stiffness of system (N/m)
$l$	-plate length or general body dimension (m)
$m$	-oscillating mass of system (kg)
$n$	-perturbation of longitudinal force on the model (N)
$p(u')$	-probability density function of $u'$
$p$	-instantaneous pressure (N/m <sup>2</sup> )
$\bar{p}$	-mean pressure (N/m <sup>2</sup> )
$p'$	-fluctuating pressure (N/m <sup>2</sup> )
$u$	-instantaneous longitudinal velocity (m/s)
$\bar{u}$	-mean longitudinal velocity (m/s)
$u'$	-fluctuating longitudinal velocity (m/s)
$\bar{u}_l$	-local mean longitudinal velocity (m/s)
$v'$	-fluctuating lateral (y-direction) velocity (m/s)
$w'$	-fluctuating lateral (z-direction) velocity (m/s)
$x, y, z$	-coordinate system as shown in Fig. 2
$I\phi I^2$	-overall admittance of system
$I\psi I^2$	-mechanical admittance of system
$\delta$	-logarithmic decrement of damped oscillations
$\lambda$	-wavelength (m)
$\rho$	-air density (kg/m <sup>3</sup> )
$\delta_{ij}$	-kronecker delta
$\varepsilon$	-error in r.m.s. measurement
$\sigma_{u'}$	-standard deviation of $u'$
$\sigma_{u'^2}$	-variance of $u'$
$\omega$	-circular frequency of system ( $s^{-1}$ )
$\omega_0$	-natural circular frequency of system ( $s^{-1}$ )

$\omega_d$  -damped natural frequency (circular) of system ( $s^{-1}$ )  
 $O( )$  -order of.

- Note\*
1. This table is not complete in that some symbols are not included or are used in other definitions than listed here. In these cases the symbols are locally defined and should not lead to confusion.
  2. The units in which the different quantities are expressed depend on the nature of the individual experiment.

LIST OF FIGURES.

FIG. No.

Spectrum of horizontal wind speed near the ground for an extensive frequency range.....	1
Definition sketches.....	2 - 5m
Mean velocity profiles at the test section.....	6 - 10
Mean velocity variation in the longitudinal direction.....	11
Typical hot-wire calibration curve.....	12
Typical hot-wire verification curve.....	13
Intensity profiles at the test section .....	14 - 18
Intensity variation in the longitudinal direction.....	19
Composite of the three turbulent components for all baffles at the expected stagnation point of the models....	19a
Space correlations at the test section.....	20 - 21
Spectra of longitudinal velocity at the test section.....	22 - 24
Spectrum of longitudinal velocity component at the stagnation point.....	25
Cross-correlation coefficient of the longitudinal velocity.....	26 - 29
Hot-wire instrumentation noise spectrum.....	30
Statistical r.m.s. error of power spectrum measurement with filter and time lag.....	31
Spectrum variation of the longitudinal velocity along the stagnation line flow.(including intensity level variation along the stagnation line flow).....	32 - 41b
Probability density of the longitudinal velocity component.....	42 - 68
Decay of energy spectrum along the stagnation line flow...	69
Vibrations in the z-direction for the square section cylinder AR = 2 .....	70

Results of the energy level variation.....	71 - 121
Variation of the integral scale of turbulence in front of the models.....	122 - 133
Pressure velocity correlations and spectra.....	134 - 139
Free damped oscillations, balance + 30x120mm <sup>2</sup> plate.....	140
In-line oscillations of balance & circular section cylinder AR = 2 .....	141
Typical (initial) force balance calibration.....	142
Typical modified force balance calibration.....	143
Details of systems used, utilized in calculating the mechanical admittance.....	144 - 145
Comparative magnitude of mechanical admittance, load and overall noise spectra.....	146
Measured velocity and load spectra together with the deduced aerodynamic admittance.....	147 - 236
Aerodynamic admittance: Effect of aspect ratio Effect of frontal area Effect of turbulence level Effect of integral scale of turbu- lence.....	237 - 266
Fluctuating and mean drag results.....	267 - 274
Determination of the mean flow direction relative to the rotating hot-wire.....	275
Block diagram for the measurement of the mean and fluctuating drag forces.....	276
Block diagram for the measurement of the lateral and longi- tudinal space correlations of $u'$ .....	277
Block diagram for the measurement of the frequency-dependent correlation coefficient $R_{11} (0, r_2, 0)$ .....	278
Typical probability density function displayer calibration	

circuit..... 279

Block diagram for the measurement of the lateral and longitudinal space correlations of  $u'$  when the model is externally excited..... 280

Block diagram for the measurement of the pressure spectrum..... 281

Block diagram for the measurement of the pressure-velocity space correlation..... 282

# PLATE

Baffles used for the generation of turbulence..... I

Models tested..... II

Models tested..... III

Experimental set-up for the determination of the variation of the wavenumber in front of the models..... IV

Instrumentation used in the determination of the probability density function..... V

Strain gauge balance and shield..... VI

Turbulence baffle; model and balance assembly..... VII

Balance support..... VIII

Modified strain gauge balance..... IX

Mechanism used for the external vibrations experiments.. X

Lateral space correlation..... XI

Lateral space correlation..... XII

Correlation between hot-wire signals..... XIII

Attachment mechanism for the rigidly held model..... XIV

Schematic diagram of the pressure transducer..... XV

Mounting of the pressure transducer..... XVI

Pressure transducer used for the measurement of the fluctuating pressures on the face of the  $AR=2$  plate..... XVII

GENERAL INTRODUCTION

In 1759 when John Smeaton designed the shape of the third Eddystone Lighthouse, he chose the shape of a tree in the belief that over the aeons evolution had designed a structure to withstand the force of the wind. The first Eddystone Lighthouse built about 50 years earlier had perished in a gale. The second by fire.

In the near past there have been failures of major engineering works such as the Tacoma Narrows Bridge in the U.S.A. and that of the Ferrybridge Cooling Towers in England. In the case of the Ferrybridge Towers the fluctuating components of the wind, due to the proximity of the other towers, substantially increased the stress levels in the downstream towers.

Turbulence is a subject which, even today, presents "classical" problems which are far from being solved. It has been tentatively established that turbulence is characterized by a unique and universal flow pattern. At the same time the turbulent field can be looked upon as consisting of two components, one static and one dynamic. That is, we have an oscillating turbulent velocity component superimposed on some mean flow. For the past several decades it has been tacitly assumed that real turbulence as it occurs in nature is too complex to make a useful problem of direct research and most work was directed towards an artificially defined turbulence. The inherent complexity of the terms in the equation of motion did not permit more than a general recognition of effects and no general solution of the flow pattern of turbulence was attained. As a matter of fact, the early authors were just as close to a solution as were later authors. Indeed, the subject of turbulence, in general, has stimulated some of

the keenest intellects in historical times, yet many areas of the turbulence problem remain unconquered.

In recent years, the desired for more realistic design criteria for both Earth-fixed structures and aircraft has focussed increasing attention upon the prediction of the response of such structures to turbulence in the wind. Although the present work is primarily interested in Earth-fixed structures, applications of the present investigation could also be met with in aircraft aerodynamics, e.g. the aerodynamic characteristics of flat plates could be related to air brakes.

The general solution of the problem requires:

- (i) to obtain an adequate description of the atmospheric environment;
- (ii) to relate the atmospheric wind velocity (input) to pressures, forces, and moments on the body (outputs);
- (iii) to derive the motion response of the body, knowing the forces acting upon it.

The first two subproblems are currently under intensive investigation in many quarters, and the methods and information needed are slowly becoming available.

From the first two problems the second one presents the most interesting challenge as it involves the interaction of the model-flow system.

Unsteadiness of the flow affects the total resistance of an immersed body in three ways which could be assumed distinct and to some extent predictable. The velocity-dependent drag is so affected that it is not the same as for steady flow. A force is exerted on the body because of the pressure gradient required to



accelerate the ambient flow. An inertial force occurs because of additional accelerations throughout the fluid caused by the presence of the body. It follows that if separation occurs (as it usually does) the geometry of the wake varies with time and both the drag and the inertial force are affected markedly.

One way of estimating the three contributing effects is a series of experiments. In the present work the investigation is carried out only on the upstream (to the model) turbulent field. The downstream turbulent field has already been studied by a number of workers, (Ref. 1, 2, 3, 4).

The way the different parameters change as these turbulent field parameters approach the model is the subject of the first part of the present thesis. Bearman (Ref. 5) has shown that the turbulence level — based on the local mean velocity — increases as a flat plate is approached from upstream. This is taken further by investigating the change in the longitudinal turbulence level, by considering the field in front of the square and circular section cylinders.

The last of the above subproblems involves the application of well-known principles by well developed techniques, and hence the investigation methods used could be considered to be in a quite satisfactory state.

The dynamic response of bluff structures immersed in turbulent flow fields could exhibit a variety of features depending on the mechanism by which a bluff body may be set into some mode of vibration by the action of the wind. Oscillations may be induced by some form of aerodynamic instability such as galloping or caused by regular shedding of vortices. The oscillatory forces may develop from the general unsteady nature of the structure's

immediate wake.

In general the oscillations could be divided into the following categories:

- a) in-line oscillations,
- b) oscillations at right angles to the mean flow direction,
- c) a combination of the above two cases which refers to the general case.

In the second part of the present work, in-line oscillations are of primary importance. These oscillations are produced by fluctuating forces induced in the direction of the mean flow velocity, i.e. the fluctuating drag forces. Prediction of these forces in any degree of accuracy presents an extremely difficult problem in fluid dynamics. It is for this reason that a high proportion of research effort has been directed towards predicting fluctuating drag forces. A series of highly sophisticated wind tunnel experiments, in which the properties of the atmosphere and the structure were correctly modelled, could probably lead to an accurate estimation of the above forces. At the same time the required sophistication of the wind tunnel experiments are not a practicable proposition and consequently the need arises of some form of empirical prediction method.

As a first step in the analysis of the experimental data a linear system could be assumed in which the power spectral density function of the random input disturbance and the output response are related through the frequency-response characteristics of the system. The general relations for linear systems between power spectra of the random input disturbance and the output response are used to relate the spectrum of the structure load in rough air

to the spectrum of the atmospheric turbulent velocity.

The coherence function being one of the most important functions by which the turbulent field could be described ( in relation to the correlation of the forces over the body) an attempt is being made, in the third part of the present thesis, in producing an analytical model by which the coherence function could be calculated from the velocity power spectrum.

PART I

(References are on pp 131 - 139  
in Volume II)

ON THE FLOW PHENOMENA RELATED TO BLUFF BODIES

IMMERSED IN TURBULENT FLOW FIELDS

PART ION THE FLOW PHENOMENA RELATED TO BLUFF BODIESIMMERSED IN TURBULENT FLOW FIELDS1. INTRODUCTION.

The first sub-problem of the overall problem of predicting the dynamic response of structures to turbulence in the atmospheric boundary layer - as pointed out in the "General Introduction" of the present thesis - is the statistical description of the turbulent wind properties. To date the research effort into the fundamental aerodynamics of even simple shapes exposed to turbulence has been sparse. Notable exceptions are the investigations of Bearman (Ref. 5) into the forces on rigid flat plates and of Vickery (Ref. 6) into those on rigid square cross-sectioned cylinders. No work, known to the author, has been carried out on the interaction of the structure-flow field when the model vibrates, or on how the turbulent field changes as the structure is approached, especially for in-line phenomena. This part of the report presents an investigation of this question. The investigation goes on further than a mere statistical description of the turbulence field itself, in that, it tries to show how the turbulence field changes as it approaches the model. In this way an attempt is being made to look deeper into the questions arising when we consider the second subproblem mentioned in the "General Introduction". Oscillations of the model produce their own changes in the approaching ( the model ) turbulent field and this interaction is looked at.

Definition of the atmospheric environment requires an adequate presentation of the ground atmospheric boundary layer formed by the wind blowing over the earth's surface. It extends to altitudes of the order of four hundred metres and hence is shared both by buildings and low-flying aircraft. It is typically a non-homogeneous region of strong vertical shear and severe turbulence with intensities of the order of 20% or more. Furthermore, its properties depend on such variables as atmospheric stability, type of terrain, altitude, e.t.c. ( Ref. 7, 8, 9 ).

Following standard procedure the definition of the turbulent field is carried out by determining the velocity profiles, the turbulence level profiles, the three integral scales of turbulence,  $L_x$ ,  $L_y$ ,  $L_z$ , by considering the respective space correlations, the spectra of the longitudinal velocity components at the test section, the variation of the longitudinal velocity spectrum in the x-direction as well as the probability density function of the longitudinal velocity component at the test section.

An overall picture of the turbulent wind properties could be obtained, as it has been shown by Davenport ( Ref. 10 ), by Etkin ( Ref. 11 ), and Harris ( Ref. 12 ), by specifying the general two-point cross-spectrum or, more conveniently the coherence function. The coherence of the free flow ( without the model ), as well as the change of the coherence function in front of the model when this is held rigidly and when it is free to oscillate, are looked at. At the present there are few

measurements of the coherence function in the atmospheric boundary layer and for the purpose of predicting the structural response, it is necessary to resort to a simplified model of the natural wind, which retains as many of its essential features as possible. The simplest and most useful model, isotropic turbulence, has been adopted by several authors, Davenport ( Ref. 10 ) Vickery ( Ref. 6 ). The turbulence fields in this investigation are also ( almost ) isotropic and their use could be justified by the fact that a number of fundamental wind tunnel studies of the interaction of structures with the turbulent wind have employed grid-generated turbulence as a simulation of the natural wind. It is well known that such turbulence has approximately isotropic characteristics, ( provided the suitable test section downstream of the grid is found ).

In the present work no attempt is being made to simulate the atmospheric boundary layer precisely, but rather the approach has been to provide a variety of controlled turbulence fields so as to study the effect of turbulence parameter changes. However, an awareness of the atmospheric problem is reflected in the choice of the turbulent field parameters to be realistic atmospheric values as far as the restriction of uniformity, homogeneity and isotropicity allows.

Attenuation or amplification of the  $u'$ -component, as the model is approached from upstream is investigated by considering the probability distribution of the  $u'$ -component.

The way the energy level of the different eddies develops



as they approach the model is investigated and at the same time the way the spectrum of the longitudinal component of the velocity changes when the model is held rigidly and when the model is free to oscillate is looked at.

Great interest is attached to the integral scale of turbulence in relation to the dimensions of the body. The scale of turbulence could dictate, up to a certain extent, the degree of the correlation of the fluctuating forces on the model. Consequently the variation of the integral scale of turbulence in front of the model is investigated. This is done under the following conditions and for the undermentioned reasons:

1. For the empty wind tunnel along its central line and upstream of the test section; this constitutes part of the definition of the turbulence field under consideration.
2. Investigation of the variation of the scale of turbulence in front of the rigidly held model.
3. Investigation of the change of the turbulence macroscale in front of the freely oscillating model.  
Examination of the change occurring in the scale of turbulence under the last two conditions give us an indication of the effect the oscillating model has on the scale of turbulence in comparison with the case of the rigidly held model. In this way the model-flow interaction is partly examined.
4. Looking at the problem more deeply the effect of individual vibration frequencies have on the macroscale of turbulence is looked at. For this reason the model is externally excited at discrete frequencies.

In understanding the flow induced vibrations of structures immersed in turbulent flow fields it is important to study both the distortion of the turbulence field as it approaches the body and the pressure fluctuations on the body, (Ref. 13, 14, 15, 16). Until recently the structural engineer has been concerned about wind loading on structures primarily in regard to design of the structural frame of the building. However, current architectural practice is to use large areas of glass windows, thin cladding panels of marble, granite, stainless steel or aluminium and exterior surfaces with features which project outward from the generally plane wall. This combination of trends results in the outer skin of modern high-rise buildings being susceptible to wind damage. Unfortunately, the instantaneous wind pressure on a localized area of a building varies greatly with both time and position and of course, with the geometry of the surface. For both the above reasons a study of the fluctuating pressures was carried out. The pressure spectrum on the surface of the  $AR=2$  flat plate at the stagnation point was measured; measurements were also made of the correlation between the fluctuating pressures at the stagnation point and the upstream velocity.

## 2. LITERATURE SURVEY AND GENERAL DISCUSSION OF THE FLOW

### PHENOMENON

#### 2.1 Atmospheric Turbulence

In comparison with steady streamline flow, the atmosphere possesses remarkable variability. The flow of air over surfaces of varying roughness and temperatures produces a random motion termed turbulence. This is the significant characteristic of air flow, on which depends the rapid diffusion of properties such as momentum, heat, water vapour and pollutants. The presence of buildings, especially tall buildings, increases surface roughness and this has considerable influence on the structure of the wind about them.

In the early study of atmospheric turbulence, detailed properties of the flow were avoided, since complex equipment was required for their observation, recording, and analysis. Instead virtual diffusivities, analogous to molecular diffusion, were derived with mean values of the motion. Since about 1950, statistical concepts have been employed with field data to understand the processes involved and the resultant structure of turbulence.

##### 2.1.1 The Structure of Turbulence.

In general the scattering and mixing of the flow is indicated by the intensity or level of turbulence. The turbulence intensities probable in the atmosphere, and of interest in building research studies, are, at least 20% - 35% and possibly greater. Contributions to the kinetic energy can be determined from analysis of the continuous range of eddy sizes involved in the motion via spectral analysis or correlations within the fluctuating component, (Ref. 17). There is a range of scale lengths, or eddy sizes, through which the tur-

bulent flow exists. Much of the energy is available in eddies of a scale characteristic of the distribution of the mean velocity (the integral or macroscale of turbulence,  $L_i$ ). Significant eddies would be expected to be about the average building height. In the 6 - 30m air layer above the ground important eddies would lie in the range 3 - 90m. Measurements taken by pressure gauges indicate the presence of gusts of period 0.1s so that a range of frequencies of up to 10Hz at least should be examined.

The unsteadiness of the wind both in magnitude and direction is the result of several different phenomena; there are large-scale low-frequency phenomena associated with diurnal effects and the movement of large air masses on a continental basis; there are relatively high frequency effects caused by thermal convective instability due to the absorption of the heat from the sun and, finally, what turns out to be of most importance from the standpoint of aerodynamic loads, the turbulence from surface roughness and the high viscous shear in the boundary layer.

From the point of view of estimating wind loads, it is important to know certain statistical properties of the turbulence. Of particular importance are the probability density and the power spectral density functions of the velocity components and the power spectral density function of the cross-correlation coefficients.

#### 2.1.2 Probability Density Function of the Horizontal Wind Speed.

The probability density function of the wind velocity has been examined by a number of writers (Ref. 18,19,20,21) and shown to agree fairly well with the familiar Gaussian probability density

function:

$$p(u) = \frac{1}{\sqrt{2\pi} \sigma_u} e^{-\frac{(u-\bar{u})^2}{2\sigma_u^2}}$$

From a study of "one - second" wind velocity measurements taken over a large number of separate five-minutes periods on a 350 ft. mast, Huss and Portmann (Ref. 21) concluded that: "The assumption of a normal frequency distribution curve for representing the wind - velocity distribution, while not accurate for any given case, would appear to be justifiable for a large number of cases".

In this context it must be noted that turbulence, although it is the sum of a large number of processes (velocity fields of elementary vortex lines), these processes are not completely independent. This independence is a prerequisite for a true Gaussian process. The small departures from a Gaussian probability distribution are, moreover, the most interesting feature of turbulence; for instance, the triple products like  $\overline{u'^2 v'}$  which would be zero in a Gaussian process, are connected with energy transfer by the turbulence, either from one point to another or one eddy size to another. The non-linearity of the Navier-Stokes equations is responsible.

### 2.1.3 Power Spectral Density of the Horizontal Wind Speed.

The energy of the wind is widely distributed in frequency as shown in fig.1 (Ref.10). The energy of particular importance is represented by the peak at the right-hand end of this curve which is caused by surface roughness, viscous shear, and thermal instability. Since the effects of viscosity and roughness vary as the square

of the velocity the thermal effects become relatively small at the higher velocities. It is reasonable, therefore, to conclude that this peak is due to roughness and viscosity.

The very low energy level in the gap between that peak and the next one that has a period of 12 hours or greater is of importance. First of all, it becomes a relatively simple matter to simulate this right hand peak with reasonable accuracy in the wind tunnel, while ignoring the lower frequencies; secondly, the natural frequencies of large modern buildings characteristically lie in this range.

The shape of the spectrum will depend, to a large extent, on the local surface roughness. On the other hand, it has been shown by Davenport (Ref. 22) that if the spectrum is plotted in the non-dimensional form  $\frac{f S_u(f)}{K \bar{u}^2}$  (where K is a surface friction coefficient) against a wavenumber  $f/\bar{u}$ , available data are in reasonable agreement over a large range of the value of the coefficient K, representing, for example, "open grassland" conditions with say, "wooded areas".

#### 2.1.4 Spatial Correlations.

When considering the fluctuating loads on large buildings or generally large structures, the spatial correlation of the velocity fluctuations is clearly important. A measure of the spatial correlation can be obtained by considering the co-variance  $\overline{u'_1 u'_2}$  of simultaneously fluctuating velocity components at two points displaced by a distance y.

A convenient correlation is then:

$$R_{11}(0, u_2, 0) = \frac{\overline{u'(y) u'(y+dy)}}{\{\overline{u'^2(y)} \overline{u'^2(y+dy)}\}^{1/2}}$$

$$\text{and if } \overline{u'^2(y)} \approx \overline{u'^2(y+dy)}$$

$$\text{then } R_{11}(0, u_2, 0) = \frac{u'(y) u'(y+dy)}{u'^2(y)}$$

In turbulent flow, when the displacement between the probes approaches zero, it can be expected that this coefficient will approach unity in the limit, whereas it will approach zero as  $y$  becomes large. The mean integral scale of turbulence is given by the integral of this coefficient with respect to  $y$ .

It is also useful to consider a frequency-dependent correlation coefficient based on the cross-spectrum  $S_{u_1 u_2}(f)$  of the velocities  $u_1'$  and  $u_2'$  a distance  $y$  apart.

$$\text{Then } R_{11}(0, u_2, 0)(f) = \frac{S_{u_1 u_2}(f)}{\{S_{u_1}(f) S_{u_2}(f)\}^{1/2}}$$

$$\text{where } u_1' = u'(y) \quad \text{and} \quad u_2' = u'(y+dy)$$

$$\text{or } R_{11}(0, u_2, 0)(f) = \frac{S_{u_1 u_2}(f)}{S_{u_1}(f)}$$

$$\text{if we assume that } S_{u_1}(f) = S_{u_2}(f)$$

Generally it is found that the correlation can be expressed in the form:

$$R_{11}(0, u_2, 0)\left(\frac{fy}{u}\right) = e^{-c\left(\frac{fy}{u}\right)}$$

where the value of  $c$  will depend on the surface roughness and thermal stability.

This relation, deduced by curve fitting to experimental data should be taken only as an approximation.

The so called scale of turbulence is, as pointed out above, the integral of the correlation coefficient over all values of  $y$ , so that the integral of the above coefficient will give the scale of

turbulence at a specific frequency.

The scale therefore becomes:

$$\int_0^{\infty} e^{-c \frac{f y}{\bar{u}}} dy = \frac{1}{c} \cdot \frac{\bar{u}}{f}$$

If the turbulence is thought of as consisting of eddies occurring at different frequencies then with each frequency there is a corresponding wavelength  $\frac{\bar{u}}{f}$ . Therefore we can look upon the frequency-dependent scale as the longitudinal wavelength divided by the constant  $c$ .

Davenport (Ref.11) has reviewed available measurements of the correlation coefficient in the earth's atmosphere for different surface conditions and suggests that the vertical scale of the longitudinal velocity is about 1/6 to 1/8 of the longitudinal wavelength (i.e.  $c=6-8$ ), and the along-wind scale is about 1/6 of the wavelength. The cross-wind scale was found to be about 1/10 the wavelength in unstable conditions but as small as 1/25 to 1/40 in stable conditions.

Unlike the spectrum itself, the cross-spectrum  $S_{u,u'}(f)$  can be a complex quantity having both in-phase and quadrature components. The existence of the quadrature component can be taken to indicate a preferred orientation of the eddies and therefore only occurs when there is asymmetry present in the flow.

The square of the absolute value of the cross-correlation spectrum is termed the "coherence". For practical purposes it is probably quite adequate to neglect the quadrature spectrum, as such, and take the cross-correlation as equal to the square root of the coherence.

$$\text{Coherence} = \left| \frac{S_{u,u'}(f)}{S_{u'}(f)} \right|^2 \approx e^{-2c \frac{f y}{\bar{u}}}$$



The coherence is expected to present the degree of correlation of the velocity input signals at the two positions.

Knowledge of the coherence (or a coherence function) provides information about the reliability of linear approximations or viewed from another direction it furnishes an estimation of the degree of the uncorrelation of the turbulent field. As the correlation of the signals is looked at as a function of frequency (within a certain frequency band) the coherence is equal to 1 when the signals are completely correlated and it is equal to zero when the signals are completely uncorrelated.

#### 2.1.5 Development of the Energy-content of the Different Eddies

In considering the eddy development, as the different eddies approach the model the aspect of the problem under investigation is the change that occurs in the energy level of each wavenumber as it approaches the model from upstream. When the flow incident on a body is turbulent the external flow obviously is turbulent even in the region outside the boundary layers and the wake. Provided the Reynolds' No. is high enough for the boundary layers to be turbulent, the effects of the incident turbulence on the boundary layers are probably not very significant.

On the wake there must be some effects, but it appears from experiments by Petty (Ref.23) that the effects of the wake on the turbulence in the region outside the boundary layers are statistically unrelated to the effects of the incidence turbulence. The latter effects are amenable to analysis (Ref.24) which is a generalization of the "Rapid Distortion theory" developed by Batchelor and Proudman (Ref.25). The essential physical basis of the theory is that if the turbulence is disturbed rapidly enough by changes in the

mean velocity (produced by the body) then each wavenumber or eddy is distorted separately before it can exchange energy, non-linearly, with the other wavenumbers. This variation in the energy level constitutes part of the investigation in the present thesis.

### 2.1.6 Pressure Fluctuations.

Pressure fluctuations in turbulence were first investigated by Heisenberg (Ref.26), Obukoff (Ref.27), and Batchelor (Ref.28) for the case of isotropic homogeneous turbulence. This work has been summarised by Batchelor (Ref.29). From experimental data, for the practical realisation of isotropic turbulence, namely that behind a grid placed in a uniform air stream, Batchelor estimated the root mean square pressure fluctuation,  $\sqrt{p'^2}$  to be:

$$\sqrt{p'^2} = 0.58 \rho \overline{u'^2}$$

Uberoi (Ref.30) evaluated the root mean square pressure from measurements of second order velocity correlations in grid turbulence and obtained values at several Reynolds' No. The average value was about:

$$\sqrt{p'^2} = 0.7 \rho \overline{u'^2}$$

It has not yet been possible to make direct measurements of pressure fluctuations within a turbulent flow since no general purpose instrument capable of measuring static pressure fluctuations without introducing a major flow disturbance has yet been devised. Pressure measurements have been made in isolated cases, for example by Kobashi (Ref.31) who measured correlations between pressure and velocity in the wake of a circular cylinder in order to obtain the pressure transport terms in the turbulent energy balance. However in one particular type of flow, namely that of turbulent shear flow in the presence of a solid surface it is possible to measure pres-

sure fluctuations on the surface without disturbing the flow in any way, since the pressure sensitive element can be mounted so as to form an essentially integral part of the boundary surface.

A turbulent flow on a rigid surface gives rise to acoustic radiation, the acoustic power of which can be expressed in terms of the pressure fluctuations on the surface (Ref.32). If the surface is flexible the acoustic radiation is amplified. The phenomenon of sound generation by turbulent flow over a flexible structure is important in relation to problems of submarine detection and noise levels inside the fuselage of high speed aircraft. In these problems and more important - in the context of the present work - in the problem of structure fatigue due to boundary layer pressure fluctuations, where calculation of the response of the structure is required, the excitation must be defined in terms of the statistical properties of the wall pressure field. Another interesting aspect of the problem is considered to be the interaction between turbulence in the oncoming air stream and the separation induced pressure disturbances on the model surface. Measurements made by Cermak (Ref.33) on the Bank of America Headquarters Building indicated that turbulence can increase the maximum pressure fluctuations substantially.

## 2.2 On the Mechanics of Flow Around Bluff Bodies.

In general the basic equations defining the chief characteristics of the mechanics of fluid flow past a solid body are the Navier - Stokes equations together with the equation of conservation of mass.

The Navier - Stokes equations are not, generally, integrable over the whole domain of the flow and it has usually been necessary to discard the highest order terms involving the viscosity of

the fluid.

The Navier - Stokes equation is given by:

$$\rho \frac{Dv_i}{Dt} = \rho F_i - \frac{\partial P}{\partial x_i} + \frac{\partial}{\partial x_j} \left\{ 2\mu \left( e_{ij} - \frac{1}{3} \Delta \delta_{ij} \right) \right\}$$

If we discard viscosity, the above equation reduces to:

$$\rho \frac{D\vec{u}}{Dt} + \frac{\text{grad } P}{\rho} = 0$$

This is the Euler equation, which together with the equation of conservation of mass, they are said to define the motion of an ideal fluid. If we also assume that the flow is irrotational, the equations define a potential flow.

The equations of potential flow cannot describe a physically real flow past a solid boundary as the order of the Euler equation allows only one boundary condition at the surface to be satisfied, whilst physical considerations reveal that it is necessary to stipulate two. In addition the condition of zero vorticity is invalid for a streamline which lies on the surface of a solid body.

In the case of a real flow, the streamlines follow the surface of a solid body for some time, and then become separated from it and continue into the fluid. The resulting flow pattern is characterised by a surface of discontinuity which corresponds to a surface on which the vorticity is non-zero.

When such discontinuities are admitted, the equations of motion for an ideal fluid do not give a unique solution. In addition, to a flow in which the streamlines follow the surface of the body, there is an infinite number of separated flow solutions. If the equations of an ideal fluid are being used it is now necessary to introduce some criterion which will allow a particular solution to be chosen.

There are problems, however, in which no flow separation takes place from the surface of the body, and the body is said to be

streamlined. In such a case the effect of viscosity is negligible except in very small regions along the boundary of the body and in the wake, which in this case is very thin and takes the form of a vortex street.

Refinements to the potential flow solution for a streamlined body have been made with the advent of boundary layer theory, which essentially constitutes a perturbation technique. A first approximation in the estimation of the flow characteristics is made using a classical potential flow method. Then knowing the pressure and velocity distribution approximately at the boundary of the body it is possible to use the boundary layers equations (which include viscosity terms) to refine the solution. Unsteady effects in the wake can be estimated using the classical theory of vortex motion together with the potential motion around the body itself.

When flow separation is admitted, as in the case of flow around bluff bodies, it is immediately obvious that no perturbation techniques are possible. The fluid can no longer be treated as a quasi-continuum where the effect of viscosity and consequently rotation can be considered as confined to very small regions of the flow field of interest.

Many attempts have been made to obtain solutions to the case of steady flow past bluff bodies using the equations of potential flow. This has taken the form of obtaining particular solutions to the equations defining potential flow with the help of arbitrary criteria, thereby setting up flow models. Numerical solutions of the Navier-Stokes equations together with the equations of conservation of mass, have been used to study the case of unsteady flow, but only for low Reynolds' Nos.

Kirchhoff (Ref. 34) has developed a free streamline model for steady flow past a flat plate at  $90^\circ$  incidence. The free streamline solution predicts a coefficient of resistance but it describes an unrealistic type of flow which cannot persist as the surface of discontinuity defined by the free streamline soon breaks up into individual vortices.

An interesting flow model which is a modification of Kirchhoff's method has been developed by Roshko (Ref. 35) in which the base pressure is taken as a disposable parameter which is adjusted to fit the experimental data.

The problem of unsteady flow past bluff bodies has been mainly studied by numerical means. Thom (Ref. 36) initiated an approach which has been furthered by Fromm (Ref. 37) and in which the Navier-Stokes equations and the equation of conservation of mass for an incompressible fluid are solved numerically. Flows past bluff bodies up to Reynolds' numbers of 300 are investigated, and wake development and variation of induced drag is studied.

Recently unsteady flows past bluff bodies have been studied semi-empirically with the use of flow models. Sarpkaya (Ref. 38) has provided a flow model which includes the effect of an acceleration of the ambient flow. The strength and location of these vortices and the rate of change of circulation is not specified, and can only be determined by experiment.

To take a broad view of the problem of unsteady flow past a bluff body, it is obvious that the techniques used in aerofoil theory, i.e. an outer potential motion and a boundary layer effect, are ineffectual as the wake induced by a bluff body cannot be treated as a perturbation of a steady flow. Potential flow models can not enable closed solutions, which are realistic and exhibit scale effects, to be obtained.

### 3. THEORETICAL CONSIDERATIONS

#### 3.1 The Probability Distribution of the Longitudinal Velocity Component.

The velocity of the flow at a point in a turbulent field is subjected to the influence of a large number of random eddies. If we could make a rough use of the Central Limit Theorem, -"For an arbitrary population with mean  $\bar{x}$  and finite variance  $\sigma_x^2$ , the cumulative distribution function  $G_n(x)$  of the sampling distribution of  $z = (\bar{x} - \bar{x})\sqrt{n}/\sigma_x$ , for samples of size  $n$ , approaches the normal distribution (uniformly in  $z$ ) as  $n \rightarrow \infty$ , that is,

$$\lim_{n \rightarrow \infty} G_n(x) = \frac{1}{\sqrt{2\pi}} \int_{-\infty}^z e^{-u^2/2} du$$

$\bar{x}$  = sample mean

-we might expect that this velocity has approximately a normal probability distribution.

Stated somehow differently it could be said that, under general conditions the distribution of the sum of a large number of random variables tends towards a normal distribution.

The energy containing eddies have their origin in a mechanical stirring action, i.e. the passage of air through the baffle holes, and it is therefore expected to give rise to a velocity at a point distributed approximately according to an error law.

In general we are much more interested in the interrelation between the velocities at two points i.e. the joint distribution of the velocities. In other words it could be said that we are interested not at what happens at one point in the flow field or at a point on the surface of the body but on how good is the correlation of the

impact of the eddies over the whole model surface.

It is thought that the argument used above for the probability distribution of the velocity at a point would not serve for the joint distribution. The equations of motion and of continuity dictate the velocities at the two points and these are unlikely to permit a distribution of the pure chance type. The inertia terms of the equation of motion, in particular, will exercise a strong influence on the relation between the two velocities and will lead to such effects as difference between the probability distribution of positive relative velocities, i.e. the extension of the fluid between the two points, and a difference between the probability distribution of negative relative velocities, i.e. the contraction of the fluid between the two points. The analysis that should be followed in considering the joint probability distribution is presented in appendix A.

The relation between the velocities at the two points is very strong when the points are close together and the difference between the velocities will have a probability distribution which is governed to a large extent by the Navier-Stokes equation.

Eddies smaller than a certain size owe their existence entirely to the linear transfer down the spectrum, and the smaller the eddy the more prolonged, so to speak, has been the influence of the non-linear terms. We may expect that the statistical characteristics of the small eddies would reflect this influence, and that the distribution of the velocity difference  $u_1' - u_2'$  will probably depart furthest from a normal distribution at very small values of  $r$ ; ( $r$  = separation distance between the points considered).



### 3.2 The One-Dimensional Spectrum

The kinetic energy of the turbulence fluctuations could be analysed according to its distribution over the various frequencies occurring in these fluctuations. If  $S(f) df$  is the contribution to  $\overline{u'^2}$  of the frequencies  $f$  and  $f+df$ , then the distribution function  $S(f)$  has to satisfy the condition:

$$\int_0^{\infty} S(f) df = \overline{u'^2}$$

As it can be proved in any book on the treatment of random quantities, e.g. (Ref. 39,40), the spectral density function  $S_{u'}(f)$  and the correlation function  $\phi(x)$  form a Fourier transform pair. Consequently it could be said that the one could be found from the other, either analytically (if an analytical equation of the function to be integrated is known) or graphically. This is only a theoretical method. The experimental determination of the spectrum function as well as that of the correlation function, with our present methods, are not free from inaccuracies. In general, a correlation function is measured more accurately when the distance between the two points is not too small while the spectrum function is measured more accurately in the higher frequency range.

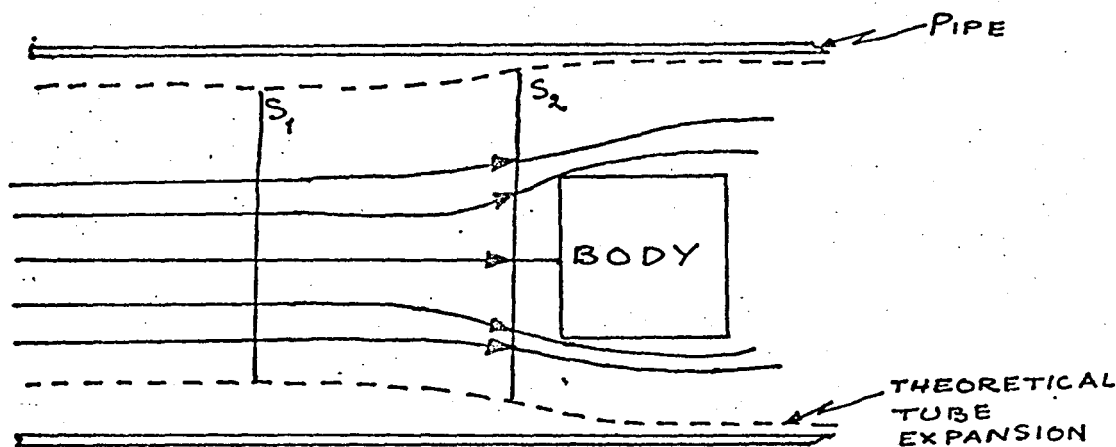
The spectrum measured by the hot-wire is a one-dimensional section of what is in fact a three-dimensional spectrum function.

### 3.3. The Wavenumber Variation as the Flow Approaches the Model.

It has been known empirically, for many years, that a sharp contraction in the area of a pipe, with the consequent

acceleration of the stream, produces a substantial decrease in the kinetic energy of the turbulence relative to that of the stream.

Theoretically the flow round a bluff body could be assumed to represent the opposite to the above case. If we consider an imaginary pipe, in the flow, as shown in the figure below,



then as we move downstream the principle of conservation of mass would require that: cross-section  $S_1 < \text{cross-section } S_2$ . (Both cross-sections are taken in front of the model).

In such a case Batchelor's "Rapid Distortion Theory" (Ref. 25) could be assumed to apply. The turbulence will be distorted by stretching and twisting of the vortex line filements as they are convected past the body.

The above theory requires the following assumptions to be made:

- a) The mean flow is irrotational. This in turn requires that the analysis is limited to that region of the flow outside the boundary layers and the wake.
- b) The fluctuating component is much smaller than the mean flow velocity, i.e.  $\sqrt{u'^2} \ll \bar{u}$  and the only contribution to vortex line stretching and twisting comes from changes in the mean flow.

c) The time a fluid element requires to be swept past the body is small so that the turbulent energy dissipated by the viscous stresses is small. This leads to the condition  $\frac{L}{D} \gg \frac{\sqrt{\epsilon}}{\bar{u}}$ .

Hünt (Ref.24), with these assumptions, has shown that the problem reduces to the solution of a number of linear equations in which there will be no interaction between the different wavenumbers of the turbulence as they approach the model.

#### 4. GENERATION OF TURBULENCE

##### 4.1. Baffle Design

The basic baffle design objective for this work was to produce uniform and homogeneous turbulence of various scales but of approximately the magnitude of the model width ( a characteristic body dimension), together with turbulence intensities in the range 10% - 20%. In general, these baffle design requirements are essentially separable. The primary determinants of the turbulent flow are:

1. The drag per unit area, since it directly determines the amount of turbulent energy created by the baffle.
2. Some physical dimension associated with the baffle since this determines the dimensions of the initial wakes.

It was thought that by using a baffle instead of a grid, use could be made of the fact that the flow in a free jet attains high levels of turbulence intensity and that the turbulent scale increases with the jet dimensions downstream of its origin, so that relatively large-scale turbulence can exist in large free jets. It was intended that the test section could be situated in the turbulent region of the jets where the jet central core and the mixing region blend into a complete turbulent stream. The fact was also considered that the turbulence intensity varies rapidly with downstream distance, while the turbulence scale increases slowly due to the dissipation of the high frequency turbulence components. Studies by Van der Hegge Zijnen (Ref. 41) suggested that at about 20 slot diameters downstream of the baffle the intensity of turbulence would be roughly 15 to 20 percent and other work by Corssin and Uchroil (Ref. 42) on a round jet suggested that, at this distance, the tur-

bulence would be approximately isotropic and the scale would be about  $1/20$  of the jet width.

The design process for a baffle using the above is straight forward. The width of the slot determines the scale and the required intensity is obtained by using a certain solidity and downstream distance. Two more baffles were used with only circular holes of different diameters to produce different turbulent flow fields.

#### 4.2 Baffle Development

When the baffle design was finalized as above and built, it was generally found that the slotted baffle did not conform closely enough to design requirements. This baffle was equipped with two movable plates so that the slot height could be varied at will and thus producing different turbulent fields.

The first problem encountered was that, with the slotted baffle the issuing jet was oscillating in a plane perpendicular to the slot's length. This effect, was later found, was also observed by Whitelaw (Ref. 43). Three rows of holes on each side of the slot were therefore drilled with the hope of stabilizing the jet and preventing its oscillations.

However, a further problem remained, in that the flow at the working section was not as uniform as desired. It became apparent, and has also been reported by others, that the flow is more sensitive than expected to the grid construction tolerances (which in this case with the movable plates in the slot were quite loose), especially for large solidities. A non-uniformity of the flow field was traced back - by a trial and error method - to these plates which were made of rather thick - in comparison to the thickness of the baffle itself - perspex. Consequently it was decided to totally

remove the plates. This decision resulted in the use of the other baffles for the production of different turbulent fields. Photographs of the baffles used are shown in Plate I.

#### 4.3 Final Baffle Design and Verification

The final outcome of the above considerations was three baffles producing longitudinal scales between, approximately, 23mm and 26mm and intensities from 8% to 11% at the intended model position. The slotted baffle had a 36.5mm wide slot along the centre-line width of the wind tunnel test section. The holes mentioned parag. 4.2 were proved satisfactory in stabilizing the jet. The other two baffles had holes of 30mm and 50mm. In the subsequent paragraphs the different turbulent fields are named after the baffle producing them. The overall dimensions of the baffles were 350mm x 180mm, as shown in Plate I.

An indication of the degree of anisotropy present at the working section is given in Fig. 19a, which shows mean values (over the test section) of the three turbulent velocity components for each turbulent case considered. Anisotropy is present in all cases but it is most severe for the case of the 50mm holes baffle. Other workers in the past have found that some anisotropy is inherent in grid or baffle generated turbulence. The flow at the test section was also investigated to determine the local gradients of the mean velocity there.

The location of the baffle in the wind tunnel as well as the distance between the baffle and the test section are shown in Fig. 5. The insert to Fig. 5 presents the method of the baffle attachment to the walls of the wind tunnel.

## 5. THE STRUCTURE OF THE BAFFLE GENERATED TURBULENCE FIELD

### 5.1 General

In connection with the different aspects of the problem examined in this investigation the turbulent field generated by each baffle was defined by considering the following parameters of the turbulent field in the empty test section:

- a) Intensity of turbulence,
- b) Scale of turbulence and variation of the turbulent scale in the longitudinal direction,
- c) The spectrum of the longitudinal velocity component,
- d) Probability density function of the longitudinal velocity component,
- e) Space correlations and two-point cross-spectrum of the turbulent fields,
- f) Spectrum variation along the stagnation line flow.

### 5.2 Intensity of Turbulence.

A single hot wire was used to measure the  $u'$ -component of the turbulent intensity. The method of calibration of the hot-wire is presented in appendix 8. The intensity measurements were made at various values of  $y/Y$  for different values of  $z/Z$ , at the test section. The variation of the  $u'$ -component of the turbulence intensity in the longitudinal direction along the stagnation line for the empty tunnel was also investigated.

### 5.3 Scale of Turbulence and Variation of the Turbulent Scale in the Longitudinal Direction

The scale of turbulence in the three directions,  $(x,y,z)$  was determined from the respective space correlation. These measure-

ments were made at the test section. The variation of the longitudinal turbulent scale along the wind tunnel central line and in front of the test section was also investigated. The effect the model presence had on this variation was looked at.

#### 5.4 The Spectrum of the Longitudinal Velocity Component.

The spectrum of  $u'$  was measured at three lateral positions at the test section for each turbulent field, i.e.  $y/Y=0.5$ ,  $z/Z=0.0$  and  $y/Y=0.5$ ,  $z/Z=+0.318$  and  $y/Y=+0.582$ ,  $z/Z=0.0$ .

#### 5.5 Probability Density Function of the Longitudinal Velocity Component.

The probability density  $p(u')$  represents the rate of change of probability with amplitude; where probability denotes the probability that the amplitude of the sample record will be in a particular narrow amplitude window at various amplitude levels.

The probability density function of the  $u'$ -component for the empty tunnel was only investigated for the slotted baffle produced turbulent field. This was because of time limitations. The way the probability density function changes along the wind tunnel central line (which corresponds to the stagnation line flow when the model is present) was investigated. The results obtained were compared with those obtained when the model was present.

#### 5.6 Space Correlations and Two-point Cross-spectrum of the Turbulent Field.

The space correlation of the  $u'$ -component of the velocity was measured in order to obtain the integral scales of turbulence. The measurements made are reported in section 5.3.



As the experiments were concerned with the forces on bodies the lateral correlation of the velocity (i.e. the correlation along the length of the model) is of the utmost importance.

The lateral correlation is also of interest if it is considered in terms of frequency.

The correlation coefficient of the longitudinal velocity perturbations  $u_1'$  and  $u_2'$  at two points  $y$  apart, is:

$$R_{11}(0, x_1, 0) = \frac{\overline{u_1' u_2'}}{\left\{ \overline{u_1'^2} \overline{u_2'^2} \right\}^{1/2}}$$

$x_2 = y$

If  $e_1'$  and  $e_2'$  are corresponding hot-wire voltages it can be shown (appendix C), that, if the hot-wires sensitivities are nearly equal, and if  $\overline{u_1'^2} \approx \overline{u_2'^2}$  then:

$$R_{11}(0, x_1, 0) \approx \frac{\overline{(e_1' + e_2')^2} - \overline{(e_1' - e_2')^2}}{\overline{(e_1' + e_2')^2} + \overline{(e_1' - e_2')^2}}$$

If the signal can be presented by a stationary time series (i.e. its statistical properties do not vary with time), then the correlation coefficient  $R_{11}(0, x_1, 0)$  can be calculated from measurements of  $\overline{(e_1' + e_2')^2}$  and  $\overline{(e_1' - e_2')^2}$  made at different times.

By obtaining the spectrum of each in turn, a frequency-dependent correlation coefficient of the turbulence could be obtained as:

$$R_{11}(0, x_1, 0) (f) = \frac{\text{Spectrum of sum} - \text{Spectrum of difference}}{\text{Spectrum of sum} + \text{Spectrum of difference}}$$

The instrumentation used in measuring the above quantities is shown in a block diagram depicted in Fig. 278.

### 5.7 Spectrum Variation Along the Stagnation Line Flow.

The flow field in front of number of models was investigated to examine the variation of the spectrum along the stagnation line flow. In order to have some measure of comparison, between the changes induced in the spectrum by the different models, the variation of the spectrum of the longitudinal component of the velocity along the centre line of the wind tunnel and upstream of the test section at different positions was measured.

The results obtained from all the measurements mentioned in this chapter are discussed in section 8.

## 6. DESCRIPTION OF APPARATUS.

### 6.1 Model Hardware.

Conventional wind tunnel practice restricts the frontal area of a model to about five percent of the test section cross-sectional area, so that blockage effects are kept at a reasonable low level. Consequently in these experiments whenever possible the two-dimensional flat plates and solid bodies used had a width of 3cm, thus keeping the model frontal area within or near the above limit. The purpose of the investigation required models of greater frontal area to be used. In these cases blockage corrections were applied. The plate edges were chamfered at an angle of  $45^\circ$  and mounted with the largest plane surface looking upstream.

The models included:

Rectangular plates of:

- a)  $30 \times 30 \text{ mm}^2$
- b)  $30 \times 60 \text{ mm}^2$
- c)  $30 \times 120 \text{ mm}^2$  (blockage cor. applied)
- d)  $42.5 \times 42.5 \text{ mm}^2$
- e)  $60 \times 60 \text{ mm}^2$  (blockage cor. applied)
- f)  $85 \times 85 \text{ mm}^2$  (blockage cor. applied)
- g)  $120 \times 120 \text{ mm}^2$  (block. cor. applied)

Circular plates of:

- a) 20mm dia.
- b) 40mm dia.

Parallepipeds of:

- a)  $30 \times 30 \times 30 \text{ mm}^3$
- b)  $30 \times 30 \times 60 \text{ mm}^3$  (blockage cor. appl.)
- c)  $30 \times 30 \times 120 \text{ mm}^3$  (blockage cor. appl.)

Circular cylinders of

30mm dia. and AR of:

- a)  $AR=1$
- b)  $AR=2$  (blockage cor. applied)

c)  $AR = 4$  (blockage cor. applied)

All models were made of perspex with the parallelepipeds and circular cylinders hollow to eliminate adverse effects, i.e. to reduce the inertia of the system and decrease the friction between the sting and the sleeve within which it slides (Part A of Plate X), and consequently preserving a high frequency response. The models used are shown in Plate II and Plate III.

## 6.2 Method of Model Mounting.

### 6.2.1 Model Held Rigidly.

The models were mounted on a 4mm diameter tubular sting which was attached on the mechanism shown in Plate XIV. The mechanism was installed on the top of a zero camber, about 7cm chord, aerofoil section. In order to minimize the effect of general tunnel and ground vibrations the aerofoil section was extended through the wind tunnel floor and rigidly attached (with three 1cm thick screws) to a heavy frame, resting on the laboratory floor, which included rubber damping pads.

### 6.2.2 Model Free to Oscillate.

The models were again mounted on the 4mm diameter tubular sting (each model had its own sting) which was attached to a strain-gauge balance. The balance was shielded from the airflow by mounting it inside a zero-camber aerofoil section. The initial balance used is shown in Pl. VI. With this arrangement it was found (by manually displacing, by small distances, the model in the z-direction in no flow conditions) that transverse oscillations of the models resulted in additional inputs to the balance.

As the result of the coupling of the longitudinal and

transverse oscillations was difficult to interpret, the balance was modified by extending the distance between the two members of the balance and by incorporating a pin jointed upper spacer. In this way it was thought that the effect of the transverse oscillations of the models did not introduce unwanted inputs to the balance. Comparison between the results obtained with the modified balance (present work) and the results obtained with the initial balance V.K.I. report No. 74-12, by G. Skordilis, Ref. 44) show considerable improvement. The modified balance is shown in Pl. IX.

### 6.2.3 Model Externally Excited.

The mechanism used in externally exciting the model at discreet frequencies and amplitudes is shown in Pl. X. The mechanism consisted of a variable-speed motor which drove a mechanism below the wind tunnel floor imposing a front and back reciprocating motion on the model in the wind tunnel above and in the drag direction. The eccentricity of the mechanism shown in Pl. X could be adjusted for the desired amplitude of motion, because of the complicated arrangement it was not possible to shield the mechanism from the airflow. The reason for using the present mechanism, and not using a simpler one, was, that the mechanism used was already ready at the time required, and the time available to the author for the investigation was limited. The fact that the mechanism was not shielded from the airflow, it is not considered to have a great influence of the flow field in front of the model or on the motion of the model itself as in this case the latter is driven from the outside. The components of the mechanism were made of aluminium and as thin as possible to reduce inertial effects. Even with these improvements it was found advisable not to exceed an oscillation frequency of 12 - 15Hz.

## 7. INSTRUMENTATION.

### 7.1 Wind Tunnel.

The open-return L-2 wind tunnel at Von-Karman Institute was used. A new wind tunnel intake was used to eliminate some unsteadiness and spatial non-uniformity present with the original intake. A general velocity profile survey carried out before the actual experiments proved that the change in the intake section gave a satisfactory uniformity, the maximum velocity variation with respect to the mean velocity was about 0.4% to 0.5%.

The test section has a rectangular cross-section of  $0.35 \times 0.18 \text{ m}^2$  at the end of the contraction. The top wall of the test section was made of perspex, which allowed observation inside the test section and it was removable.

To avoid the growth of a thick boundary layer the initial test section of 5.3m length was reduced to about 1.3m, while unwanted vibration from the fan motor was avoided by joining the test section with the downstream section - carrying the fan - with a rubber band ring thus eliminating any contact between the two sections. A schematic - not to scale - diagram is shown in Fig.5. The tunnel's reference wind speed was taken as the equivalent test section speed  $\bar{u}$ , and was derived from measurement of the test section dynamic pressure  $\frac{1}{2} \rho \bar{u}^2$ . This was read directly from a Betz manometer connected to a N.P.L standard pitot-static tube at the test section. Long plastic tubing connections of about 3m from the pitot-static tube to the manometer helped in damping down the turbulence oscillations.

### 7.2 Hot-wire Instrumentation.

The fluctuating properties of the flow were investigated

using hot-wire techniques. The hot-wires used in the present work were the DISA constant temperature anemometers 55A01 and 55D01 described in Ref. 45 and Ref. 46. Two other constant-temperature anemometers built at V.K.I. were also used.

The reasons for the use of constant-temperature anemometers - instead of constant current anemometers - ~~and~~ which were thought to be necessary in the present work are presented below:

1. The wire current is controlled by an electronic servo-system that protects the wire against accidental burn-out when the flow is suddenly changed (reduced).
2. Since the bridge balance is maintained during flow changes, there are no compensation controls to set and no testing to determine whether the compensation is effective.
3. Finally, the instrument can follow large fluctuations in the flow without appreciable error.

The unlinearized hot-wire signals were fed into the linearizer 55D10 as far as the 55D01 anemometer was concerned while all the other anemometers had their own linearizers built in them. The same was true for the square wave generators used in the calibration of the instruments.

All hot-wires employed were single hot-wire probes. They used 0.002" dia. tungsten wire with an active length of 0.125". The non-active length of the wire was copper plated. The probes were made at V.K.I. and this helped in adjusting the length of the probe's body according to requirements.

The three degrees of freedom mechanism <sup>used</sup> for the hot wires is shown in Fig. IV. A four degrees of freedom mechanism was used in measuring the turbulent energy. The first mechanism, mentioned abo-

ve, was used for measuring the longitudinal and lateral space correlation coefficients, the probability density function of the longitudinal component of the wind as well as the spectrum and its variation (of the longitudinal velocity component) in front of the models.

Repeatability of the position was within  $\pm 0.003\text{cm}$ .

The hot-wires, while in operation, could be observed through a set of lenses. Thus any vibrations detected could be eliminated.

The calibration of the hot-wires together with the frequency response of the system and the effect of the finite hot-wire length on the measurement of the three-dimensional turbulence are considered in appendix C.

### 7.3 Spectral Analysis System. (Ref. 47)

A Bruel & Kjaer Frequency Analyser Type 2120 was used for "on line" spectral analysis. It is a constant percentage bandwidth analyser whose central frequencies are continuously tunable from 2Hz to 20kHz. It could be used as a constant bandwidth filter having four selectable bandwidths, 1%, 3%, 10%, and 1/3 octave. In the present work the 3% bandpass filter was used. As no level recorder was available, the central frequency, each time it was changed, it was selected by hand. This was proved cumbersome and time consuming but, at the time of the experiments, no other method was available.

In general the accuracy of the power spectral density function measured, is a function of the bandwidth and the averaging time. The bandwidth is associated with the spectral precision of the power spectral density function, i.e. the measurement resolution, while the averaging time is associated with the statistical variability of the power spectral density function, i.e. the measurement



uncertainty.

In obtaining the readings from the frequency analyser the following random signal analysis was assumed:

The r.m.s. value of  $u'(t)$  is defined as:

$$(\sqrt{u'^2})^2 = \lim_{T \rightarrow \infty} \frac{1}{T} \int_0^T u'^2(t) dt \quad \text{----- (1)}$$

where  $T$  is the analysis averaging time, which for 100% accuracy must tend to infinity. In practise this is impossible, and  $T$  must be restricted to a finite value. This restriction leads to an error in the r.m.s. measurement. A commonly used expression for the normalized standard deviation (or error)  $\pm \varepsilon$  of a r.m.s. measurement is:

$$\varepsilon = \frac{1}{2\sqrt{BT}} \quad \text{for } BT > 5 \quad \text{----- (2)}$$

where  $B$  is the analysis bandwidth in Hz and  $T$  the averaging time of the analysis in seconds.

A common parameter in analyses of this type is the number of statistical degrees of freedom  $k$ , which is given by:

$$k = 2BT \quad \text{----- (3)}$$

It is common practice to work with a value of 50 for  $k$ , this being an efficient analysis value.

$$\text{Therefore if: } 2BT = 50 \quad \text{----- (4)}$$

$$BT = 25 \quad \text{----- (5)}$$

Substituting back for  $BT$  in eqn.(2) gives:

$$\varepsilon = 10\% \quad \text{for } BT = 25$$

This is the value that is taken in the subsequent analysis.

With constant bandwidth analysis  $B$  assumes a constant

value, but for a constant percentage bandwidth analysis  $B$  increases linearly with frequency according to the relationship:

$$B = (rf)/100 \dots \dots \dots (6)$$

where  $r$  is the percentage bandwidth. The minimum analysis averaging time,  $T_{AV}$ , can be calculated for a  $BT$  product of 25 as:

$$T_{AV} \geq 25/B \quad \text{for} \quad \varepsilon < \pm 10\%$$

The analysis rate may be connected with the calculated averaging time by specifying that one bandwidth must never be scanned in less than two averaging times. The time taken to scan one bandwidth is given by the "dwell-time",  $T_D$ , where in the present case:

$$T_D \geq \frac{50}{B} \quad \text{for} \quad \varepsilon < \pm 10\%$$

#### 7.4 Microphone:

The fluctuating and mean pressures at the stagnation point of the  $AR=2$  plate for all three turbulent fields were investigated with the use of an ultra miniature pressure sensor made by Kulite Semiconductors Products Inc.

It consists of a miniature silicon diaphragm on which a fully active four arm Wheatstone bridge has been atomically bonded using solid state diffusion. This monolithic construction affords excellent hysteresis and thermal characteristics. The silicon diaphragm and the transducer housing are constructed to eliminate all internal lead flexing. This removes any lead fatigue and undesirable secondary resonances caused by internal lead vibrations. The pressures for which the transducer was applicable were from 5p.s.i. to 50p.s.i. and it had a natural frequency of about 125kHz. A reference tube

emerging from the back of the transducer made its calibration extremely easy. The calibration was carried out in the wind tunnel in no flow conditions against a pitot tube by merely sucking on the reference tube.

The typical installation of the transducer requires the use of silicon rubber so that it is permanently stuck on the model. The transducer in this way comes flush to the surface without any cavities. This eliminates any frequency resonance coupled to the cavity characteristics.

Because of the expense involved in the transducer it was found necessary not to install the transducer permanently so avoiding any possible damage to it when it was time to remove it from the model. The method of installation using rubber "O" rings is shown in Plat. XVI, while a photograph of the transducer is included in Plat. XVII. The overall dimensions of the transducer are shown in Plat. XV.

### 7.5 Probability Density Function Displayer.

In general, the following three functions, though not sufficient to describe the random process involved in turbulence, are very useful in its study:

1. The autocorrelation function or the space correlations.
2. The power spectral density function.
3. The amplitude probability density function.

This last function was investigated using an amplitude probability analyser. Following the nomenclature used at V.K.I. - where the analyser was designed and built - the whole system of the analyser and the x-y recorder used in the presentation of the data was given the name of probability density function displayer.

## 7.6 Accuracy of Measurements.

Ref. 47 and Ref. 48 discuss the accuracy of the hot-wire measurements made with a constant-temperature anemometer. It is sufficient to say here that the present measurements were made as accurately as any usual hot-wire measurements. Particular attention has been paid in the case of investigating the energy level variation as the different eddies approach the model. Due to the small variations in the reading for the energy level for each wavenumber the mean of four readings was taken as a representative value of the situation. Generally when measuring quantities that vary randomly with time, a certain amount of discretion must be used in obtaining average readings of metre pointers that are jumping about.

No corrections have been made to any of the hot-wire results for the finite length of the wire. At the same time it must be taken into account that in the present work the scales of turbulence were 25 - 30 times the length of the hot-wires. In measuring the intensities of the turbulent fields the usual method of employing the r.m.s. of the voltage fluctuations was used in place of their instantaneous values. This approximation is valid only for small values of the fluctuations. Nevertheless, vibration studies (Ref. 49) have shown that the hot-wire anemometer is capable of following fluctuations in a single direction faithfully up to 60 - 70 percent. When the fluctuations in  $u'$  become large, errors will be introduced because of the interaction of the components of the turbulence; that is, the effect of  $u'$ ,  $v'$  and  $w'$  on  $u'$  and on each other. These errors are considered in Ref. 48, where actual corrections are worked out. No such corrections have been applied to the results shown in this report.

The coherence of the turbulence measured using summing and

subtracting circuits shows negative values or values greater than unity. This is, of course, impossible and such readings must be the result of inaccuracies in the process. In most of these cases enough points were available to show the trend without considering the points for which  $R_{11}(0, \alpha_2, 0)(f) < 0$  or  $R_{11}(0, \alpha_2, 0)(f) > 1$ .

To keep the clarity of the graphs to a reasonable level when curves in the same figure collapse towards a single curve not all points are shown. This was the case in the investigation of the energy level variation of the different eddies as they approach the model. The same was true in the case of the investigation of the variation of the integral scales of turbulence in front of the model when the latter was externally oscillated.

In measuring the surface pressure the only fundamental difficulty present in using the flush mounted pressure transducer of finite size was in calculating its spatial resolution. The distribution of the sensitivity over the area of the hole is unknown and there may be some response, via the fluid flow, to pressures applied at a short distance from the hole; this makes corrections for the effect of transducer size conjectural. Consequently no such corrections were applied. The largest sources of error in these experiments were:

1. Inaccuracies in repeating set ups after the probes were changed;
2. Effects of the presence in the flow of periodic fluctuations due to sound, pressure waves in general or floor vibrations.;

To find how much of a given set of readings was due to electrical noise in the instrumentation and extraneous vibrations from the test stand, the hot-wire was shielded using a cup, the flow was stopped and then the overall noise spectrum was obtained. This

is shown in Fig.30. In general the noise spectrum presented a noise level that was negligible for the measurements reported here.

For the forced oscillations tests two sources of error could be possible. First, there might be errors in setting up the shaker amplitudes. Although the set amplitude was checked before and after each test there is always a certain play in the bearings of the mechanism. The effects of that play when the model oscillates at the frequencies used, is not known. The second source of errors could be any vibrations of the shaker linkage and vertical channel, from the motor itself. These resulted in keeping the oscillation frequencies used comparatively low.

#### 7.6.1 Wall Interference Corrections.

For some of the models the lateral dimensions were a little larger than might have been desirable from the point of view of wind tunnel blockage. With a breadth of the model of  $d=120\text{mm}$  and tunnel breadth of  $z=250\text{mm}$ , the largest blockage ratio was  $d/z = 120/250 = 0.48$ . To correct for wall interference effects use was made of the formulae presented below.

These formulae were given by Allen and Vincenti (Ref.51) and give the corrected values of velocity and drag coefficient,  $\bar{u}$  and  $C_{d(\text{mean})}$  in terms of the measured values  $\bar{u}_m$  and  $C_{d(\text{mean})m}$ .

$$\frac{\bar{u}}{\bar{u}_m} = 1 + \frac{1}{4} C_{d(\text{mean})m} \frac{d}{z} + 0.82 \left(\frac{d}{z}\right)^2 \dots \dots (A)$$

$$\frac{C_{d(\text{mean})}}{C_{d(\text{mean})m}} = 1 - \frac{1}{2} C_{d(\text{mean})m} \left(\frac{d}{z}\right) - 2.5 \left(\frac{d}{z}\right)^2 \dots \dots (B)$$

These formulae were obtained following the earlier work of Lock, Glauert and Goldstein, by using image doublets to represent the

interference between wall and model, and image sources to represent the interference between wall and wake; the two effects give the third and second terms, respectively, in the formulae. The drawback in these formulae is the fact that such an analysis does not take into account possible interference effects on the separation mechanism and the structure of the wake close behind the body; changes in these could have an important effect on the drag. The maximum corrections to  $\bar{u}_m$  and  $C_{l(mean)m}$  were about 9% and 17% respectively.

## 8. RESULTS AND DISCUSSION

### 8.1 Mean Velocity Profiles.

In the present study it was desirable to work in a region where the distributions of both the mean velocity and the fluctuating component were uniformly distributed across the tunnel.

A survey of the mean velocity at the test section is shown in Fig. 6 to Fig. 10. The lateral mean velocity profiles investigated were determined at different positions on the y-z plane at the test section, ( i.e. without variation in the value of the x-coordinate). The plots include mean velocity profiles for the three turbulent fields used.

As a first step the above mentioned lateral mean velocity profiles were determined at different y-z planes, for different values of x. In this way the location of the best position for the test section, downstream of the baffle, followed a trial and error method. As the test section had to be fixed, the uniformity of the three turbulent fields used at the test section, required some degree of compromise between them.

Consequently the initial mean velocity profile survey was carried out for two interrelated reasons, i.e. a) to find an optimum position, as explained below, along the wind tunnel length for the location of the test section and b) to have an idea on how good was the uniformity of the turbulent field with respect to the mean velocity. The optimization was concerned in keeping the internal turbulent scale, and the respective turbulent levels at high values. At the same time the investigation required an acceptable uniformity in the flow field.

According to Corrsin and Van der Hegge Zijnen, (Ref. 41)

-----  
 Note: Throughout the thesis the wording "Empty Tunnel" refers to the absence of the model and its support only. The respective baffle is always present.



and (Ref. 41), an acceptable uniformity in the flow field could be expected at a distance downstream from the baffle equal to 20 hole diameters. Additionally, previous studies, such as those reported by Batchelor, (Ref. 29), have shown that both the mean velocity and the intensity are uniform at about ten mesh sizes downstream from the grid. In order to increase the scale of turbulence and obtain the uniformity suggested by Corrsin and Van der Hegge Zijnen it was, in this case, preferred to work further downstream than the distance suggested by Batchelor. At the test section chosen the development of the wind tunnel walls boundary layers was not expected to be significant.

As shown in Fig. 5 the test section was situated at about 0.77 m downstream from the baffles, or at about  $x/d_g = 21.3$ .

Fig. 6 to Fig. 10 present the results in terms of a normalized velocity and a normalized length. The wind tunnel's height and width are taken as the respective normalizing length for the  $z$  and  $y$  velocity distributions. For the  $y$ -distribution of the mean velocity the normalization velocity is taken as the velocity  $\bar{u}_0$  at  $z/Z = 0.5$  and  $y/Y = 0.5$ , while for each for the  $z$  distributions the normalization velocity  $\bar{u}_c$  is taken as the velocity at  $z/Z = 0.5$  and at the  $y/Y$  section considered.

Fig. 11 presents the variation of the mean velocity in the longitudinal direction along the wind tunnel longitudinal central axis. At an  $x/d_1 \approx -0.6$  distance upstream from the test section the mean velocity shows a sharp rate of increase.

Wherever possible curves are drawn through the data points. To avoid confusion, in those curves for which the points intermingle for the different cases, the curves are not traced.

With the turbulence baffles installed the mean velocity

attained as registered by a pitot static tube connected to a Betz manometer and spot galvanometer was given by  $\frac{\bar{u}}{u_0} \approx 1 \sim 0.96$ , with  $\bar{u}$  for the slotted baffle of about 12.5m/s.

From Fig.6, the variation of the normalized velocity in the y-direction, above  $y/Y = +0.74$ , shows a mean variation, as the walls of the wind tunnel are approached, of about  $\pm 2\%$  of the median. Except from this fact the distribution seems to have an acceptable level of uniformity. Near the wind tunnel walls the velocity profile is expected to change, anyway, because of the wall boundary layer.

The z-distribution of the mean velocity seems satisfactory between  $y/Y = +0.284$  and  $y/Y = +0.740$ . Below and above the  $y/Y$  limits given above the mean velocity profiles - for the z-distribution - are no longer uniform. The interaction of the boundary layers at the corners of the wind tunnel section with the mean flow is thought to be responsible for the changes observed in the z-distribution of the normalized mean velocity profiles at  $y/Y = 0.228$  and  $y/Y = 0.795$ .

It should be noted that for Fig.6 to Fig.10, y is measured from one of the walls of the wind tunnel and not as shown in the definition sketch of Fig.2.

The Reynold's No. based on the mean velocity and the width of the models tested ( or the diameters of the cylinders) was  $Re_b = 2.6 \times 10^4$ . Although in this work the influence of the variation of the Reynold's No. is not considered it should be pointed out that:

- a) for sharp edged bodies there is little effect of  $Re_b$ .
- b) for rounded sections, the points of separation of

the airflow from the surface move back at a critical value of the Reynold's No., with a decrease in the width of the wake and a consequent decrease in  $C_p$ .

In general the mean flow velocity field of the present case could be a reasonable representation of the actual atmospheric wind, only for a case where the velocity distribution of the latter is near uniform and the structure of turbulence is independent of the detail of the terrain.

## 8.2 Intensity Profiles of the Turbulent Fields.

The values of the turbulence level were measured using a typical r.m.s. voltmeter and all values were derived from hot wire anemometer measurements. The intensities have not been corrected for any hot-wire frequency response effects (appendix B.2) or measuring instrumentation truncation errors. At the same time it should be remembered that all hot-wire outputs were linearized. It was noted that variation of the wind tunnel's running speed produced a change in turbulence level; specifically an increase in the tunnel's speed produced a decrease in turbulence level.

The intensity of turbulence based on the local mean velocity at  $y/Y = 0.5$  for the y-distribution and at  $z/Z = 0.5$  for each y-section for the z-distribution, are shown in Fig.14 to Fig. 18. A typical hot-wire calibration curve followed by a typical hot-wire verification curve are shown in Fig.12 and Fig.13.

From Fig.14 presenting the y-distribution of  $\frac{\sqrt{u'^2}}{u}$  at the test section, it can be seen that for the slotted baffle the value of the turbulence level was about 11%, for the 30mm holes baffle a turbulence level of about 9.5%, while the 50mm holes

baffle produced a turbulence level of about 8%. A peculiar feature of the level of turbulence profile, for the y-distribution, produced by the 30mm holes baffle is the sharp increase in the level of turbulence as the wind tunnel walls are approached. This is thought to result from some peculiarity of the baffle producing a flow pattern which when it interacts with the wind tunnel boundary layer results in the above mentioned increase in turbulence level. For Fig.14 to Fig.18 the distance  $y$  is measured from one of the walls of the wind tunnel and not as shown in the definition sketch of Fig.2.

Fig.19 presents the intensity variation - for the three turbulent fields - along the x-axis and along the wind tunnel's central axis. A very small increase in turbulence level is noted as we move upstream.

An indication of the degree of anisotropy present at the working section is given by Fig.19a, which shows mean values (at the expected stagnation point) of the three turbulent velocity components for each turbulence case considered. A certain amount of anisotropy is present in all cases, but it is most severe for the 50mm holes baffle turbulent field. In this context it should be remembered that a certain amount of anisotropy is inherent in grid generated turbulence.

In general the intensity level achieved is lower than that normally encountered in urban areas. On the other hand it would be expected to occur frequently at elevations of 30m or higher in open country.

### 8.3 Integral Scales of Turbulence.

The physical size of the eddies (in a statistical manner)

could be found from measurements of the correlations between the velocity components. However it should be noted that in a statistical method, average values are used and consequently individual configurations and events disappear in the process. This, on the other hand, is of no great importance in the study of turbulence. The immediate engineering application of correlation measurements ( in the context of the present work) is to give an estimate of the size of the eddies acting on the structure or on a part thereof. For example, when the size of the structure is small in comparison with the size of the eddies, it can be assumed that the relative velocity and angle of attack with which the wind strikes the structure, are variable with time, but practically constant over the length or width of the structure. It is interesting to note that between the two wires, in measuring the longitudinal correlation coefficient new eddies are expected to be created from the old ones at a rate given by the decay of the correlation curve.

The longitudinal scale of turbulence as well as the two lateral scales were determined by integrating the area under the respective space correlation curves. A sample of these curves is presented in Fig.20, while the integral scales for the remaining cases are tabulated in Fig.21. The values presented include a certain approximation as it was impossible to determine the space correlation for separation distances very near to zero and for separation distances tending to infinity. The correlation coefficients for the slotted and 30mm holes baffles could be correlated by dividing the separation distance of the two hot-wires by the slot and hole diameters respectively. This way of plotting the results is shown in Fig. 20. This is not the case for the 50mm holes baffle generated turbulence field. In this case it is thought that

the wind tunnel test section is found at the beginning of the turbulent region of the air jets generated by the baffle. This is only a conjecture.

The turbulent scales, in general, are approximately the same as the width of the model.

The values of the integral scales of turbulence in the longitudinal direction could also be compared with those obtained from the large scale normalization spectra of the longitudinal velocity component for the three turbulent fields, shown in Fig. 22, 23, and 24. It should be remembered that the values of the respective integral scales of turbulence found in this way are not more accurate than those found from the respective space correlations curves mentioned above. The reason for this is that the determination of the spectrum in the lower frequency range suffers from comparatively high inaccuracies. The values of the integral scales of turbulence found in this way could be used as a check for those obtained from the space correlation curves.

Starting from the fact that there is a Fourier transform relationship between the spectral density  $S(f)$  and the correlation function  $f(x)$  we could get the following relation, (assuming an isotropic turbulent field):

$$\begin{aligned} \lim_{f \rightarrow 0} \frac{S(f)}{u'^2} &= \lim_{f \rightarrow 0} \frac{4}{u} \int_0^{\infty} \cos(fx) \cos \frac{2\pi fx}{u} dx \\ &= \frac{4}{u} \int_0^{\infty} \cos(fx) dx = \frac{4}{u} L_x \\ \text{i.e. } L_x &= \frac{u}{4} \left\{ \lim_{f \rightarrow 0} \frac{S(f)}{u'^2} \right\} \end{aligned}$$

or expressed with the normalization factors used in the graphs of Fig. 22, 23 and 24, (these factors are explained in section 8.4)

we get:

$$L_x = \lim_{f \rightarrow 0} \left\{ \frac{B^2 \bar{u}}{2\pi f d_i \bar{u}'^2} \times \frac{\pi f d_i}{2} \right\}$$

$B$  = analyser output.

Therefore the integral  $L_x$  can be obtained from the intersection of the  $\left\{ \frac{S C_K, d_i}{\bar{u}'^2 d_i}, K O d_i \right\}$  curve with the  $\frac{S C_K, d_i}{\bar{u}'^2 d_i}$  axis.

In this way the longitudinal integral scales of turbulence are given by:

$$\text{Slotted baffle: } L_x = \frac{5000}{10^6} \times 10^4 \times \frac{3.14}{2} \times 0.036 \approx 25 \text{ mm}$$

$$30 \text{ mm holes baffle: } L_x = \frac{5000}{10^6} \times 10^4 \times \frac{3.14}{2} \times 0.03 \approx 23.5 \text{ mm}$$

$$50 \text{ mm holes baffle: } L_x = \frac{2000}{10^6} \times 10^4 \times \frac{3.14}{2} \times 0.05 \approx 15.7 \text{ mm}$$

From the above results it is seen that for the slotted as well as the 30mm holes baffles the values of  $L_x$  obtained by both ways agree fairly well. There is a difference in the value of  $L_x$  for the 50mm holes baffle. The inaccuracies involved in the spectrum determination at lower frequencies could be the reason for this. It is thought that the value of  $L_x$  obtained for the 50mm holes baffle, from the space correlations curve is more accurate.

#### 8.4 The Spectrum of the Longitudinal Velocity Component.

In defining a turbulence field the frequency with which a velocity of a given magnitude occurs is of primary importance.

The spectrum of the longitudinal component of turbulence for three positions at the test section and for the three turbulent fields considered are presented in Fig. 22 to Fig. 24. For convenience both spectral densities and frequencies ( or reduced frequencies) are plotted on a logarithmic scale. Planimetric

measurement of the area under the spectrum curve no longer has any importance or significance; on the other hand logarithmic presentation is appropriate for the following reasons:

- a) The ratio of maximum to minimum spectral densities to be shown in one figure is about 1000 to 1 or 1000000 to 1 for the large scale normalization plot. The frequency scale exhibits similar high values.
- b) The logarithmic plot displays the power law followed by the high frequency end of the spectrum.
- c) The apparent scatter of plotted points is reduced and this enables the trend of the spectrum to be more easily discerned.

As mentioned above the spectra are plotted using a large scale normalization with the normalized power density plotted against a normalized wave number, i.e.

$$\frac{S(u, d_i)}{u^2 d} \left\{ = \frac{B^2 \bar{u}}{2\pi f d_i \bar{u}^2} \right\} \sim \kappa, d_i \left\{ = \frac{2\pi f d_i}{\bar{u}} \right\}$$

where B = analyser output.

Most of the results were obtained using a Monroe programmable printing calculator, model 1665.

Up to a normalized wavenumber of about 0.4 the energy level remains constant. A range exists,  $0.5 < \kappa, d_i < 8$  in which the energy variation is  $\propto \kappa^{-1}$  while as we move to higher wavenumbers the inertial subrange is reached, where Kolmogoroff's  $-5/3$  law seems to apply. This inertial subrange extends between  $5 < \kappa, d_i < 80$ . Above this range Heisenberg's solution of  $S(\kappa, d_i) \propto \kappa^{-7}$  seems



to be in good agreement with the results. All spectra, for all turbulent fields, measured at the test section, seem to have similar characteristics without any appreciable deviation from the above limits.

It is interesting to consider the peak of the spectra when they are plotted in the more conventional form of  $\frac{f S_{u'}(f)}{\bar{u}^2} \sim \frac{2\pi f}{\bar{u}} \cdot L_{xc}$ . An example of this way of plotting the turbulence spectra is shown in Fig. 25. It presents the turbulent spectrum of the slotted baffle generated turbulent field at the test section. The peak value of this spectrum is given by:  $\frac{f S_{u'}(f)}{\bar{u}^2} \sim 0.00004$ . For this to correspond to natural wind peak values of  $\frac{f S_{u'}(f)}{k \bar{u}^2} \sim 1.5$  as suggested by Davenport for a height, of say, 10m would require a value of k of about 0.0003 which is about 1/10 of the value of k for, say, open grassland. If on the other hand we consider that the turbulence intensity decreases while the mean velocity  $\bar{u}$  increases with increasing height above the ground, the present reduced spectrum of the simulated environment with a peak at 0.00004 could be assumed to be typical of open grassland, (Ref. 9), at an elevation of about 20m. The high energy portion of the spectrum is at much higher frequencies (around a wavenumber of about 10), than in natural wind (around a wavenumber of about  $10^{-3}$ ). This is compatible with the requirements for the use of small - scale experimental models.

### 8.5 Cross-spectrum of the Longitudinal Velocity Component.

Typical plots of the lateral (y-direction) cross-correlation coefficient of the longitudinal velocity are shown in Fig. 26 to Fig. 28. The positions of measurements are shown in the definition sketches of Fig. 5c, 5d, 5e, and 5f.

Fig. 26 presents the cross-correlation  $R_{11}(0, r_2, 0)(f)$  plotted against a reduced frequency  $\frac{f y}{\bar{u}}$ . The coefficient was

determined at the test section, for the empty tunnel, for three separation distances of the hot-wires, i.e. 10mm, 20mm and 40mm, in the y-direction. Fig.27 and Fig.28 present the variation of the cross-correlation coefficient in front of the AR=4 plate when the latter is free to oscillate and when it is held rigidly. This variation of the cross-correlation coefficient for all the models under investigation and for the three turbulent fields is presented in Fig. 29. The value of the coefficient at specific , increasing, reduced frequencies of 0.1, 0.2 and 0.3 is presented.

From the determination of the cross-correlation coefficient i.e. from the curves plotted and the results tabulated in the figures mentioned above, a measure of the coherence of the turbulence is expected to be achieved. By considering the same coefficient in front of the rigidly held and free to vibrate models, the way this coherence of the turbulent field changes as the flow approaches the model could be examined. The variation of the cross-correlation coefficient at the test section for the empty tunnel case serves two purposes:

1. It helps in defining the turbulent field in general,
2. It is taken as the reference case for comparison with the different cases when the model is present.

From Fig. 29 it can be seen that in front of the AR=4 plate and parallelepiped the coherence decreases considerably, the  $R_{11}(0, r_2, 0)(f)$  being reduced by a factor of 1/4. It is interesting to note that the coherence increases when the model is free to oscillate compared with the case when the model is held rigidly. An improvement of  $R_{11}(0, r_2, 0)(f)$  by a factor of 2 seems to be the case. Possibly this is the result - in the case the model is free

to oscillate - of the freedom of the model to move according to the structure of turbulence impinging on <sup>it</sup> or coming inside the influence zone of the model presence. In other words the model moves with the flow reducing its resistance to the flow. This is not the case for the rigidly held model. In this case the whole change had to be experienced by the flow field, the model remaining totally an external to the flow factor.

For the case of the circular cylinder this reduction in the coherence function is much less. This could be the result of the more streamlined profile presented by the cylinder to the flow compared with that of the plate and the parallelepiped.

In general it must be noted that all these measurements are expected to suffer from considerable inaccuracies. It should also be born in mind that any noise in the input measuring device reduces the coherence function to less than unity and further that as the input signal to the measuring device noise ratio becomes small, the coherence function becomes small. These ideas are fully treated in (Ref. 40). Consequently these plots must be treated with caution.

For the turbulent field in the empty wind tunnel the lateral frequency-dependent correlation coefficient could be expressed reasonably well, by an exponential function. In the present case the constant  $c$ , in the expression  $R_{11}(0, r_2, 0)(f) = e^{-c(fy/\bar{u})}$  has the value of 8, so that the lateral scale on a spectral basis will be about  $1/8$  of the longitudinal wavelength, which seems to be in reasonable agreement with measurements in the natural wind.

It could also be seen that the frequency range of the velocity spectrum containing the majority of the wind energy, results in turbulent scales of the same order of magnitude

as the model sizes. If, for example, we have  $U = 12\text{m/s}$  and let the lateral scale ( $\lambda \bar{u}/f$ ) be equal to the model length of 120mm the frequency is given by  $f = \frac{1}{8} \times \frac{12}{0.12} = 12\text{Hz}$ , which corresponds to a wavenumber of  $\text{lm}^{-1}$  coincident with the peak in the velocity spectrum, <sup>Fig. 25.</sup> Shorter model lengths (considering the models used in the present investigation) will result to higher frequencies which will also be found within the range of maximum wind energy region of the velocity spectrum due to the flatness of the spectrum peak.

The method employed in measuring the cross-correlation coefficient is described in appendix C. Due to the relative complexity of the method the coefficient could only be obtained for the frequency range  $10\text{Hz} < f < 300\text{Hz}$ . This range is assumed to be sufficient as the force spectrum (measured) does not exceed this limit.

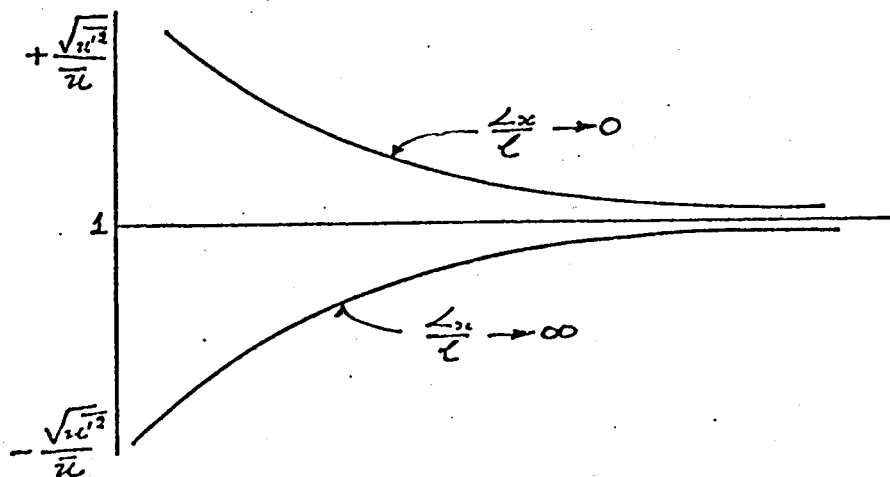
#### 8.6 Spectrum Variation of the Longitudinal Velocity along the Stagnation Line Flow in front of the Model.

The flow field, in front of a number of models was investigated in a general way in order to examine the variation of the longitudinal velocity spectrum along the stagnation line. This was carried out in front of the rigidly and free to oscillate models. (A more detailed investigation was carried out for a few of the models; the results are discussed in section 8.8). The change of the turbulence level along the stagnation line flow was also recorded. The results are tabulated in Fig. 41, 41a, and 41b, while Fig. 32 to Fig. 40 present a specimen of the resulted plots with regards to the spectrum and turbulence levels variations. The spectra, in these graphs, are being plotted against

a normalized frequency based on the respective turbulence scale.

In order to see whether the instruments produced an acceptable noise level the noise spectrum is plotted, together with the 30mm holes baffle produced turbulent field velocity spectrum, in Fig. 30. The plot shows that apart for the 50Hz frequency value (corresponding to the mains) the noise spectrum is of acceptable form.

As the model is approached the energy spectrum is shifted to higher wavenumbers, the shift being increased at a higher rate the nearer we get to the model. The distortion of the energy spectrum as the model is approached could be taken as an indication that near the object the turbulence field is quite different from that of the free flow. The change in the longitudinal level of turbulence along the stagnation line flow is compared with Bearman's results for  $L_x/D = 0.75$  and a turbulence level of 8.3%. This comparison shows that the flow could be assumed to obey Batchelor's rapid distortion theory. According to Batchelor the two extreme cases for  $L_x/D \rightarrow 0$  and  $L_x/D \rightarrow \infty$  are presented in the figure below:



For  $L_x/D \rightarrow 1$ , which is the present case, the curve should be between the above limits, and below Bearman's results (Ref. 5)

which are for a smaller  $L_x/D$  ratio.

The results also show the existence of a difference in the turbulence levels, especially as the model is approached, between the cases when the model is held rigidly and the model is left free to oscillate. The turbulence level reaches higher values in front of the rigidly held model than if the model were free to oscillate. The same indication could be obtained from the spectrum variation plots for the two cases. The spectra at  $x/D = -1/10$ , for the rigidly held models show a small but systematic increase of the peak energy region compared with the spectra at  $x/D = -1/10$  for the freely oscillating model. To examine further the above phenomenon, the fluctuating kinetic energy in front of the  $30 \times 120 \text{ mm}^2$  plate was directly measured as shown in appendix D.

#### 8.7 Probability Density Function of the Longitudinal Velocity Component.

The probability density function of the longitudinal velocity component was studied for a limited number of cases in order to get some idea of the way it varies in front of the models. The results as plotted by the x-y recorder are presented in Fig.42 to Fig.68.

Fig. 42 to Fig. 44 present the results of the variation of the probability density function along the stagnation line flow in front of the empty test section. These results are obtained only for the slotted baffle produced turbulence field.

For all the probability density curves produced, the respective probability density of a triangular wave of known frequency and r.m.s. value equal to the overall r.m.s. value of the turbulent field at the point in question, is shown, so that some kind of comparison between the different curves could be possible.

The curves representing the turbulence field of the empty tunnel show no appreciable positive or negative skew although there is a decrease in the overall r.m.s. value of the fluctuating longitudinal velocity component as we move downstream. (Note that  $-x$  indicates the distance upstream from the test section).

With reference to the above it should be noted that in work carried out by Singer (Ref. 52) it is reported that in experimentally determined probability density distributions of the natural wind varying amounts of both positive and negative skew are apparent. Singer also suggests that, on the average, the distribution may be regarded as Gaussian.

The plots of Fig. 45 to Fig. 68 present the variation of the probability density of the longitudinal velocity component in front of the 30mm side cube and the AR=2 parallelepiped for the slotted and 30mm holes baffles produced turbulent fields. The respective results for the oscillating and rigidly held models were obtained at the same position in space, i.e. in both cases the probability density function of the longitudinal velocity component was determined at  $x/D = -1, -\frac{1}{2}, -1/10$ .

A general decrease in the r.m.s. value of the longitudinal velocity component in front of the model is apparent, the decrease being slightly higher in the case of the rigidly held model for the respective positions in front of the models.

As the model is approached from upstream the skewness of the curve to smaller velocities becomes apparent. The skewness should not be taken as representing negative values. The ordinate axis representing  $p(u')$  could also have been drawn at the beginning of the curve. The way it is drawn in this report facilitates the detection of any skewness in the curves more easily. This skewness is

expected as the longitudinal velocity component decreases as the model is approached. The same is true (statistically) for both oscillating and rigidly held model configurations. Whether there is any difference between the skewness of the curves at  $x = -1/10$  between the cases of the oscillating and rigidly held models could not be said with certainty.

## 8.8 The Development of the Energy Level of the Eddies as they Approach the Model.

### 8.8.1 Reasons for the Investigation.

The expression "development of the energy level of the eddies as they approach the model" is used to signify the development or variation of the energy level of the different eddies as they approach the model from upstream. To follow a single individual eddy as it moves downstream with the convective velocity in order to investigate its changes, as it approaches the model, is extremely difficult. Instead we consider how each individual wavenumber, i.e.  $\frac{2\pi f}{u_c}$ , where  $u_c$  = convective velocity, or more loosely  $f/\bar{u}$ , changes as the model is approached from upstream. At the same time it should be pointed out that because of the way the wavenumber is defined, the wavenumber itself contains some qualitative measure of the eddy size. It was shown in section 8.6 that as the model is approached from upstream the spectrum of the longitudinal velocity component is displaced to higher wavenumbers. This as mentioned in previous sections indicates that the larger eddies break up into smaller eddies as the model is approached. In the present section this variation of eddy size or rather because we are interested in the energy transfer from the flow to the body and vice versa,



we look at the variation of the energy content of the different eddies. At the same time it should be born in mind that in a fully developed turbulent field it is not the largest eddies that will have the maximum kinetic energy but the eddies in a higher wavenumber range.

In considering the distortion of the stream, in the present case, the question arises whether we could assume that the distortion takes place so rapidly that inertial and viscous forces arising from the turbulent motion could be assumed to have no effect. In such a case the problem becomes linear. The present problem could be assumed to represent the reverse problem to that studied by G.I. Taylor (Ref. 53), i.e. the flow field through a sudden contraction in a pipe. Theoretically, on this basis, the problem can be solved by imagining that in the regions upstream and downstream of the distorting section the mean flow is uniform and the turbulence is homogeneous. Assuming a linearized theory, only the initial and final stages of the turbulence field is of consequence, and any field changes that occur during the distortion process is immaterial. In other words the assumption required for the linearized theory to hold is that the decay of turbulence as it passes the model is negligible. The condition to be satisfied, for the assumption to hold, expressed analytically is:

$$\frac{1}{\bar{u}^2} \frac{d\bar{u}^2}{dt} \ll \frac{\bar{u}}{D}$$

where  $D$  could be taken as a characteristic body dimension, (the width of the model).

It is known that  $\frac{d\bar{u}^2}{dt} = O \left\{ \frac{(\bar{u}^2)^{3/2}}{L_u} \right\}$

Consequently the above condition could be changed to:

$$\frac{(\overline{u'^2})^{1/2}}{\bar{u}} \ll \frac{L_x}{D}$$

Usually  $(\overline{u'^2})^{1/2}$  is small compared with  $\bar{u}$  and therefore

$$\frac{(\overline{u'^2})^2}{\bar{u}} \ll 1$$

In the experiments described in this work  $\frac{(\overline{u'^2})^{1/2}}{\bar{u}} \ll 1$  and  $\frac{L_x}{D} = O(1)$  i.e.  $\frac{L_x}{D} \gg \frac{\sqrt{\overline{u'^2}}}{\bar{u}}$  and consequently, in the flow region outside the body influence the conditions of the theory are met.

It was shown in previous sections that high levels of turbulence were recorded near and in front of the model and clearly the condition  $\frac{(\overline{u'^2})^{1/2}}{\bar{u}} \ll \frac{L_x}{D}$  will no longer be satisfied.

The questions thus arising in considering the turbulent field just in front of the model, - the region of the turbulent field where no general theory known to the author exists - led the author in investigating what happens to the different eddies as they get closer to the model from upstream.

### 8.8.2 Explanatory Notes on the Experiments and the Plotting of the Graphs.

The results of the above mentioned investigation are shown plotted in Fig.71 to Fig.121.

The graphs show the power spectral density of the longitudinal velocity component normalized with the local mean velocity plotted against the distance in front of the model normalized with a characteristic body dimension, the width or diameter of the model.

Because of the length of time required for the measurements three representative models were used, i.e. a) circular disc of 40mm disc, b) circular cylinder of AR=2, c) square section cylinder of AR=2. All models were rigidly held and the turbulent field

utilized was the one generated by the slotted baffle. This particular choice of turbulent field was based on its turbulence level which was approaching the natural conditions (atmospheric wind) more closely compared with the other two turbulent fields used.

The factor  $10^6$  present in the ordinates of the graphs resulted from the way the power spectral density was measured. The r.m.s. of the power spectral density was measured in mV while the mean velocity was measured in volts. Consequently the expression  $\frac{f S_u(f)}{\bar{u}^2}$  has units:

$$\frac{(mV)^2}{V^2} \propto \left(\frac{mV}{mV}\right)^2 \times \frac{1}{10^6} \propto \frac{(mV)^2}{(mV)^2} \times 10^{-6}$$

Consequently in order to avoid  $\frac{f S_u(f)}{\bar{u}^2}$  being presented with small numerical values and at the same time making comparison easier the expression was multiplied by  $10^6$ , i.e. the values of  $\frac{f S_u(f)}{\bar{u}^2}$  in the ordinates of the graphs are the true values multiplied by the factor  $10^6$ .

The absciscae of the graphs show the variation of the wavenumbers instead of the frequencies. Use of the wavenumbers makes the understanding of the spatial structure of the field at any given instant more pronounced; the field visualization just as the field presents itself to an observer who is at rest relative to the field is accentuated.

It was found rather difficult to measure the variation of the energy level above 100Hz with the method used (no other method was available at the time) and consequently the investigation was limited to frequencies  $2\text{Hz} < f < 100\text{Hz}$ .

In considering the energy level variation of the different wavenumbers in front of the model it should be noted that for the same distance, i.e.  $x/D = -0.1$  to about  $x/D = -1.1$  there is also a decrease

of the free turbulent field (wind tunnel empty). This decay of the energy spectrum is presented in Fig. 69, where the measurements are presented for the points  $x/d_s = 21.3$ ,  $x/d_s = 20.9$ , and  $x/d_s = 20.5$  on the stagnation line; distances are measured downstream from the slotted baffle. The range  $x/d_s = 20.5$  to  $x/d_s = 21.3$  represents about the same distance in space within which the main measurements were taken place.

As the decay of the energy spectrum was measured in the empty wind tunnel, the energy level was plotted against a wavenumber, normalized by the longitudinal integral scale of the turbulent field at the position of measurement. The variation of the integral scale of turbulence in the longitudinal direction is shown in Fig. 69a.

From the decay of the energy spectrum plots it can be seen that as we move downstream this decay is more pronounced in the region of the energy-containing eddies; at  $x/d_s = 20.5$  the peak value of

$\frac{\int S_u(\lambda) d\lambda}{\bar{u}^2} \approx 0.00015$  while at  $x/d_s = 21.3$  the peak value of  $\frac{\int S_u(\lambda) d\lambda}{\bar{u}^2} \approx 0.00004$ . At the same time, as we move downstream, the region of the energy - containing eddies moves to higher wavenumbers.

In the universal equilibrium range and especially in the inertial subrange the rate of decay seems to decrease as we move downstream. This statement should be treated with a certain caution, because, at the same time attention must be paid to the shift that occurs to the region of the energy-containing eddies towards higher wavenumbers.

In considering the variation of the energy level of the different wavenumbers in front of the models attention has been paid to possible transverse vibration of the three-dimensional bodies

resulting from vortex shedding phenomena. Any vibrations caused in the z-direction could have adversely affected the measurements by providing additional unwanted inputs to the measuring system. It is known that such vibrations, if present, as the models were considered rigidly held, would have the greatest effect if the Strouhal frequency of vortex shedding coincided with the natural frequencies of body-attachment systems in the z-direction. The definition sketch of Fig. 3 depicts the situation. For the above reason the free damped vibrations of the models-attachments systems used, in the z-direction, were measured in still air. An example is presented in Fig. 70, depicting the oscillations in the z-direction of the rigidly held square section cylinder,  $AR=2$ , when placed in the wind tunnel test position and with no flow conditions. The results of the oscillations in determining the damped natural frequencies of the systems are summarized below:

$AR=2$ , circular cylinder :  $f_n = 32.2\text{Hz}$

$AR=2$ , square section cylinder:  $f_n = 31.3\text{Hz}$

40mm dia. circular plate:  $f_n = 34.9\text{Hz}$

Vortex shedding could be expected to have its greatest effect in the cases of the circular and square section cylinders.

For the circular - section cylinder large amplitude oscillations are expected to occur at a mean flow speed of:

$$\bar{u} = (32.2 \times 0.03)/0.2 = 4.84 \text{ m/s}$$

where Strouhal No. = .2

For the square-section cylinder large amplitude oscillations are expected to occur at a mean flow speed of:

$$\bar{u} = (31.3 \times 0.03)/0.15 = 6.28 \text{ m/s}$$

where Strouhal No. = 0.15

This last value of the Strouhal No. is questionable.

### 8.8.3 Discussion of the Resulted Plots.

Fig. 71 to Fig. 83 present the results of the energy level variation in front of the 40mm dia. circular disc at different lateral positions. In general the variation of the energy level at low frequencies (small wavenumbers)  $2\text{Hz} < f < 6\text{Hz}$ , in front of the model seems to be rather small compared with the energy level variation at higher frequencies. All the same this increase in energy level, as the model is approached, is present in all lateral positions examined, i.e. stagnation line flow,  $y = +10\text{mm}$   $z = 0\text{mm}$ , and  $y = +20\text{mm}$   $z = 0\text{mm}$ . The energy level variation seems to be insignificant for the flow at  $y = +30\text{mm}$   $z = 0\text{mm}$ . The reason for this is thought to be the fact that we are outside the zone of direct influence of the body. At the same time it must be noted that (for the same frequency range,  $2\text{Hz} < f < 6\text{Hz}$ ) there is a decrease in the level of energy for the same value of  $x/D$  <sup>Fig. 83</sup> as we move away from the stagnation line in a lateral direction, i.e. the  $+y$ -direction. It is also worth noting that the rate of increase of the energy level as the model is approached increases as the frequency increases from 2Hz to 6Hz. The increase in the energy level becomes apparent below an absolute value of  $x/D$  of about 0.4 while above this value the energy level remains approximately constant. The reason for this comparative small change in energy level could be the more or less permanent state of the largest eddies and in any way these large eddies are not expected to have more than 20% of the total kinetic energy.

The frequency range,  $7\text{Hz} < f < 12\text{Hz}$  presents a much greater energy level variation, than the previous frequency range, as the model is approached from upstream, compared with the energy level for

upstream, e.g. for  $f = 9\text{Hz}$  the normalized energy level far upstream is about 10 while it reaches the value of about 90 near the model. As it was pointed out previously this increase in the energy level is present in all lateral positions examined although the increase is less compared with that at the stagnation line, as we move laterally in the  $+y$ -direction. This increase tends to disappear at the position  $y = +30\text{mm}$   $z = 0\text{mm}$ , i.e. outside the zone of influence of the body. As for the previous frequency range, in this frequency range,  $7\text{Hz} < f < 12\text{Hz}$ , (which is found at the beginning of the region of the energy containing eddies) the rate of increase of the energy level is greater at higher frequencies. At the same time this increase in energy level becomes apparent at about an absolute value of  $x/D$  of about 0.6. Above this value the energy level becomes approximately constant. It seems that for corresponding wavenumbers the effect of the model is to increase the normalized energy level considerably. It could be said that as the size of the eddies decreases - as we move to higher frequencies - the presence of the model has a greater effect on the eddies. At this point it must be noted that the increase in turbulent energy as the model is approached could be due to a) an increase of the energy level itself and b) a decrease of the local mean velocity, which, decreases any way as the model is approached.

The range of frequency  $14\text{Hz} < f < 40\text{Hz}$  presents some peculiar characteristics in that the energy level variation, for each frequency does not follow a smooth power law decay curve. There seems to be a relatively high scatter of the points representing the energy level at different positions in front of the model and for different frequencies. All the same the nature of a power law decay curve is maintained. This scatter seems to be more pronounced as we move nearer the model. This could lead to the possible conclusion

that the reason for the discrepancies in the energy level lies on the model itself. This could be true if we bear in mind that the natural frequency of the vibrations of the disc in the z-direction is about 34.9Hz. At the same time it is rather difficult to see how alternate vortex shedding could be strong enough, if they do exist at all, for a circular plate with  $45^\circ$  chamfered perimeter. Perhaps it could be easier to assume that additional inputs are fed into the measuring system by oscillations of the model caused by the impact of the eddies on the model and somehow exciting the latter in the region of its natural frequency. Above 40Hz and for the frequency range  $50\text{Hz} < f < 100\text{Hz}$  the energy level variation attains again its normal character as the one met with below 14Hz. These peculiarities of the different frequencies are present in all lateral, +y-direction, positions except for the  $y = +30\text{mm}$   $z = 0\text{mm}$  where, as mentioned above, we are, possibly, outside the direct zone of influence of the body.

Fig.84 to Fig.95 present the results for the energy level variation in front of the  $AR = 2$  circular cylinder at  $z = 0\text{mm}$  and for different lateral, +y-direction, positions. A general comparison of the results between the energy levels near the model between the circular disc and the circular cylinder show that the energy level in front of the cylinder is considerably less than that in front of the disc. This could be explained by the fact that the external shape of the cylinder presents a comparatively smaller distortion to the flow field than the disc. The cylinder presents to the flow field a more streamlined shaped than a flat plate placed normal to the flow. By the same reasoning we could explain the fact that the energy level increase, as the model is approached, is rather small for the frequency range  $2\text{Hz} < f < 16\text{Hz}$  for all lateral positions examined. Above 18Hz and for the frequency range  $18\text{Hz} < f < 50\text{Hz}$



the energy variation presents some peculiarities regarding the smooth decay of the curve, but which compared with those occurring in front of the circular disc for the same frequency range and for the different lateral positions are comparatively small.

The energy level variation for the frequency range  $60\text{Hz} < f < 100\text{Hz}$  does not present any features out of the ordinary and its behaviour is the same as that of the energy level in front of the circular disc (for the same frequency range).

Fig.96 to Fig.101 present the results for the energy level variation for the different frequencies in front of the circular cylinder and for the different lateral, z-direction, positions. In general the energy level increase in the z-direction is smaller than the energy level increase in the lateral, y-direction, for lateral, the corresponding frequency.

The frequency range  $2\text{Hz} < f < 12\text{Hz}$  follow the tendencies observed in the previous configurations while the peculiarities in the smooth power law decay curve are still present in the frequency range  $14\text{Hz} < f < 40\text{Hz}$ . Vortex shedding oscillations could be possible in this case, which could provide additional inputs to the measuring system. Above  $40\text{Hz}$  the previously mentioned trend is obvious.

The variation of the energy level at different frequencies was also measured in front of the  $AR = 2$  square section cylinder, for both lateral, y- and z-directions. The results are shown in the graphs of Fig.103 to Fig.120.

The normalized energy level achieved in front of the model is slightly higher than that observed for the circular cylinder at the respective position. This could be the result of the nature of the profile the square-section cylinder presents to the

flow compared to the comparatively more streamlined profile of the circular cylinder.

The region of frequencies  $2\text{Hz} < f < 8\text{Hz}$  seems to follow (as far as the variation of the energy level in front of the model is concerned) the usual pattern mentioned above.

A sudden increase in the energy level, which is maintained for  $-0.3 < x < -0.1$ , is obvious at  $f = 9\text{Hz}$ . In the opinion of the author this is of no importance and it is suspected that it is the result of mistaken readings. All the same it must be noted that for the frequency range  $2\text{Hz} < f < 8\text{Hz}$  this effect is present in two other lateral positions i.e. at  $z = 0\text{mm}$   $y = 15\text{mm}$  and  $z = 0\text{mm}$  and  $y = 30\text{mm}$ , so that the probability that the results represent mistaken readings decreases while the possibility that the results are due to some unexplained peculiarity of the flow presents itself.

In the immediately higher frequency range i.e.  $10\text{Hz} < f < 12\text{Hz}$  the variation of the energy level does not present any special features out of the general trend.

The general trend, with the energy level overlapping for different frequencies is apparent in the frequency range  $16\text{Hz} < f < 40\text{Hz}$ . Above this range the flow follows its previously observed pattern as far as the energy level is concerned.

In this part of the investigation, and as the opportunity presented itself, the turbulence level in front of the models under consideration for different  $y$  and  $z$ , lateral positions, was measured. The results are shown in Fig. 83, 102, and 121.

The general trend, with the normalized turbulence level increasing as the model is approached from upstream is the same as the one examined in sections 5.7 and 8.6. The additional fact that was observed, and was expected, was that this increase in the norma-

lized turbulence level was reduced as we moved away from from the stagnation line along the +y- and +z-directions.

### 8.9. The Variation of the Integral Scale of Turbulence in Front of the Model when the Latter is Externally Excited.

The variation of the integral scale of turbulence in front of the model, when the latter was executing simple harmonic oscillations of known amplitude and frequency, was investigated,

The intension was to examine what effect - the variation of the no. of cycles as well as the magnitude of the oscillations amplitude, for a number of models - had on the correlation of the turbulence inputs over the model surface. Therefore the work was carried out in an effort to isolate the effect of periodic model motion in the drag direction, to the upstream flow field. In particular the change of the turbulence scale and consequently the degree of correlation of the eddies along the length of the model is looked at. The higher the integral scale in front of the model the higher would be the correlation of the eddies envelopment of the model. The integral scales of turbulence were deduced from measurements of the respective longitudinal and lateral space correlations in front of the models.

The available time did not allow a great number of models to be examined. The two models examined were the  $AR=2$  circular cylinder and the  $AR=2$  flat plate, while the frequencies used did not exceed the 12Hz. The reasons for the limited frequency range used were the adverse effects of the oscillation mechanism exhibited at higher frequencies. In order to reduce the inertia of the mechanism's oscillating parts the linking arm shown in *Plat. X*, was made of aluminium and

as thin as possible. This resulted - as the frequency was increased - in the bending of the arm. The final design was the result of a compromise between the two effects. The oscillation tests were carried out with amplitudes of 2mm, 3.5mm, 5mm, for all three turbulent fields. The results for the  $AR = 2$  circular cylinder and  $AR = 2$  flat plate are tabulated in Fig.128 to Fig.133. The tabulated results present the value of the integral scale of turbulence for the following cases:

- a) empty tunnel,
- b) model free to oscillate,
- c) model held rigidly,
- d) model externally excited at discrete frequencies, for different positions of coincidence of the velocity measuring hot-wires, different oscillation frequencies and different amplitudes.

Fig.122 to Fig.127 are representative examples of the respective space correlation coefficients for the different cases. Fig.128 presents the results of the variation of the different space correlations (and consequently the respective integral scales - the area under the respective correlation curve could be taken as a quantitative measure of the respective integral scale of turbulence-) in front of the  $AR = 2$  circular cylinder when the oscillation amplitude is 2mm. In the graphs the correlation coefficient is plotted against a normalized, by the slot or respective hole diameter, distance. The estimated integral scale for the different cases mentioned above and for three  $x/d_1$  values are presented for all turbulent fields used. In the case of the externally excited model for each exciting frequency two values of the integral scale are presented. The first value refers to the value deduced from the correlation of the unfiltered signals, i.e. when the inputs of

the mean flow are not eliminated from the measuring system, while the bottom value indicates the value of the estimated integral scale of turbulence when the inputs of the oscillations of the mean flow are eliminated.

It is interesting to note that the value of the correlation coefficient of the unfiltered signal reaches the value of 1 as  $x/d_1 \rightarrow 0$ . The respective reading for the space correlation curve as  $x/d_1 \rightarrow 0$  for the filtered signal seems to be about 10% below the above value, for most cases. For the estimated values of the integral scales of turbulence, the difference between the scales calculated from the space correlation curves of the unfiltered signals compared with those calculated from the curves obtained from the filtered signals, is about 50%, the scales obtained from the filtered signals being the lower.

Considering the longitudinal space correlation the following points are noted.

Near the model, i.e. when the hot-wires become coincident at  $X/d_s = -0.49$  from the centre of the oscillations the space correlation coefficient of the unfiltered signal reaches values above those of the empty tunnel while those of the filtered signal fall below those of the empty tunnel. Considering the correlation coefficient of the unfiltered signal near the model it is seen that as the frequency of the model oscillations increases there is a tendency for the correlation to increase for most cases, all correlations remaining above those of the empty tunnel. The tendency reverses itself in some cases, i.e. the scale deduced from the unfiltered signals space correlation coefficients decreases with increasing oscillation frequency. On the other hand it is obvious that the values of the correlation coefficient of the filtered signal fall

below those of the empty tunnel, the values decreasing as the frequency of the model oscillations increases.

Results are also presented of the variation of the space correlation coefficient and thus the integral scale of turbulence when the model is held rigidly and when it is free to oscillate. In the case of the freely oscillating model (not externally excited) the integral scale of turbulence is higher compared with that in front of the rigidly held model. This could be the result of the model (in the case when the model is left free to oscillate) moving partly in unison with the oscillating flow thus increasing the correlation of the signals, compared with the case of the rigidly held model. At the same time it should be noted that both fall below the respective values of the empty tunnel indicating that the mere presence of the model results in a decrease of the integral scale of turbulence and a consequent decrease of the degree of the simultaneous envelopment of the model by the eddies.

As we move away from the model, further upstream, at  $X/d_s = -0.64$  and  $X/d_s = -0.96$  (these distances are the same for all turbulent fields used except that the normalizing distance changes) there seems to be a reduction to the values of the space correlation coefficient both for the unfiltered and filtered signals. The tendency of a reduction in the values of the correlation coefficient as the frequency of the externally excited model increases is present. A small reduction in the values of the correlation coefficient of the empty tunnel is also present. This is expected as  $L_1$  decreases as we move nearer the baffle. The further upstream we move the results for the rigidly held and freely oscillating models seem to tend to coincide showing that the effect of the oscillations decreases as  $|x/d_1|$  increases.

The results for the lateral (y-direction) space correlation coefficient are also presented. A considerable decrease in the values of the coefficient is shown in comparison with those of the longitudinal direction. It is interesting to note that, in most cases, even the values of the unfiltered signal fall below those of the empty tunnel. This could be explained by the fact that no matter what the separation distance between the hot-wires the model oscillations are felt equally strongly. The other aspects of the problem follow the previous trend, with a decrease in the values of the coefficient as the frequency of the externally excited model increases and as we move further upstream.

The results for the lateral (z-direction) space correlation coefficient are included. These show a similar trend as the previous results although there is a certain increase in the values compared with the respective values for the lateral (y-direction) space correlation coefficient.

The table also includes the results for the 30mm holes baffle the amplitude of the oscillations remaining constant at 2mm. An attempt to keep the different frequencies, for the respective cases of the longitudinal and lateral space correlation coefficient, constant was found to be impossible. In general there seems to be a decrease in the values of the space correlation coefficient compared with those of the slotted baffle produced turbulent field. The results for the 50mm holes baffle which show no difference from the general trend discussed above are also presented. It should be noted that for all turbulent fields the respective measurements were made at the same positions in space (as we move upstream from the model).

Fig. 129 shows the results for the configurations discussed above with the only difference that the amplitude of oscillations of the externally excited model was changed to 3.5mm. This increase

in amplitude seems to result to a general decrease of the respective space correlation coefficient values compared with the cases for 2mm amplitude oscillations. This decrease in the value of the correlation coefficient seems to be present for the oscillations of 5mm amplitude presented in Fig.130.

The results for the  $AR = 2$  flat plate for an oscillation amplitude of 2mm are presented in Fig.131. Apart from the general trends which are the same as those of the  $AR = 2$  circular cylinder, the only difference is a greater decrease in the level of the values of the space correlation coefficient. This might be expected because of the more streamlined profile presented to the flow by the circular cylinder compared to that of the flat plate. Increase in the oscillation amplitude results in a general decrease in the value of the correlation coefficient as shown in Fig. 132 and Fig.133.

From examination of all graphs it is found that there seems to be a tendency for all values of the correlation coefficient to collapse to a single curve as we move far upstream of the model. This is expected as the effect of the model should decrease the further away we move.

In a general sense it could be said that the effects of unsteady aerodynamics decrease and become less important as the integral scale of turbulence becomes large relative to the characteristic body dimension.

#### 8.10 Pressure - Velocity Correlations.

As pointed out in earlier sections in order to understand the structure of the flow in front of a body immersed in a turbulent stream and the consequent induced vibrations it is important to study



both the pressure fluctuations on the body and the distortion of the turbulence field as it approaches the body. The second aspect of the problem was discussed in previous sections.

In this section measurements made of the fluctuating pressures on the  $AR = 2$  flat plate and of the relation between these pressures and the upstream velocity are discussed. The correlation between these pressures and the upstream velocity is also presented.

Fig 134 to Fig.136 present the results of the relation between the velocity spectra - normalized with the local mean velocity - at  $x/D = -1/10$  on the stagnation line, and the pressure spectra - normalized with the local mean pressure at the stagnation point on the model. The reasons for the examination of the pressure spectra are that the pressure fluctuations are of the utmost importance in the understanding of flow induced structural vibrations of bodies. As the velocity and pressure spectra are non-dimensionalized and if we assume that the pressure fluctuations behave quasistatically, then the pressure spectra would be the same as the velocity spectra. In the above mentioned graphs it is seen that for low reduced frequencies, up to  $\frac{2\pi f}{U_c} L_c \approx 10^\circ$  for the slotted and 30mm holes baffles and up to  $\frac{2\pi f}{U_c} L_c \approx 10'$  for the 50mm holes baffle, this is true. At higher reduced frequencies the pressure spectra fall below the velocity spectra. Bearman (Ref. 5) has also measured stagnation pressures and finds a similar behaviour.

The pressure fluctuations were correlated with the velocity fluctuations ahead of the plate. The results are shown in Fig. 137 to Fig. 139. It seems that at the stagnation point the

pressure - velocity space correlation coefficient tends to a value of about 0.6 and as  $x/L_x$  increases falls rapidly to a low value of about 0.1. The low value of the pressure - velocity space correlation coefficient of 0.1 starts at about  $x/L_x \approx 0.9$  remaining about constant as  $x/L_x$  increases, at least up to a value of  $x/L_x = 2.2$  where the measurements stopped.

## 2. CONCLUSIONS

The following general conclusions were reached from the examination of the interaction of the flow with the model.

1) The cross-correlation coefficient of the empty tunnel seems to follow an exponential law of the form  $R_{11}(0, z_2, 0) \left( \frac{f y}{u} \right) = e^{-c \left( \frac{f y}{u} \right)}$

This correlation coefficient decreases rapidly in front of the model, the decrease being higher in front of the rigidly held model compared with that in front of the freely oscillating model. The greater the degree of the streamlining of the model the smaller the decrease of the cross-correlation coefficient. This observation applies for the region of the flow near and upstream of the model.

2) The spectrum of the longitudinal velocity moves to higher wavenumbers as the model is approached from upstream.

3) The turbulence level (based on the local mean velocity) increases in front of the model, the increase being higher in the case of the rigidly held model compared with the case of the freely oscillating model.

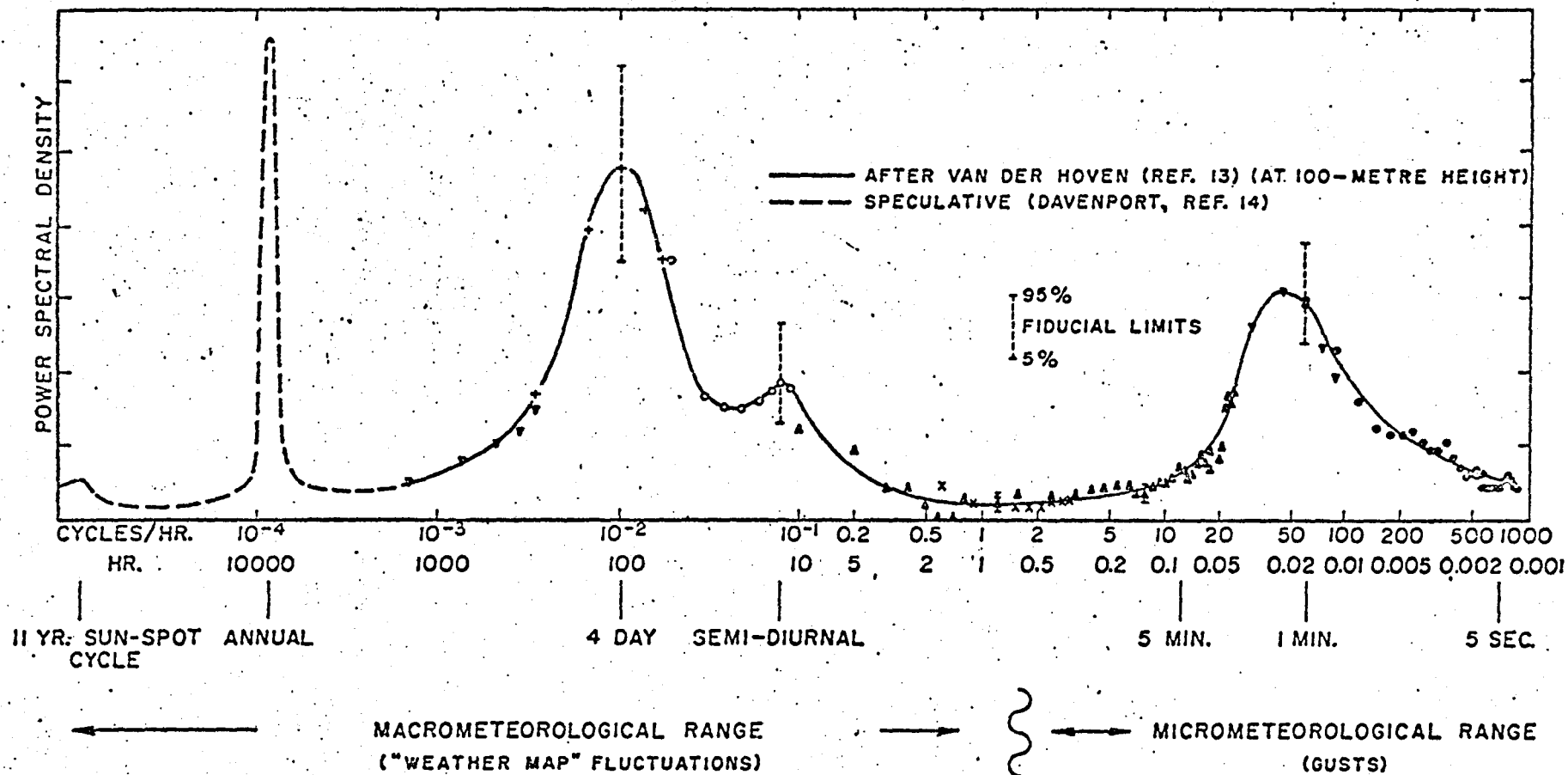
4) The decrease of the r.m.s. value of the fluctuating velocity component as the model is approached could be deduced from consideration of the probability density function of the longitudinal velocity component.

5) The variation of the energy level of the different eddies as the model is approached seems to be rather small for the frequency range  $2\text{Hz} < f < 6\text{Hz}$  increasing for the frequency range  $7\text{Hz} < f < 12\text{Hz}$ . Generally the decay seems to follow a power law. This is not quite true for the range  $14\text{Hz} < f < 40\text{Hz}$ . The range  $50\text{Hz} < f < 100\text{Hz}$  show no great variation. The greatest variation in the energy level of the different eddies is present in the stagna-

tion line flow compared with the other lateral positions.

6) The integral scale of turbulence decreases as the frequency of vibration or amplitude of oscillations increases. The more the degree of streamlining of the body the less the decrease of the scale of turbulence.

7) In low frequencies the pressure spectra ( at the stagnation point) are the same as the velocity spectra measured at  $x/D = -1/10$ . At higher frequencies the pressure spectra fall below the respective velocity spectra. The maximum pressure- velocity space correlation coefficient reaches the value of 0.6.



SPECTRUM OF HORIZONTAL WIND SPEED NEAR THE GROUND  
 FOR AN EXTENSIVE FREQUENCY RANGE

FIG: 1

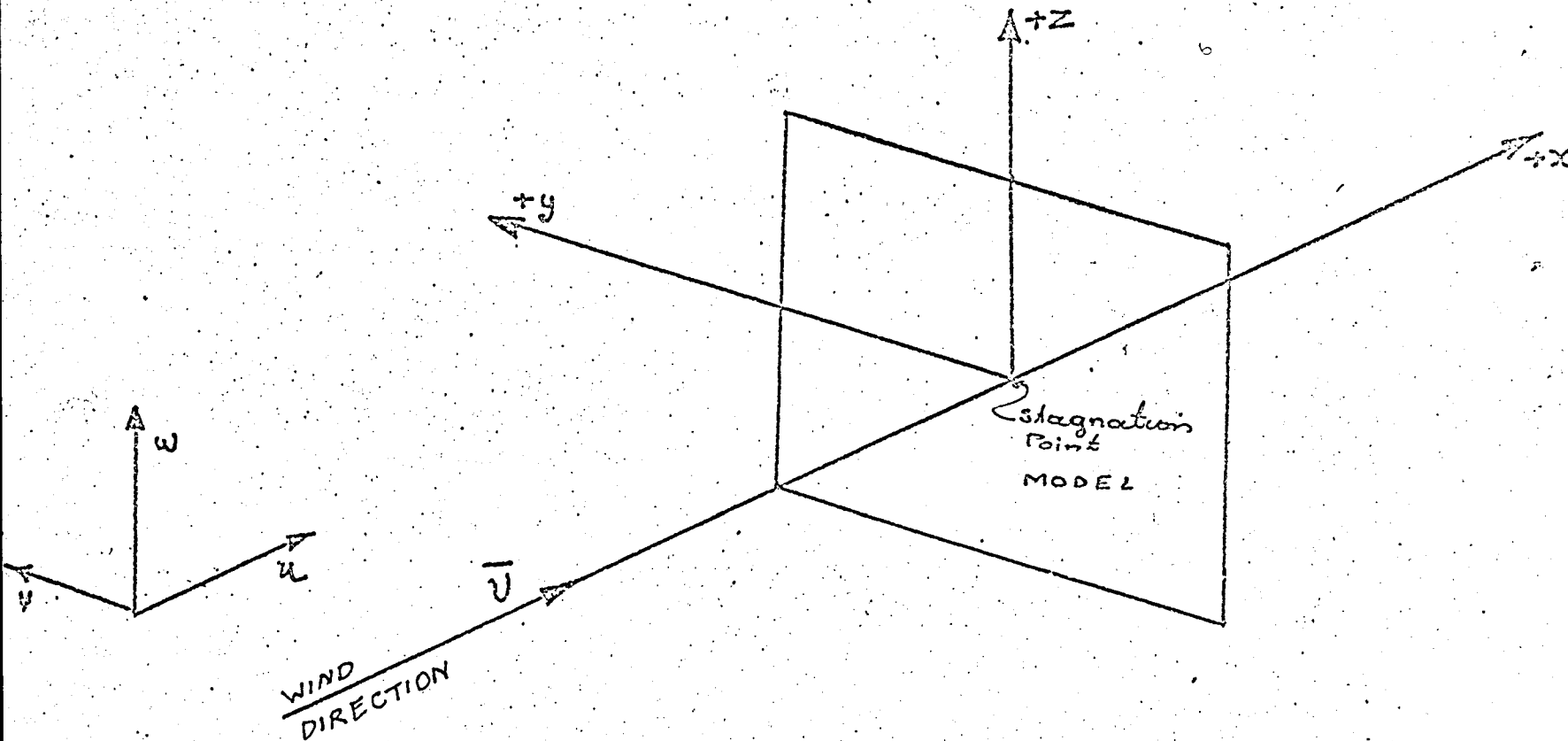
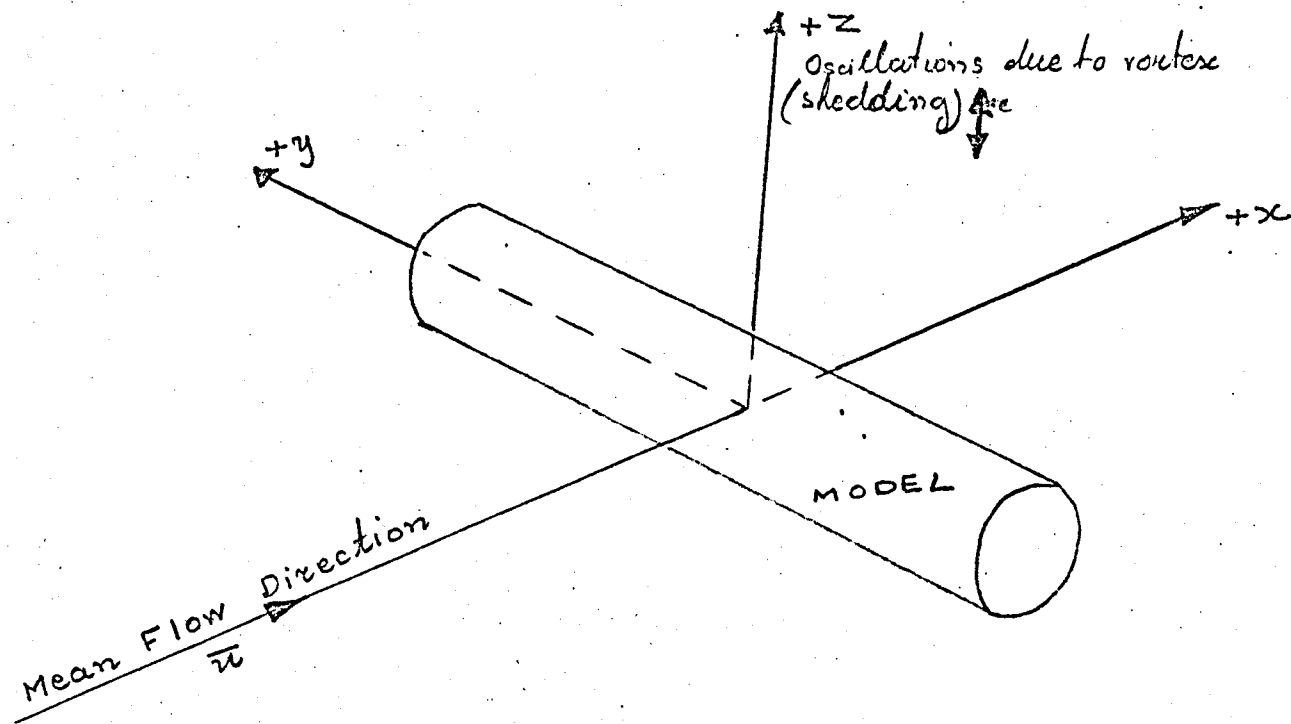


FIG: 2

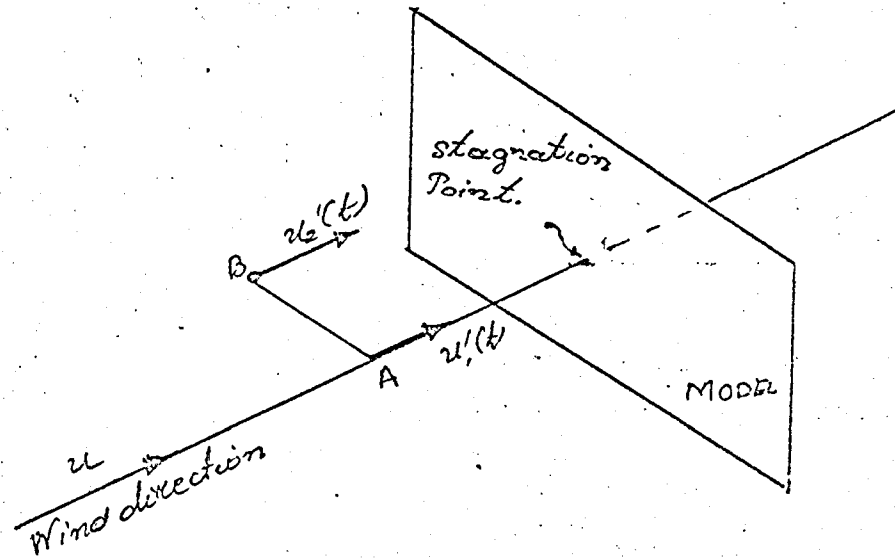
Definition Sketch

unless otherwise stated



Definition Sketch

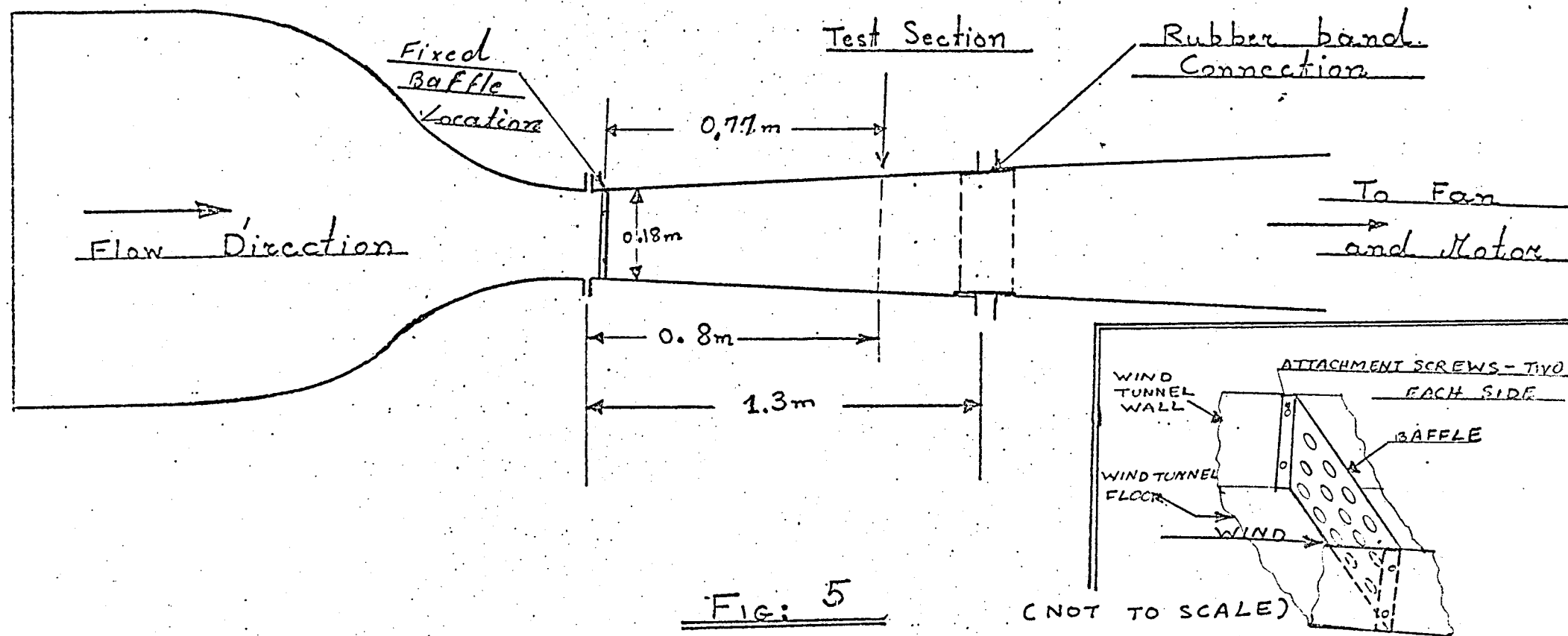
Fig 3



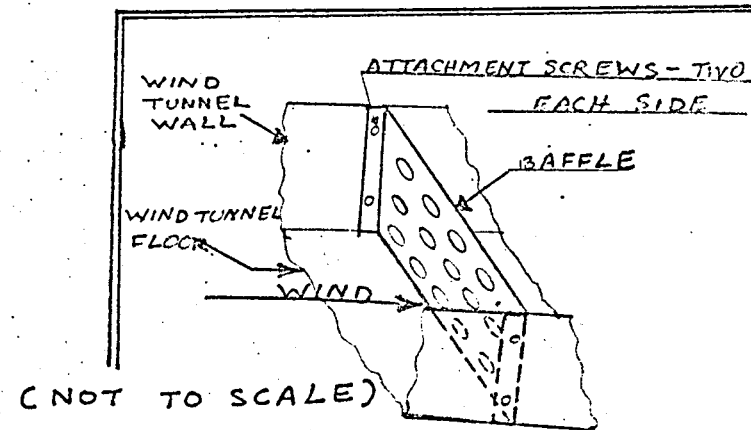
Definition Sketch      (Correlation velocities)

Fig 4





Schematic Diagram of Wind Tunnel



METHOD OF BAFFLE ATTACHMENT TO WIND TUNNEL

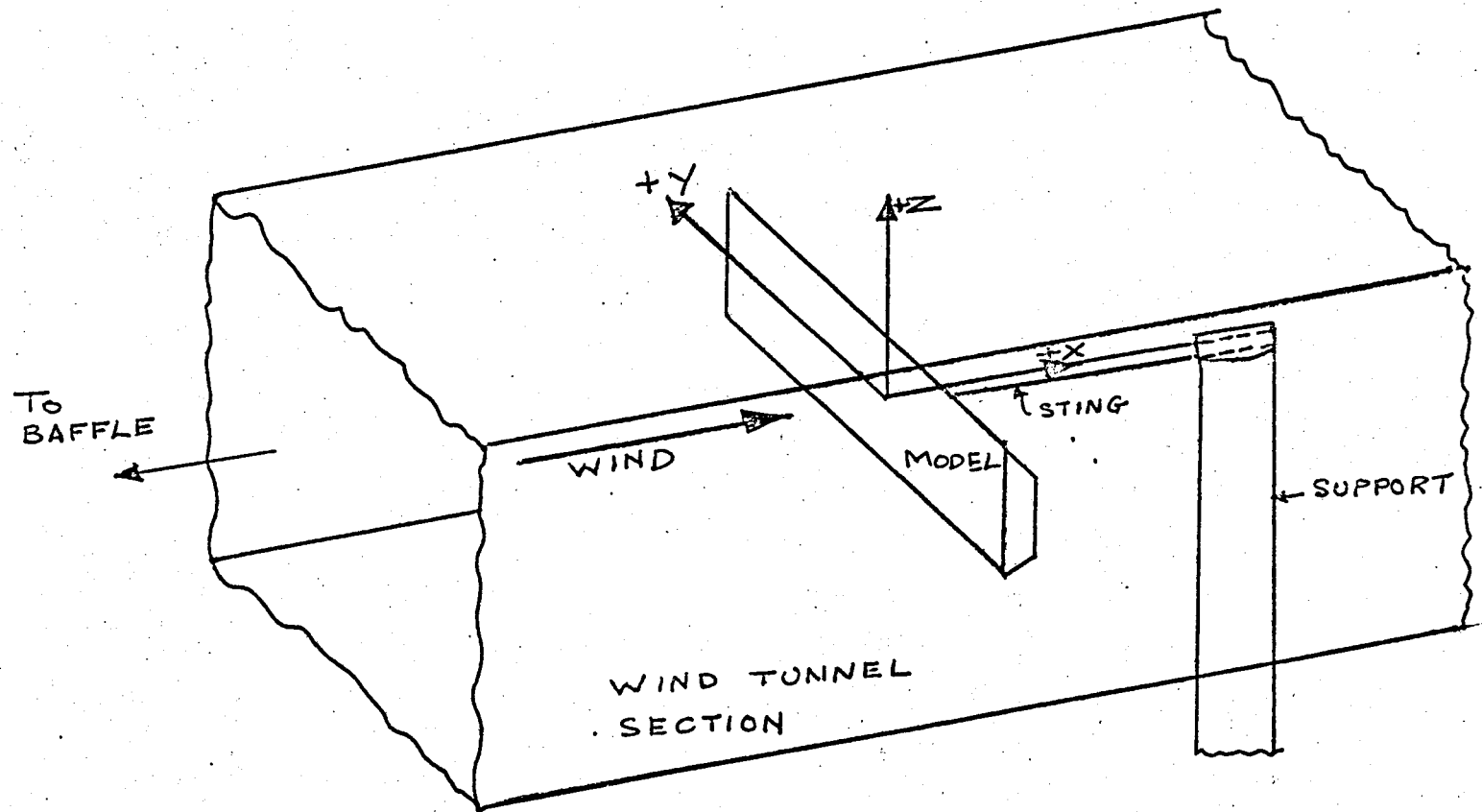
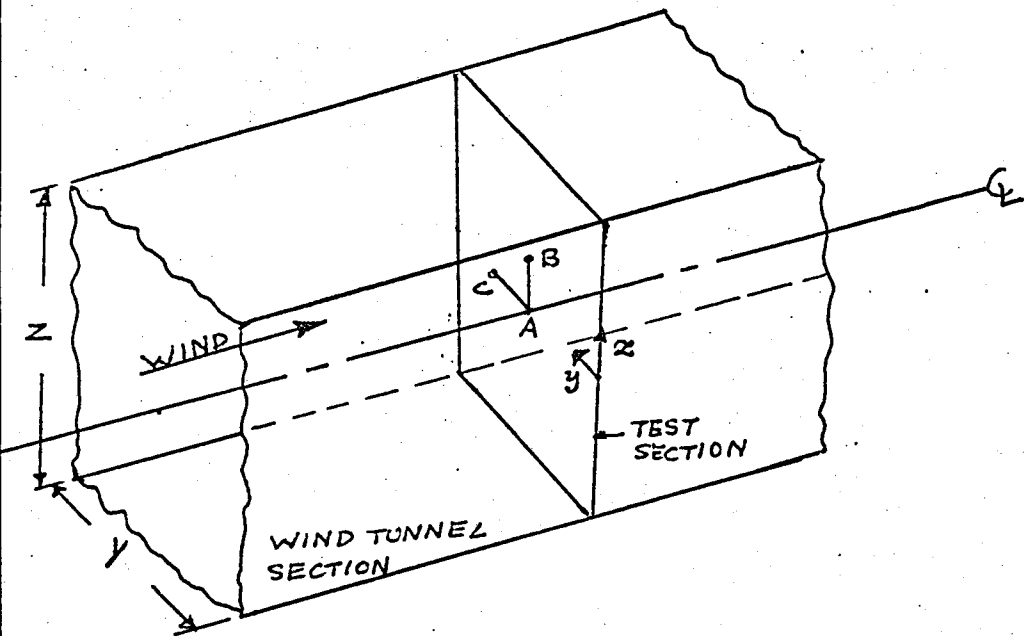


FIG. 5a

Schematic Diagram of Model in the  
Wind Tunnel.



Co-ordinates:

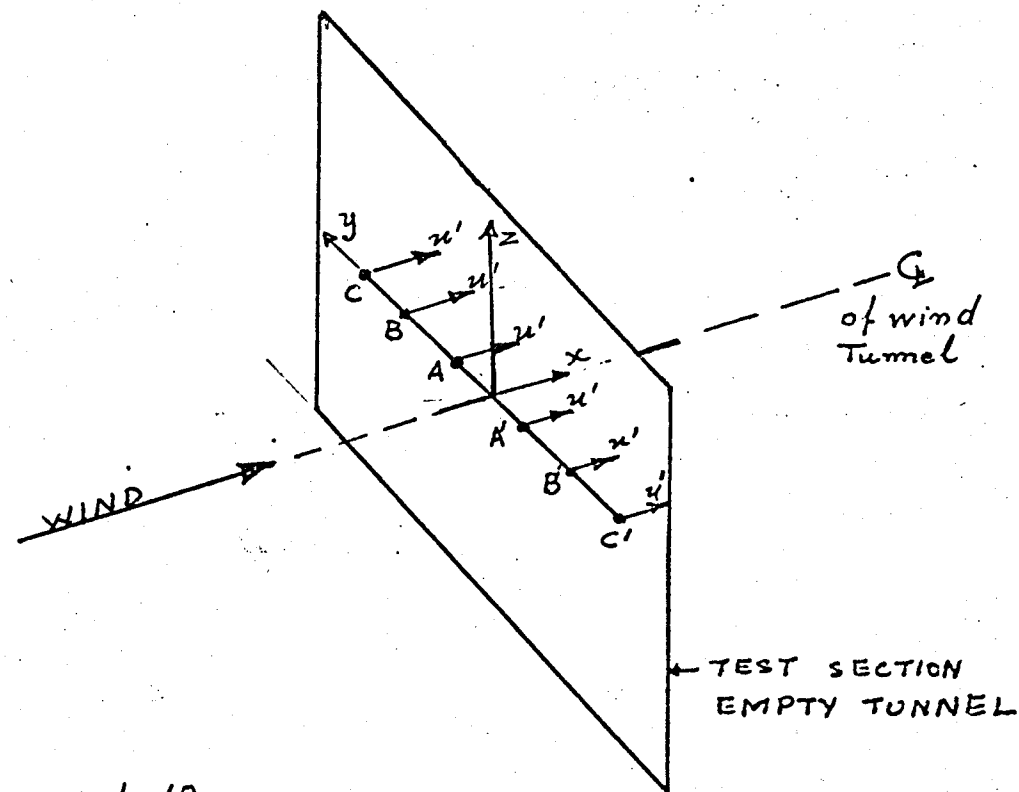
$$A, \frac{y}{Y} = 0.5, \frac{z}{Z} = 0.0$$

$$B, \frac{y}{Y} = 0.5, \frac{z}{Z} = 0.318$$

$$C, \frac{y}{Y} = 0.582, \frac{z}{Z} = 0.0$$

FIG. 5b

Definition sketch



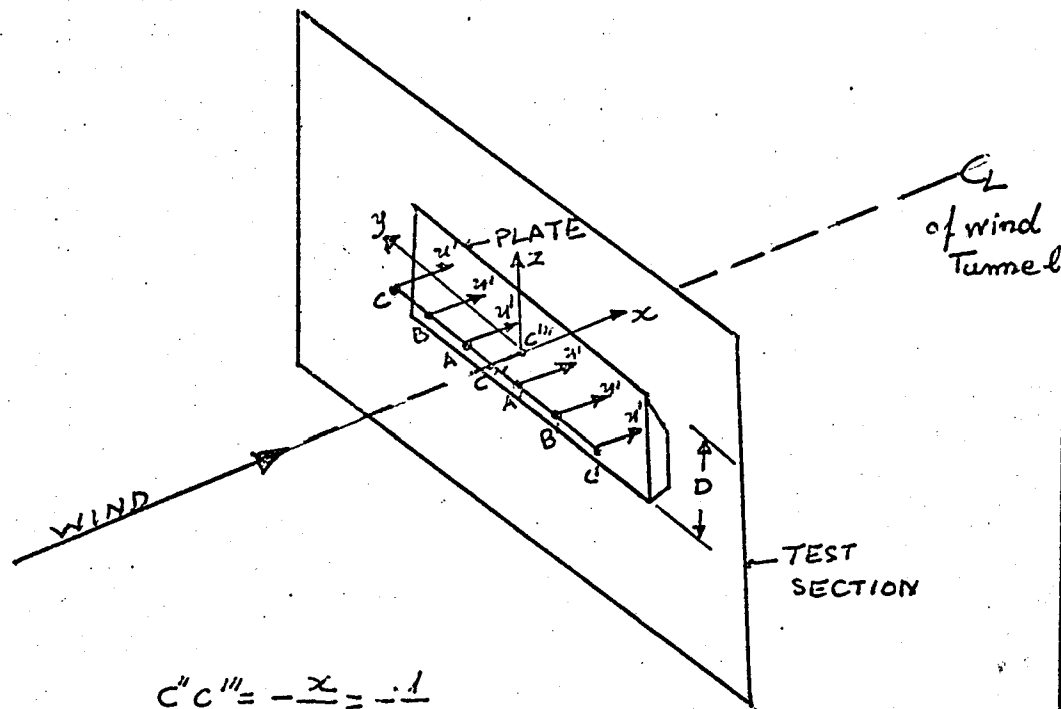
$$AA' = 10\text{mm}$$

$$BB' = 20\text{mm}$$

$$CC' = 40\text{mm}$$

FIG. 5c

Definition sketch



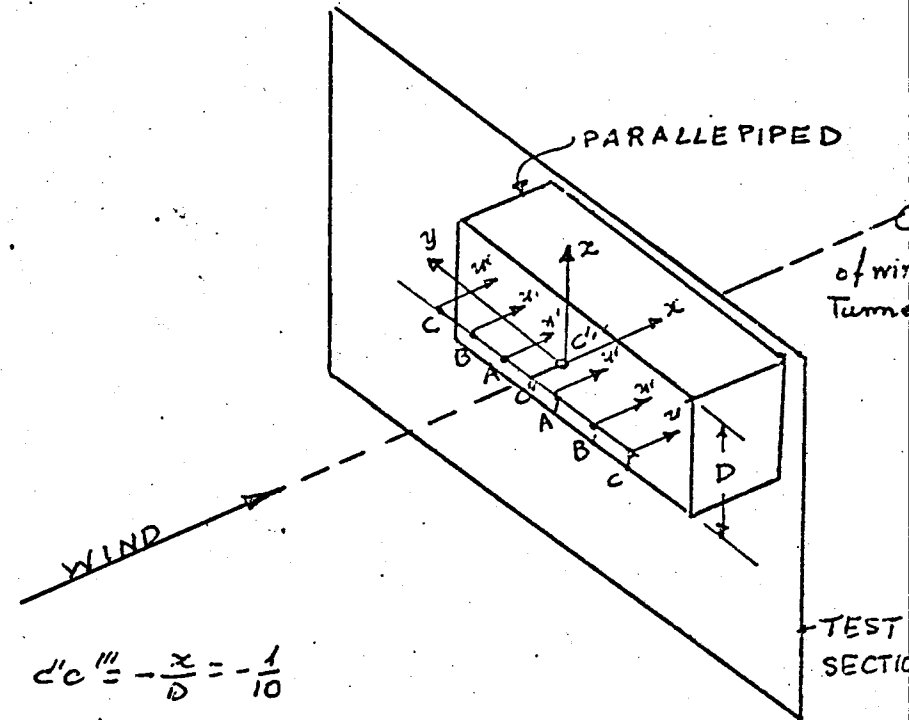
$$C''C''' = -\frac{x}{D} = -\frac{1}{10}$$

$$AA' = 10\text{mm}$$

$$BB' = 20\text{mm}$$

$$CC' = 40\text{mm}$$

FIG. 5d  
Definition Sketch



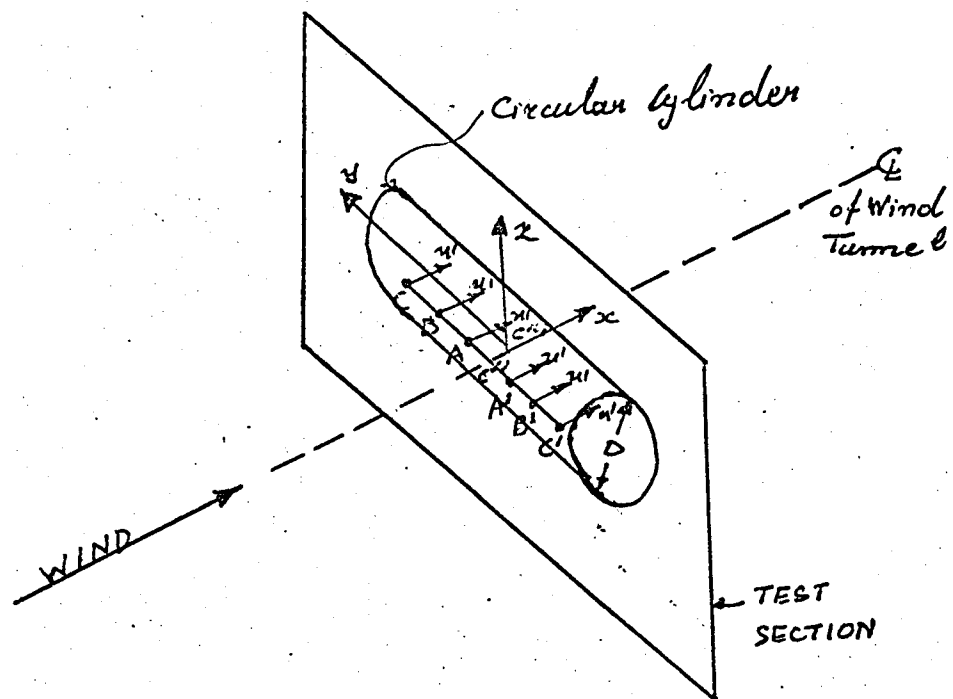
$$C''C''' = -\frac{x}{D} = -\frac{1}{10}$$

$$AA' = 10\text{mm}$$

$$BB' = 20\text{mm}$$

$$CC' = 40\text{mm}$$

FIG. 5e  
Definition Sketch



$$C''C''' = -\frac{x}{D} = -\frac{1}{10}$$

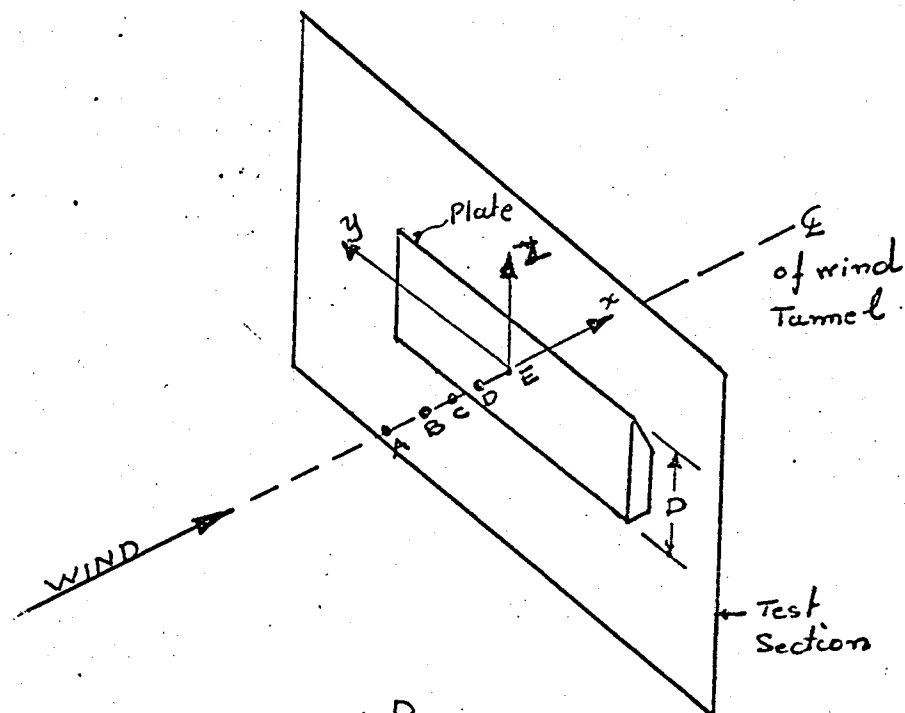
$$AA' = 10\text{mm}$$

$$BB' = 20\text{mm}$$

$$CC' = 40\text{mm}$$

FIG. 5f

Definition Sketch



$$DE = -\frac{D}{10}$$

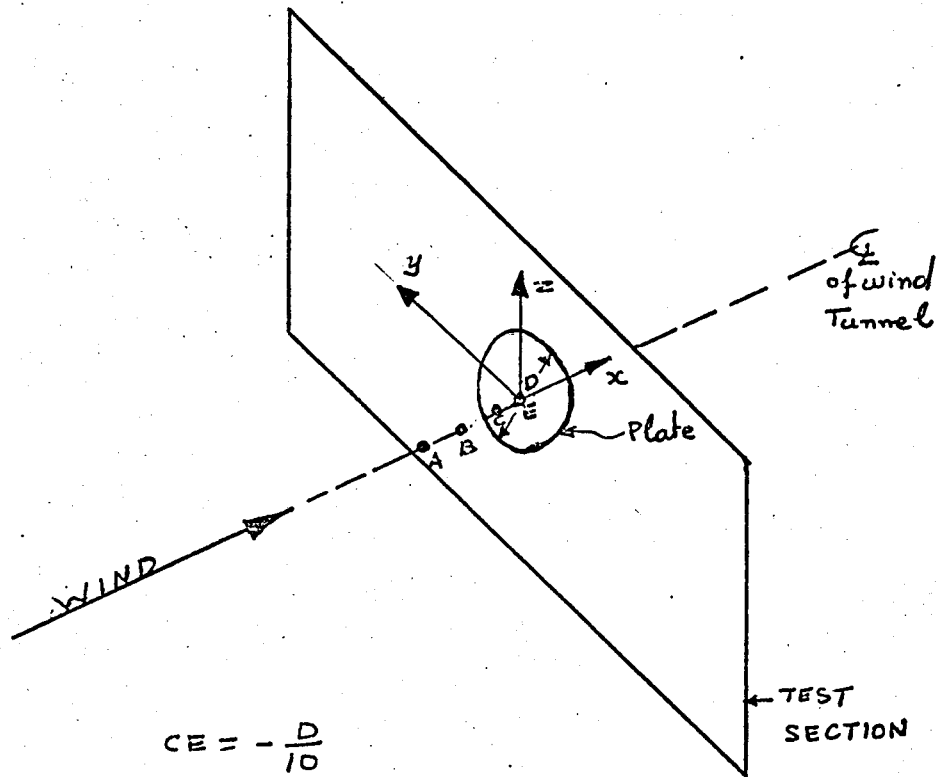
$$CE = -\frac{D}{4}$$

$$BE = -\frac{D}{2}$$

$$AE = -D$$

FIG. 5g

Definition Sketch



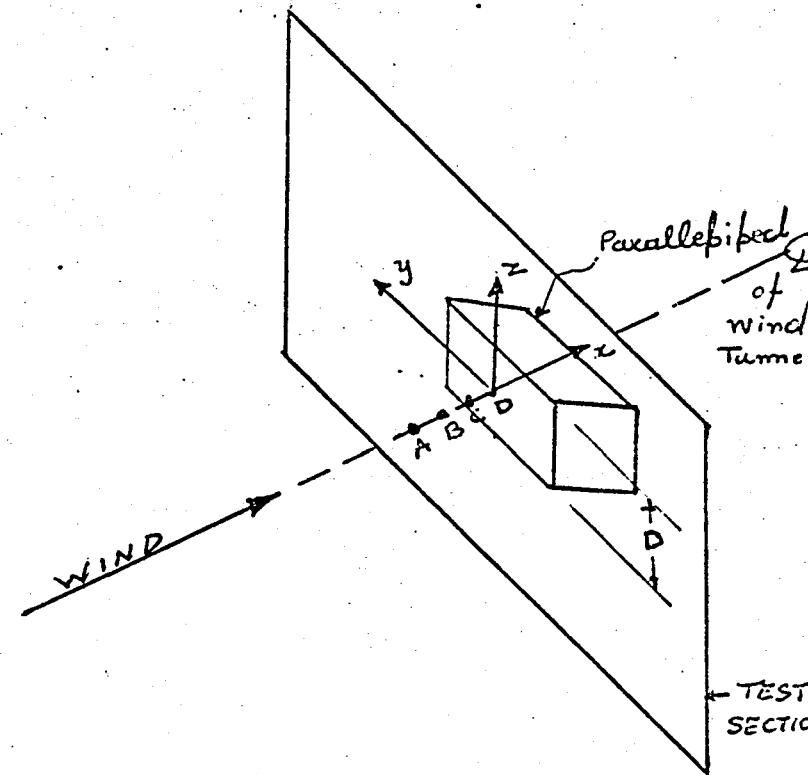
$$CE = -\frac{D}{10}$$

$$BE = -\frac{D}{2}$$

$$AE = -D$$

FIG: 5h

Definition Sketch



$$CD = -\frac{D}{10}$$

$$BP = -\frac{D}{2}$$

$$AD = -D$$

FIG: 5i

Definition Sketch

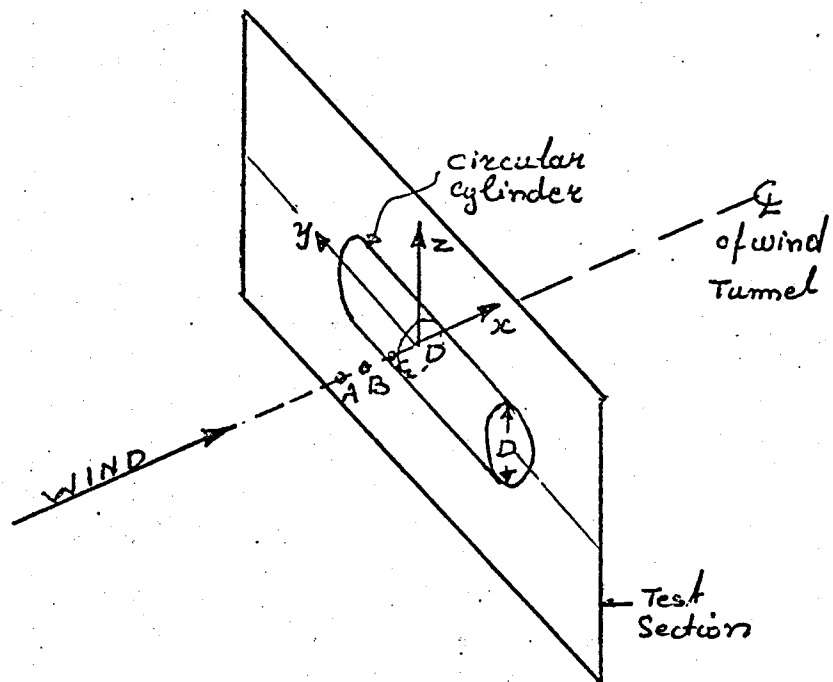


FIG: 5j  
Definition Sketch

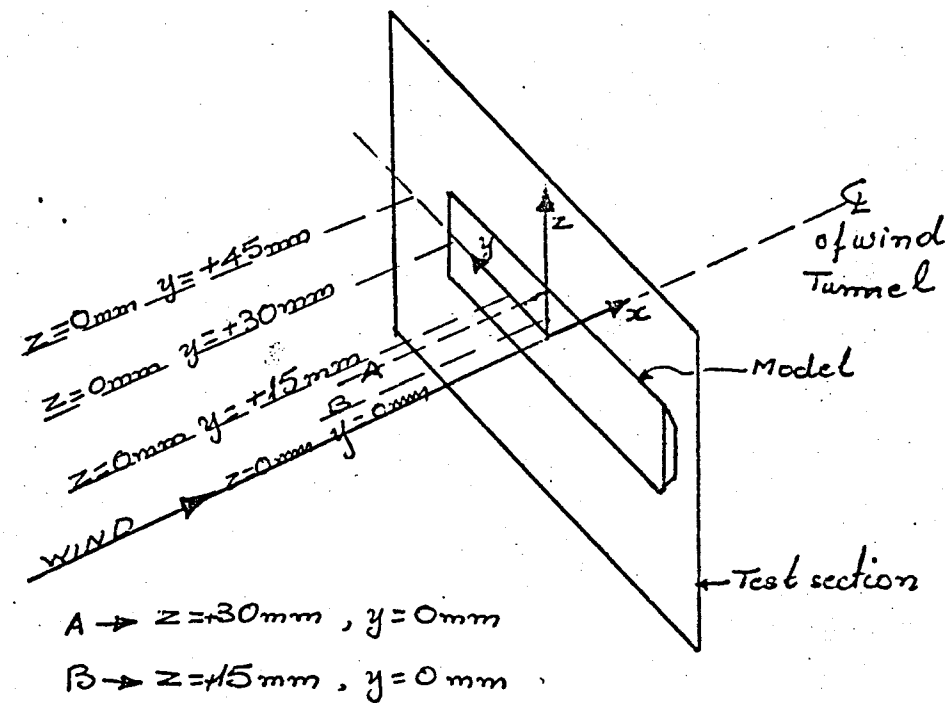
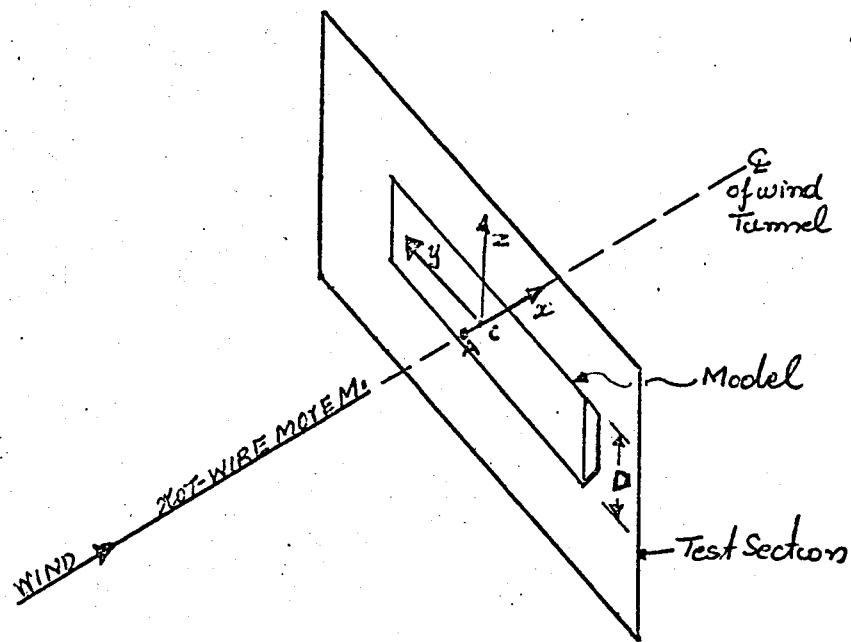


FIG: 5K  
Definition Sketch.



Pressure transducer at C (stagnation point)

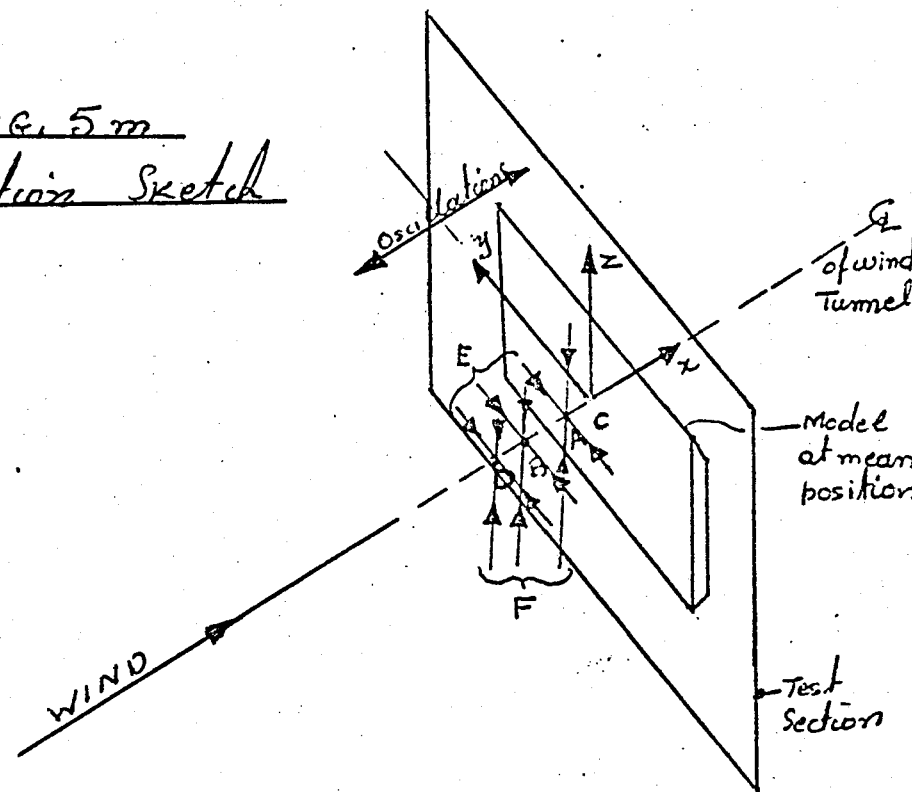
$$AC = -0.1D$$

For velocity spectrum Hot-wire stationary at A

FIG. 5l

Definition Sketch.

FIG. 5m  
Definition Sketch



C → stagnation point.

For measurement of  $L_x$  hot wires coincident at A, B, or D where:

$$\left. \begin{aligned} AC &= -0.49d_s \text{ or } -0.59d_{30} \text{ or } -0.35d_{50} \\ AB &= -0.64d_s \text{ or } -0.77d_{30} \text{ or } -0.46d_{50} \\ DC &= -0.96d_s \text{ or } -1.14d_{30} \text{ or } -0.69d_{50} \end{aligned} \right\} \text{ Depending on the baffle used.}$$

Arrows E indicate hot-wires movement for measurement of  $R_{11}(0, y_2, 0)$  and in succession of  $L_y$ .

Arrows F indicate hot-wires movement for measurement of  $R_{11}(0, 0, y_3)$  and in succession of  $L_z$ .



MEAN VELOCITY PROFILES AT TEST SECTION

(Empty tunnel)

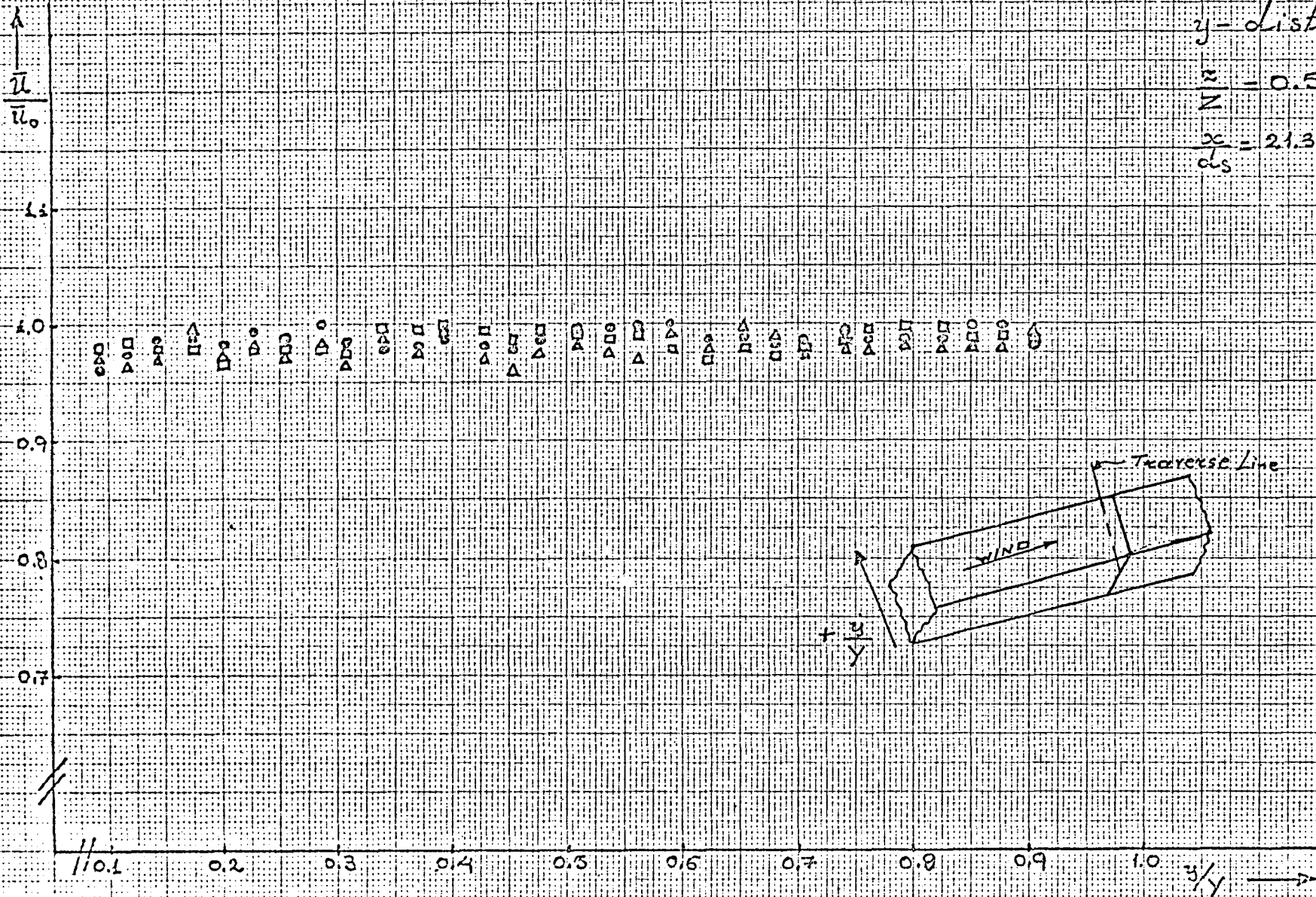
(Throughout the work the turbulence  
baffles are always present)

# Mean Velocity Profiles at Test Section

$y$ -Distribution

$$\frac{z}{Z} = 0.5$$

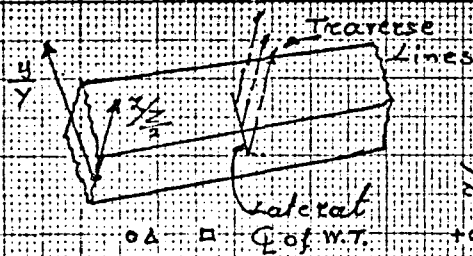
$$\frac{x}{d_s} = 21.3, \quad \frac{x}{d_{30}} = 25.9, \quad \frac{x}{d_{50}} = 15.5$$



Legend

- Slotted Baffle
- △ 30mm Holes Baffle
- 50mm Holes Baffle

FIG: 6



# Mean Velocity Profiles

at Test Section

( $\alpha$ -distribution)

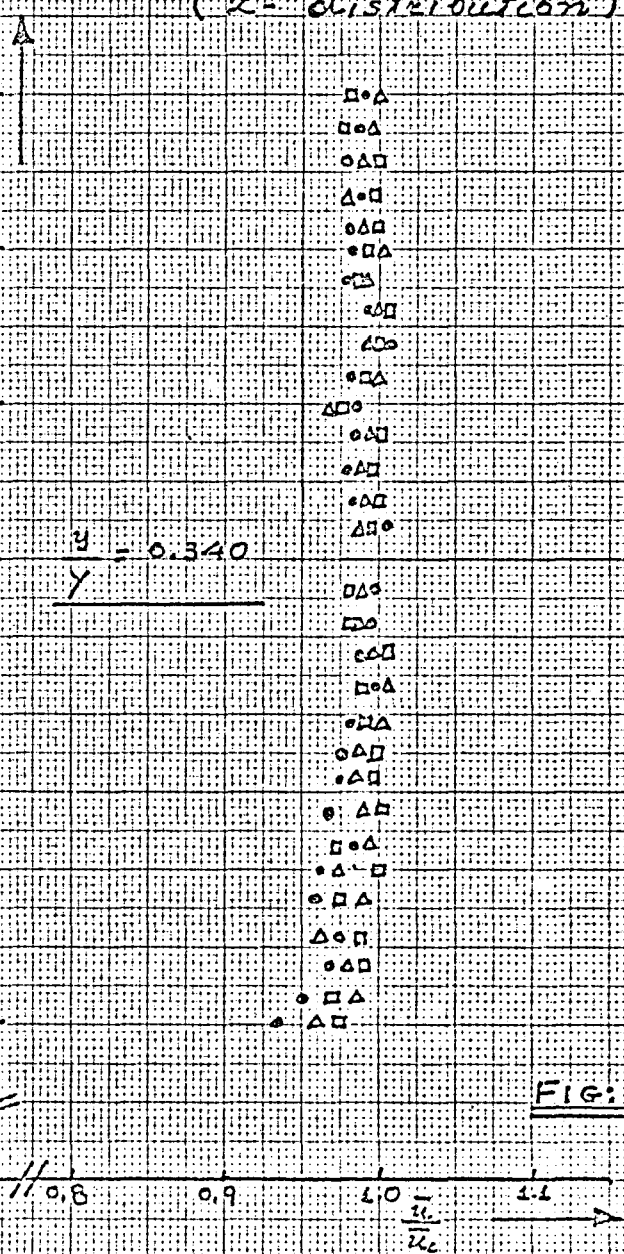
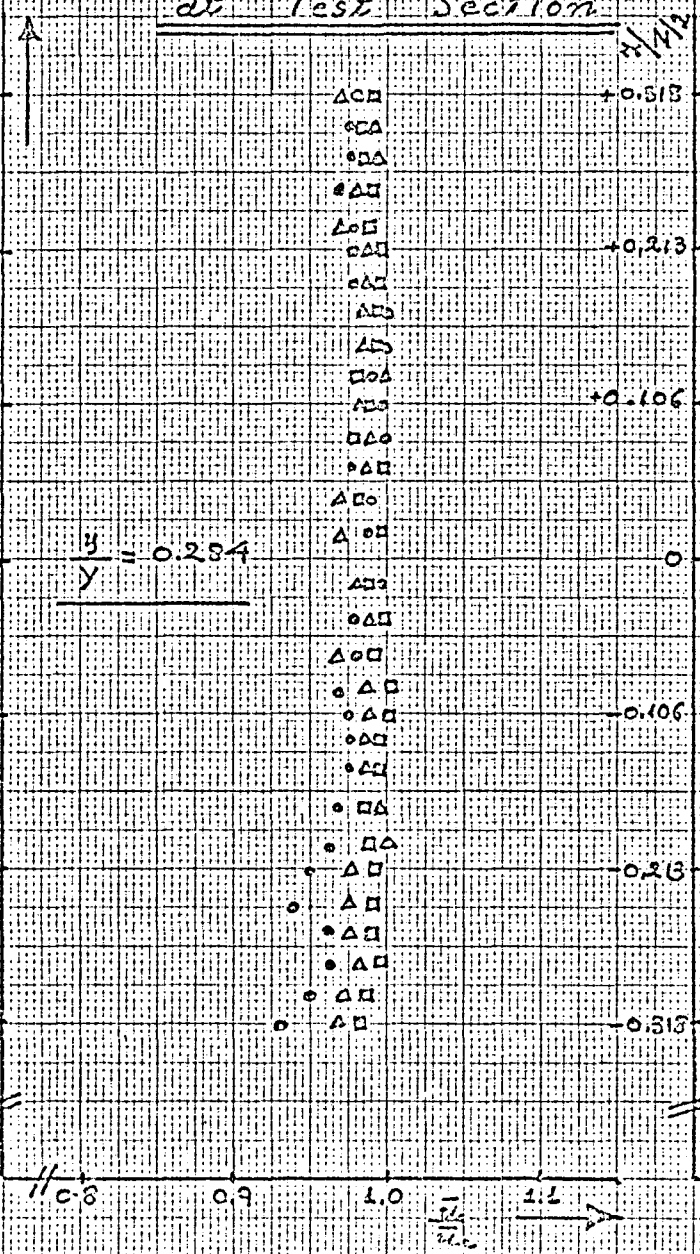
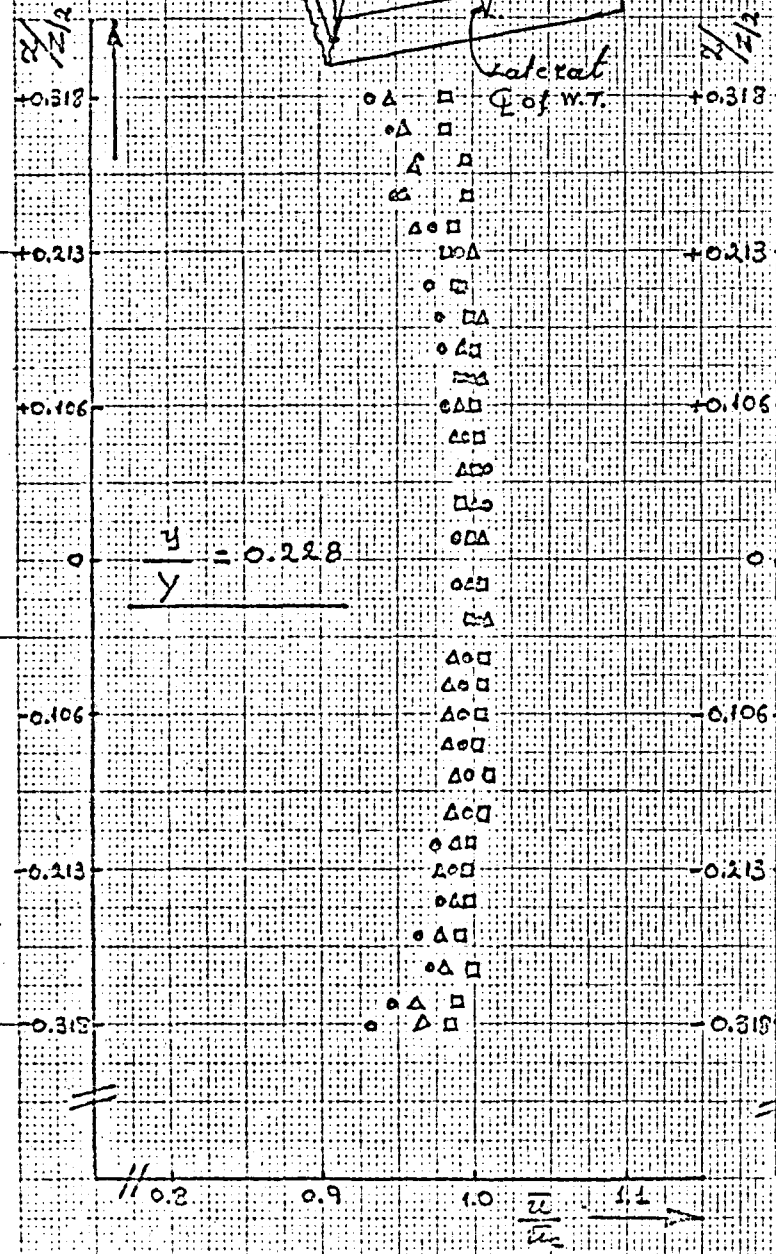
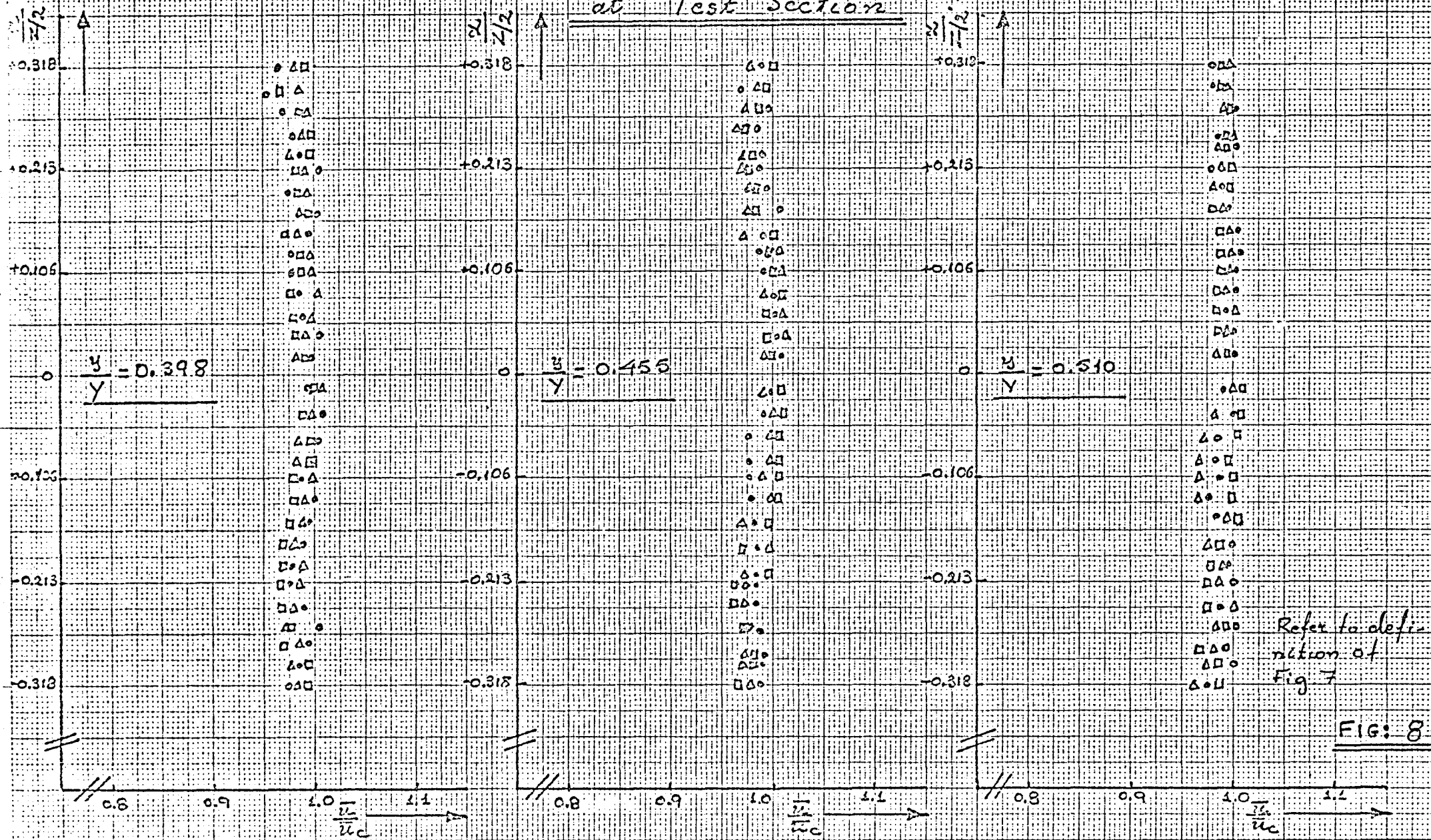


FIG. 7

# Mean Velocity Profiles

at Test Section

( $z$ -distribution)



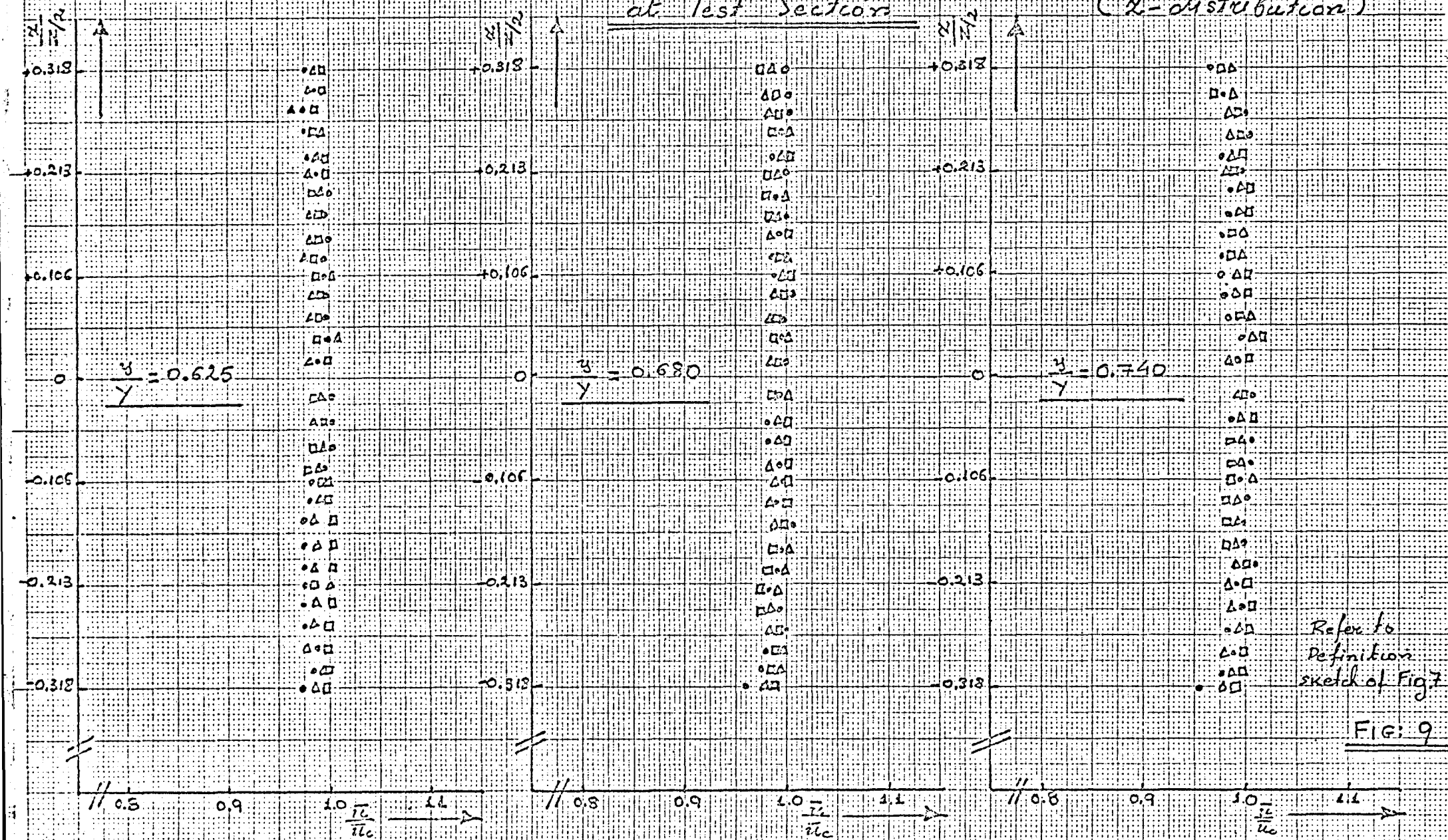
Refer to definition of  
Fig. 7

FIG: 8



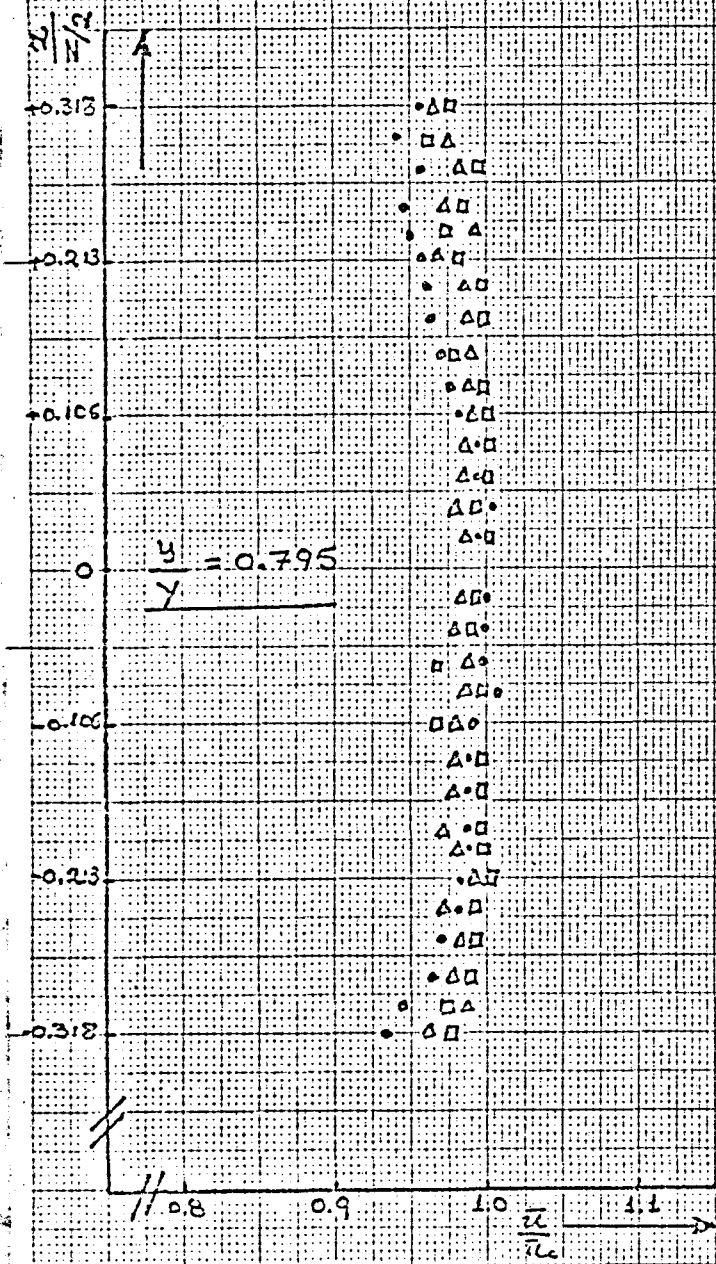
# Mean Velocity Profiles at Test Section

( $x$ -distribution)



# Mean Velocity Profiles at Test Section

( $\alpha$ -distributions)

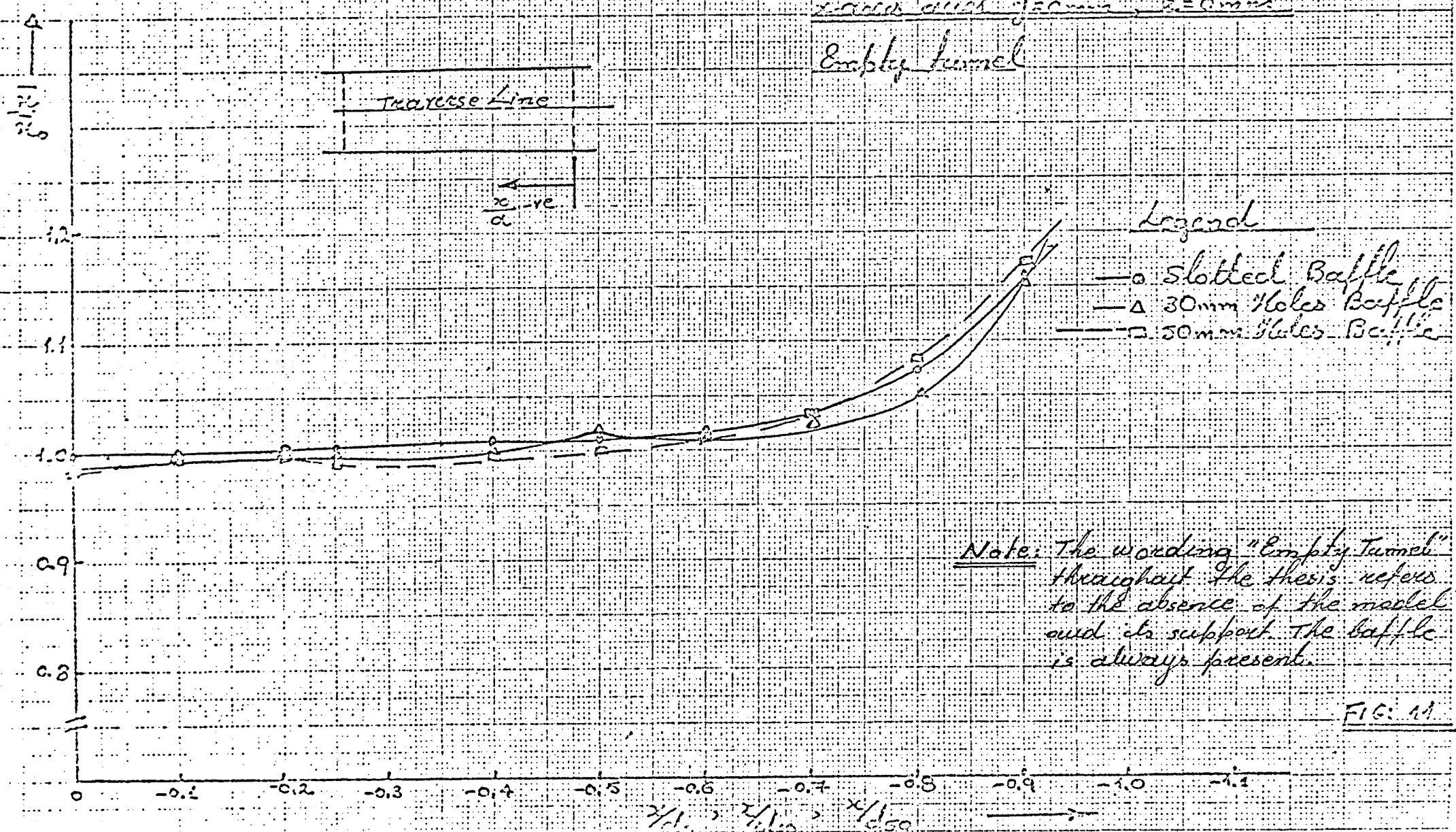


## Legend

- Slotted Baffle
- △ 30mm Holes Baffle
- 50mm Holes Baffle

Refer to definition sketch of  
Fig. 7

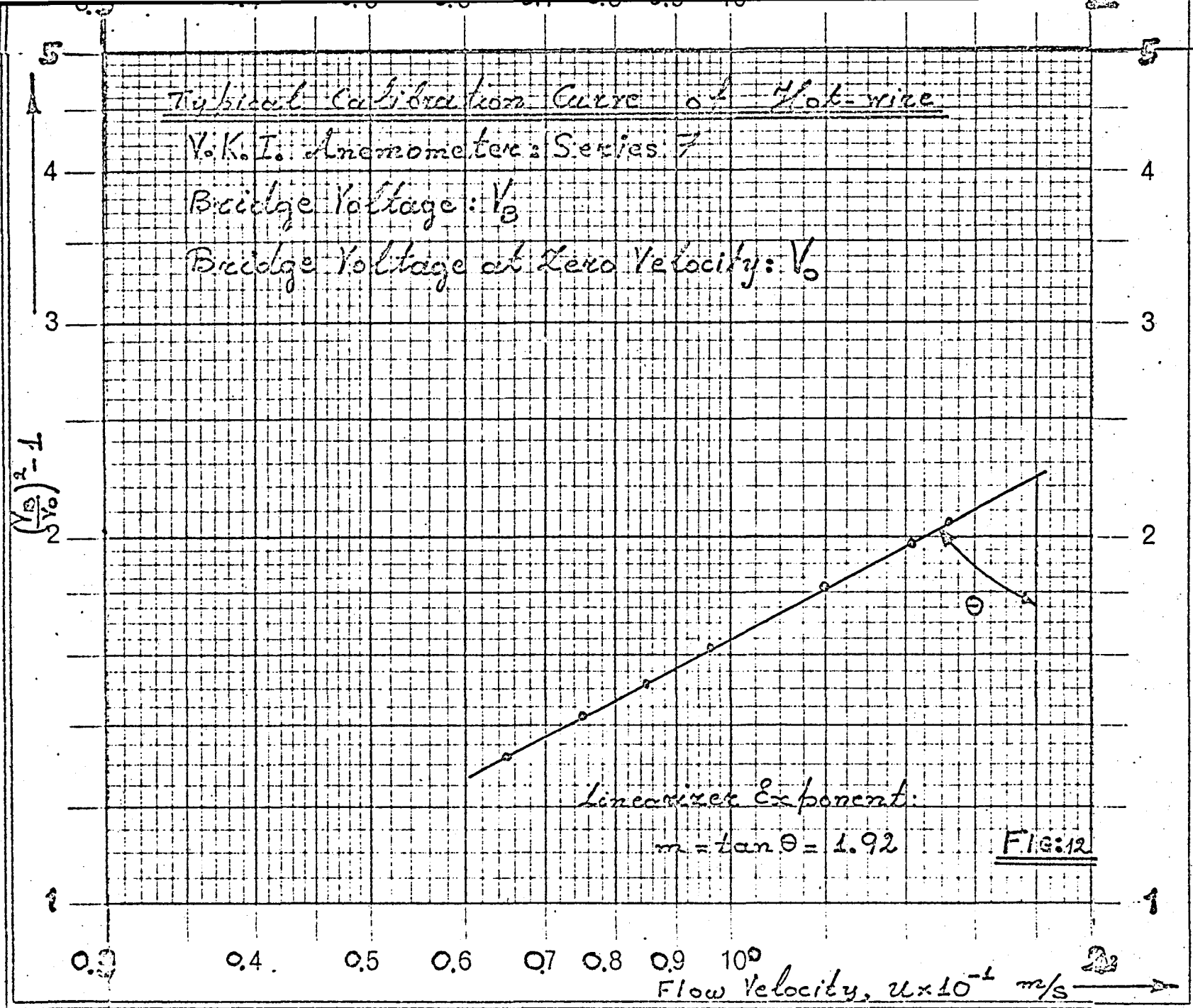
Stream Velocity Variation along the  
axis and y=0mm, z=0mm  
Empty tunnel



INTENSITY PROFILES AT THE TEST SECTION

(Empty Tunnel)



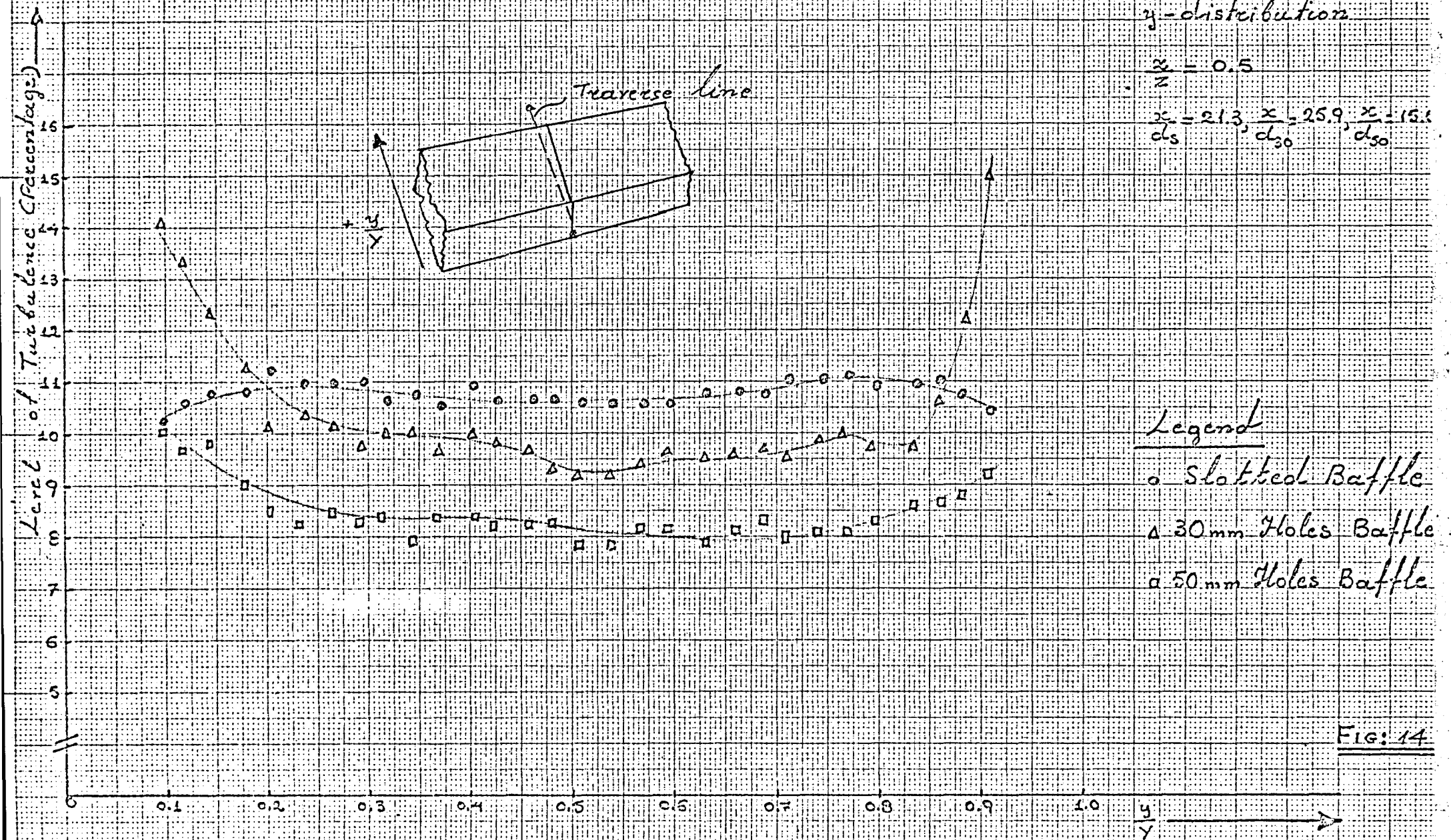


Typical Water-mine Verification Curve  
after Linearisation  
 { V.K.I. Instrument Series 7 }



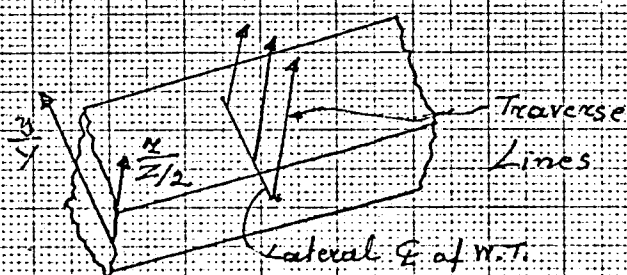
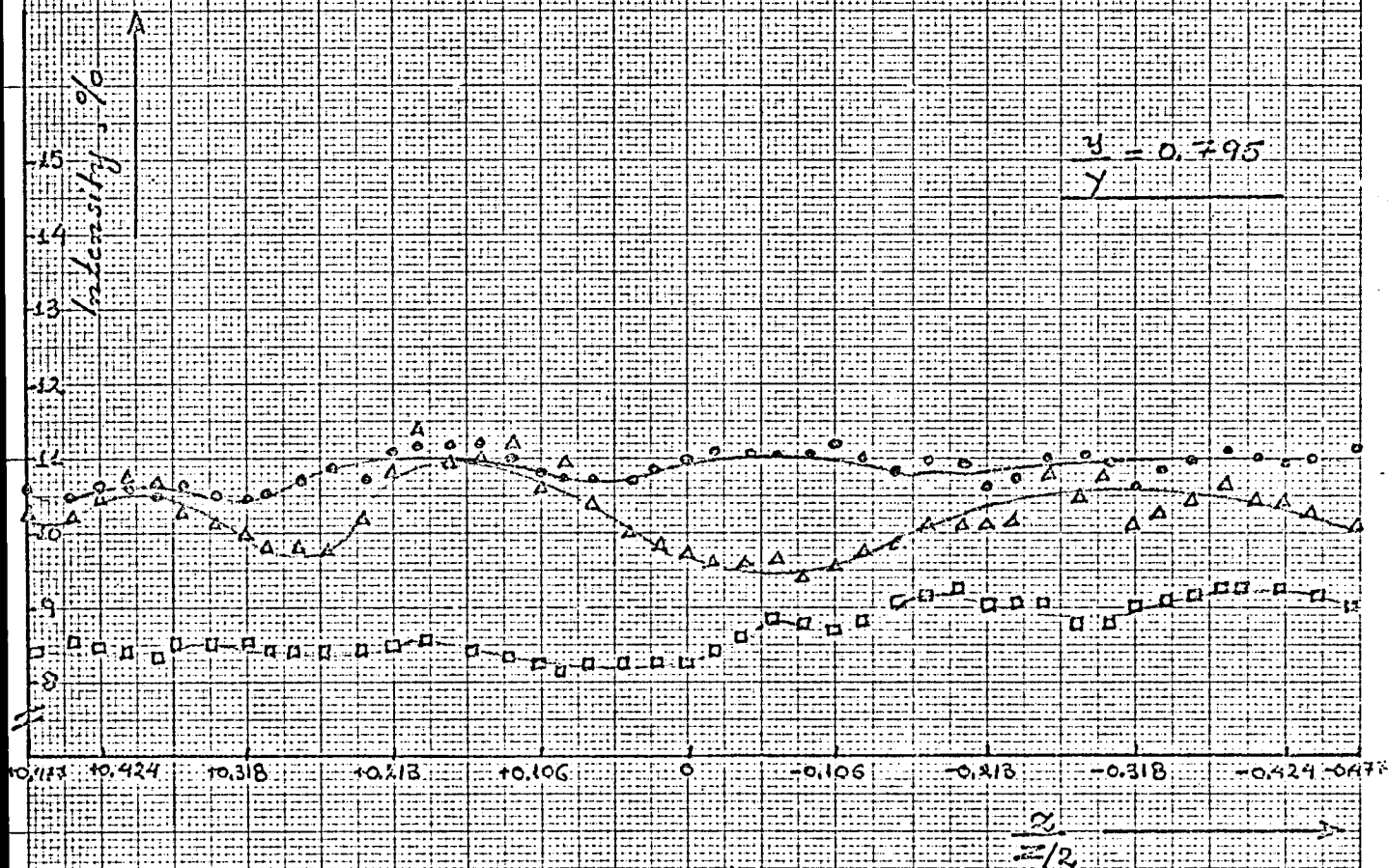
FIG. 13

# Intensity Profiles at Test Section



at Test Section 2

(z-distribution)



Legend

- Slotted Baffle
- 30mm Holes Baffle
- 50mm Holes Baffle

FIG: 15

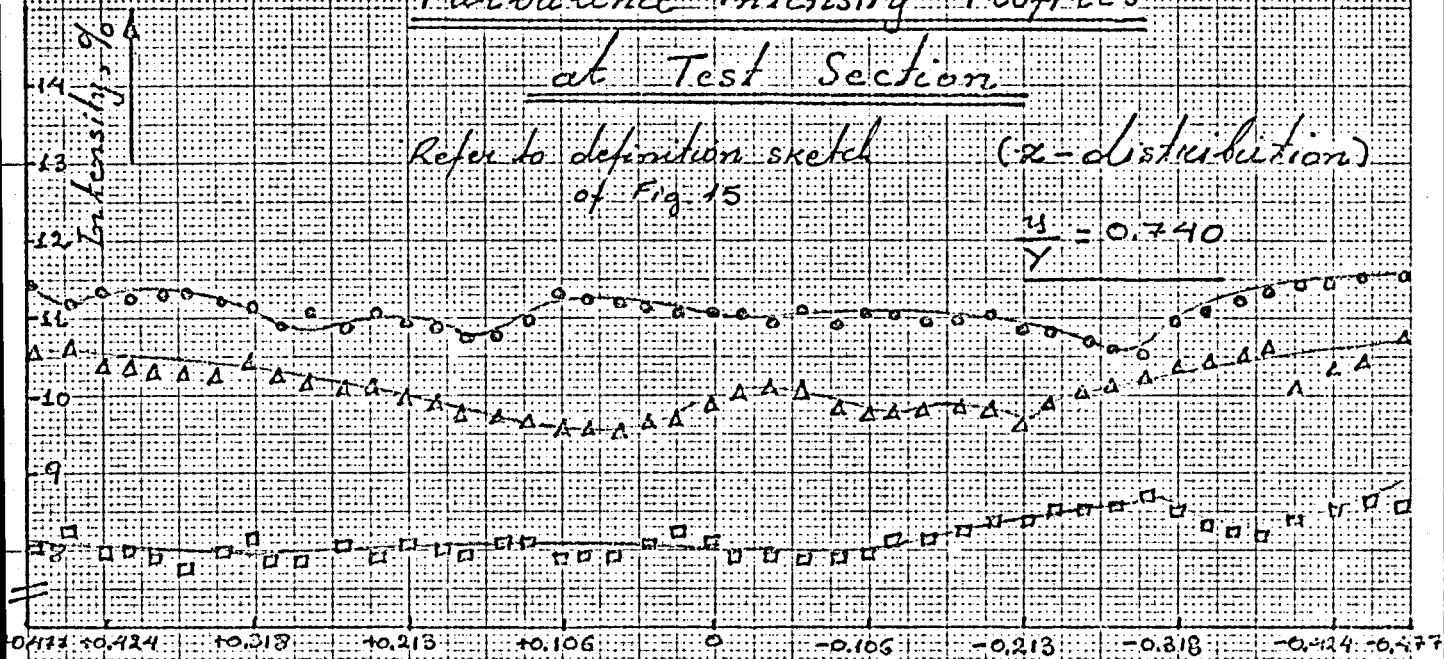


# Turbulence Intensity Profiles at Test Section

Refer to definition sketch  
of Fig. 15

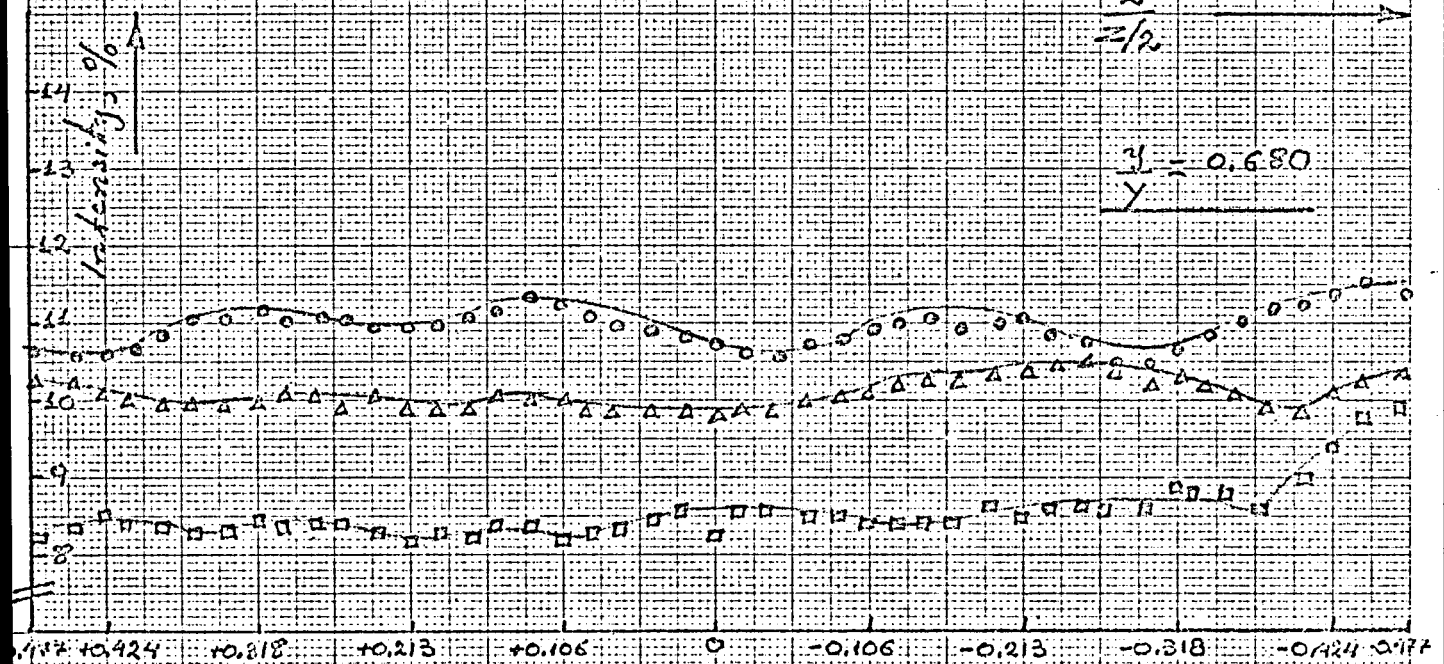
( $\alpha$ -distribution)

$$\frac{y}{Y} = 0.740$$



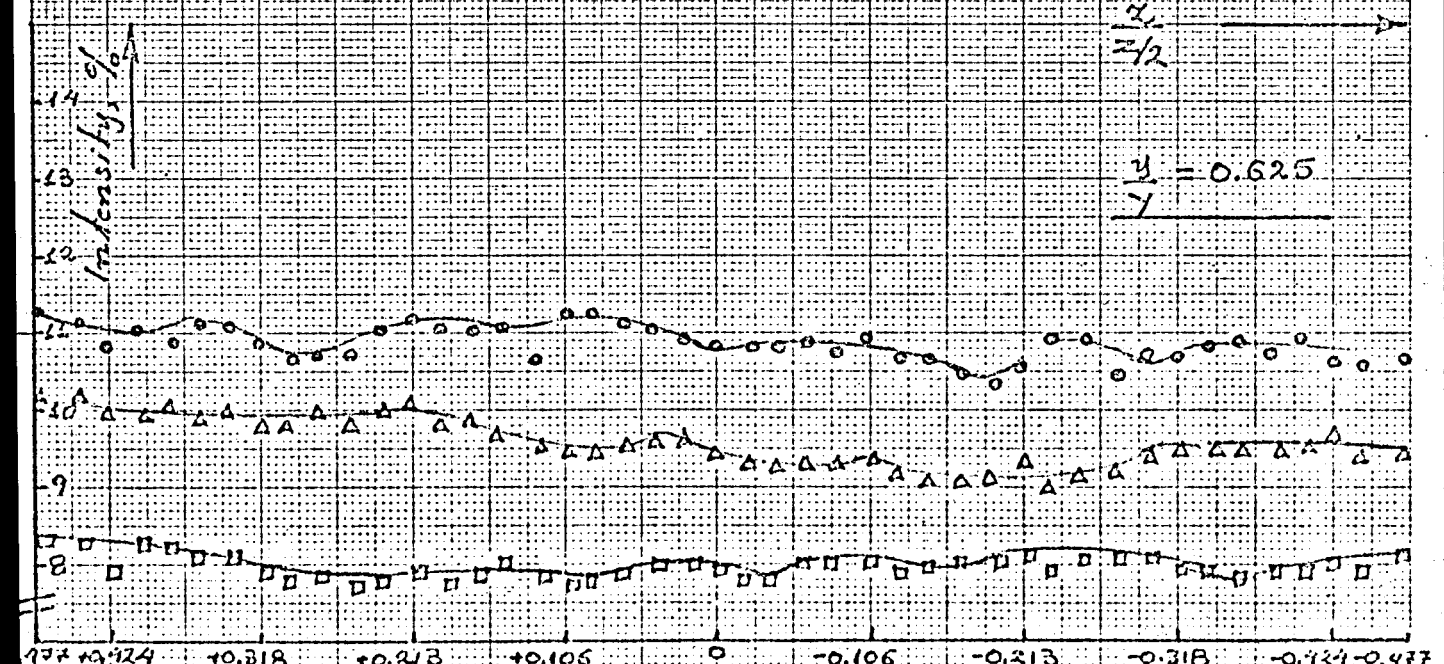
$$\frac{x}{z} = \frac{1}{2}$$

$$\frac{y}{Y} = 0.680$$



$$\frac{x}{z} = \frac{1}{2}$$

$$\frac{y}{Y} = 0.625$$



$$\frac{x}{z} = \frac{1}{2}$$

FIG: 16

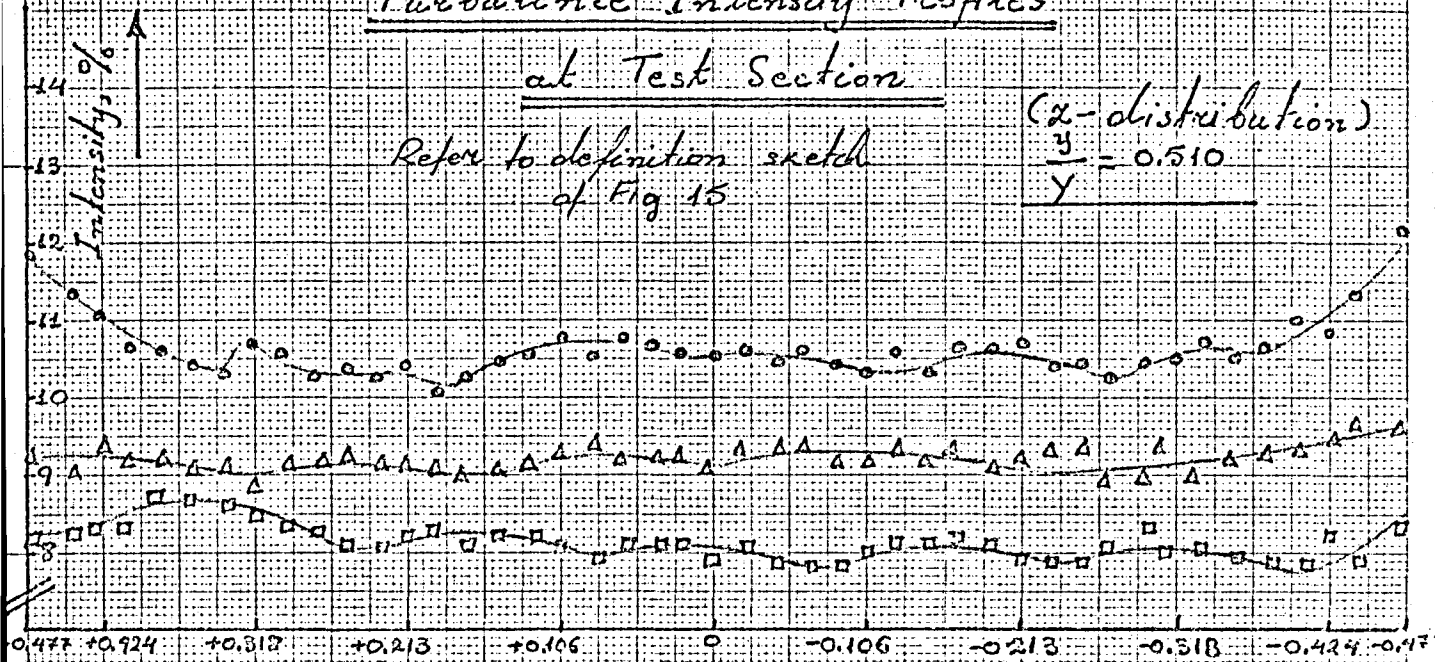
# Turbulence Intensity Profiles

at Test Section

Refer to definition sketch  
of Fig 15

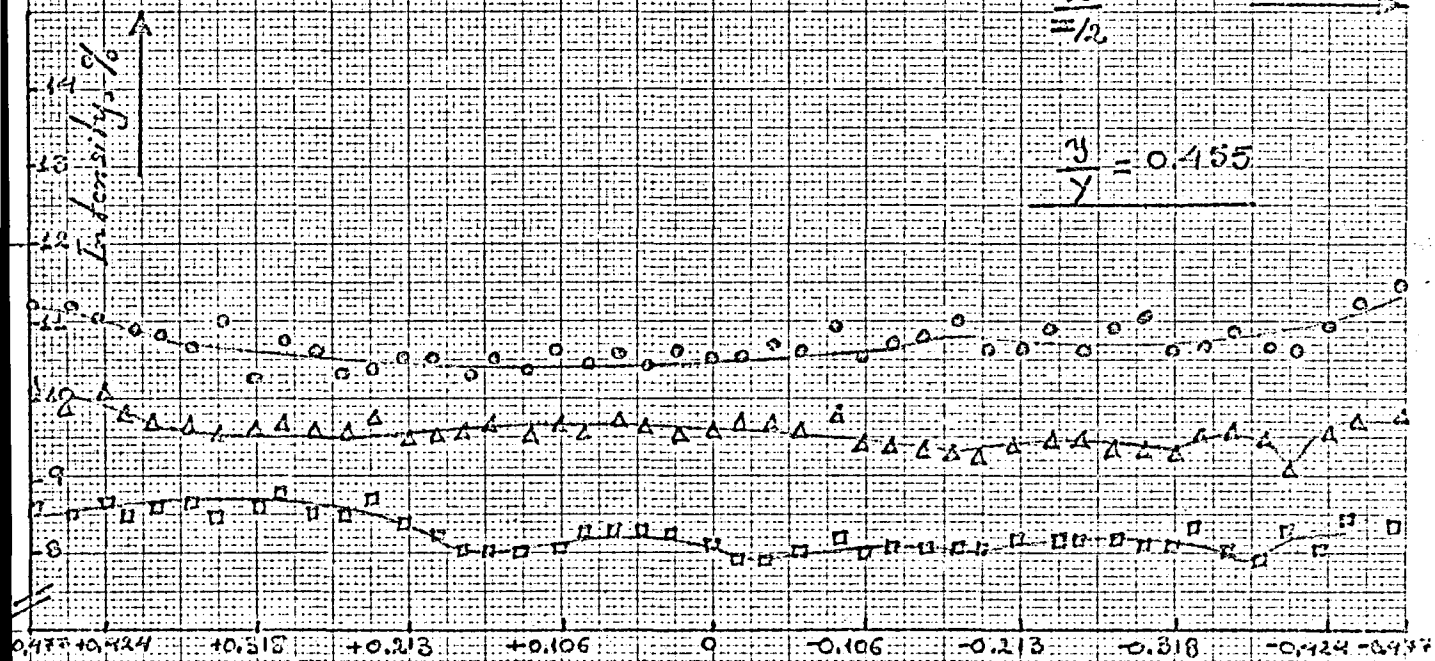
( $\alpha$ -distribution)

$$\frac{y}{Y} = 0.510$$



$$\frac{z}{z/2}$$

$$\frac{y}{Y} = 0.455$$



$$\frac{z}{z/2}$$

$$\frac{y}{Y} = 0.396$$

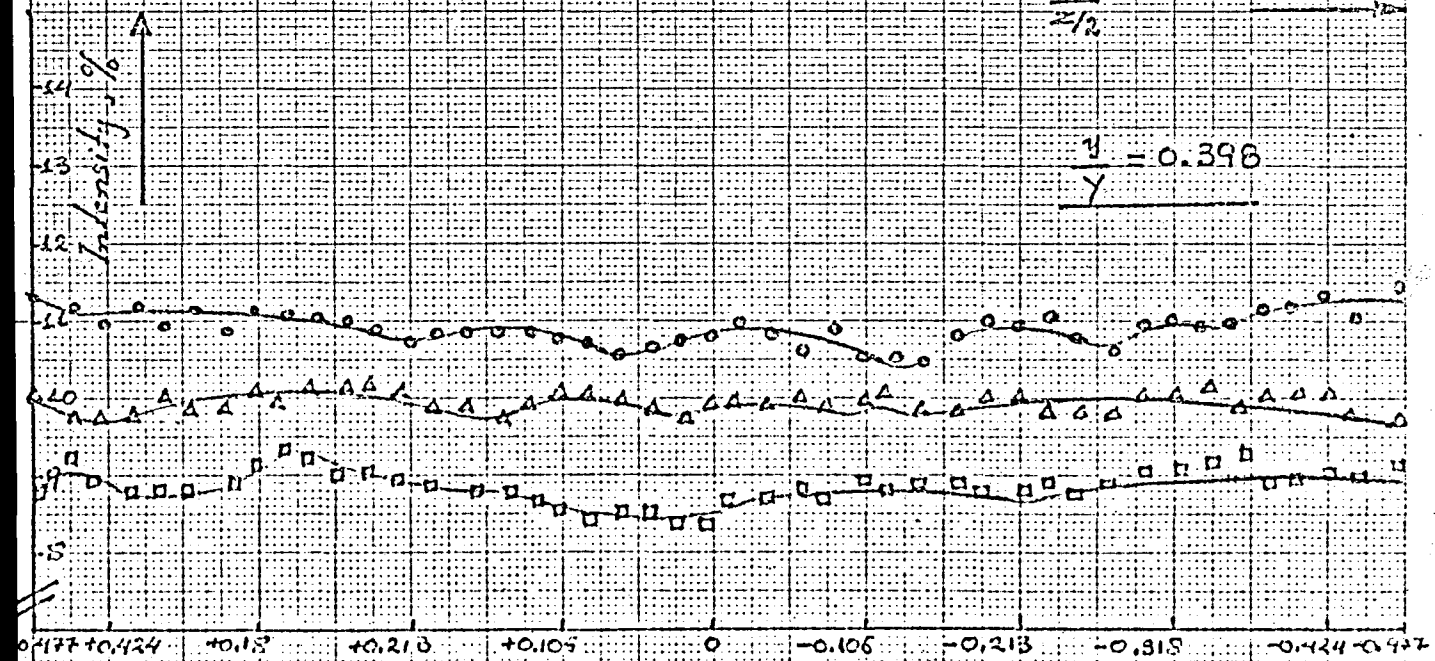


FIG: 17

$$\frac{z}{z/2}$$

# Turbulence Intensity Profiles

at Test Section

Refer to definition sketch of Fig. 15

( $\alpha$ -distribution)

$$\frac{u}{Y} = 0.340$$

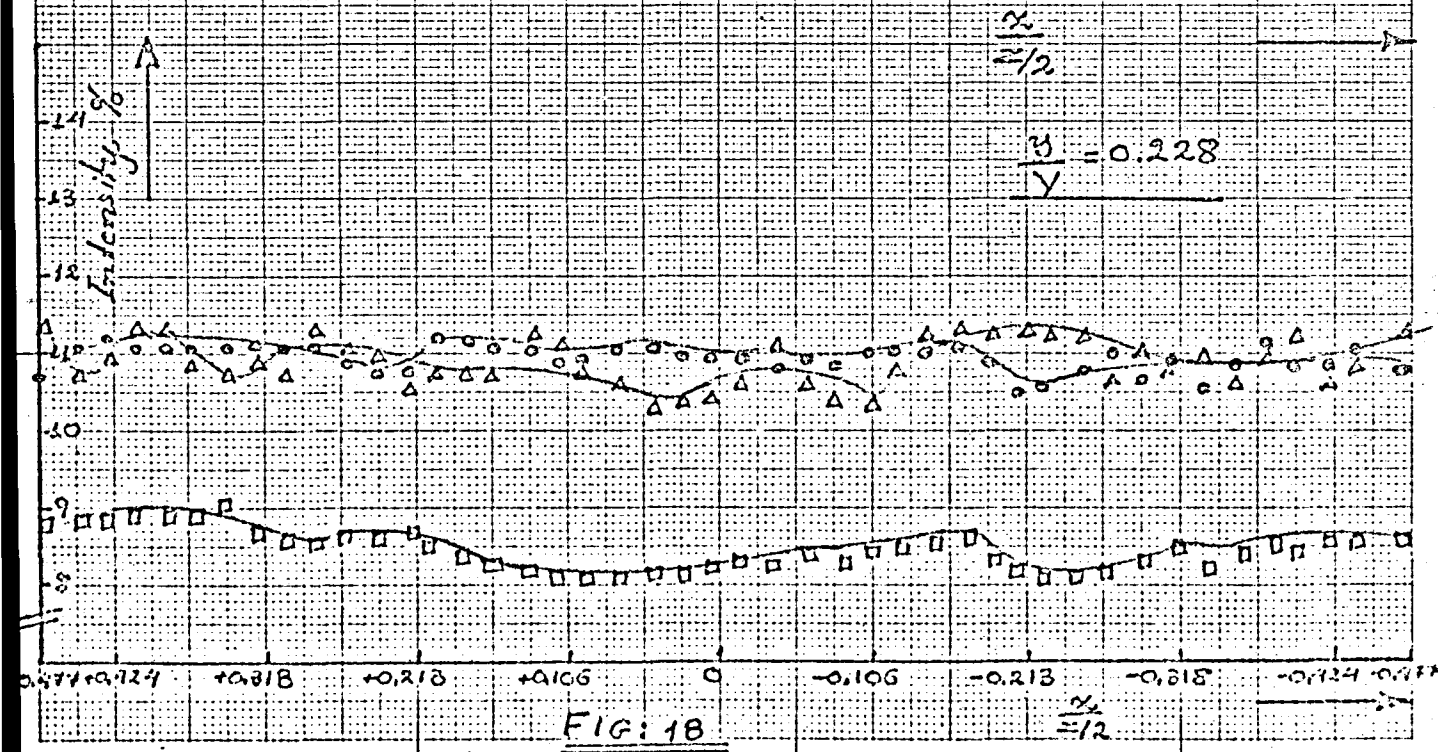
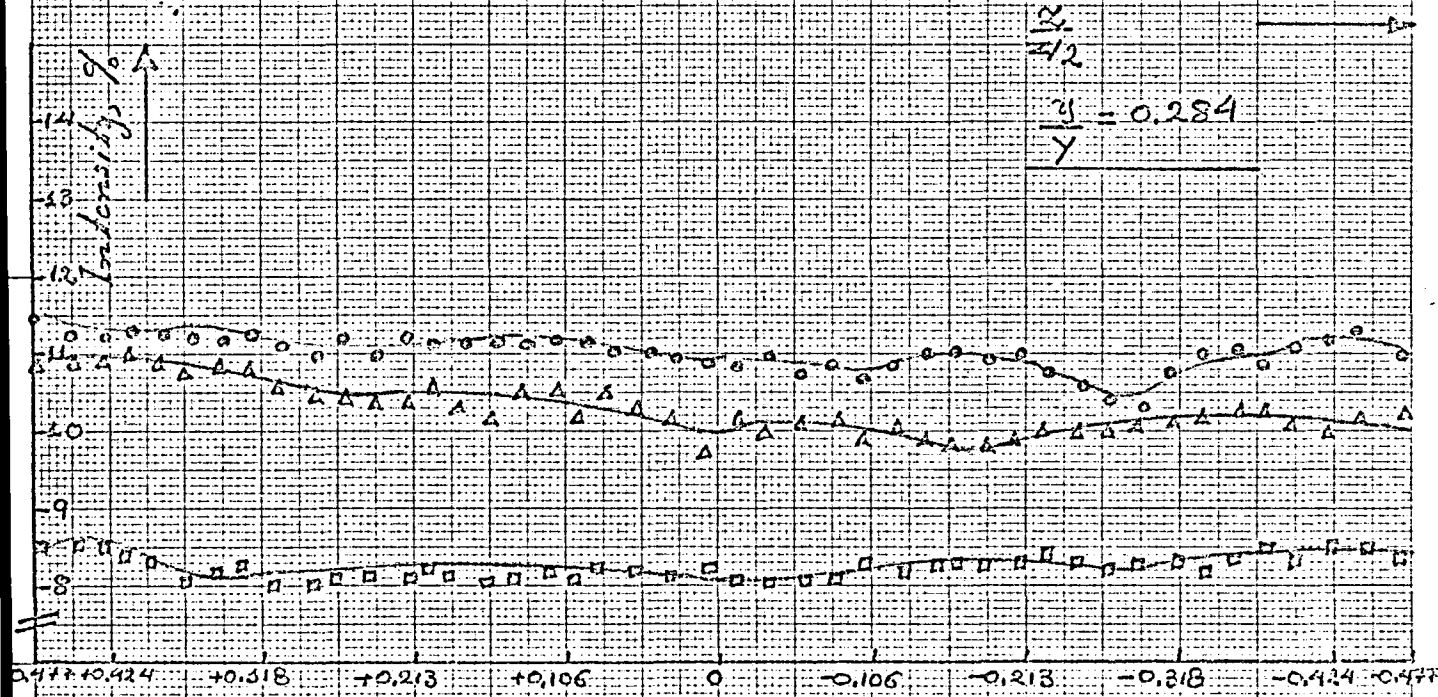
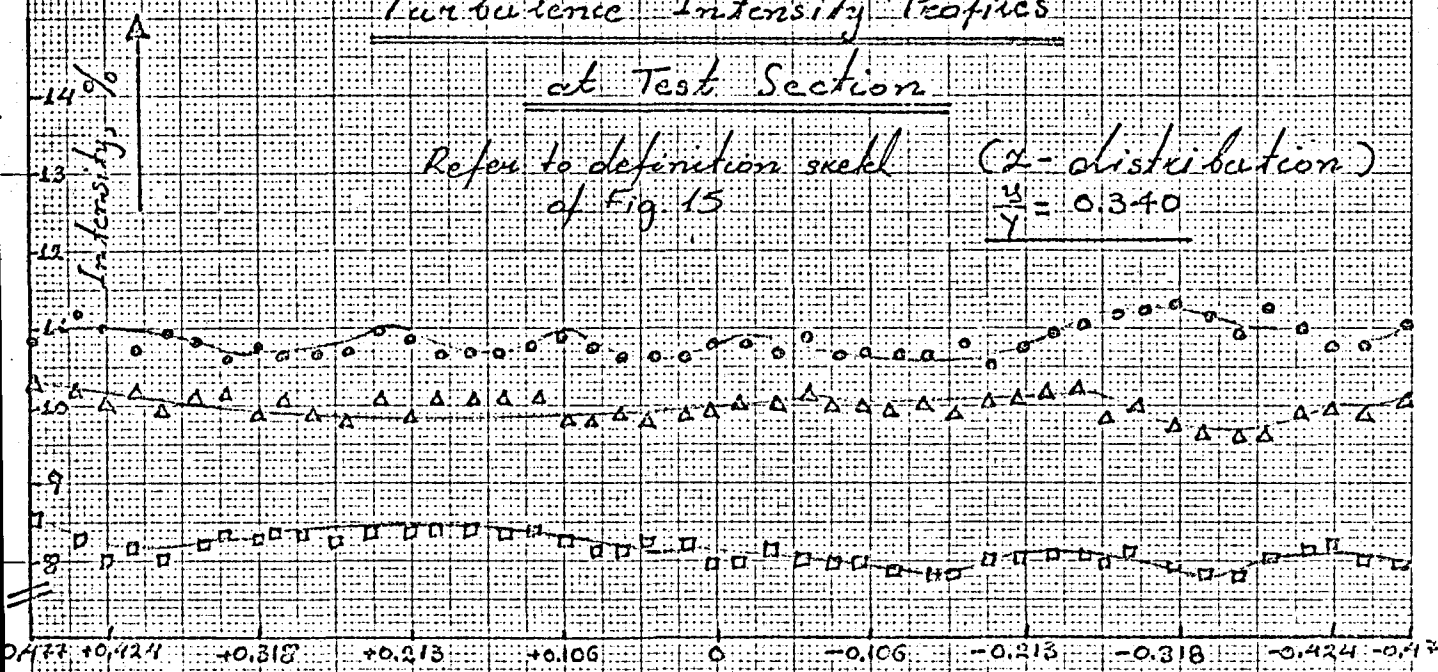
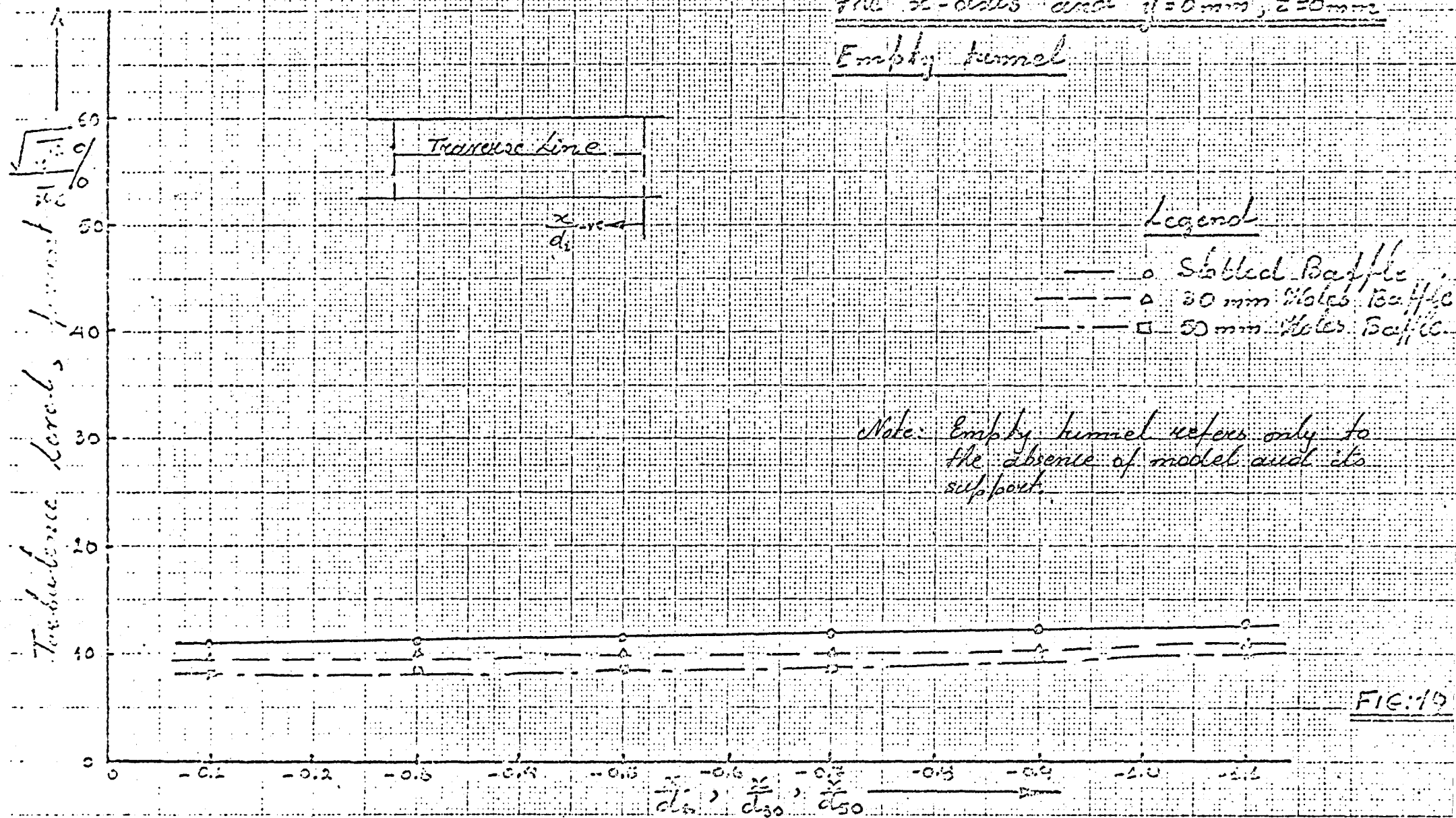


FIG: 18

Intensity variation along  
the x-axis and  $y=0\text{ mm}$ ,  $z=0\text{ mm}$   
Empty tunnel





Composite of the three Turbulent  
Components for all baffles at  
the Expected Stagnation point  
of the models (Empty Tunnel)

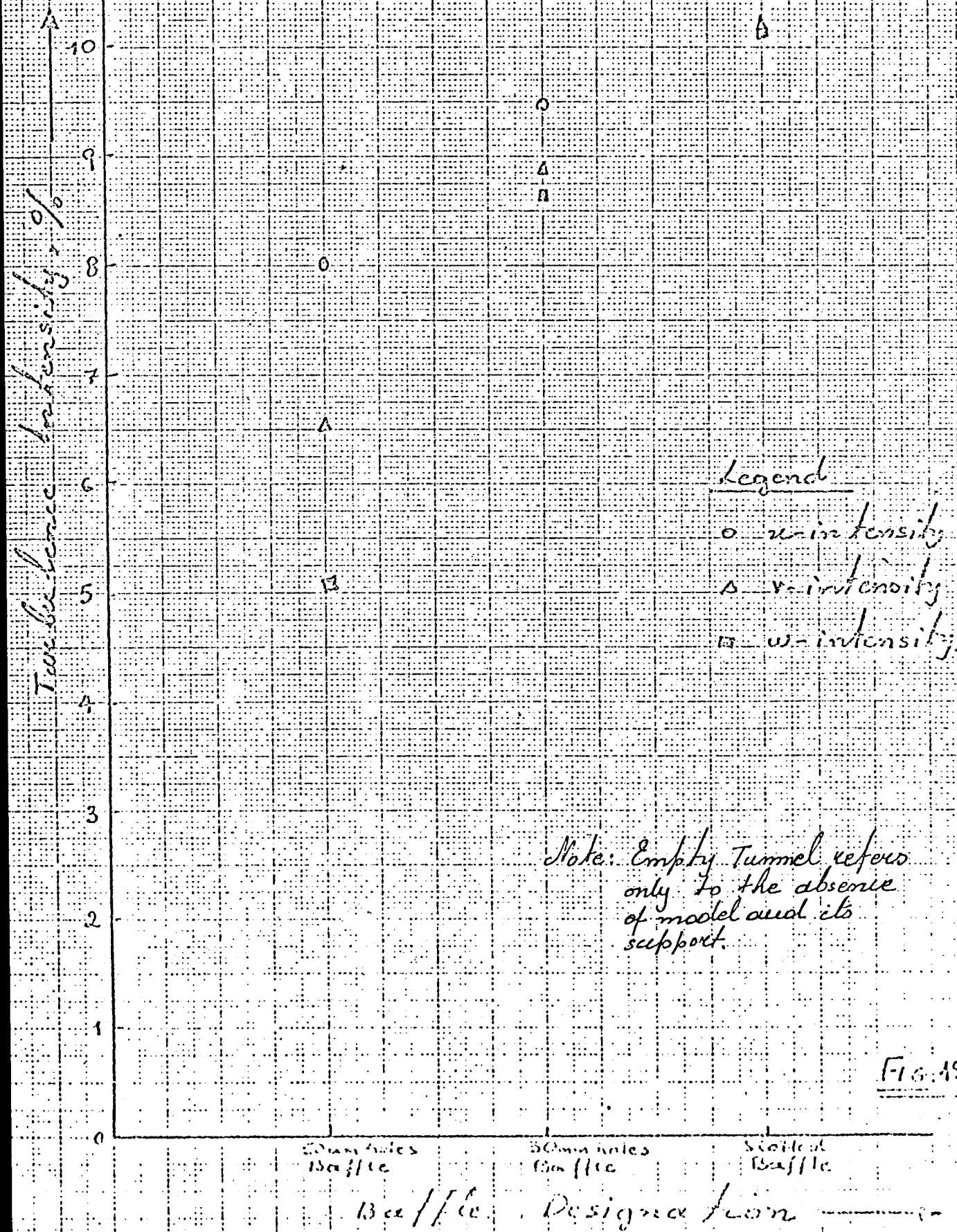
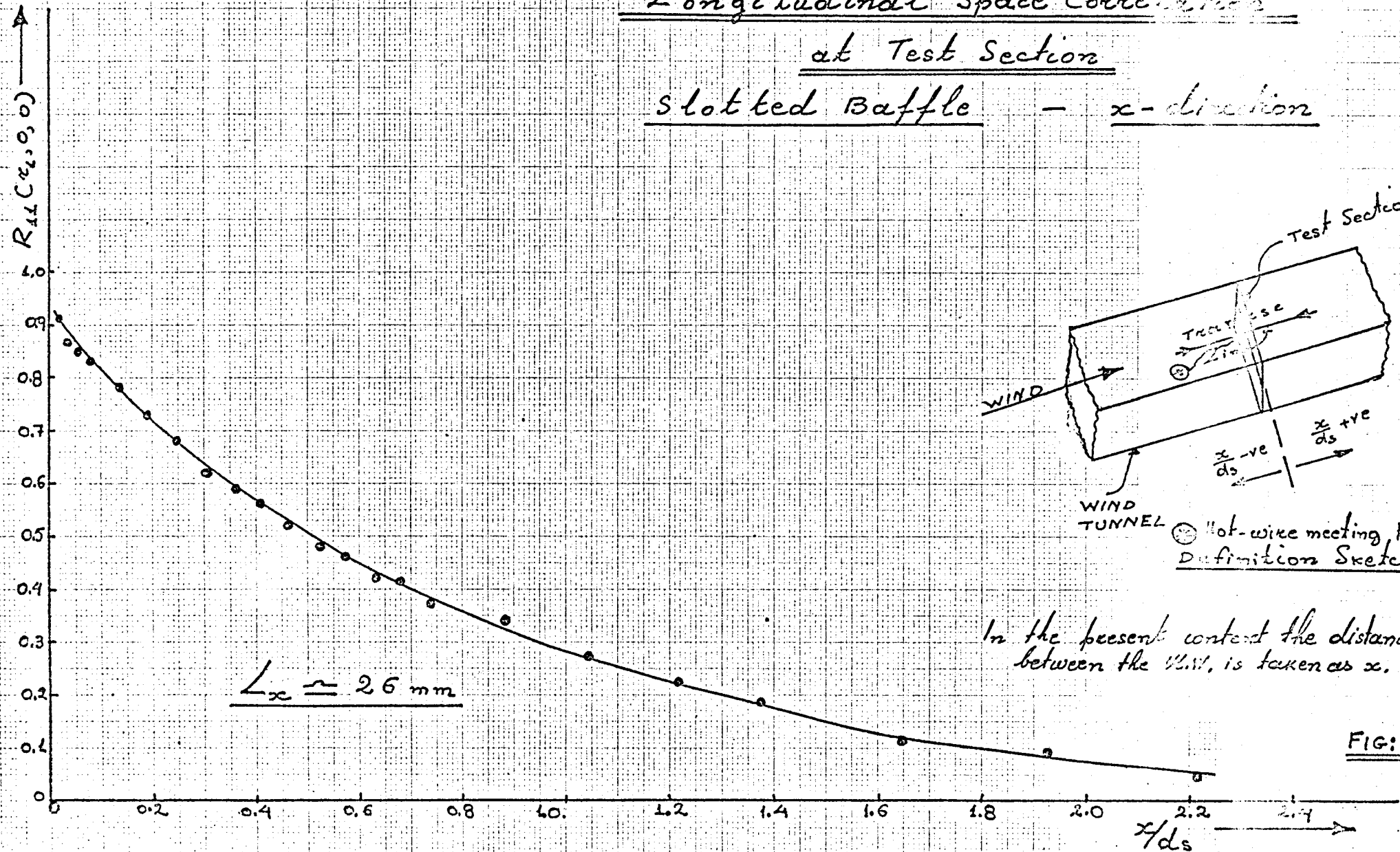


Fig. 49a

SPACE CORRELATIONS AT THE TEST SECTION

(Empty Tunnel)

Longitudinal Space Correlation  
at Test Section  
Slotted Baffle - x-direction



Space Correlations at the Test Section

Integral Scale of Turbulence	Slotted Baffle	30mm Holes Baffle	50mm Holes Baffle
$L_x$ (mm)	26	23	23
$L_y$ (mm)	16	13.5	36.5
$L_z$ (mm)	14	12.9	26.5

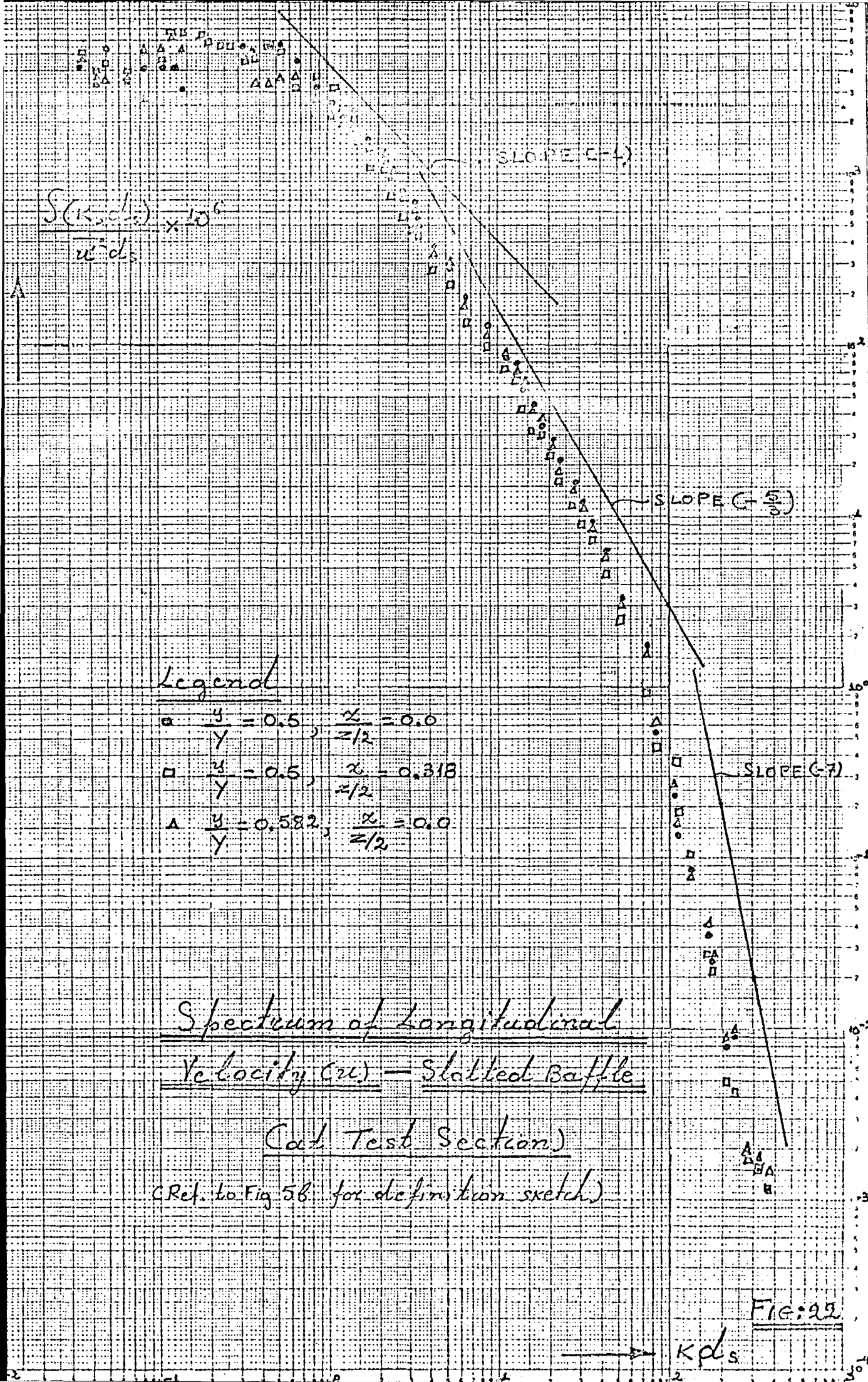
FIG. 21

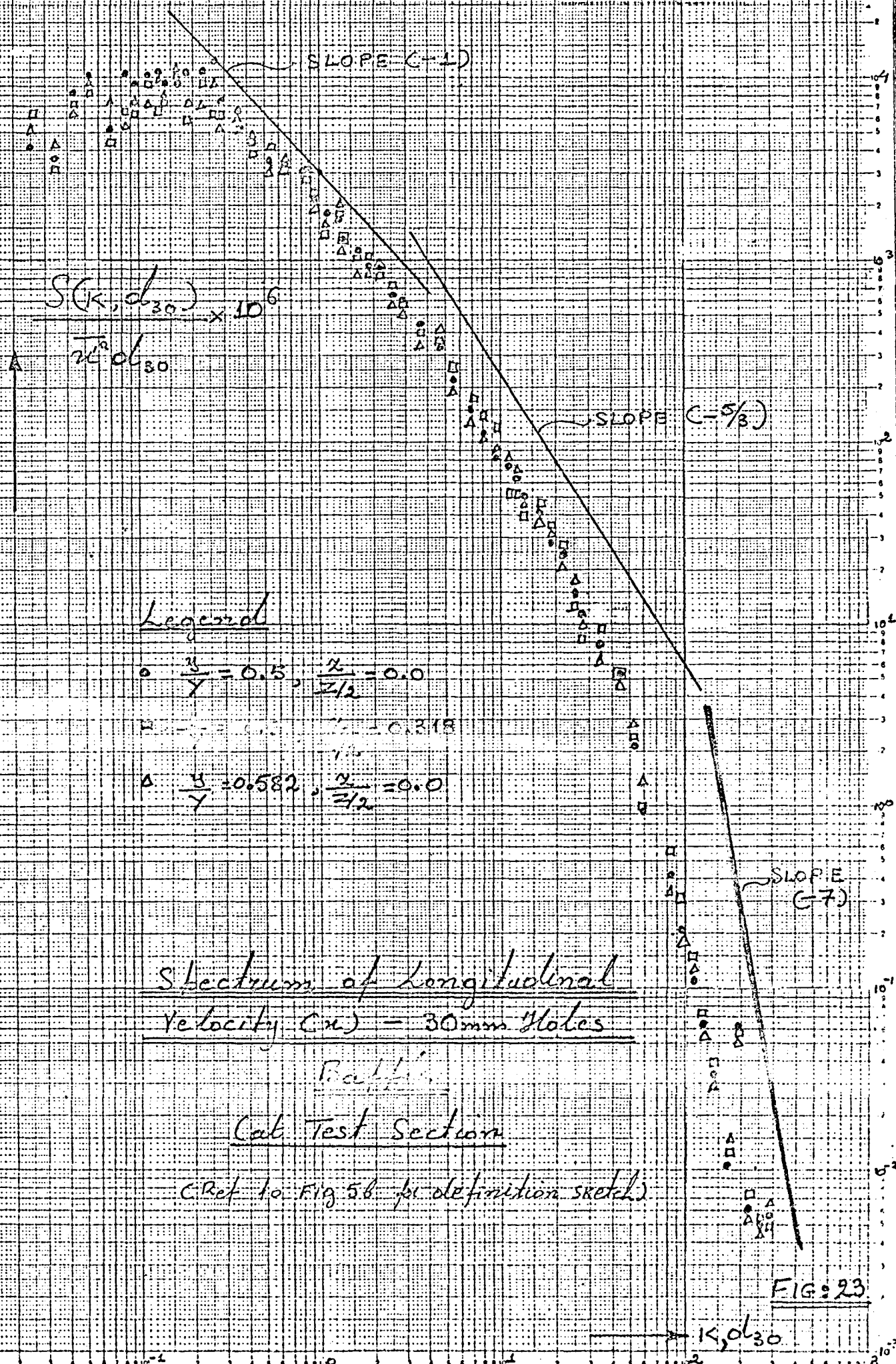
SPECTRA OF LONGITUDINAL VELOCITY

AT THE TEST SECTION

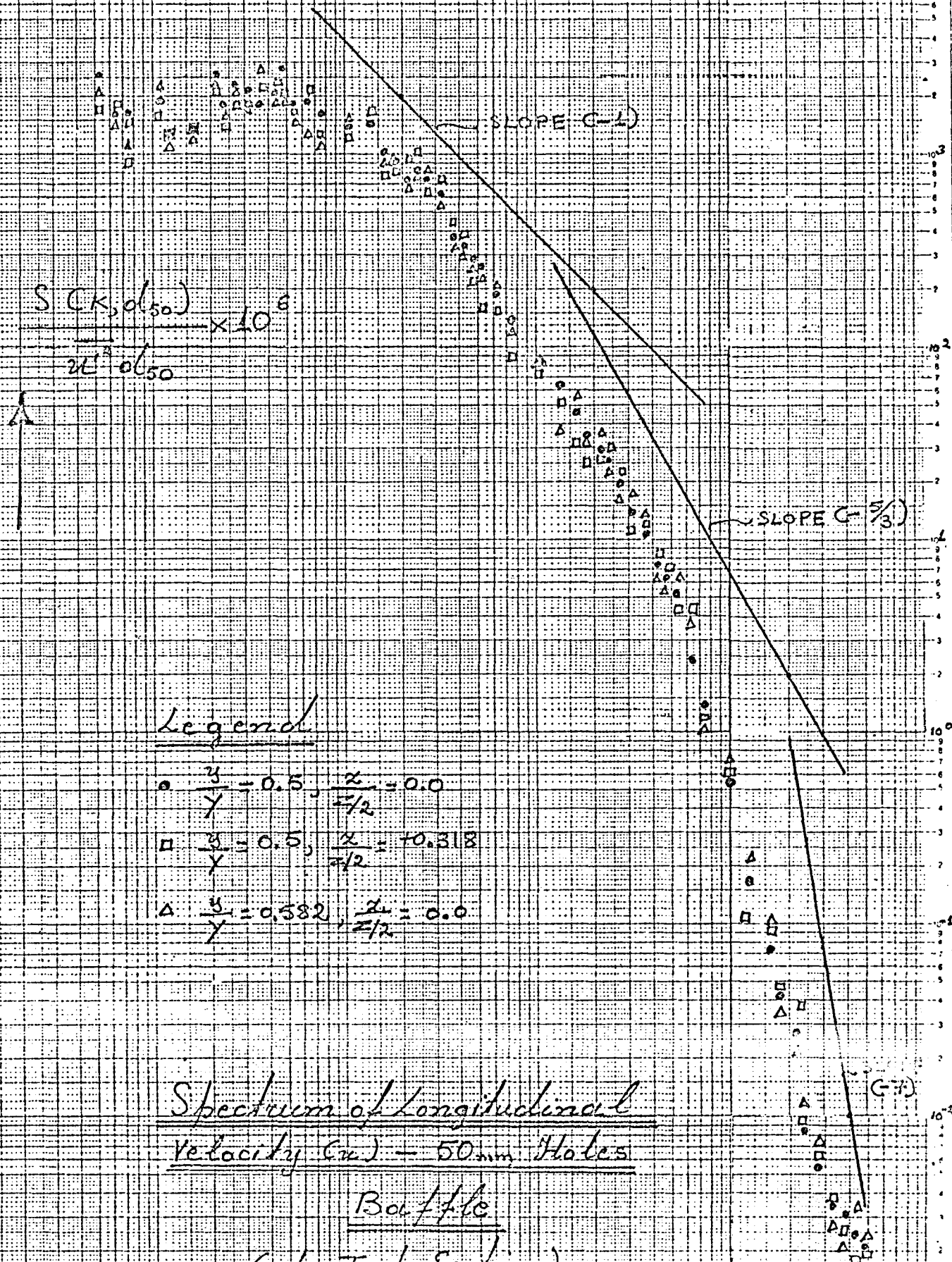
(Empty Tunnel)

(Refer to Fig. 5b for definition  
sketch)









Spectrum of Longitudinal  
Velocity (cm) - 50mm Holes

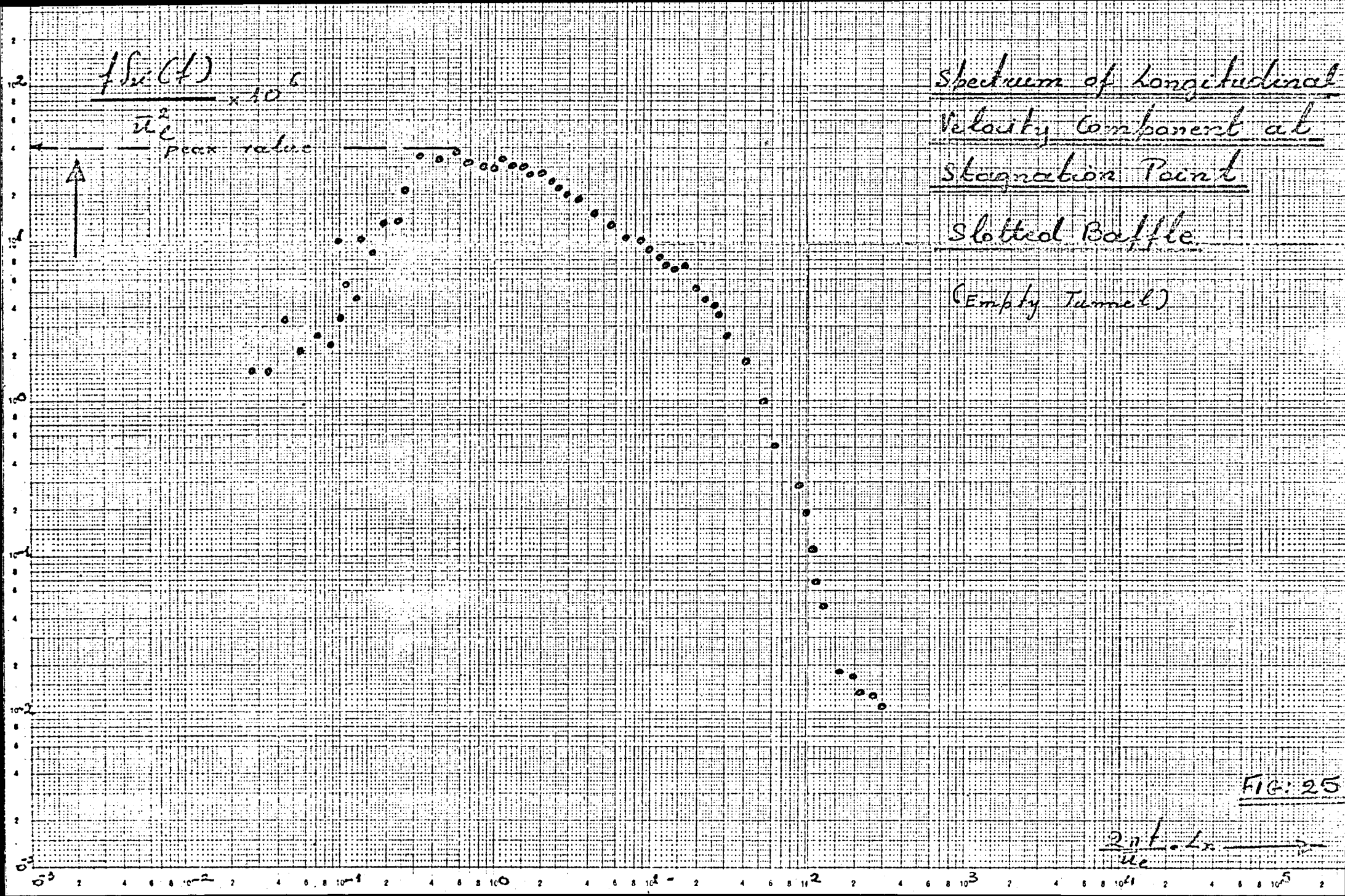
Baffle

Cool Test Section

(Ref. to Fig. 5B for definition sketch)

FIG: 2A



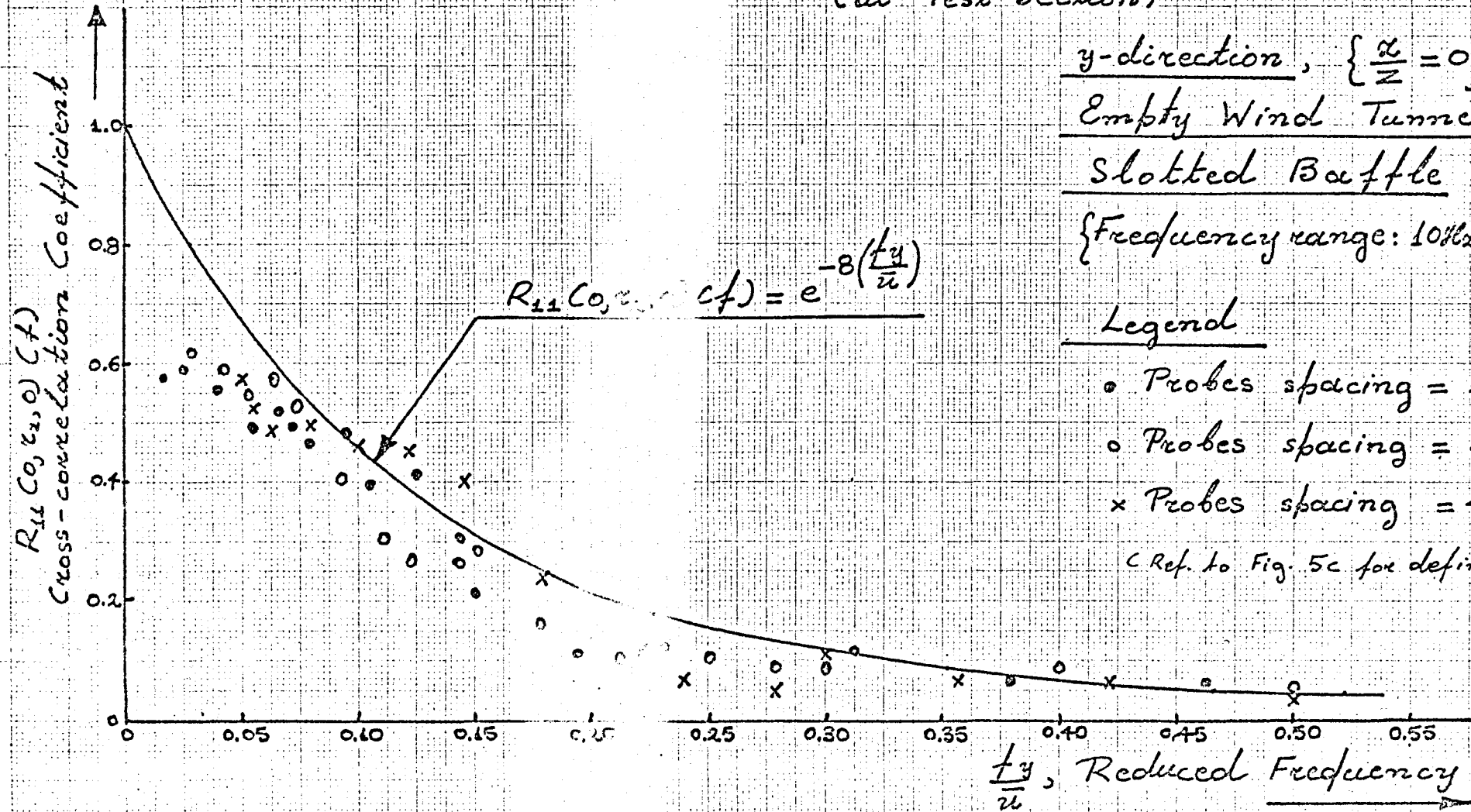


CROSS-CORRELATION COEFFICIENT OF THE LONGITUDINAL  
VELOCITY

(For the empty tunnel at the test section  
and in front of the models)

(Refer to Fig.5c, 5d, 5e, and 5f, for  
definition sketches)

# Lateral Cross-correlation Coefficient of Longitudinal Velocity (at Test Section)



y-direction,  $\left\{\frac{x}{z} = 0\right\}$   
Empty Wind Tunnel  
Slotted Baffle

{Frequency range:  $10\text{Hz} \rightarrow 300\text{Hz}$ }

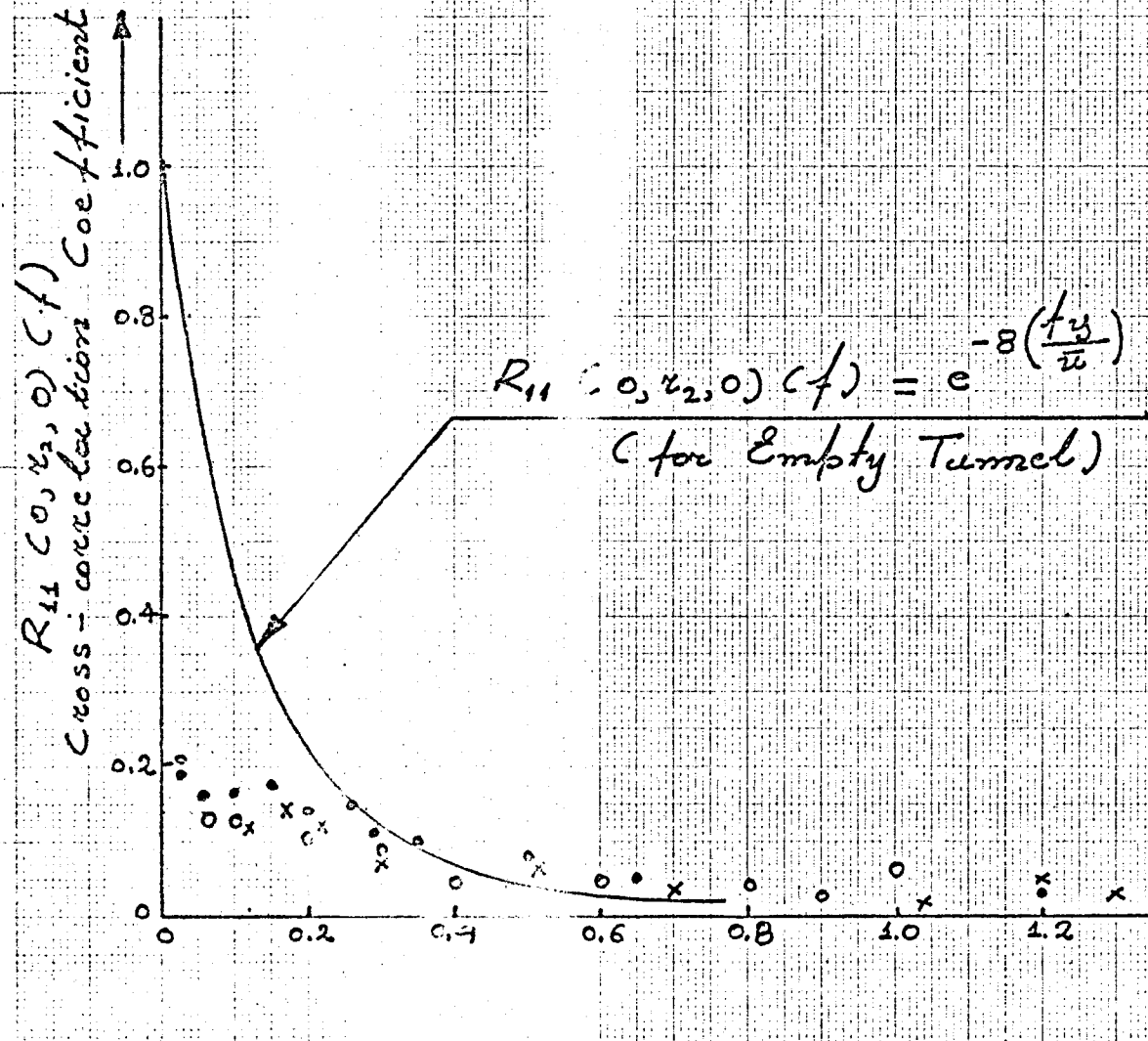
## Legend

- Probes spacing = 10mm
- Probes spacing = 20mm
- × Probes spacing = 40mm

(Ref. to Fig. 5c for definition sketch)

FIG:26

# Lateral Cross-Correlation Coefficient of Longitudinal Velocity in front of the $30 \times 120 \text{ mm}^2$ Plate and at $\frac{z}{D} = -\frac{1}{10}$



y-direction,  $\left\{\frac{z}{D} = 0\right\}$

Model Free to Oscillate

Slotted Baffle

{Frequency range:  $10 \text{ Hz} \rightarrow 300 \text{ Hz}$ }

Legend

- o Probes spacing = 10mm
- o Probes spacing = 20mm
- x Probes spacing = 40mm

(Ref. to Fig. 5d for definition sketch)

FIG: 27

# Lateral Cross-correlation Coefficient of Longitudinal Velocity in front of the $30 \times 120 \text{ mm}^2$ Plate and at $\frac{x}{D} = -\frac{1}{10}$

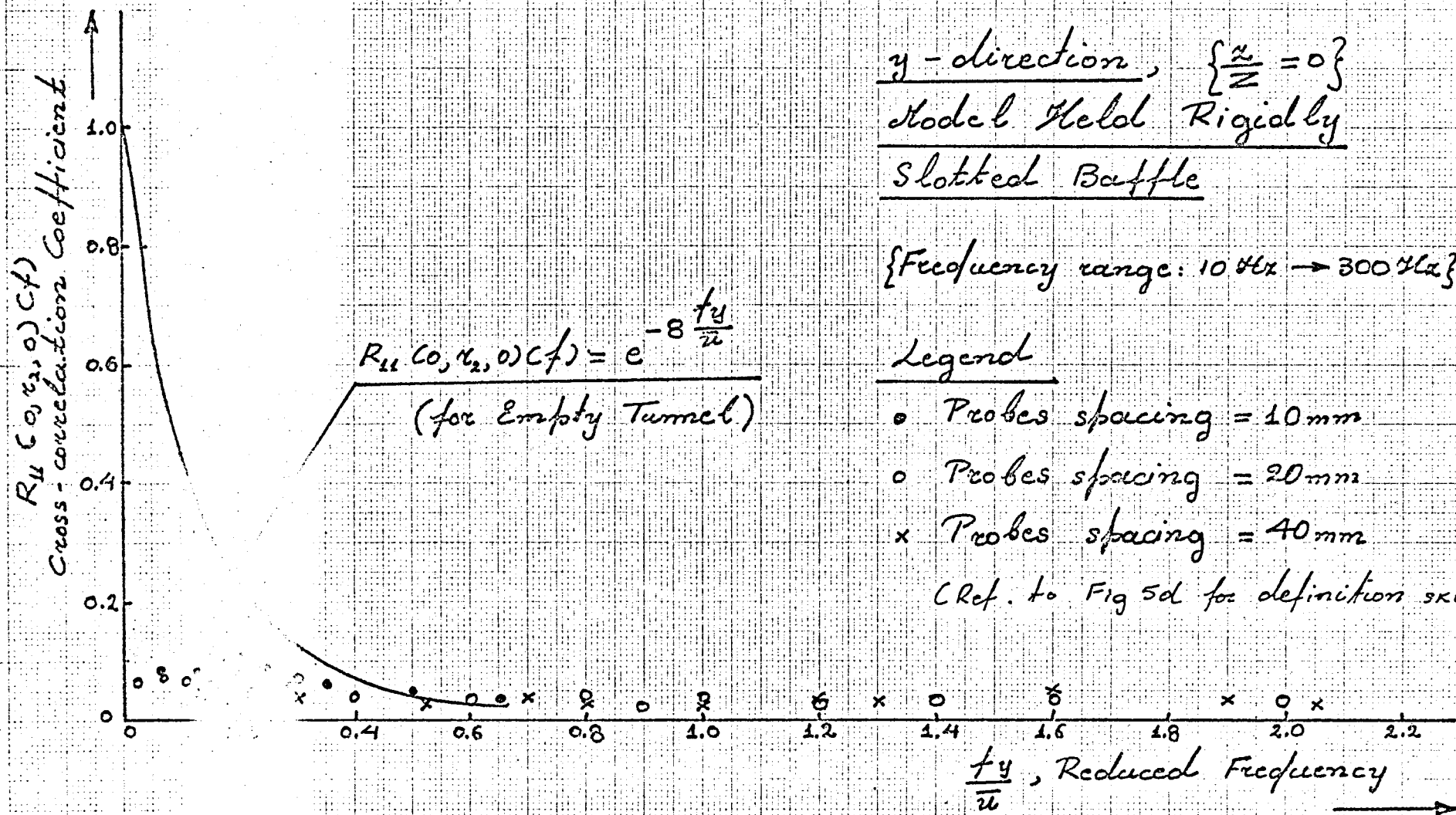


Fig 28

# Longitudinal Velocity

Frequency Range: 10% - 300%

Refer to Fig 5c, 5d, 5e, 5f, for Definition Sketches.

FIG: 29

		CROSS - CORRELATION COEFFICIENT																		NATURE OF MOVEMENT
		EMPTY TUNNEL									SLOTTED BAFFLE			30mm HOLES BAFFLE			50mm HOLES BAFFLE			
MODEL UNDER INVESTIG.	Spacing of Probes	Reduced Frequency, $f\sqrt{z}/\omega$									Reduced Frequency, $f\sqrt{z}/\omega$ at $\frac{x}{D} = -\frac{1}{10}$			Reduced Frequency, $f\sqrt{z}/\omega$ at $\frac{x}{D} = -\frac{1}{10}$			Reduced Frequency, $f\sqrt{z}/\omega$ at $\frac{x}{D} = -\frac{1}{10}$			
		SLOTTED BAFFLE			30mm HOLES BAFFLE			50mm HOLES BAFFLE			0.1	0.2	0.3	0.1	0.2	0.3	0.1	0.2	0.3	
		0.1	0.2	0.3	0.1	0.2	0.3	0.1	0.2	0.3										
Plate  R=4	10mm	0.49	0.11	0.11	0.53	0.19	0.10	0.52	0.22	0.10	$\frac{0.08}{0.18}$	$\frac{0.08}{0.11}$	$\frac{0.06}{0.10}$	$\frac{0.09}{0.21}$	$\frac{0.10}{0.2}$	$\frac{0.08}{0.16}$	$\frac{0.10}{0.22}$	$\frac{0.12}{0.20}$	$\frac{0.09}{0.17}$	Rigid Oscillation
	20mm	0.39	0.11	0.11	0.53	0.13	0.09	0.60	0.21	0.11	$\frac{0.07}{0.17}$	$\frac{0.07}{0.11}$	$\frac{0.06}{0.09}$	$\frac{0.10}{0.19}$	$\frac{0.10}{0.19}$	$\frac{0.08}{0.16}$	$\frac{0.11}{0.19}$	$\frac{0.11}{0.18}$	$\frac{0.11}{0.17}$	Rigid Oscillation
	40mm	0.45	0.15	0.08	0.52	0.15	0.06	0.51	0.20	0.10	$\frac{0.06}{0.17}$	$\frac{0.06}{0.10}$	$\frac{0.06}{0.08}$	$\frac{0.10}{0.16}$	$\frac{0.11}{0.16}$	$\frac{0.06}{0.10}$	$\frac{0.11}{0.22}$	$\frac{0.10}{0.20}$	$\frac{0.09}{0.17}$	Rigid Oscillation
Parallepi- ped  R=4	10mm	0.49	0.11	0.11	0.53	0.19	0.10	0.52	0.22	0.10	$\frac{0.09}{0.18}$	$\frac{0.09}{0.11}$	$\frac{0.07}{0.10}$	$\frac{0.10}{0.18}$	$\frac{0.06}{0.17}$	$\frac{0.06}{0.12}$	$\frac{0.12}{0.20}$	$\frac{0.12}{0.20}$	$\frac{0.11}{0.15}$	Rigid Oscillation
	20mm	0.39	0.11	0.11	0.53	0.13	0.09	0.60	0.21	0.11	$\frac{0.07}{0.18}$	$\frac{0.07}{0.12}$	$\frac{0.07}{0.10}$	$\frac{0.08}{0.17}$	$\frac{0.05}{0.15}$	$\frac{0.05}{0.10}$	$\frac{0.11}{0.18}$	$\frac{0.10}{0.17}$	$\frac{0.09}{0.13}$	Rigid Oscillation
	40mm	0.45	0.15	0.08	0.52	0.15	0.06	0.51	0.20	0.10	$\frac{0.08}{0.17}$	$\frac{0.08}{0.13}$	$\frac{0.07}{0.09}$	$\frac{0.05}{0.12}$	$\frac{0.05}{0.13}$	$\frac{0.04}{0.12}$	$\frac{0.11}{0.18}$	$\frac{0.10}{0.18}$	$\frac{0.06}{0.12}$	Rigid Oscillation
Circular cylinder  R=4	10mm	0.49	0.11	0.11	0.53	0.19	0.10	0.52	0.22	0.10	$\frac{0.24}{0.37}$	$\frac{0.20}{0.33}$	$\frac{0.15}{0.30}$	$\frac{0.32}{0.42}$	$\frac{0.30}{0.40}$	$\frac{0.15}{0.38}$	$\frac{0.39}{0.50}$	$\frac{0.25}{0.45}$	$\frac{0.20}{0.26}$	Rigid Oscillation
	20mm	0.39	0.11	0.11	0.53	0.13	0.09	0.60	0.21	0.11	$\frac{0.25}{0.37}$	$\frac{0.18}{0.32}$	$\frac{0.13}{0.31}$	$\frac{0.30}{0.42}$	$\frac{0.30}{0.39}$	$\frac{0.20}{0.36}$	$\frac{0.40}{0.46}$	$\frac{0.25}{0.42}$	$\frac{0.19}{0.23}$	Rigid Oscillation
	40mm	0.45	0.15	0.08	0.52	0.15	0.06	0.51	0.20	0.10	$\frac{0.24}{0.29}$	$\frac{0.20}{0.29}$	$\frac{0.14}{0.28}$	$\frac{0.32}{0.41}$	$\frac{0.28}{0.40}$	$\frac{0.20}{0.32}$	$\frac{0.39}{0.48}$	$\frac{0.25}{0.41}$	$\frac{0.17}{0.30}$	Rigid Oscillation

SPECTRUM VARIATION OF THE LONGITUDINAL VELOCITY

ALONG THE STAGNATION LINE FLOW.

(INCLUDING TURBULENCE LEVEL VARIATION)

(For the empty tunnel at the test section

and in front of the models)

(Refer to Fig.5g, 5h, 5i, and 5j for

definition sketches)

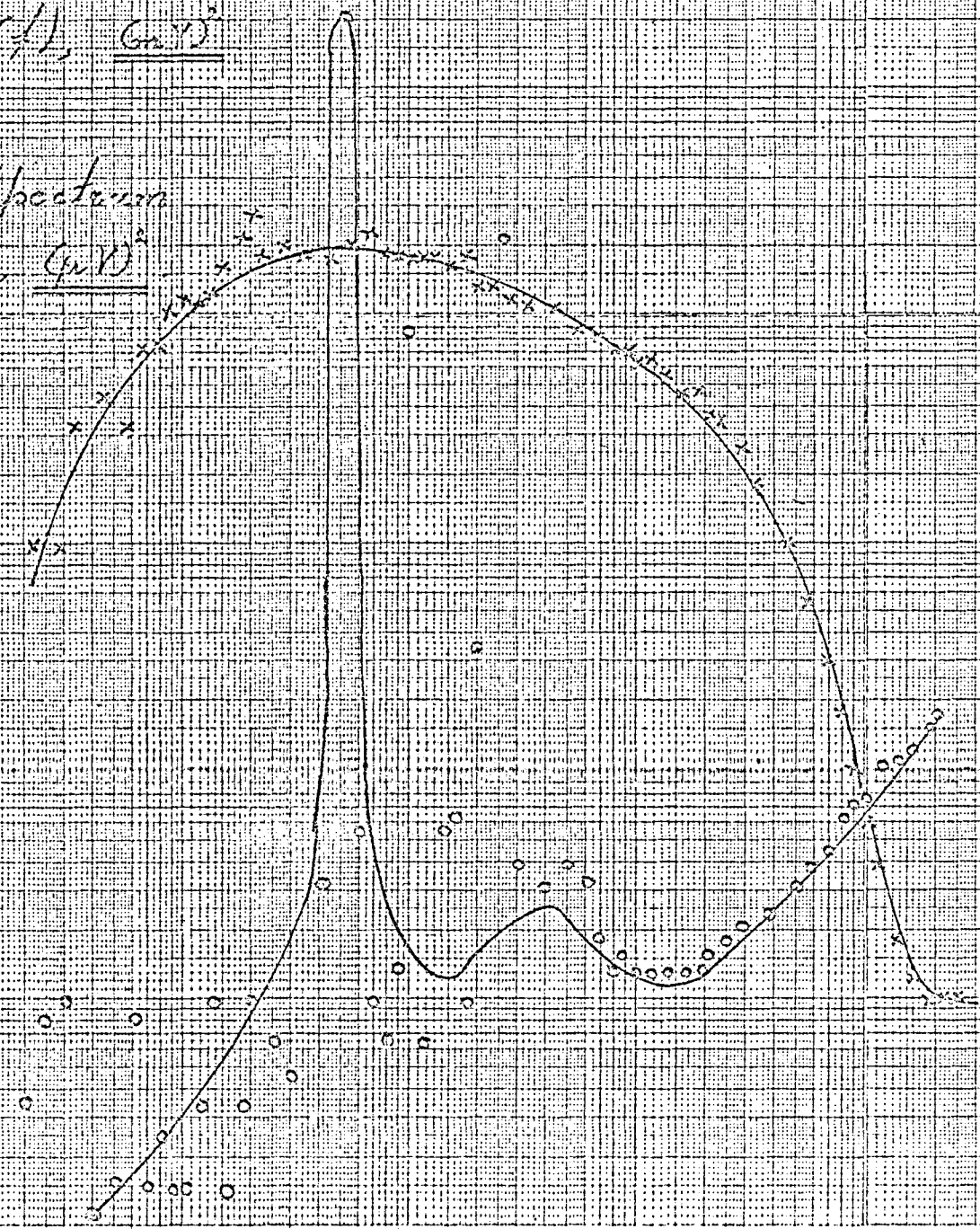


Turbulence Spectrum

$$f_{Turb}(f), \text{ (GrV)}^2$$

Noise Spectrum

$$f_S(f), \text{ (GrV)}^2$$



Hot-Wire Instrumentation

Noise Spectrum  
Cult. Test Section

Legend

- o Turbulence Spectrum  
30 ms. Hot-Wire
- x Hot-Wire Instrumentation  
Noise Spectrum

Hz

Frequency Spectrum



Statistical analysis of power behavior  
in a circuit with a filter and time delay

Notation:

$\alpha(\omega, \omega_0)$  - filter response curve

$Q$  - filter-bandwidth parameter  
in  $|\alpha(\omega, \omega_0)|^2 = \frac{1}{1 + 4Q^2 \left( \frac{\omega - \omega_0}{\omega_0} \right)^2}$

$T_c$  - device time constant (sec)

$T_i$  - integration time (sec)

$\gamma$  - dimensionless device time constant

$e$  - dimensionless integration time

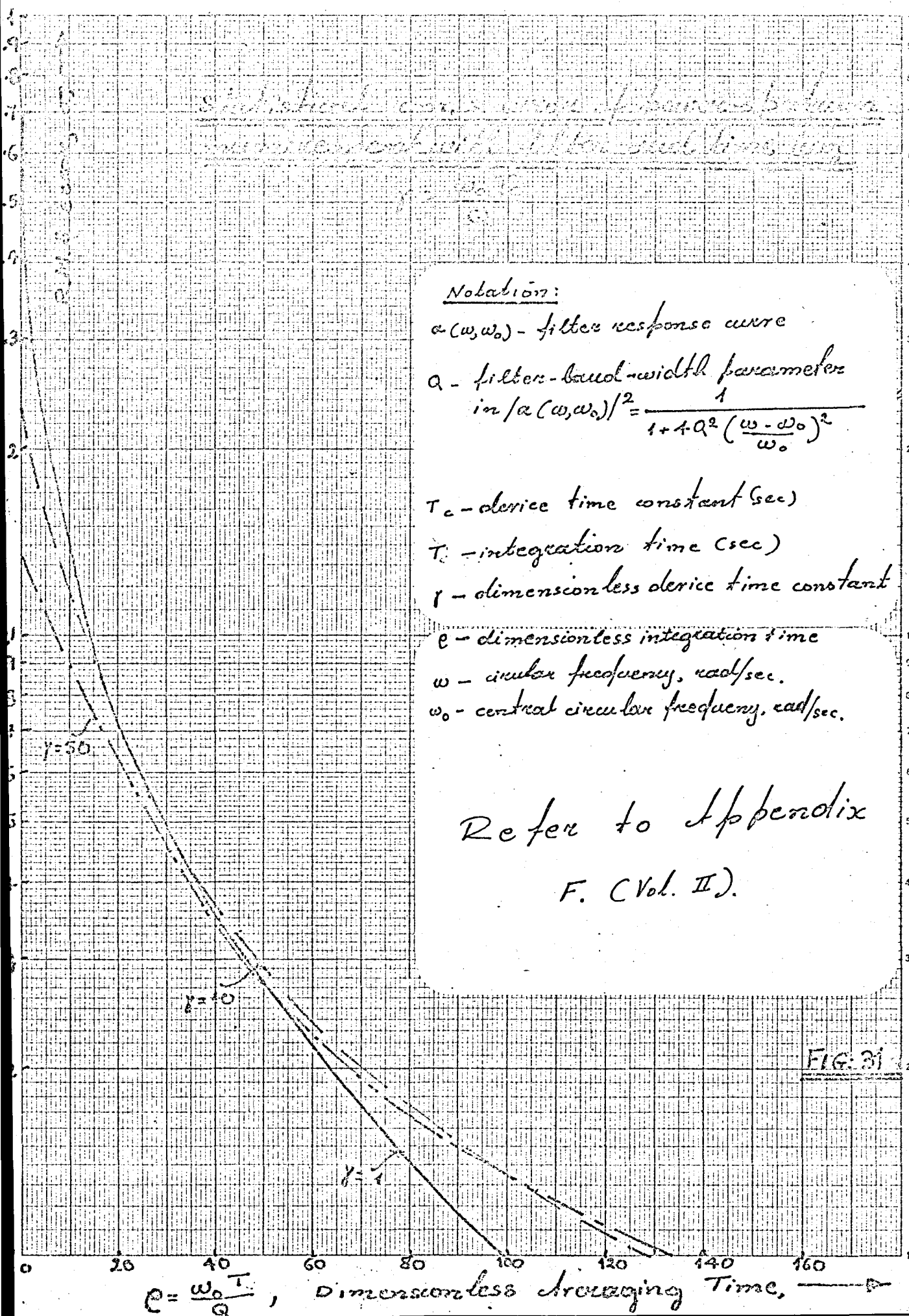
$\omega$  - circular frequency, rad/sec.

$\omega_0$  - central circular frequency, rad/sec.

Refer to Appendix

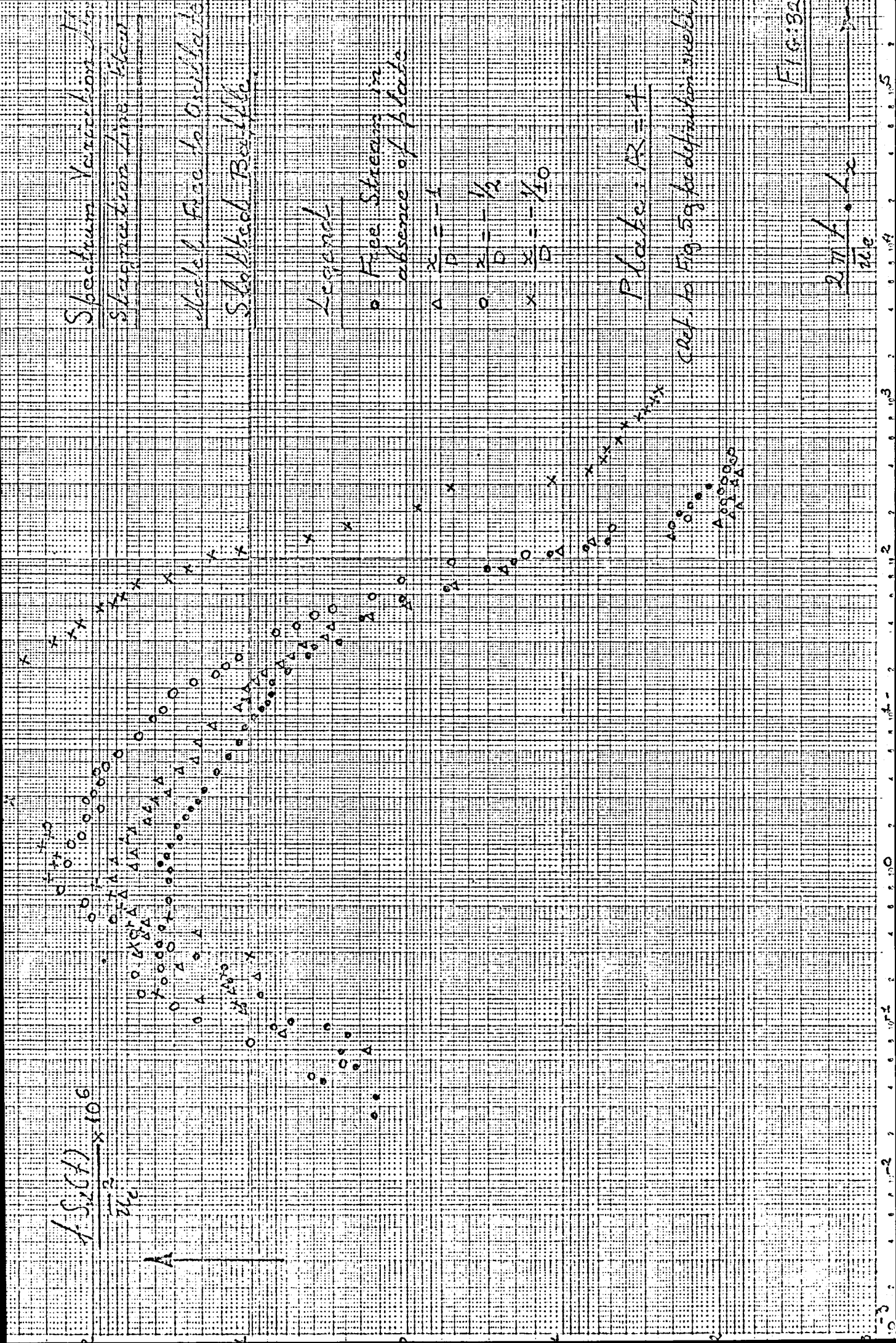
F. (Vol. II).

FIG. 31



$$\frac{f_s(x)}{u_0} \times 10^6$$

A



Spectrum Vacuum tube  
 Stopper line closed  
 Model Free to Oscillate  
 Shocked Be-114

Legend

Free Stream in  
 absence of plate

$\Delta \frac{x}{D} = -1$   
 $\circ \frac{x}{D} = -\frac{1}{2}$   
 $\times \frac{x}{D} = -\frac{1}{10}$

Plate:  $R=4$

Ref. to Fig. 59 for definition symbols

FIG. 32

$\frac{2.7}{u_0} \cdot Lx$

$\frac{1}{2} S(1) \times 10^6$

Spectrum Variation Along  
Stagnation Line Flow

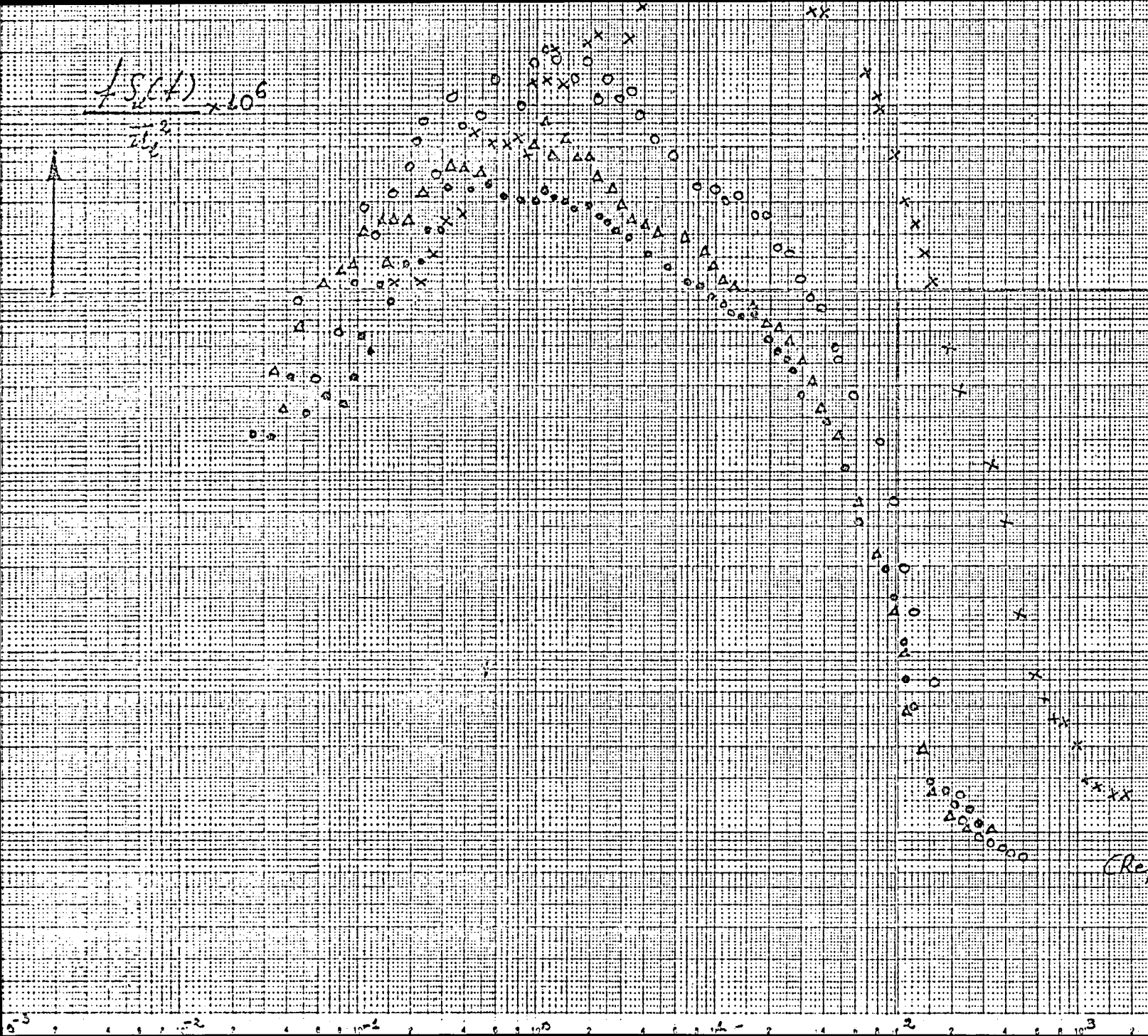
Model Held Rigidly  
Shocked Boundary

Legend  
o Free Stream in absence  
of plate  
 $\Delta \frac{x}{D} = -\frac{1}{2}$   
o  $\frac{x}{D} = -\frac{1}{3}$   
x  $\frac{x}{D} = -\frac{1}{10}$

Plate:  $AZ = 4$   
(Ref. to Fig 59 for definition sketch)

FIG: 33

$\frac{2\pi}{\lambda} \cdot \frac{1}{\lambda_c}$





Turbulence Level Variation  
Along Stagnation Line Flow

Plate:  $R=4$  - Slotted Baffle

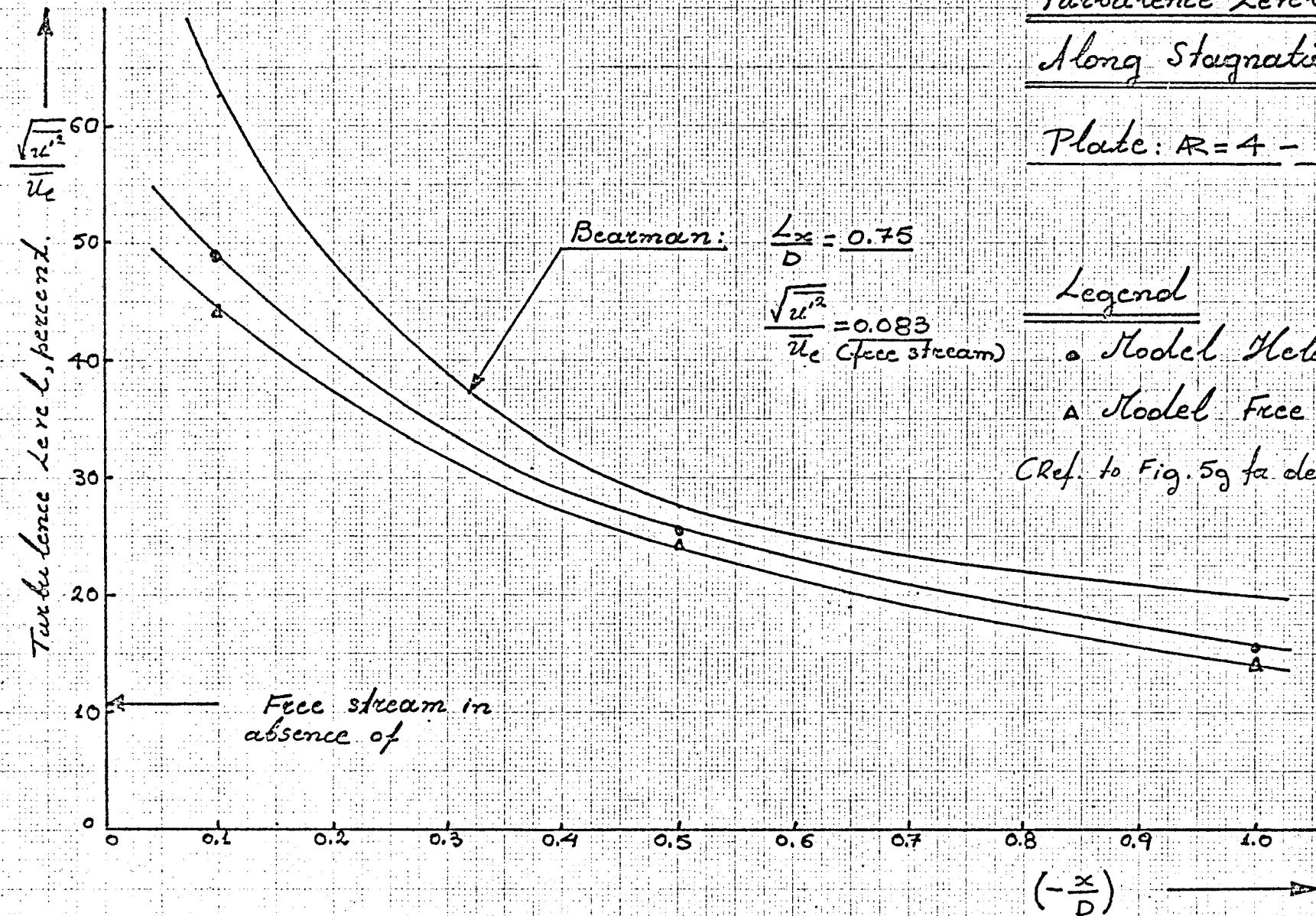
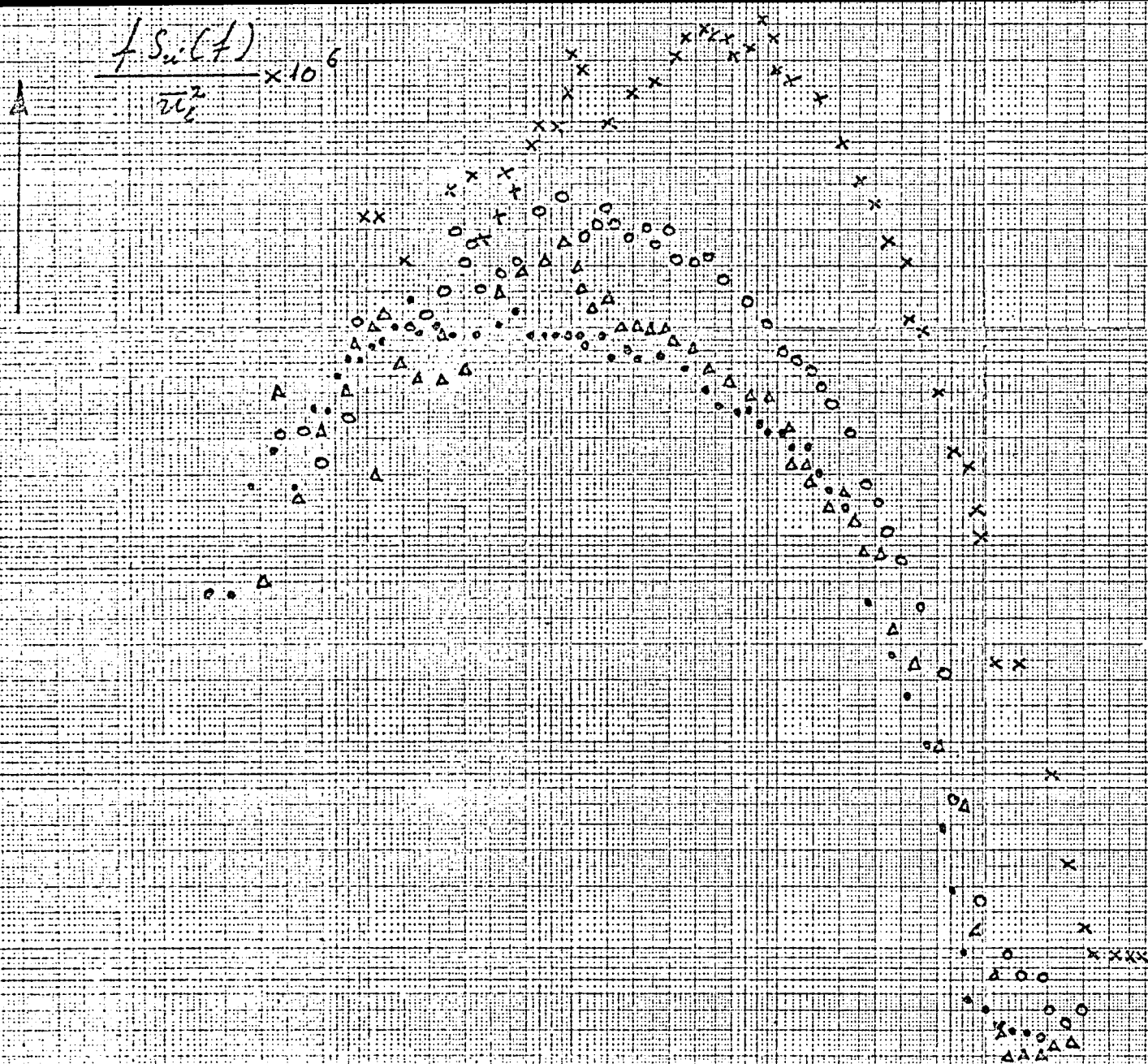


FIG: 34



Spectrum Variation  
Along Stagnation Line

Model Free to Oscillate

30mm Holes Baffle

Legend

• Free stream in absence  
of plate

$\Delta \frac{x_0}{D} = -1$

$\circ \frac{x_0}{D} = -\frac{1}{2}$

$\times \frac{x_0}{D} = -\frac{1}{10}$

Plate  $R=4$

(Ref. to Fig 5g for definition sketch)

Fig: 35

$\frac{2\pi f}{\bar{u}_i} \cdot L_x$

# Spectrum Variation Along Stagnation Line Flow

Model Held Rigidly  
30mm Holes Baffle

## Legend

o Free stream in disc of plate

$\Delta \frac{x}{D} = -1$

$\circ \frac{x}{D} = -\frac{1}{2}$

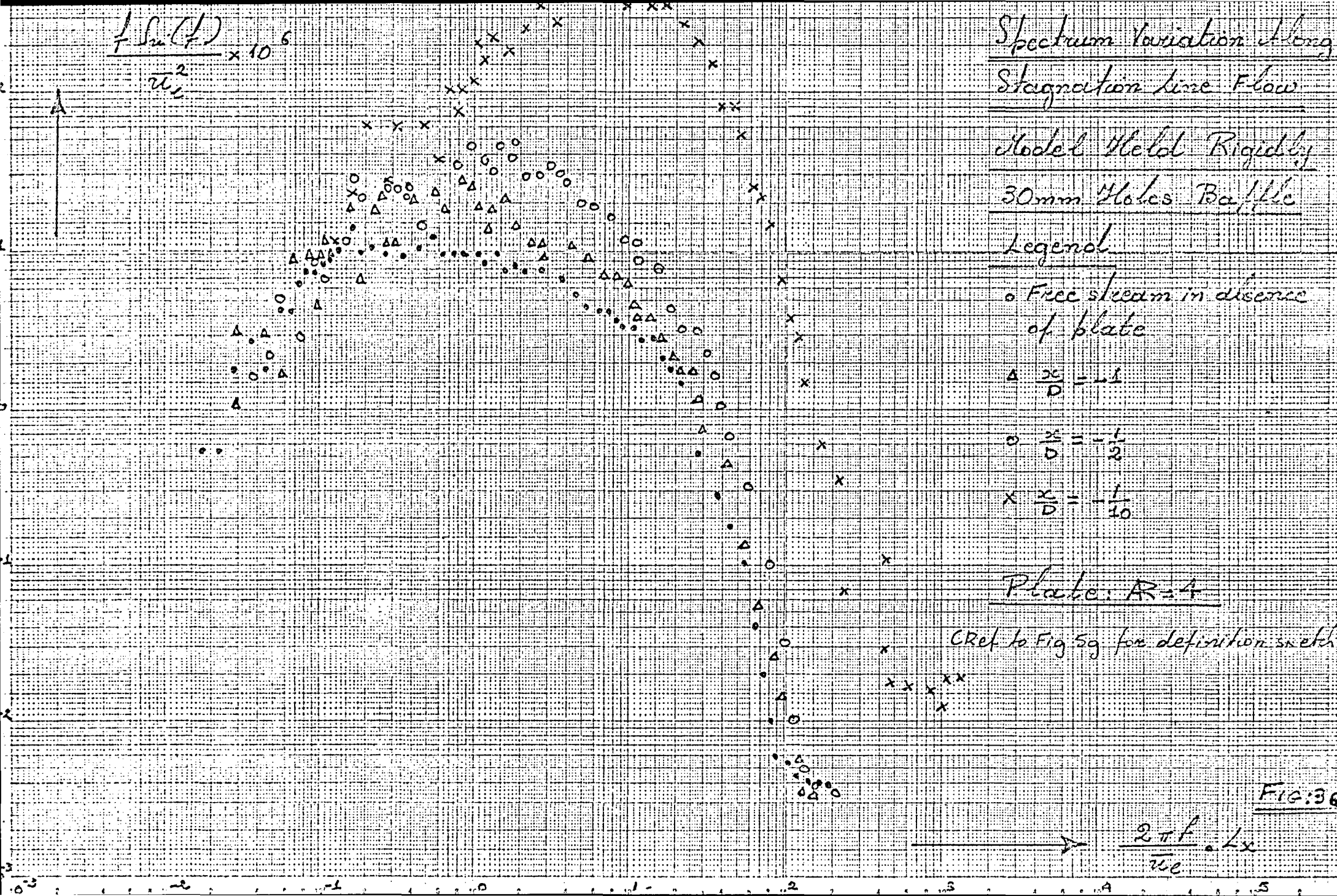
$\times \frac{x}{D} = -\frac{1}{10}$

Plate:  $R=4$

Ref to Fig 5g for definition sketch

Fig: 36

$$\frac{f \sin(\frac{f}{2})}{u_1^2} \times 10^6$$



# Turbulence Level Variations Along Stagnation Line Flow

Plate: AR=4

30 mm Holes Baffle

Legend

- Model Held Rigidly
  - △ Model Free to Oscillate
- (Ref to Fig 5g for definition sketch)

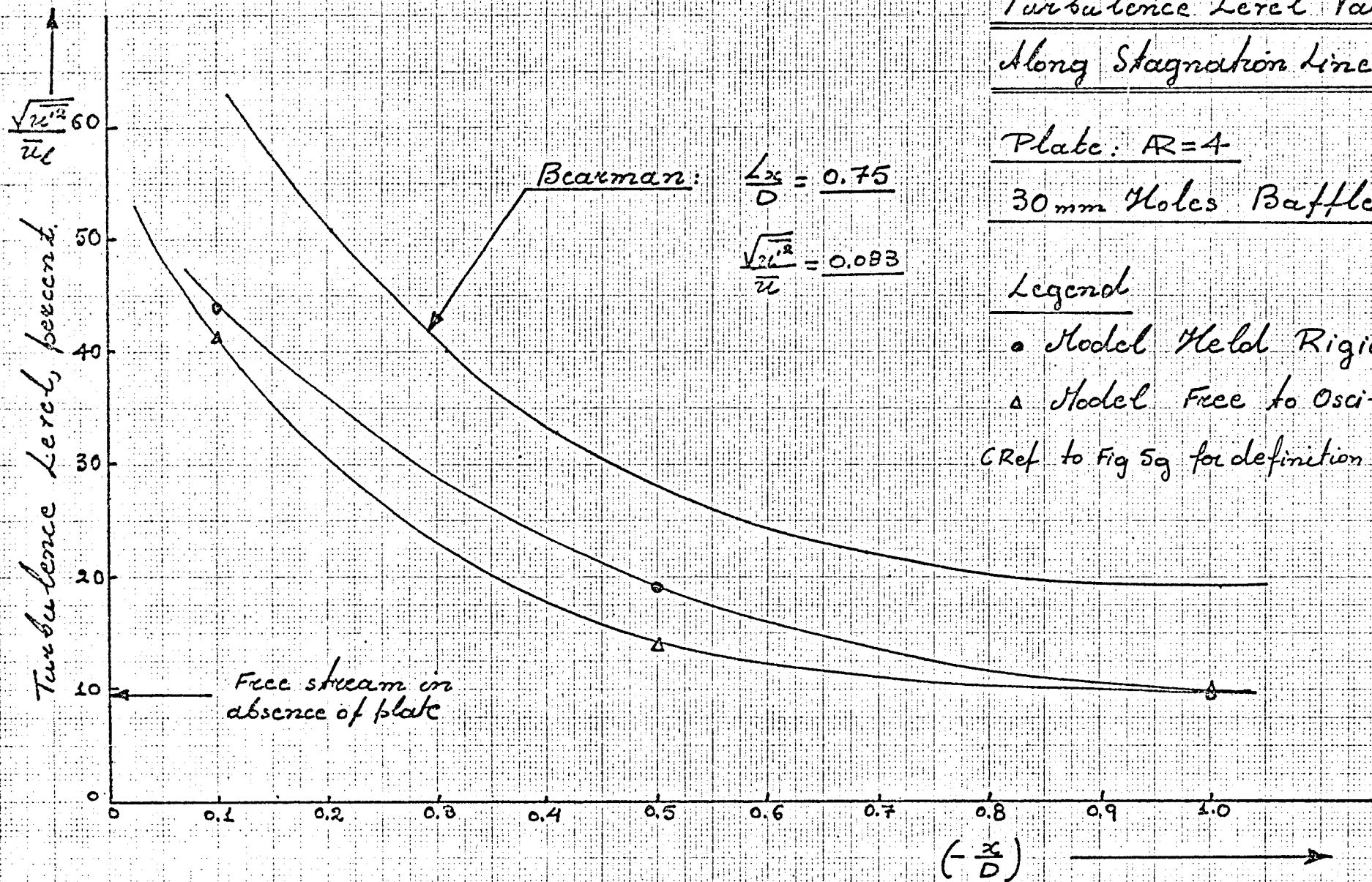
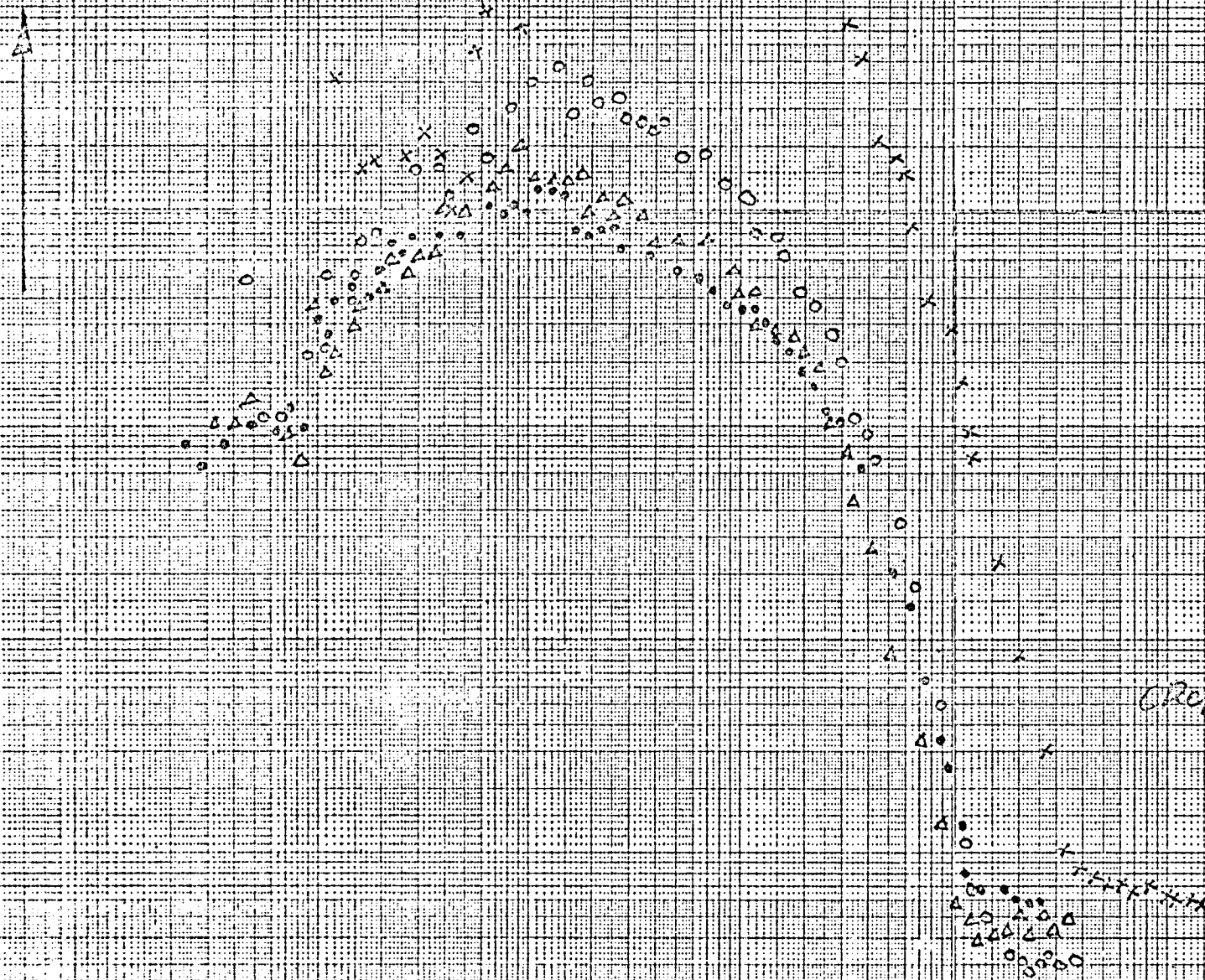


FIG: 37



$$\frac{1}{\pi} \frac{\Delta u}{u_c} \left( \frac{1}{r} \right) \times 10^6$$



Spectrum Variation along  
Stagnation Line Flow

Model Free to Oscillate  
50mm Glass Baffle

Legend

- o Free stream in absence of plate
- $\Delta \frac{x}{D} = -1$
- $\circ \frac{x}{D} = -\frac{1}{2}$
- $\times \frac{x}{D} = -\frac{1}{40}$

Plate A-4

Ref to Fig 5g for definition  
symbols

FIG: 38

$$\frac{2\pi f}{u_c} \cdot L_{sc}$$



$$\frac{f(\Omega_1(t))}{\pi_0^2} \times 10^6$$

Spectrum Variation along  
Stagnation Line Flow

Model Model Rigidity  
50mm. Holed Baffles

- Legend
- o free stream indicator of plate
  - $\Delta \frac{x}{D} = 1$
  - $\circ \frac{x}{D} = 1/2$
  - $\times \frac{x}{D} = 1/10$

Plate: R=4

Ref. to Fig 59 for definitions and etc.

Fig: 39.

$$\frac{2\pi f}{\pi_0} \cdot L_x$$

5-3    -2    -1    0    1    2    3    4    5

Turbulence Level Variations  
Along Stagnation Line Flow

Plate:  $R=4$

50 mm Holes Baffle

Legend

- Model Held Rigidly
- △ Model Free to Oscillate

(Ref. to Fig 5g for definition sketch.)

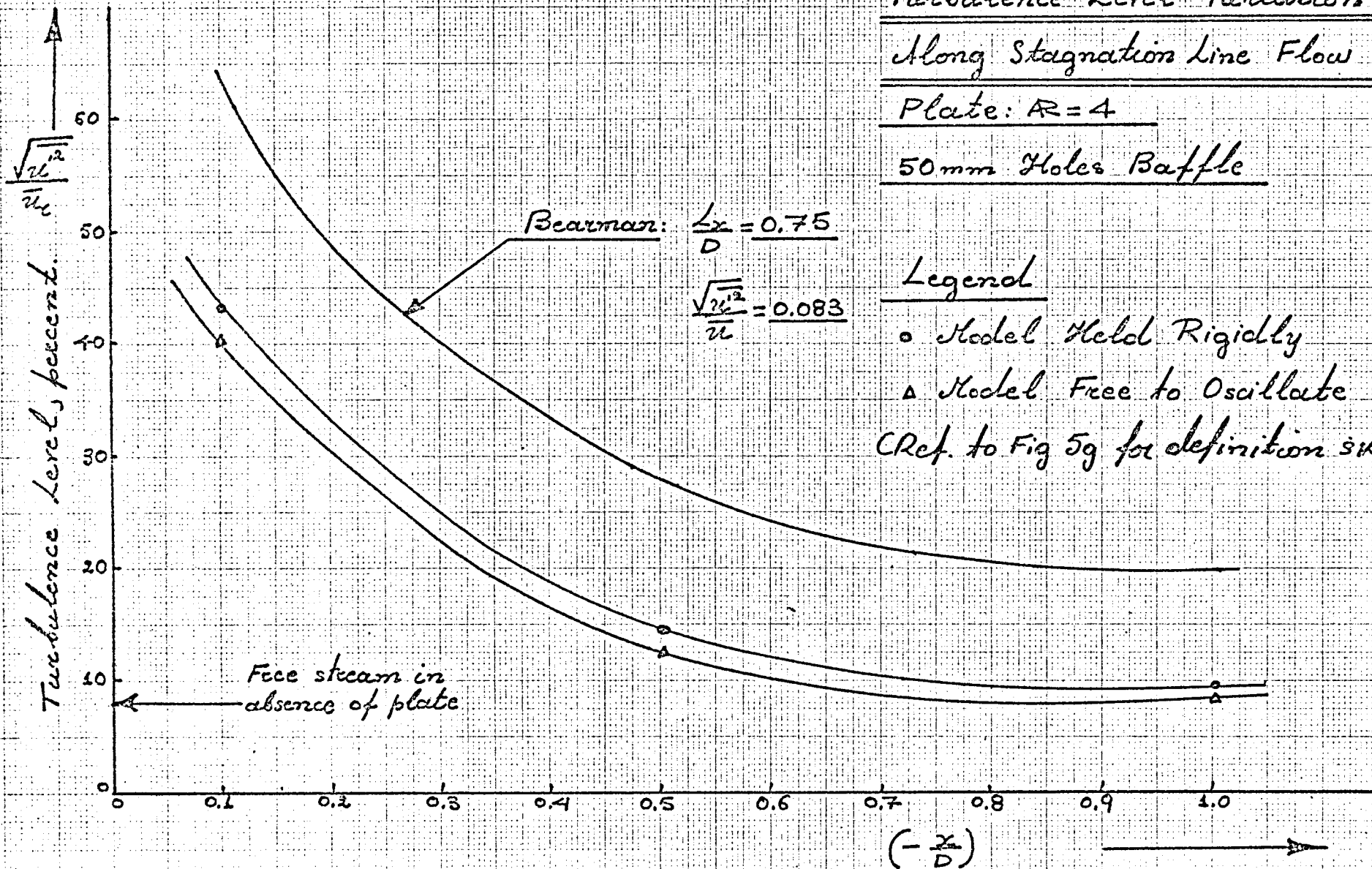


FIG:40

Turbulence Level Value Along Stagnation Line

FIG: 4.1

Model Under Investigation	POSITION OF MEASUREMENT ALONG STAGNATION LINE	EMPTY TUNNEL TURBULENCE LEVEL (%)			SLOTTED BAFFLE		30mm HOLES BAFFLE		50mm HOLES BAFFLE		NATURE OF MOVEMENT
		SLOTTED BAFFLE	30mm HOLES BAFFLE	50mm HOLES BAFFLE	TURBULENCE LEVEL IN FRONT OF THE MODEL (%)	Percentage Increase of Turbulence Level with Respect to the Free Stream Value	TURBULENCE LEVEL IN FRONT OF THE MODEL (%)	Percentage Increase of Turbulence Level with Respect to the Free Stream Value	TURBULENCE LEVEL IN FRONT OF THE MODEL (%)	Percentage Increase of Turbulence Level with Respect to the Free Stream Value	
Late $R = 1$	TEST SECTION	10.8	9.1	8							
	$\frac{x}{d} = -0.1$	11	9.5	8.1	$\frac{42}{40}$	$\frac{281\%}{263\%}$	$\frac{32.5}{28}$	$\frac{242\%}{195\%}$	$\frac{31}{25.5}$	$\frac{369\%}{215\%}$	Model Held Rigid Model Oscillating
	$\frac{x}{d} = -0.5$	11.5	10	8.5	$\frac{20}{16}$	$\frac{82\%}{40\%}$	$\frac{12.5}{10.1}$	$\frac{25\%}{1\%}$	$\frac{10.5}{10}$	$\frac{23\%}{17.6\%}$	Model Held Rigid Model Oscillating
	$\frac{x}{d} = -1.0$	12.5	10.1	10	$\frac{14.5}{13}$	$\frac{16\%}{4\%}$	$\frac{10.1}{10}$	$\frac{0}{-99\%}$	$\frac{10}{10}$	$\frac{0\%}{0\%}$	Model Held Rigid Model Oscillating
Late $R = 4$	TEST SECTION	10.8	9.1	8							
	$\frac{x}{d} = -0.1$	11	9.5	8.1	$\frac{149}{44}$	$\frac{345\%}{300\%}$	$\frac{44}{41}$	$\frac{363\%}{331\%}$	$\frac{43}{40}$	$\frac{430\%}{394\%}$	Model Held Rigid Model Oscillating
	$\frac{x}{d} = -0.5$	11.5	10	8.5	$\frac{25.5}{24}$	$\frac{121\%}{108\%}$	$\frac{19}{14}$	$\frac{90\%}{40\%}$	$\frac{14.5}{12.5}$	$\frac{70.5\%}{47\%}$	Model Held Rigid Model Oscillating
	$\frac{x}{d} = -1.0$	12.5	10.1	10	$\frac{15.5}{14}$	$\frac{24\%}{12\%}$	$\frac{10}{10}$	$\frac{-99\%}{-99\%}$	$\frac{10}{10}$	$\frac{0\%}{0\%}$	Model Held Rigid Model Oscillating

continues:

irregular  
cube

d: 40mm

TEST SECTION	10.3	9.1	8							
f=0.1	11	9.5	8.1	$\frac{45}{41}$	$\frac{309\%}{272\%}$	$\frac{31}{28}$	$\frac{226\%}{194\%}$	$\frac{31}{29.5}$	$\frac{282\%}{252\%}$	$\frac{\text{Model Model Rig.}}{\text{Model Oscillation}}$
f=0.5	11.5	10	8.5	$\frac{21}{18}$	$\frac{82.6\%}{56\%}$	$\frac{11.5}{10}$	$\frac{15\%}{0}$	$\frac{12}{10}$	$\frac{41\%}{17.6\%}$	$\frac{\text{Model Model Rig.}}{\text{Model Oscillation}}$
f=1.0	12.5	10.1	10	$\frac{15}{14}$	$\frac{20\%}{12\%}$	$\frac{10}{10}$	$\frac{-99\%}{-99\%}$	$\frac{10}{10}$	$\frac{0\%}{0\%}$	$\frac{\text{Model Model Rig.}}{\text{Model Oscillation}}$

0 mm  
cube

TEST SECTION	10.8	9.1	8							
f=0.1	11	9.5	8.1	$\frac{42}{37.5}$	$\frac{221\%}{240\%}$	$\frac{33}{27}$	$\frac{247\%}{184\%}$	$\frac{31.5}{25}$	$\frac{289\%}{208\%}$	$\frac{\text{Model Model Rig.}}{\text{Model Oscillation}}$
f=0.5	11.5	10	8.5	$\frac{21}{16}$	$\frac{82\%}{39\%}$	$\frac{13}{10}$	$\frac{30\%}{0\%}$	$\frac{11}{10}$	$\frac{29.4\%}{17.6\%}$	$\frac{\text{Model Model Rig.}}{\text{Model Oscillation}}$
f=1.0	12.5	10.1	10	$\frac{14}{13}$	$\frac{12\%}{4\%}$	$\frac{10}{9.5}$	$\frac{-99\%}{-5.9\%}$	$\frac{10}{10}$	$\frac{0\%}{0\%}$	$\frac{\text{Model Model Rig.}}{\text{Model Oscillation}}$

irregular  
cube

= 2

TEST SECTION	10.3	9.1	8							
f=0.1	11	9.5	8.1	$\frac{43}{35.5}$	$\frac{200\%}{222\%}$	$\frac{31}{23}$	$\frac{226\%}{142\%}$	$\frac{36.5}{30}$	$\frac{350\%}{270\%}$	$\frac{\text{Model Model Rig.}}{\text{Model Oscillation}}$
f=0.5	11.5	10	8.5	$\frac{21.5}{15}$	$\frac{87\%}{30\%}$	$\frac{12}{10}$	$\frac{21\%}{0\%}$	$\frac{13}{10.5}$	$\frac{53\%}{23\%}$	$\frac{\text{Model Model Rig.}}{\text{Model Oscillation}}$
f=1.0	12.5	10.1	10	$\frac{14}{12.5}$	$\frac{12\%}{0\%}$	$\frac{10}{9.5}$	$\frac{-99\%}{-5.9\%}$	$\frac{10}{10}$	$\frac{0\%}{0\%}$	$\frac{\text{Model Model Rig.}}{\text{Model Oscillation}}$

eccentric  
linder

R=2

TEST SECTION	10.8	9.1	8							
$\frac{y}{x} = -0.1$	11	9.5	8.1	$\frac{4.6}{4.2}$	$\frac{318\%}{218\%}$	$\frac{38}{30}$	$\frac{300\%}{215\%}$	$\frac{37.5}{32.5}$	$\frac{362\%}{325\%}$	$\frac{\text{Model Model Rig.}}{\text{Model Oscillation}}$
$\frac{y}{x} = -0.5$	11.5	10	8.5	$\frac{2.0}{17.5}$	$\frac{30\%}{34.2\%}$	$\frac{12.5}{10}$	$\frac{25\%}{0\%}$	$\frac{13.5}{11}$	$\frac{58.2\%}{29.4\%}$	$\frac{\text{Model Model Rig.}}{\text{Model Oscillation}}$
$\frac{y}{x} = -1.0$	12.5	10.1	10	$\frac{12.5}{11}$	$\frac{0\%}{-12\%}$	$\frac{10}{10}$	$\frac{-0.99\%}{-0.99\%}$	$\frac{10}{10}$	$\frac{0\%}{0\%}$	$\frac{\text{Model Model Rig.}}{\text{Model Oscillation}}$

PROBABILITY DENSITY OF THE LONGITUDINAL VELOCITY

COMPONENT



Note: The r.m.s of the triangular wave is the same as that of  $\mu'$

Calibrating  $\mu(x)$  from triangular wave at  $f = 150 \text{ Hz}$  and R.M.S = 0.65V



Probability density of the longitudinal component of the velocity  
Slotted Raffle

Flow at  $x = -26 \text{ mm}$ ,  $y = 0 \text{ mm}$ ,  $z = 0 \text{ mm}$   
Empty tunnel

FIG. 42

Note: The r.m.s. of the triangular wave is the same as that of  $\mu$

Calibrating band from  
triangular wave at  $f = 100 \text{ Hz}$   
and R.M.S. = 0.62 V



Probability density of the  
longitudinal component  
of the velocity:

Slotted Raffle

Flow at  $x = -13 \text{ mm}$ ,  $y = 0 \text{ mm}$ ,  $z = 0 \text{ mm}$

Empty tunnel

FIG: 43



Note: The r.m.s of the triangular wave is the same as that of  $u'$

Calculating  $p(x)$  from triangular wave at  $f=100\text{Hz}$  and R.M.S = 0.5V.



Probability density of the longitudinal component of the velocity  
Slotted Baffle

Flow at  $x=0\text{mm}$ ,  $y=0\text{mm}$ ,  $z=0\text{mm}$   
Empty tunnel

FIG. 44

Note: The rms of the triangular wave is the same as that of  $x$ .

Probability Density of the Longitudinal Component of the Velocity in front of the Cus.

Slotted Baffle

Flow at  $\frac{x}{D} = -1$

Model Free to Oscillate

Calibrating  $p(x)$  from triangular wave at  $f = 100 \text{ Hz}$  and R.M.S. = 1.25 Y

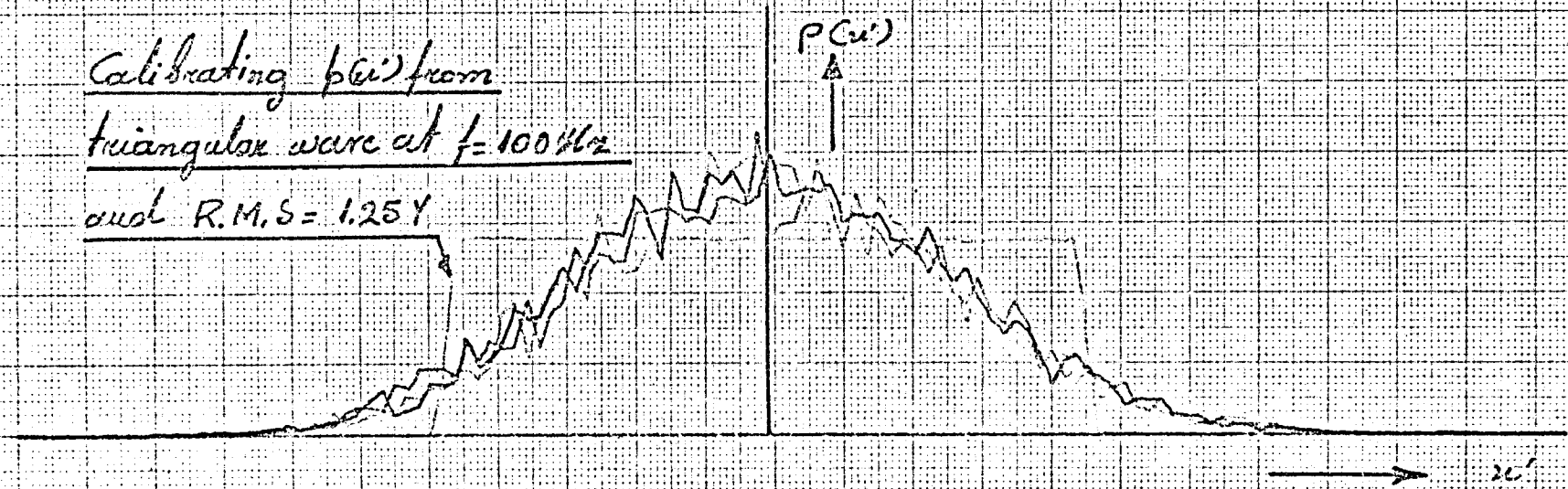


FIG. 45

Note: The r.m.s of the triangular wave is the same as that of  $u'$ .

Probability Density of the Longitudinal Component of the Velocity in front of the Cube.

Slotted Baffle

Flow at  $\frac{2c}{D} = -\frac{1}{2}$

Model Free to Oscillate

Calibrating  $p(u')$  from triangular wave at  $f = 100\text{ Hz}$   
and R.M.S = 1.151

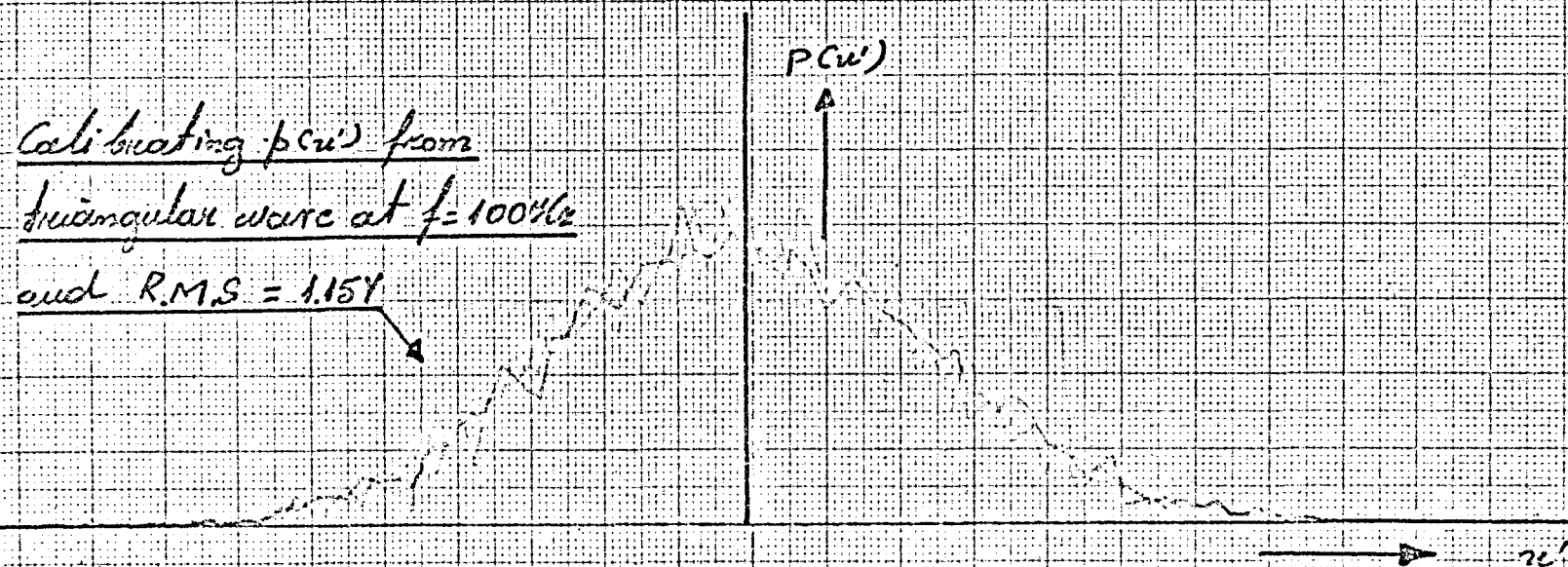


FIG. 46

Note: The r.m.s of the triangular wave is the same as that of  $u'$

Probability Density of the Longitudinal Component of the Velocity in front of the Cube

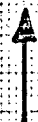
Slotted Baffle

Flow at  $\frac{x}{D} = -1/10$

Model Free to Oscillate

Calibrating  $p(u')$  from triangular wave at  $f = 100\text{Hz}$  and  $\text{RMS} = 0.951$

$p(u')$



$u'$

FIG. 47



Note: The r.m.s of the triangular wave is the same as that of  $u'$

Probability Density of the Longitudinal Component of the Velocity in front of the Cube

Slotted Baffle

Flow at  $\frac{x}{D} = -1$

Model Held Rigidly

Calibrating  $p(u')$  from triangular wave at  $f = 100\text{ Hz}$  and R.M.S = 1.25

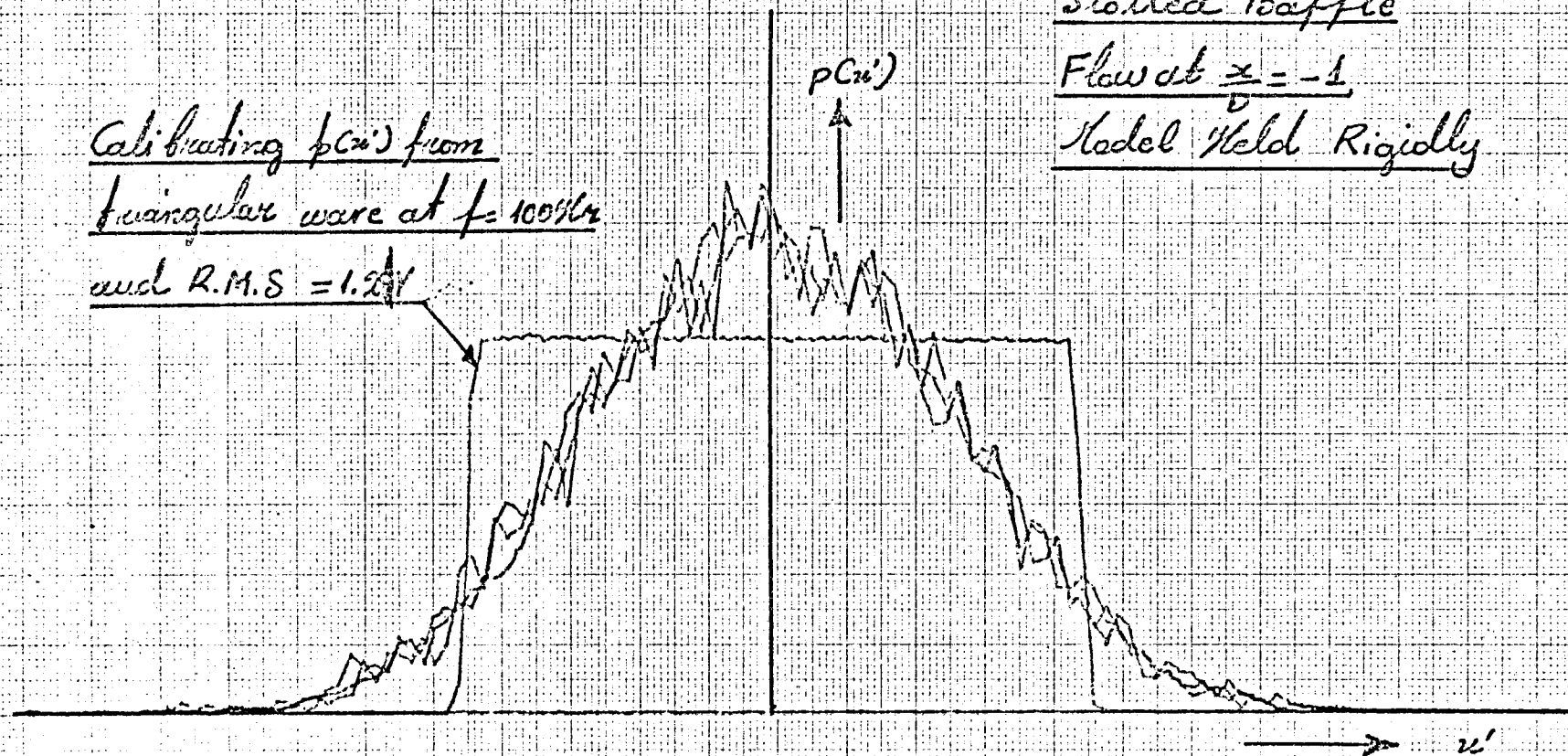


FIG: 18

Note: The r.m.s of the triangular wave is the same as that of  $u'$

Probability Density of the longitudinal Component of the Velocity in front of the Cube

Slotted Baffle

Flow at  $\frac{x}{D} = -\frac{1}{2}$

Model Held Rigidly

Calibrating  $p(u')$  from triangular wave at  $f = 100\text{ Hz}$  and R.M.S = 1.1 ft/s

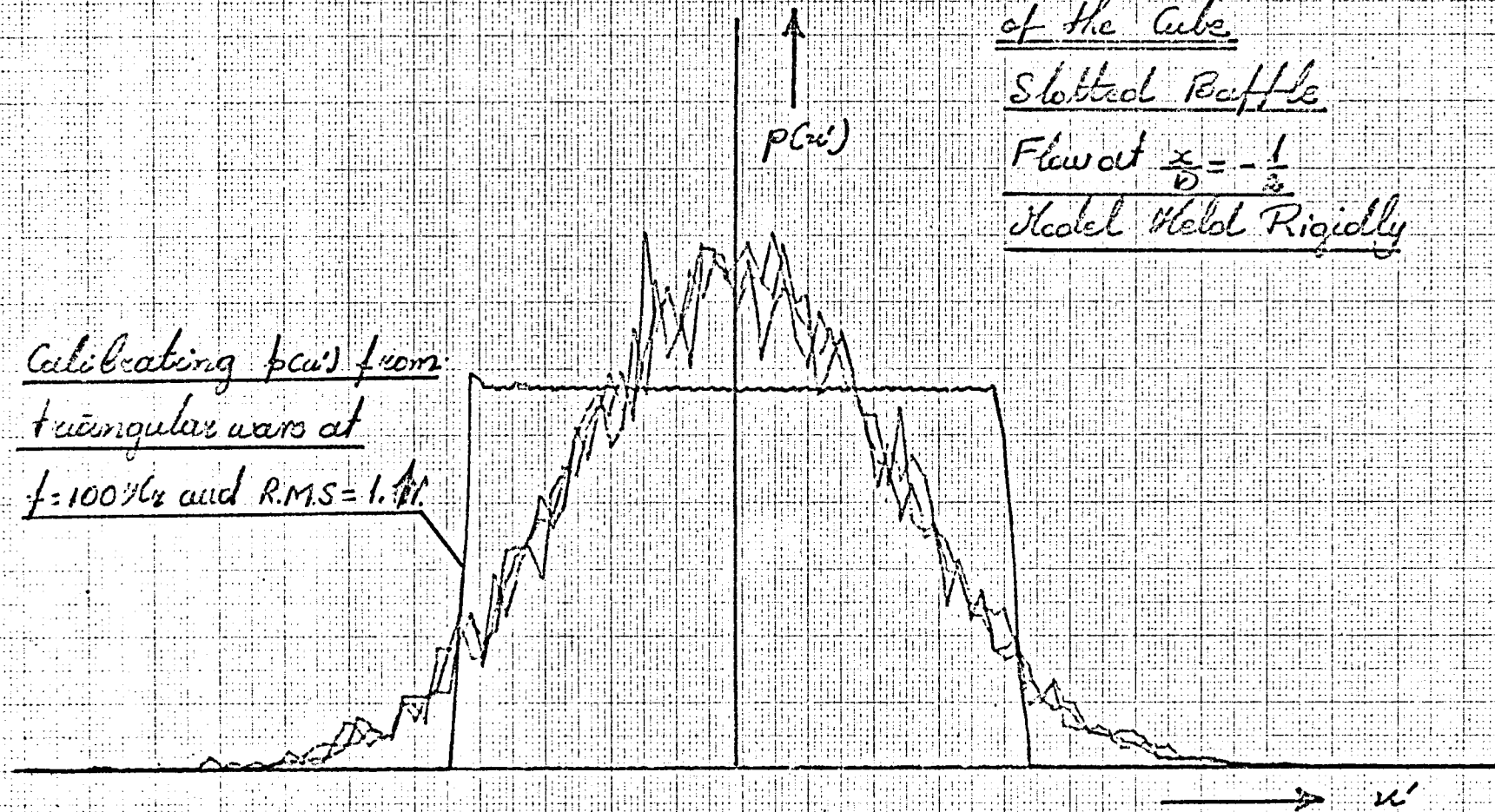


FIG: 49

Note: The r.m.s of the triangular wave is the same as that of  $u$

Calibrating  $p(u')$  from triangular wave at  $f = 100 \text{ Hz}$  and R.M.S =  $0.05 \text{ V}$

Probability Density of the Longitudinal Component of the Velocity in front of the Cube

Slotted Baffle

Flaw at  $\frac{x_c}{D} = -\frac{1}{10}$   
Model Held Rigidly

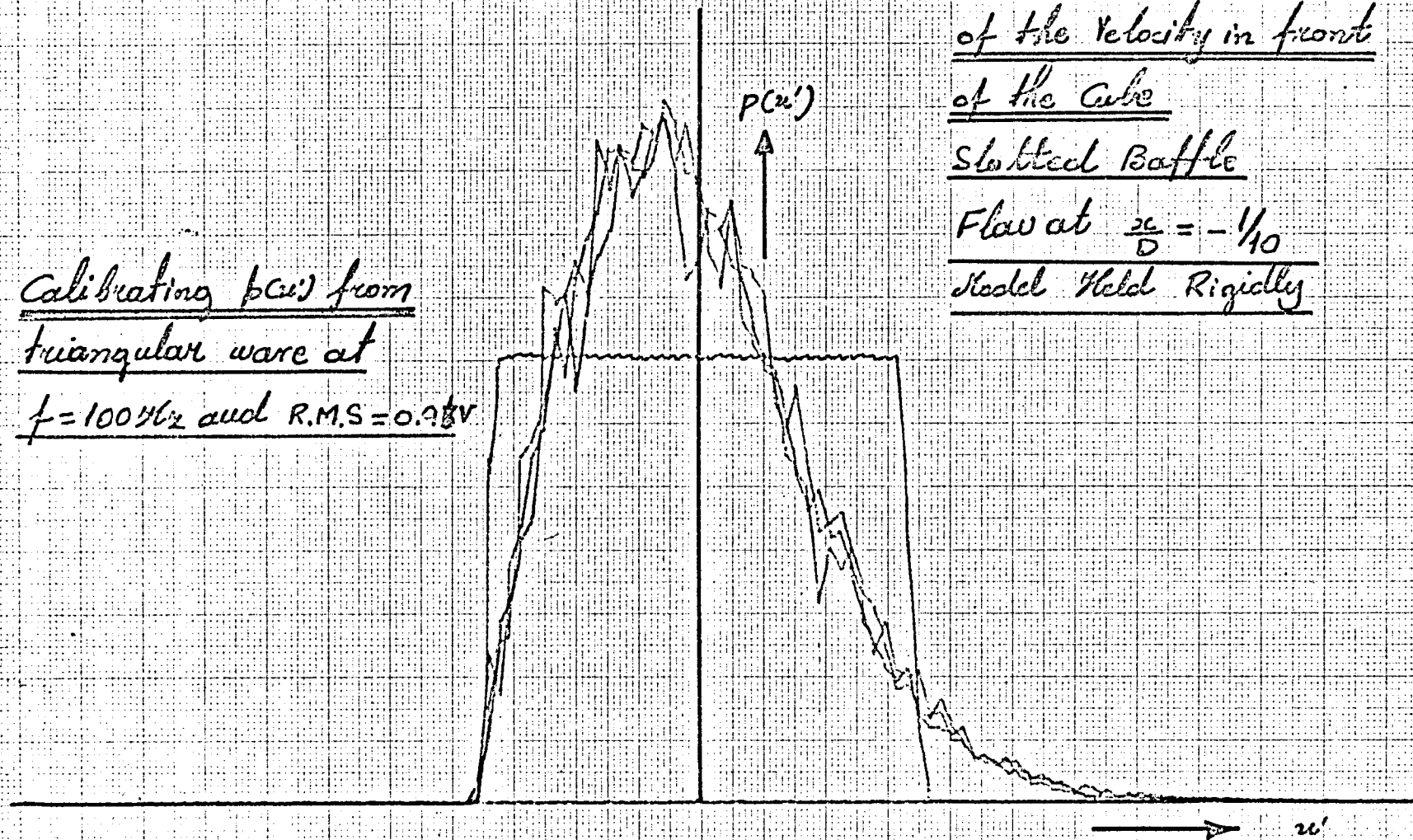
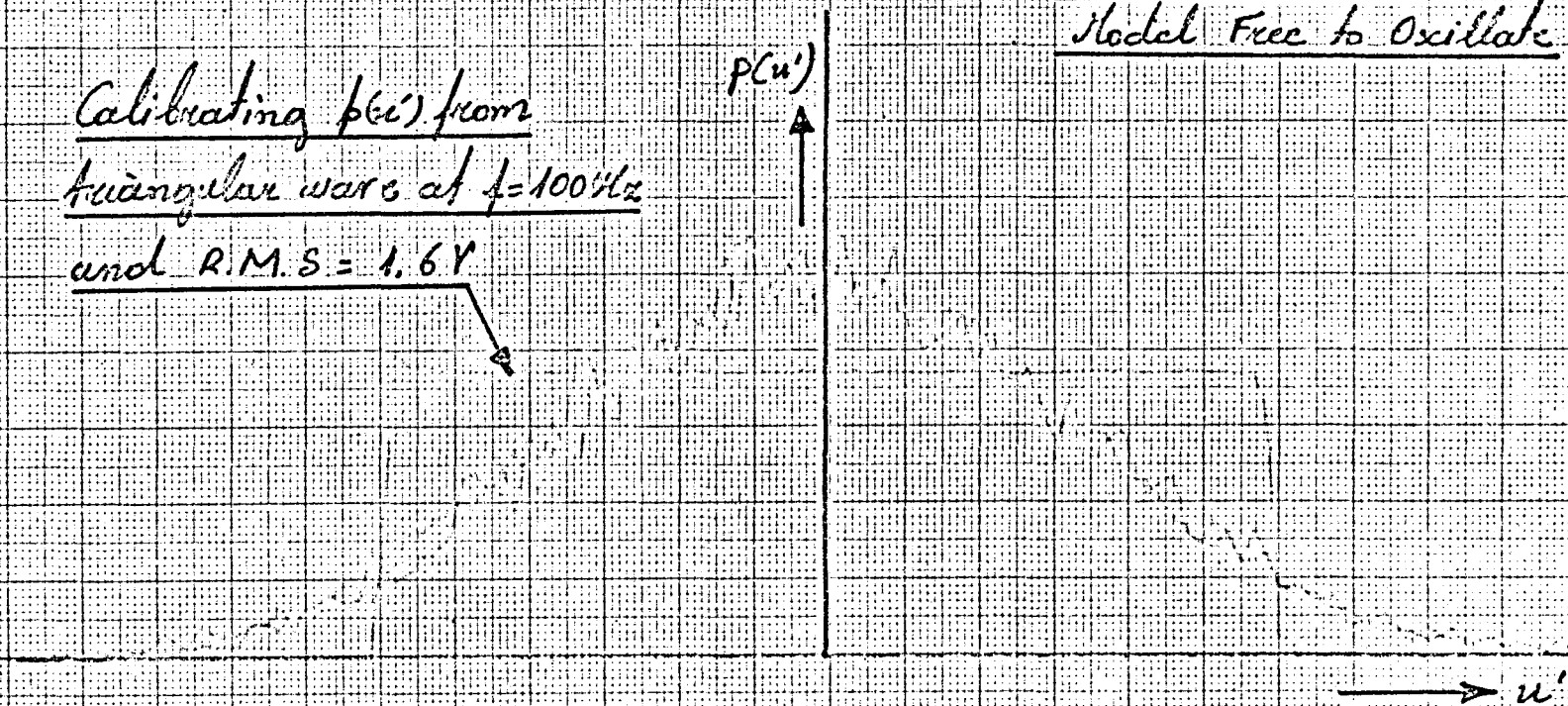


FIG:50

Note: The r.m.s of the triangular wave is the same as that of  $u'$

Calibrating  $p(u')$  from  
triangular wave at  $f = 100 \text{ Hz}$   
and R.M.S = 1.6 V



Probability Density of the  
Longitudinal Component of  
the Velocity in front of the  
 $R = 2$  Parallelepiped  
Slotted Baffle  
Flow at  $\frac{x}{D} = -1$   
Model Free to Oscillate

FIG: 54



Note: The r.m.s of the triangular wave is the same as that of  $u'$

Calibrating  $p(u)$  from triangular wave at  $f=100\text{Hz}$  and  $\text{R.M.S} = 1.5\%$

$p(u)$   
↑

Probability Density of the Longitudinal Component of the Velocity in front of the

$AR=2$  Parallelepiped

Slotted Baffle

Flow at  $\frac{x}{D} = -\frac{1}{2}$

Model Free to Oscillate

FIG: 52

Note: The r.m.s. of the triangular wave is the same as that of  $u'$

Calibrating  $p(u')$  from triangular wave at  $f = 100\text{ Hz}$  and R.M.S. = 0.95V

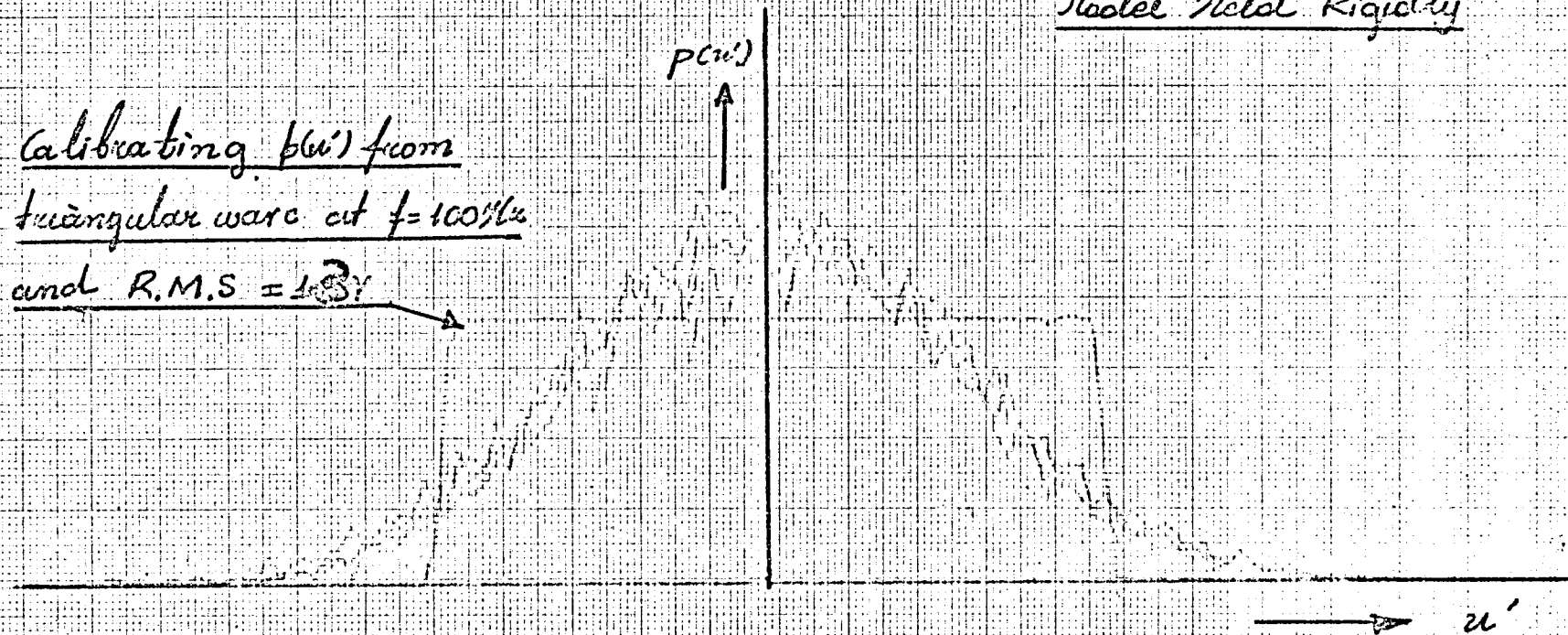
Probability Density of the Longitudinal Component of the Velocity in front of the  $AR = 2$  Parallelepiped Slotted Baffle  
Flow at  $\frac{u_c}{U} = -\frac{1}{10}$   
Model Free to Oscillate

$p(u')$

FIG: 53

Note: The r.m.s of the triangular wave is the same as that of  $u'$

Calibrating  $p(u')$  from  
triangular wave at  $f=100\%$   
and R.M.S = 1.3



Probability Density of the Longi-  
tudinal Component of the Velo-  
city in front of the AR=2  
Parallelepiped  
Slotted Baffle  
Flow at  $\frac{x}{D} = -1$   
Model Held Rigidly

FIG. 54

Note: The r.m.s of the triangular wave  
is the same as that of  $u'$

Calibrating  $p(u')$  from  
triangular wave at  $f = 100\text{ Hz}$   
and R.M.S = 1.25 V



Probability Density of the  
Longitudinal Component of  
the Velocity in front of the  
 $AR=2$  Parallelepiped  
Slotted Baffle  
Flow at  $\frac{x}{D} = -\frac{1}{2}$   
Model Held Rigidly

FIG:55



Note: The r.m.s of the triangular wave is the same as that of  $u'$

Probability Density of the Longitudinal Component of the Velocity in front of the

$AR=2$  Parallelepiped Slotted Baffle

Flow at  $\frac{x}{D} = -\frac{1}{10}$   
Model Held Rigidly

Calibrating  $p(u')$  from triangular wave at  $f=100\text{Hz}$  and  $R.M.S} = 1.25\text{V}$

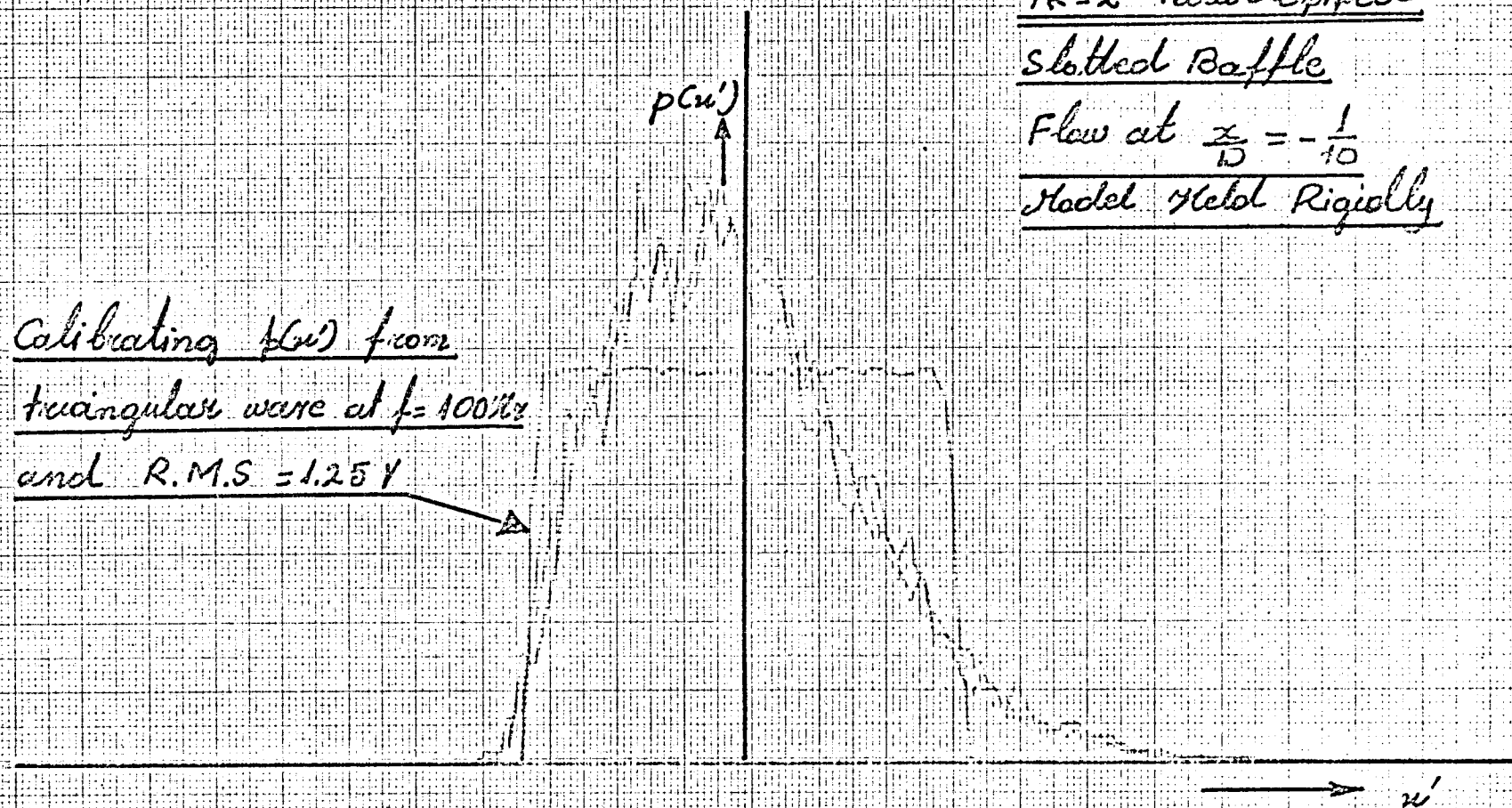


FIG:56

Note: The r.m.s of the triangular wave is the same as that of  $u'$

Calibrating  $p(u')$  from  
triangular wave at  $f = 100\text{ Hz}$   
and R.M.S = 0.01

$p(u')$

A

$u'$

Probability Density of the Longi-  
tudinal Component of the Velocity  
in front of the Cube.

30 mm Holes Baffle

Flow at  $\frac{x}{D} = -1$

Model Free To Oscillate

FIG: 57

Note: The r.m.s of the triangular wave is the same as that of  $u'$

Calibrating  $p(u')$  from  
triangular wave at  $f = 100\text{ Hz}$   
and R.M.S = 0.75 V

$p(u')$



Probability Density of the Longitudi-  
nal Component of the Velocity in front  
of the Cube

30mm Nucleo Baffle

Flow at  $\frac{x}{D} = -\frac{1}{2}$

Model Free to Oscillate

FIG:58

$u'$

Note: The r.m.s of the triangular wave is the same as that of  $u'$

Calibrating  $p(u)$  from triangular wave at  $f = 100 \text{ Hz}$  and R.M.S. = 0.61

Probability Density of the Longitudinal Component of the Velocity in front of the Cube.

30mm Noses Baffle

Flow at  $\frac{x}{D} = -1/10$

Model Free to Oscillate

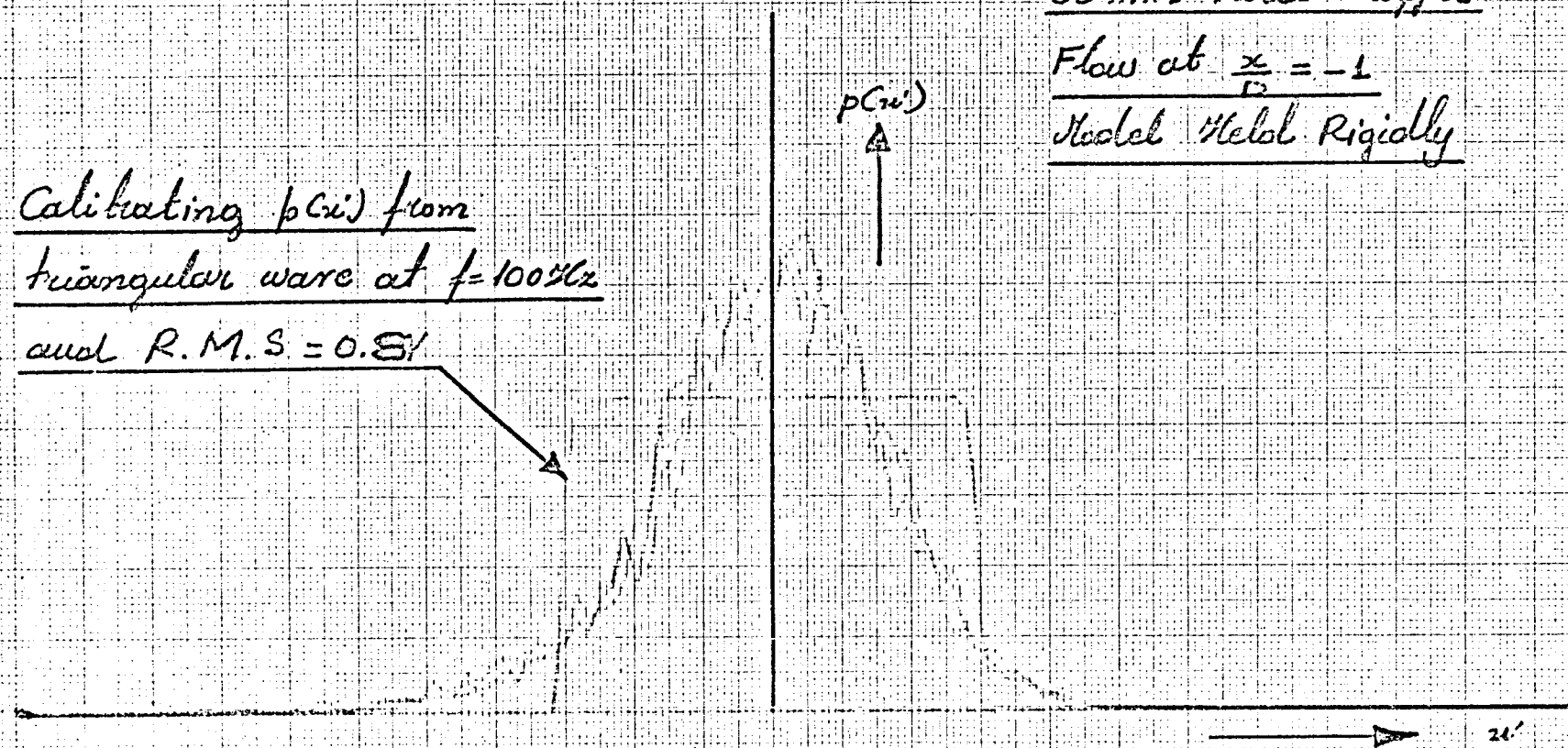
$P(u')$

FIG:59



Note: The r.m.s of the triangular wave is the same as that of  $u'$

Calibrating  $p(u')$  from  
triangular wave at  $f = 100\%$   
and R.M.S. = 0.81



Probability Density of the  
Longitudinal Component of  
the Velocity in front of the  
Cube

30 mm Holes Baffle

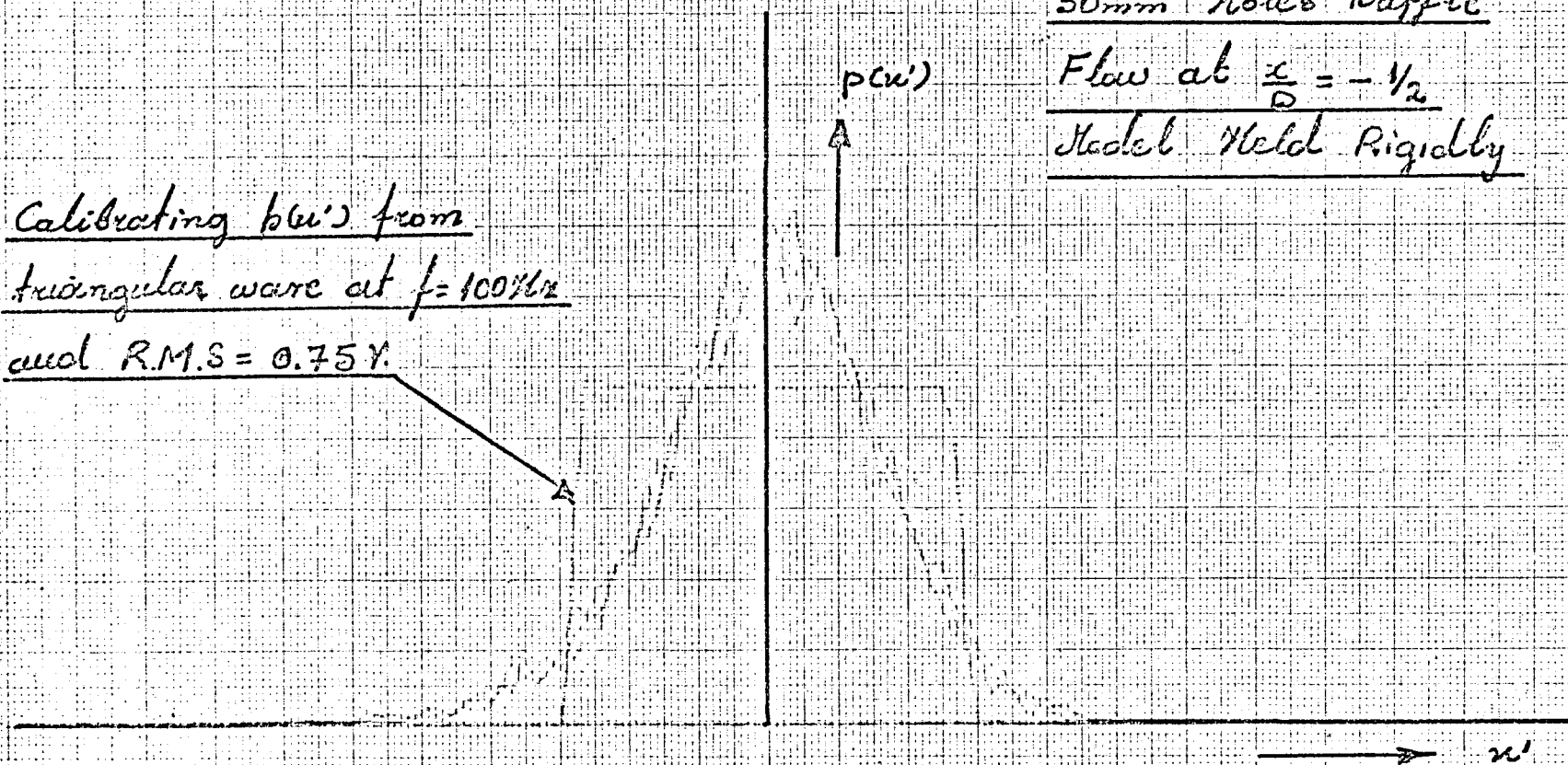
Flow at  $\frac{x}{D} = -1$

Model Helix Rigidly

FIG: 60

Note: The r.m.s of the triangular wave is the same as that of  $u'$

Calibrating  $h(u')$  from  
triangular wave at  $f = 100\text{ Hz}$   
and R.M.S = 0.75 V.



Probability Density of the  
Longitudinal Component of  
the Velocity in front of the  
Cube.

30mm Holes Baffle

Flow at  $\frac{x}{D} = -\frac{1}{2}$

Model Held Rigidly

FIG: 61

Note: The r.m.s. of the triangular wave is the same as that of  $u'$

Calibrating  $p(u')$  from triangular wave at

$f = 100 \text{ Hz}$  and  $\text{R.M.S} = 0.6 \text{ V}$  →

Probability Density of the Longitudinal Component of the Velocity in front of the Cube

30 mm Holes Baffle

Flow at  $\frac{x}{D} = -\frac{1}{10}$

Model Held Rigidly

$p(u')$



FIG: 62

Note: The r.m.s of the triangular wave is the same as that of  $u'$

Calibrating  $p(u')$  from triangular wave at  
 $f = 100 \text{ Hz}$  and R.M.S =  $0.85V$

Probability Density function of the longitudinal component of the Velocity in front of the

$AR = 2$  Parallel piped.

30mm Holes Baffle

Flow at  $\frac{x}{D} = -1$

Model Free to Oscillate

$P(u')$



$u'$

FIG:63



Note: The r.m.s of the triangular wave is the same as that of  $u'$

calibrating  $p(u)$  from  
triangular wave of  
 $f=100\text{ Hz}$  and R.M.S =  $0.75\text{ V}$

$p(u)$

Probability Density Function of  
the longitudinal component  
of the velocity in front of the  
 $AR=2$  Parallelipiped  
 $30\text{ mm}$  slots Raffle  
Flow at  $\frac{u}{D} = -\frac{1}{2}$   
Model Free to Oscillate

$u'$

Fig. 64

Note: The r.m.s of the triangular wave is the same as that of  $u'$

Calibrating  $p(u')$  from  
triangular wave at  $f = 100 \text{ Hz}$   
and R.M.S = 0.6 V

$p(u')$   
↑

Probability Density Function of  
the Longitudinal Component of  
the Velocity in front of the  
 $R=2$  Paralleled

30 mm Holes Baffle

Flow at  $\frac{x}{D} = \frac{1}{10}$

Model Free to Oscillate

FIG 65

Note: The r.m.s of the triangular wave is the same as that of  $u'$

Probability Density of the  
Longitudinal Component  
of the Velocity in front of  
the  $AR=2$  Parallelepiped  
30mm Holes Baffle  
Flow at  $\frac{x}{D} = -1$   
Model Held Rigidly

Calibrating  $p(u')$  from  
triangular wave at  
 $f = 100 \text{ Hz}$  and  $R.M.S = 0.83 \text{ V}$

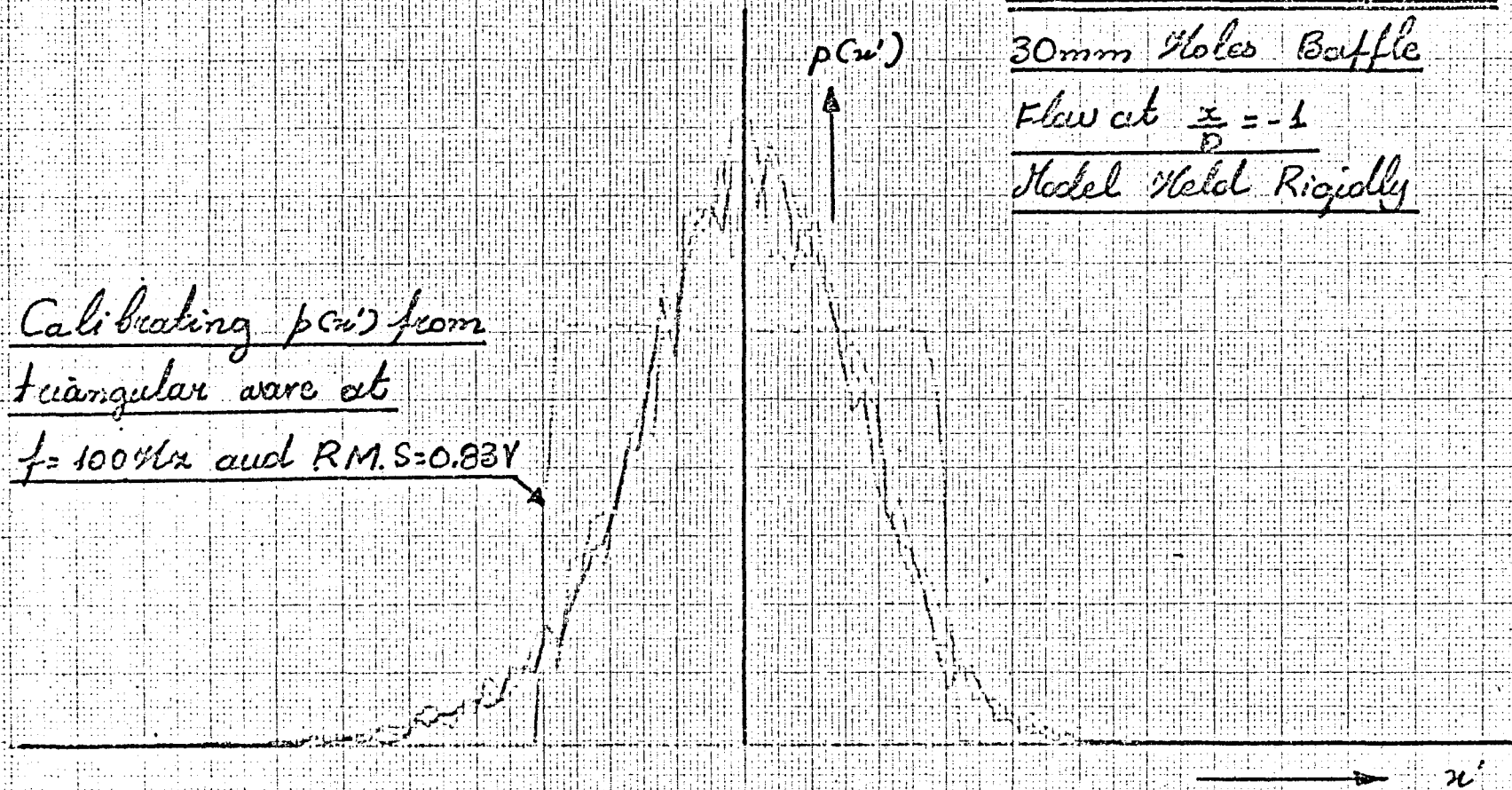
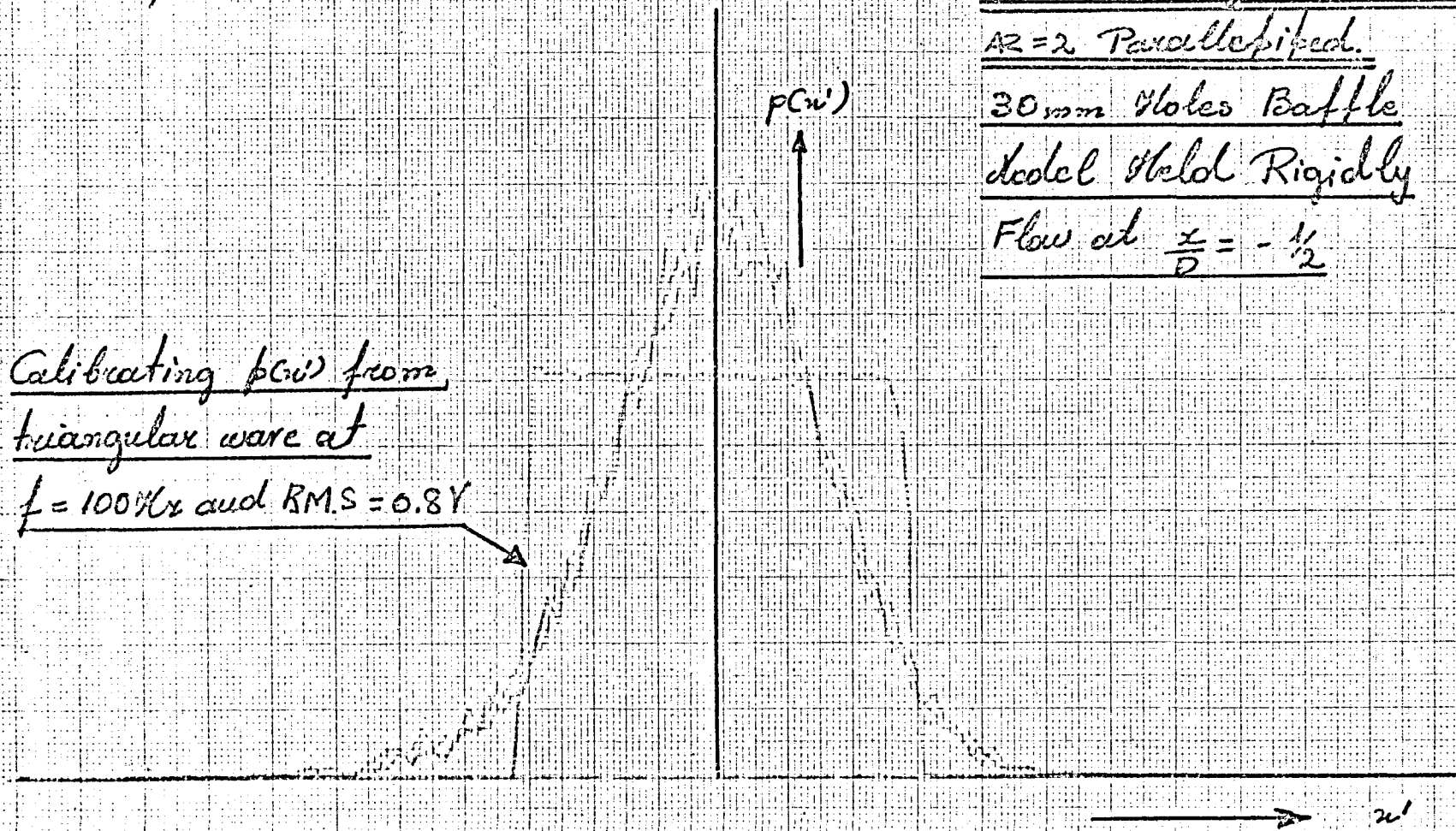


FIG: 56

Note: The r.m.s of the triangular wave is the same as that of  $u'$

Calibrating  $p(u')$  from triangular wave at  
 $f = 100\text{ Hz}$  and  $\text{R.M.S} = 0.8\text{ V}$



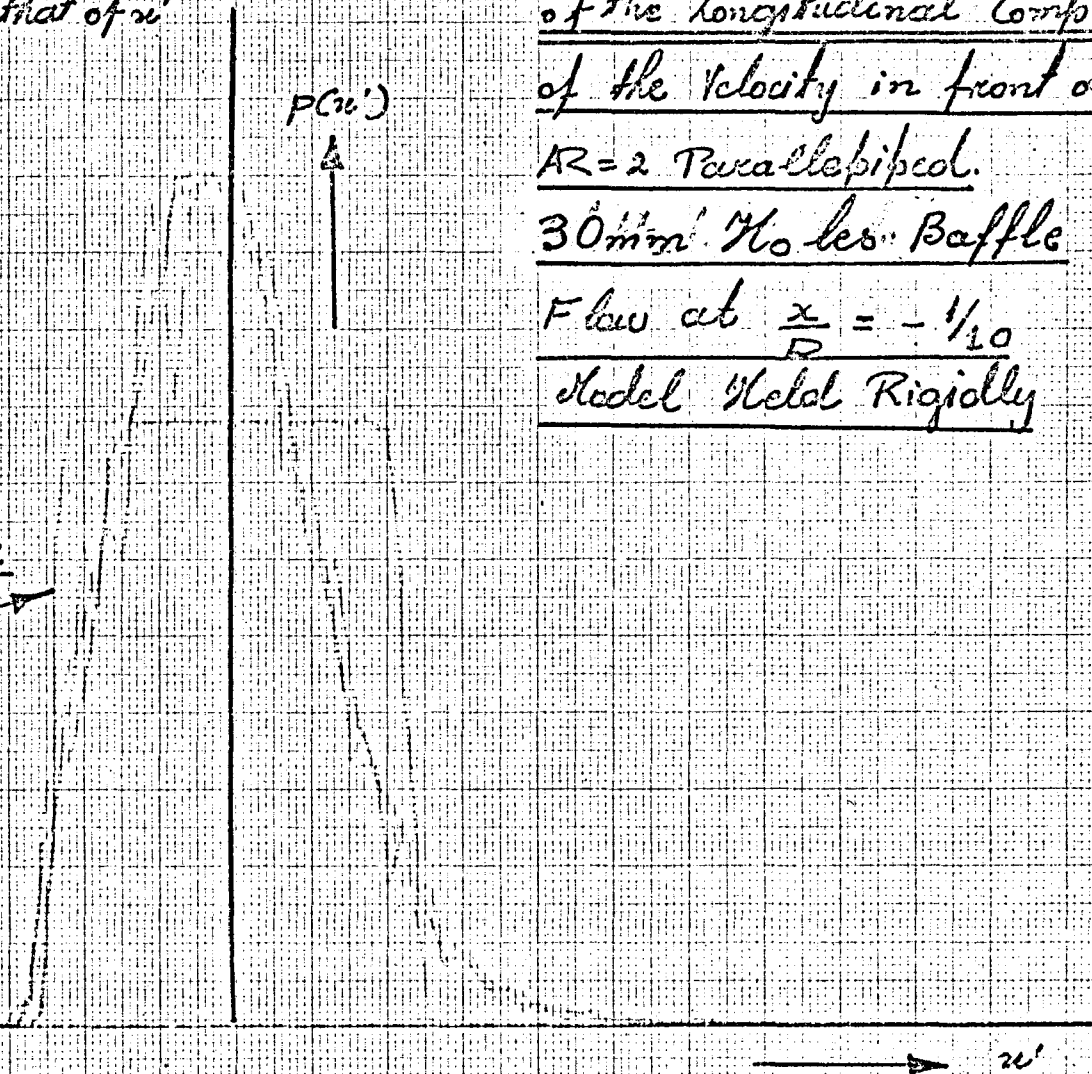
Probability Density Function  
of the longitudinal component  
of the velocity in front of the  
 $AZ = 2$  Parallelepiped.  
30 mm Holes Baffle  
Model Held Rigidly  
Flow at  $\frac{x}{D} = -\frac{1}{2}$

FIG: 63



Note: The r.m.s of the triangular wave is the same as that of  $u'$

Calibrating  $p(u')$  from  
triangular wave at  $f=100\text{Hz}$   
and R.M.S = 0.6V



Probability Density Function  
of the Longitudinal Component  
of the Velocity in front of the  
AR=2 Parallelepiped.  
30mm. Ho les. Baffle  
Flow at  $\frac{x}{D} = -\frac{1}{10}$   
Model Held Rigidly

FIG:68

RESULTS ON THE ENERGY LEVEL VARIATION

(Refer to Fig. 5k for definition sketch)

$$\frac{f(\lambda)}{\sigma_c^2} \times 10^3$$

Decay of Enzyme Activity  
at  $\lambda = 4.5 \times 10^3$  in the  
Slotted Bottle

Legend

•  $\frac{\lambda}{\sigma_c} = 2.53$

△  $\frac{\lambda}{\sigma_c} = 2.09$

x  $\frac{\lambda}{\sigma_c} = 2.05$

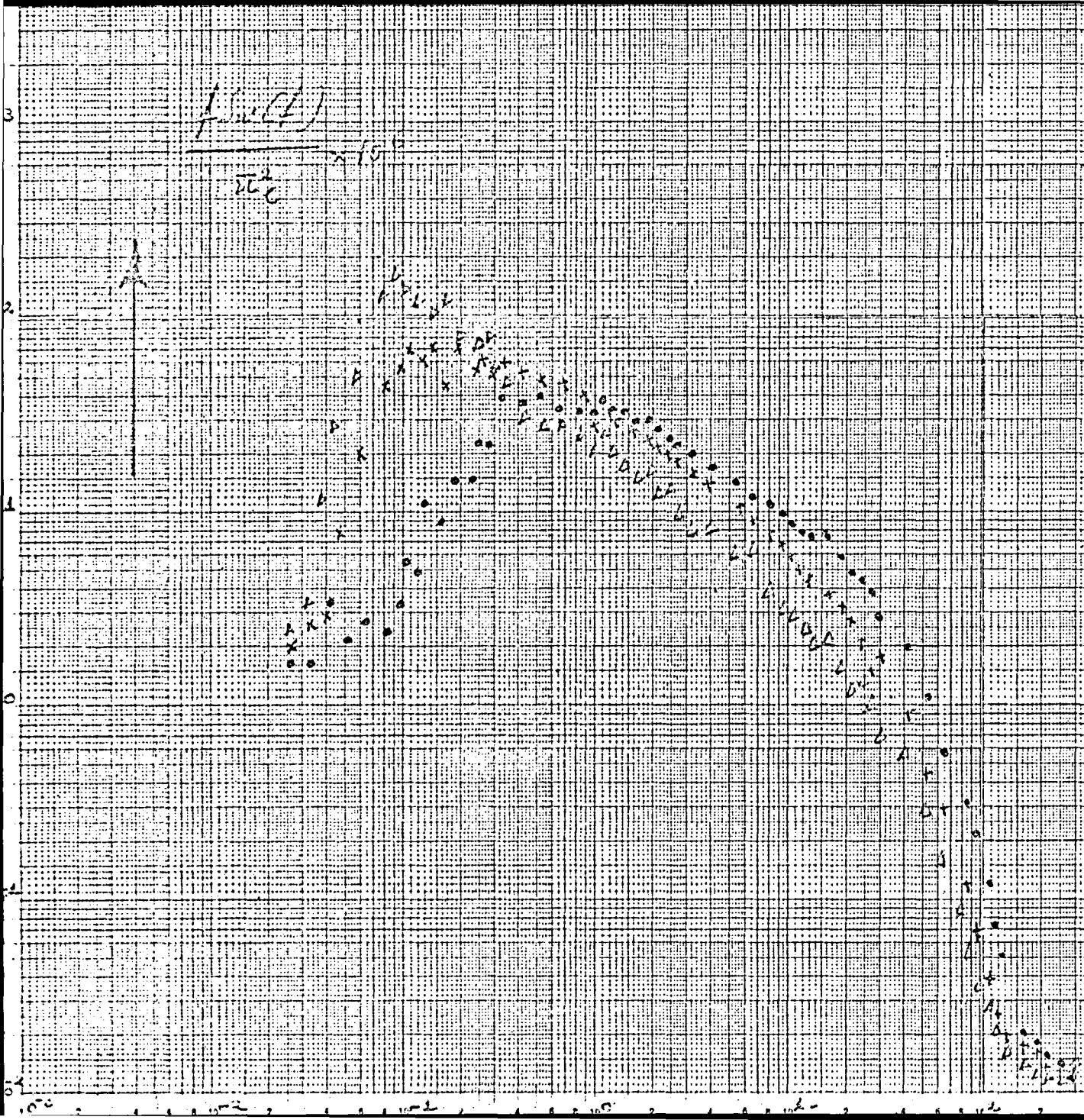
Empty Tissue

Temperature 21°

$\frac{\lambda}{\sigma_c} = 2.0$

F1-69

$\frac{\lambda}{\sigma_c} = 2.0$



# Variation of Integral Scale of Turbulence in the Longitudinal Direction

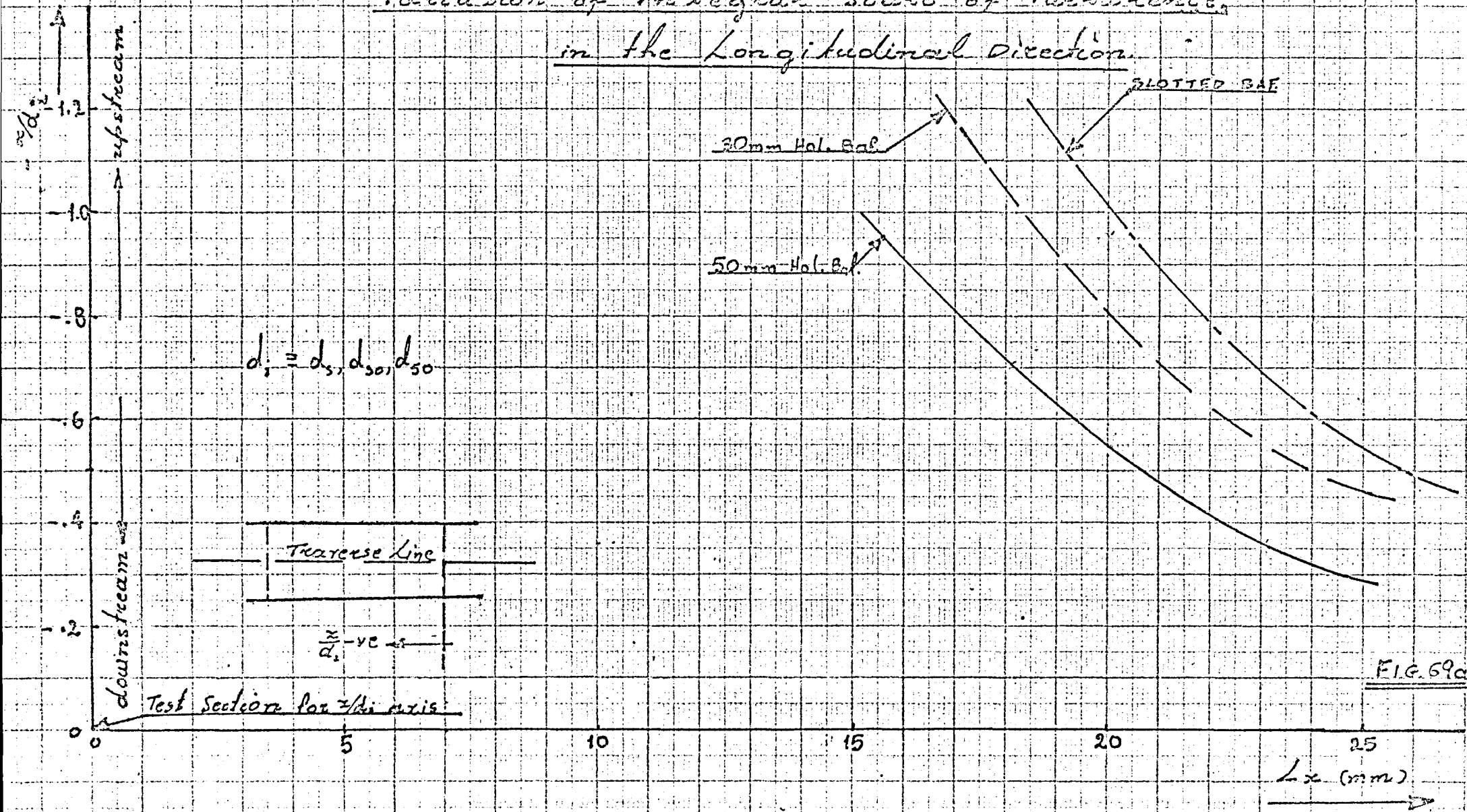
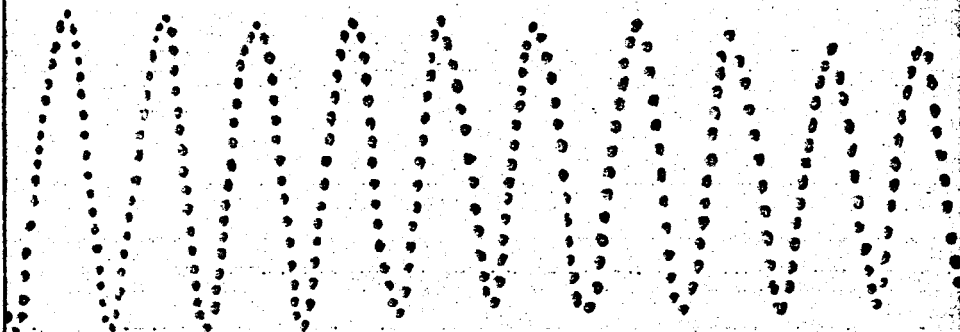


FIG. 69a

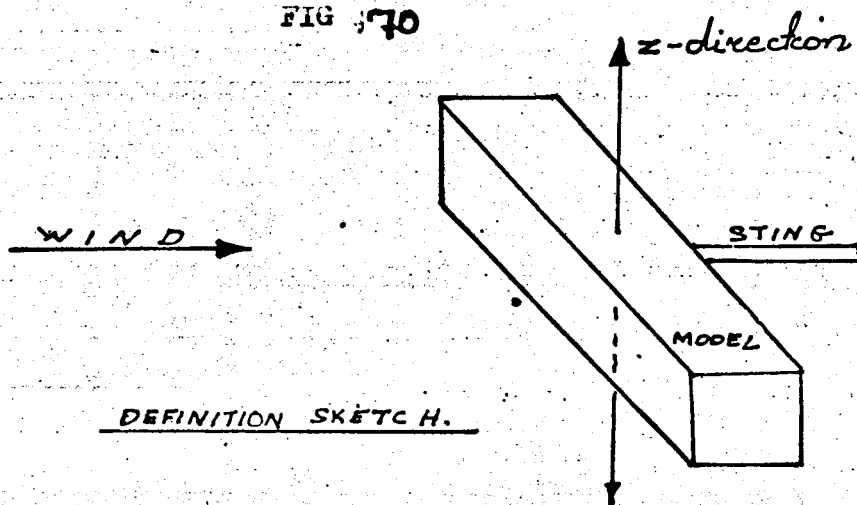
Paper speed = 400mm/s  
timer at 0.1 s.

Natural frequency of  
vibration = 52.2 cycles/s



Vibrations in the z-direction  
Square Section Cylinder  $ARR = 2$

FIG 70



Wavenumber Variation

Stagnation Line Flow

Slotted Baffle

40 mm Dia. Disc

Legend

- o  $f = 2\% \alpha$
- $\Delta$   $f = 2.5\% \alpha$
- o  $f = 3\% \alpha$
- $\square$   $f = 4\% \alpha$
- o  $f = 5\% \alpha$
- $\square$   $f = 6\% \alpha$
- o  $f = 7\% \alpha$
- $\Delta$   $f = 8\% \alpha$
- x  $f = 9\% \alpha$

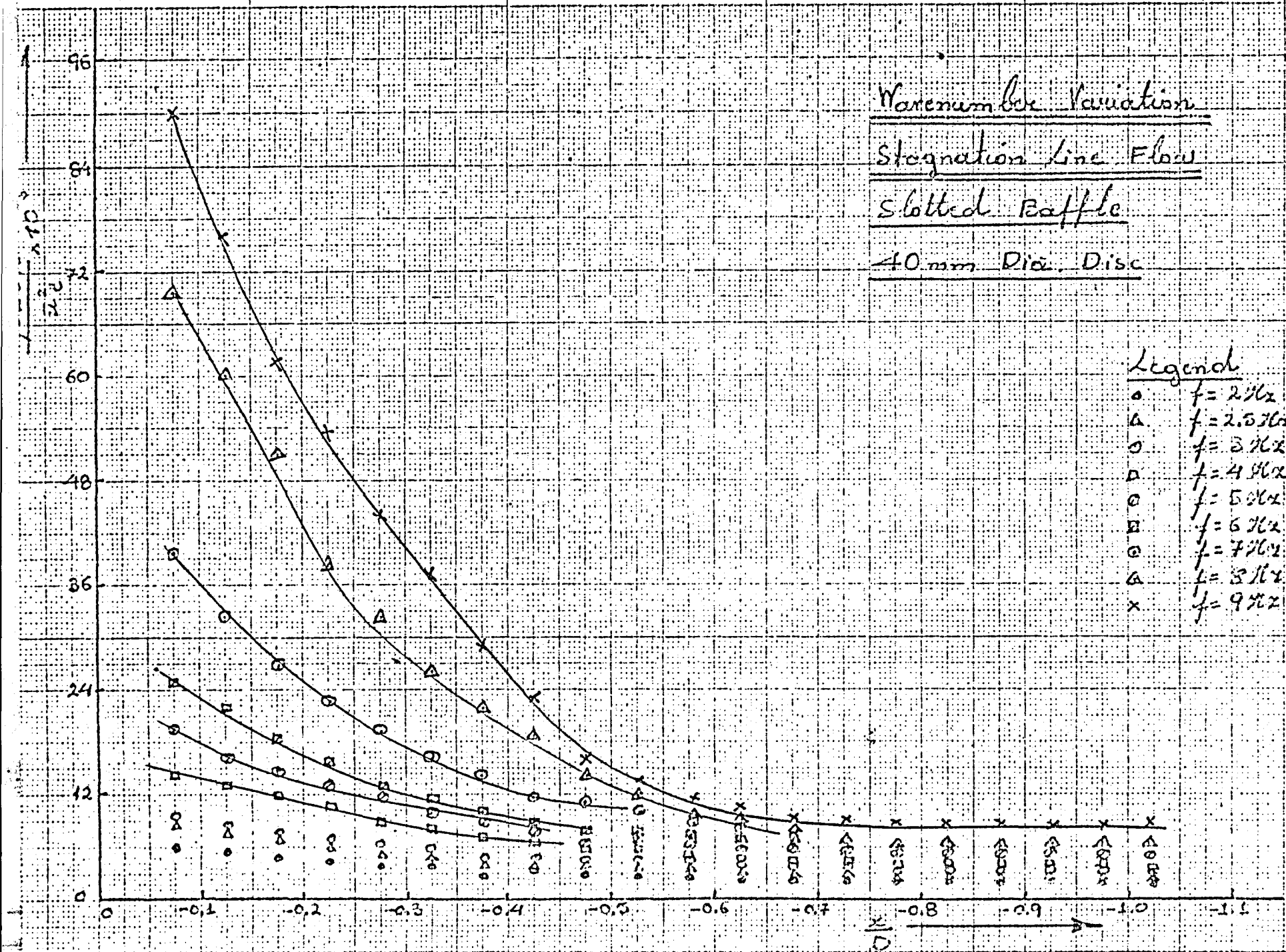


FIG: 71



Warcum number Variation

Stagnation Line Flow

Slotted Raffle

40mm Dia. Disc.

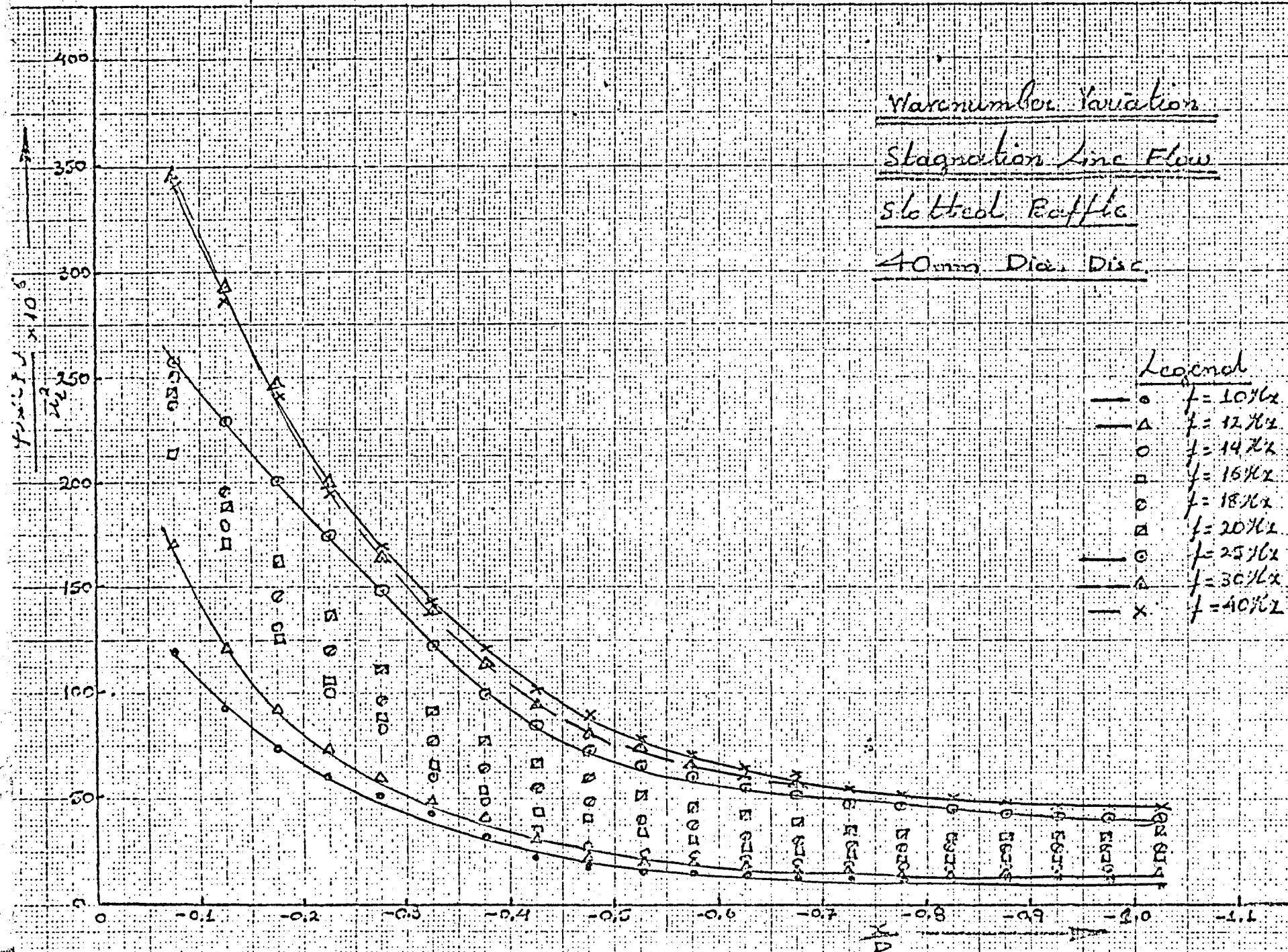


FIG: 72

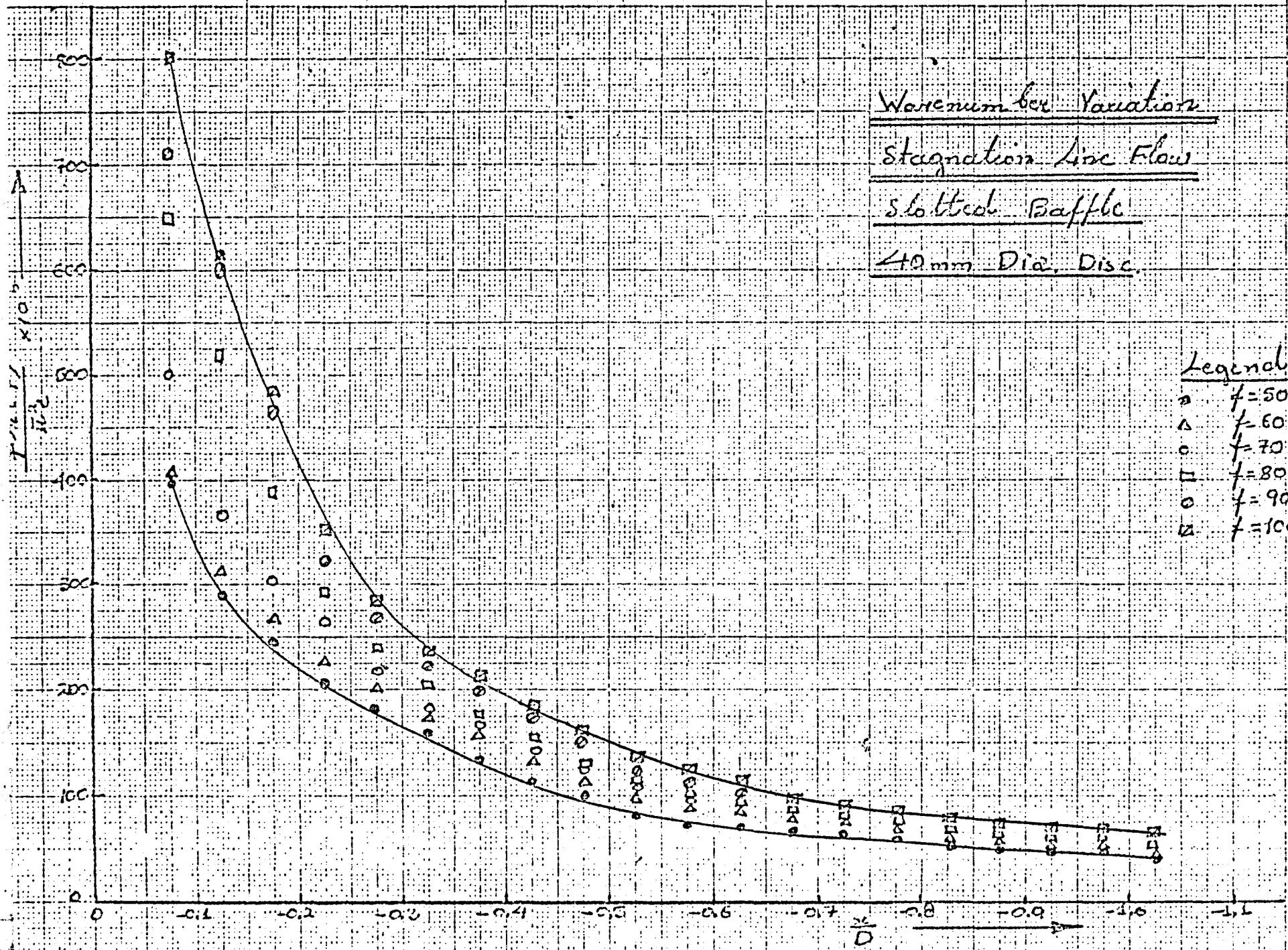


FIG: 73



# Wave number Variation

Flow at  $z=0\text{ mm}$ ,  $y=+10\text{ mm}$

Slotted Baffle

40 mm Dia. Disc

## Legend

- $\circ$   $f = 2\% \lambda$
- $\Delta$   $f = 2.5\% \lambda$
- $\square$   $f = 3\% \lambda$
- $\square$   $f = 4\% \lambda$
- $\circ$   $f = 5\% \lambda$
- $\square$   $f = 6\% \lambda$
- $\circ$   $f = 7\% \lambda$
- $\Delta$   $f = 8\% \lambda$
- $\times$   $f = 9\% \lambda$

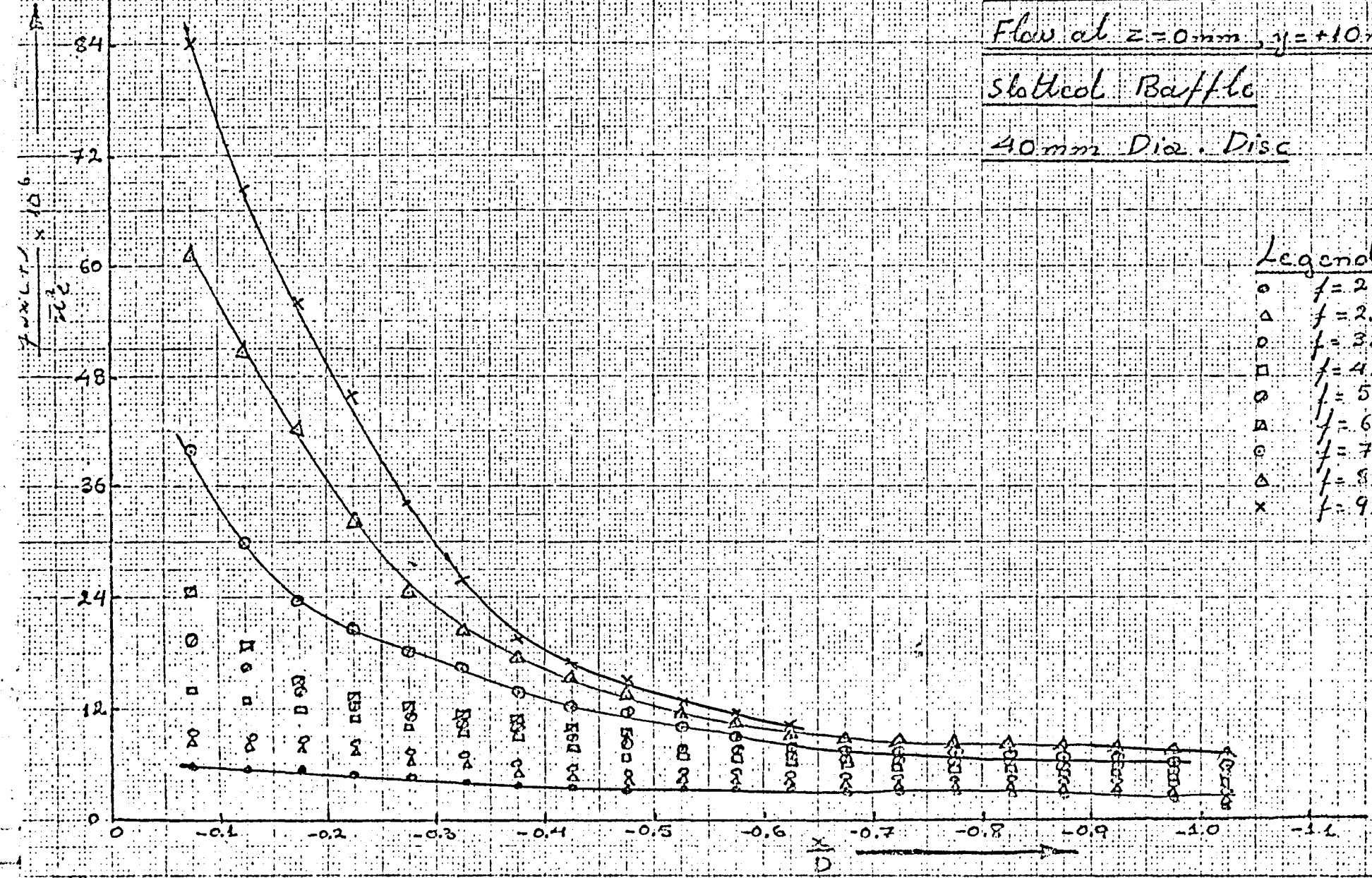


FIG: 74

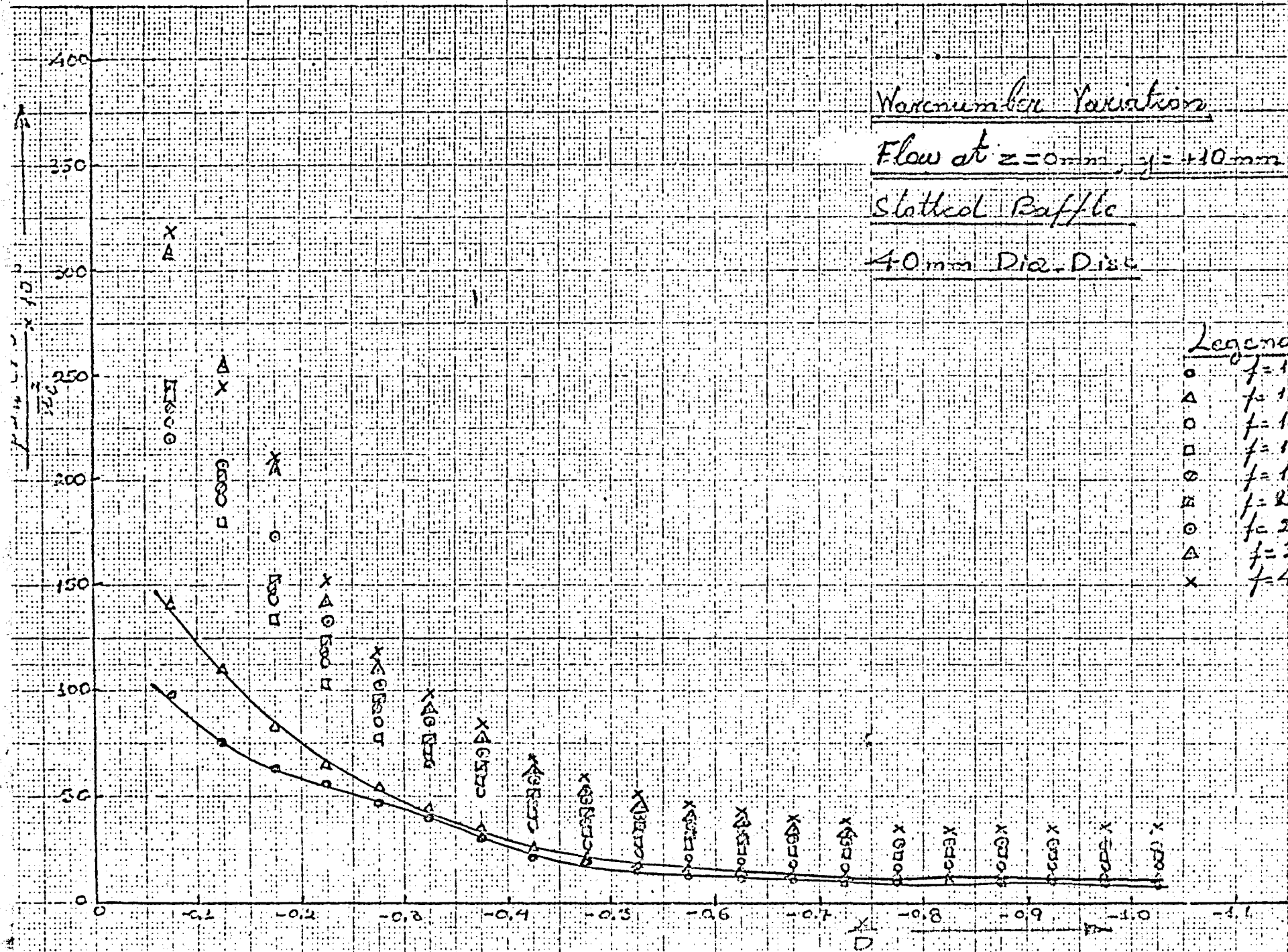


FIG:75

Wavenumber Variation

Flow at  $z=0\text{ mm}$ ,  $y=+10\text{ mm}$

Slotted Baffle

40 mm Dia. Disc.

Legend

- $\circ$   $f = 50\text{ Hz}$
- $\Delta$   $f = 60\text{ Hz}$
- $\circ$   $f = 70\text{ Hz}$
- $\square$   $f = 80\text{ Hz}$
- $\circ$   $f = 90\text{ Hz}$
- $\square$   $f = 100\text{ Hz}$

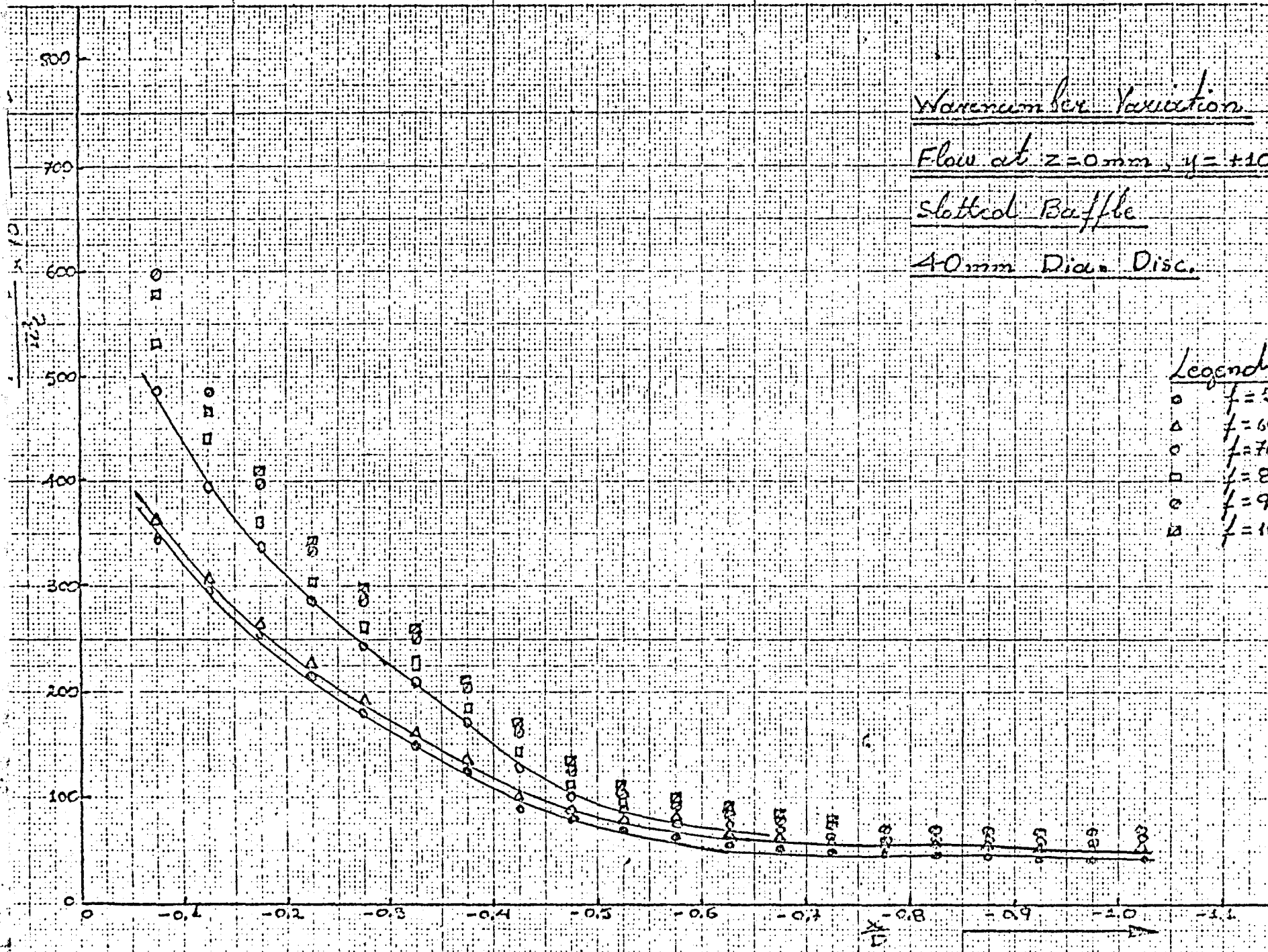


FIG: 76

# Wavenumber Variation

Flow at  $z=0\text{ mm}$ ,  $y=+20\text{ mm}$

Slotted Baffle

40 mm Dia. Disc.

Legend

- $\circ$   $f=2\%x$
- $\Delta$   $f=2.5\%x$
- $\circ$   $f=3\%x$
- $\square$   $f=4\%x$
- $\circ$   $f=5\%x$
- $\square$   $f=6\%x$
- $\circ$   $f=7\%x$
- $\Delta$   $f=8\%x$
- $\times$   $f=9\%x$

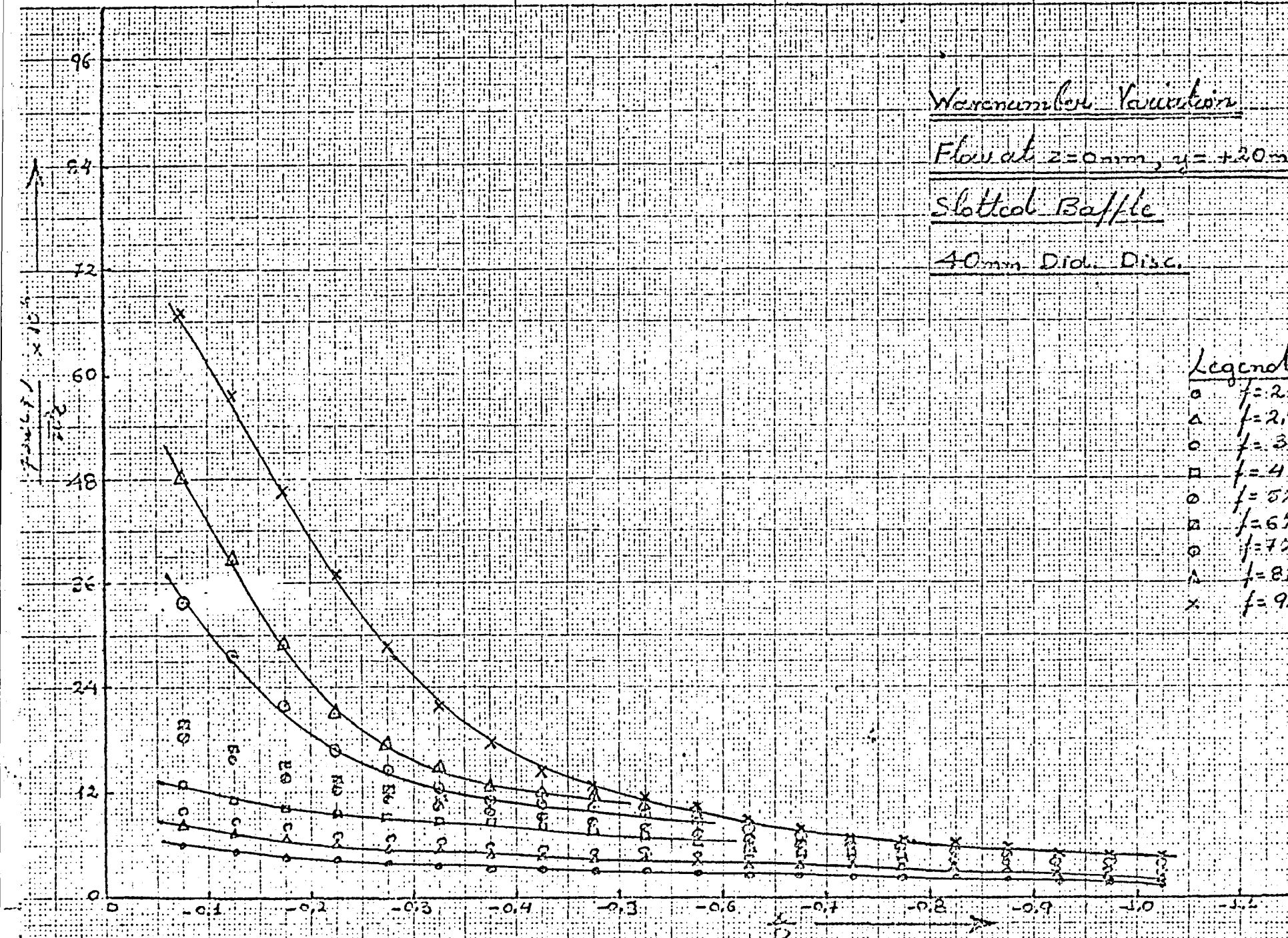


FIG: 77



Reynolds Number Variation

Flow at  $z=0\text{ mm}$ ,  $y=+20\text{ mm}$

Slot Hole Baffle

40mm Dia. Disc

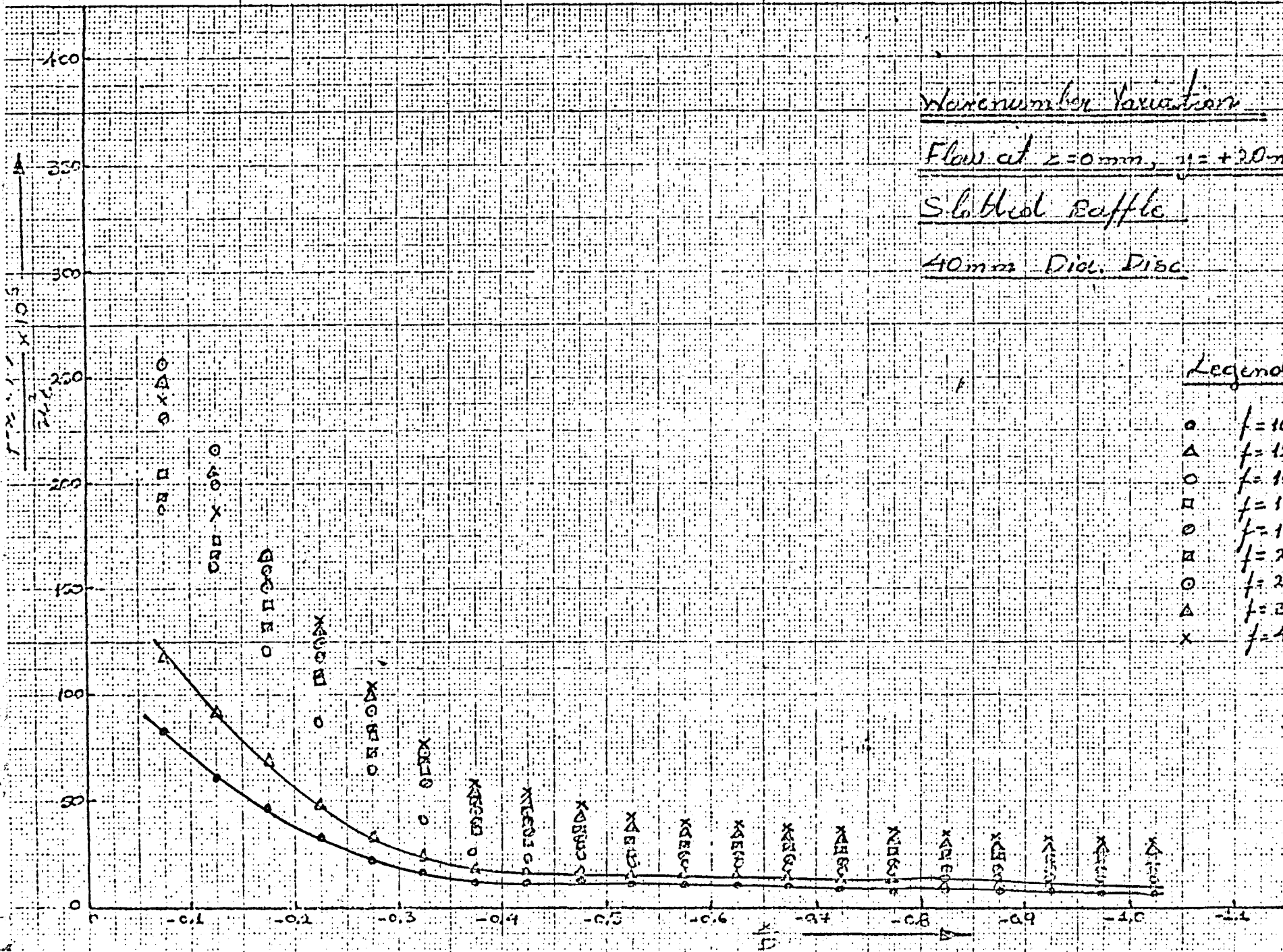


FIG: 78

# Wavenumber Variation

Flow at  $z = 0 \text{ mm}$ ,  $y = \pm 20 \text{ mm}$

Slotted Baffle

40mm Dia. Disc

## Legend

- $f = 50\% \lambda$
- △  $f = 60\% \lambda$
- $f = 70\% \lambda$
- $f = 80\% \lambda$
- ◇  $f = 90\% \lambda$
- ⊠  $f = 100\% \lambda$

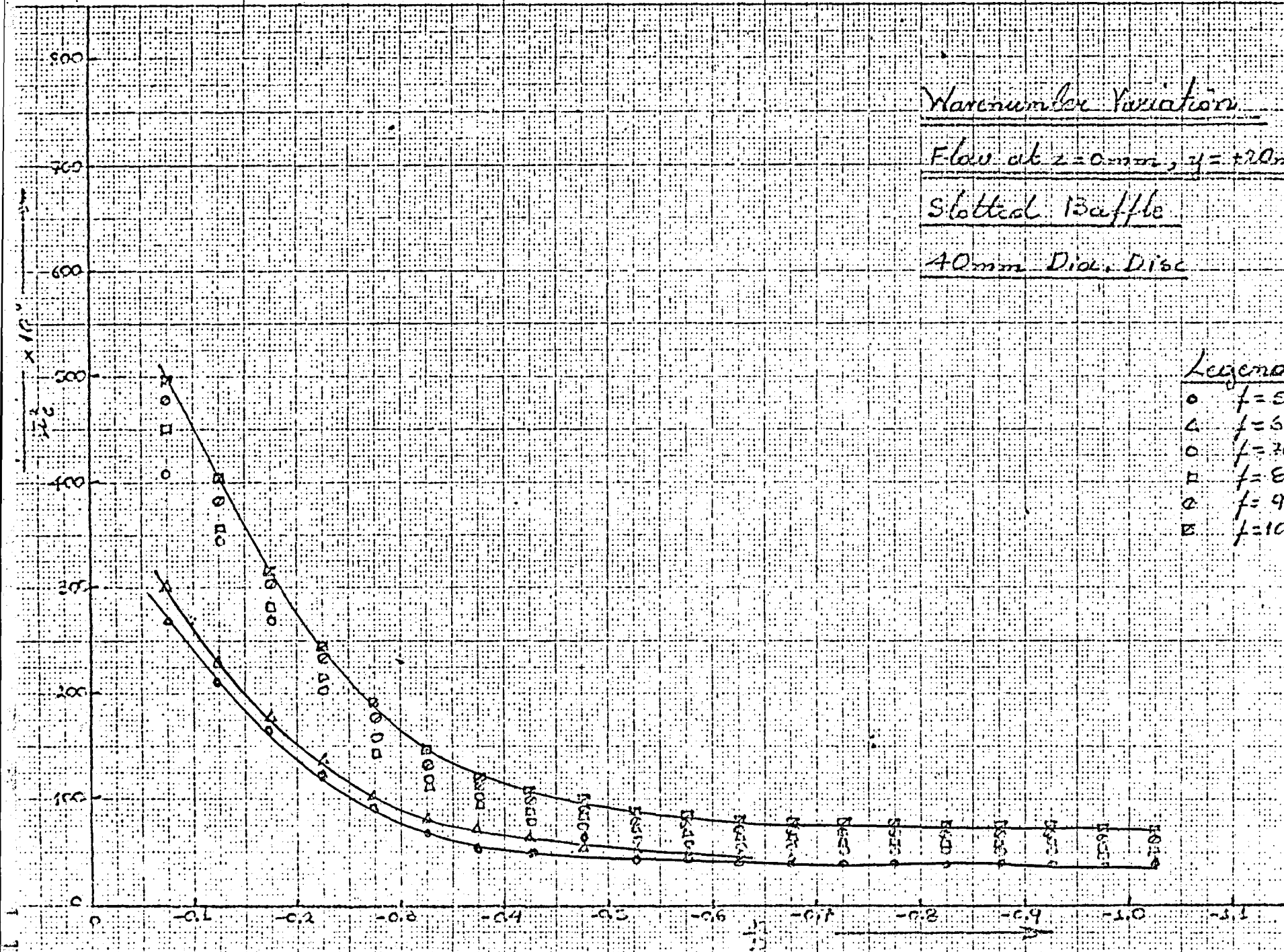


FIG: 29

Wavenumber Variation

Flow at  $z=0\text{mm}$ ,  $y=\pm 20\text{mm}$

Slotted Baffle

40mm Diam. Disc

Legend

- o  $f = 2\% \lambda$
- $\Delta$   $f = 2.5\% \lambda$
- o  $f = 3\% \lambda$
- $\square$   $f = 4\% \lambda$
- o  $f = 5\% \lambda$
- $\square$   $f = 6\% \lambda$
- o  $f = 7\% \lambda$
- $\Delta$   $f = 8\% \lambda$
- x  $f = 9\% \lambda$

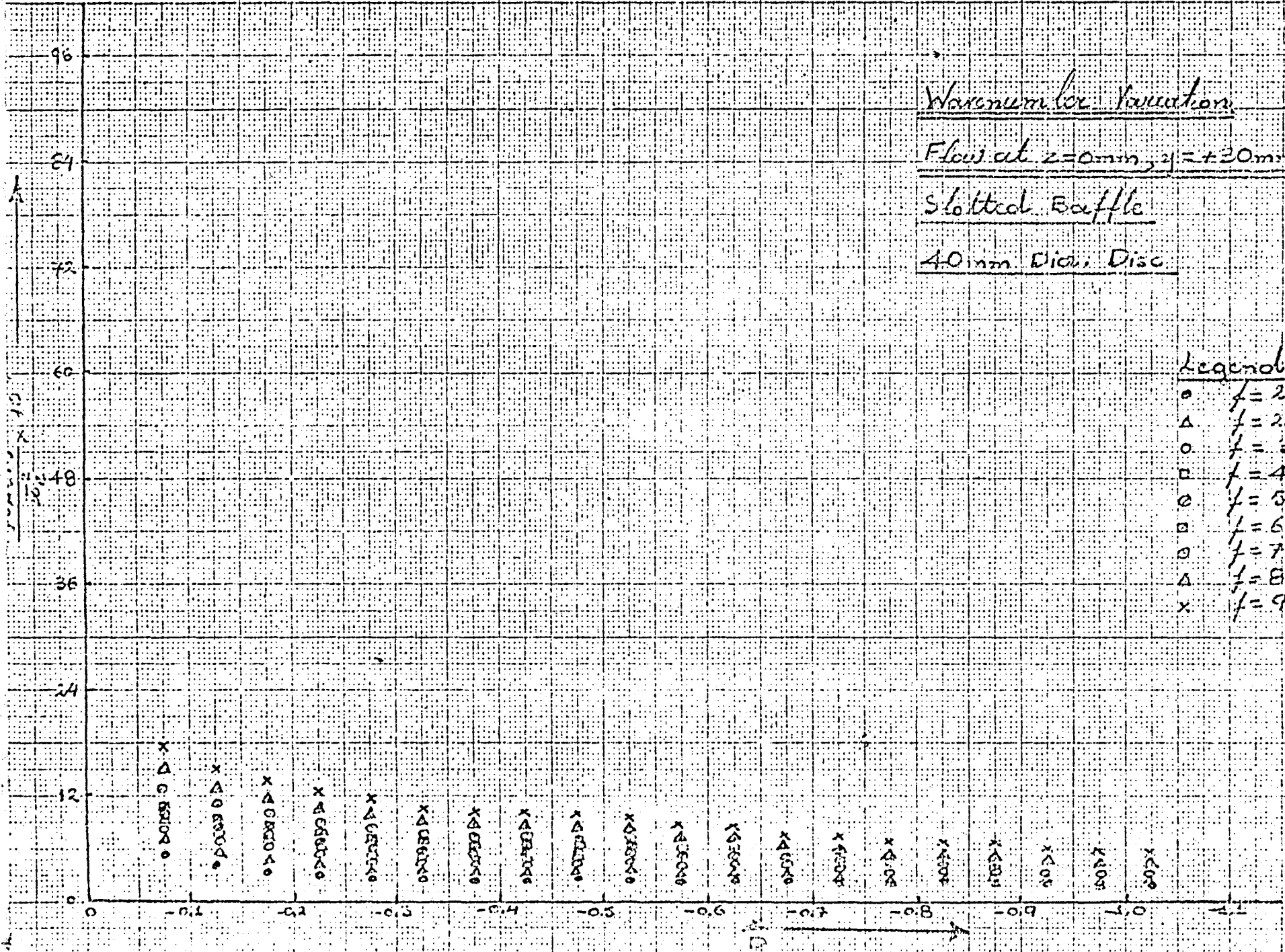


FIG: 80

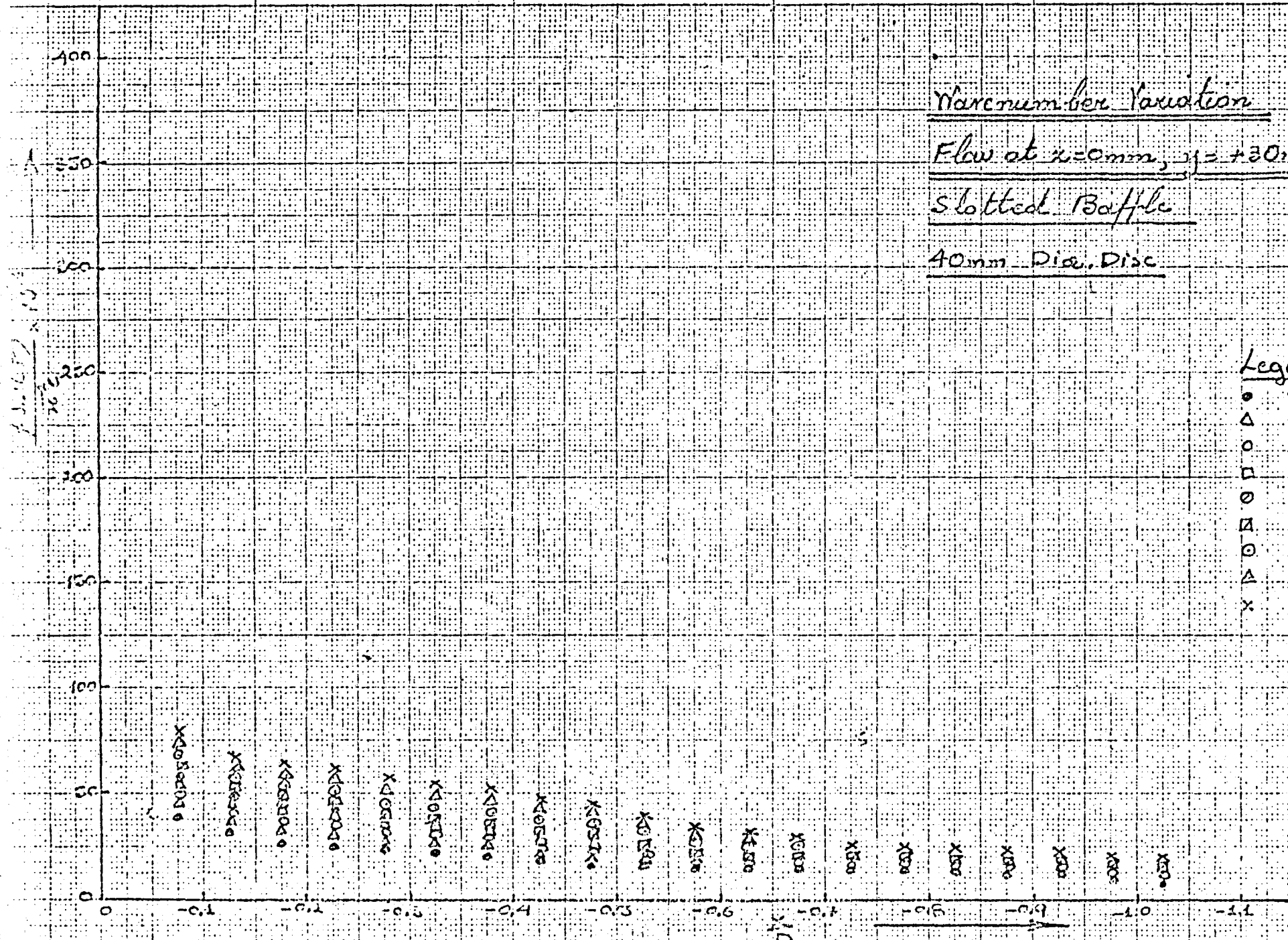


FIG. 8



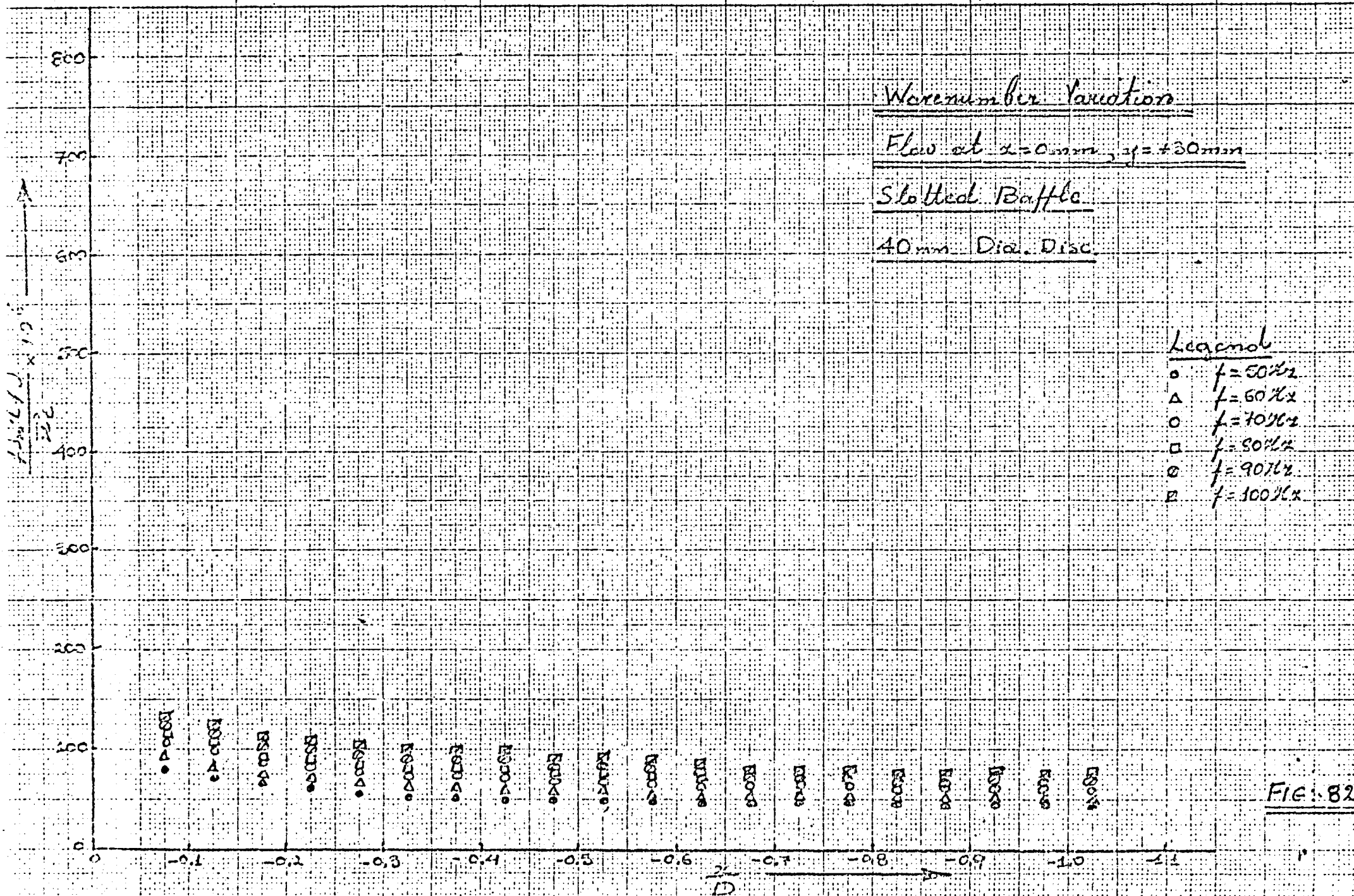


FIG. 82

Turbulence Level Variations  
in Front of the 40mm Dia. Disc  
Slotted Baffle

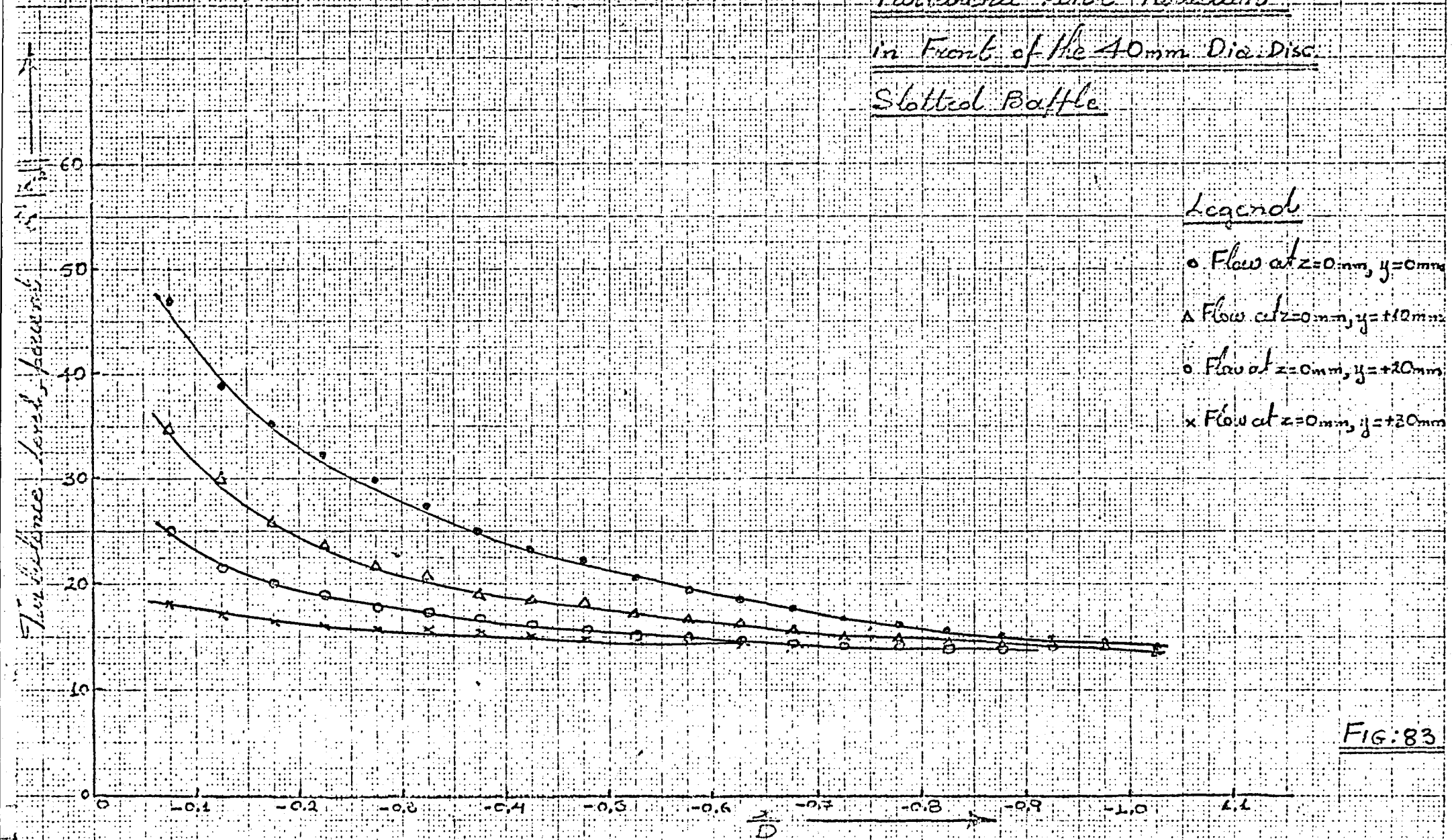


FIG:83

Wavenumber Variation

Stagnation Line Flow

Slotted Baffle

Circular Cylinder  $AR=2$

Legend

- $f = 2\% \alpha$
- △  $f = 2.5\% \alpha$
- $f = 3\% \alpha$
- $f = 4\% \alpha$
- $f = 5\% \alpha$
- ×  $f = 6\% \alpha$
- $f = 7\% \alpha$
- △  $f = 8\% \alpha$
- ×  $f = 9\% \alpha$

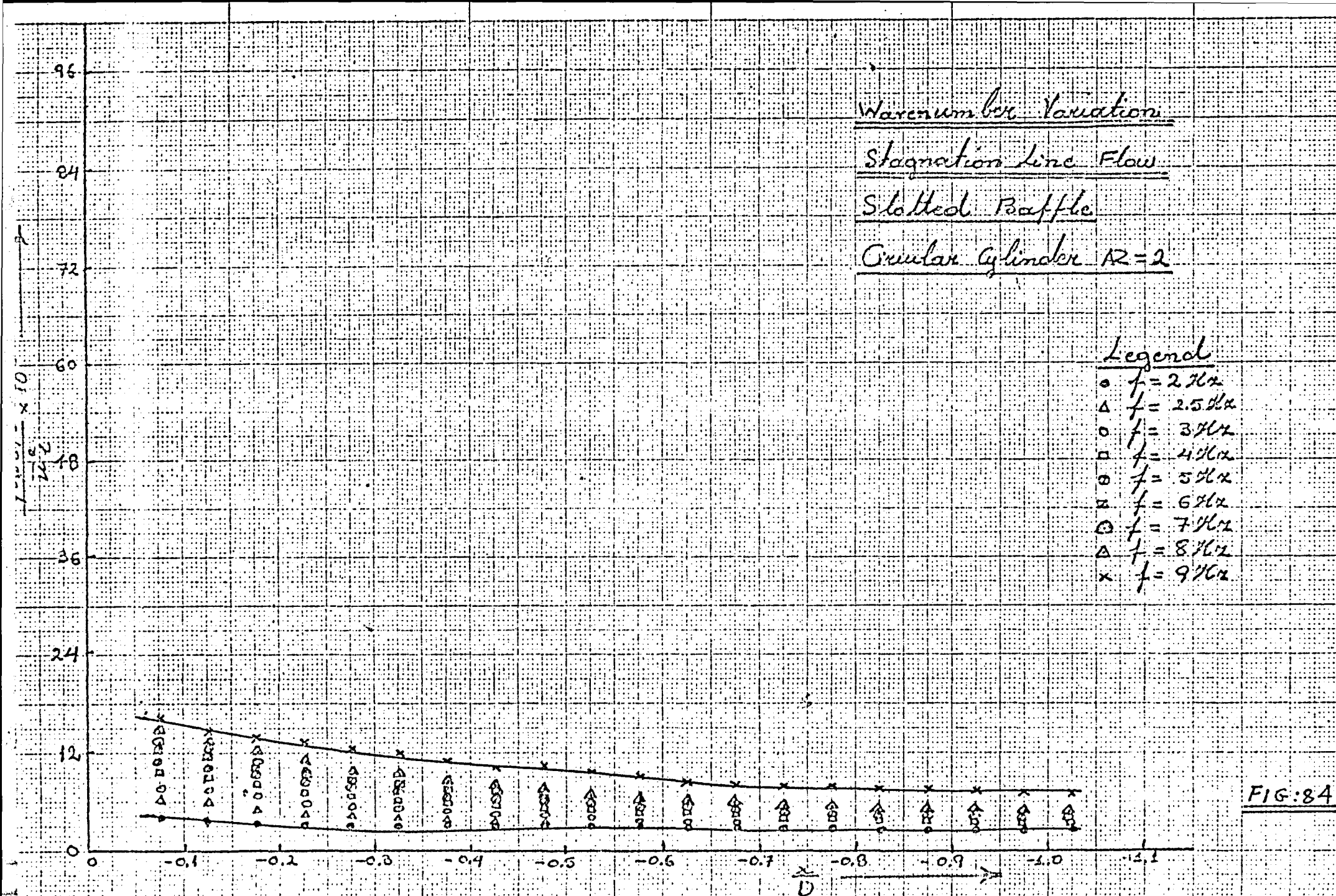


FIG:84

Wave number Variation

Stagnation Line Flow

Slotted Baffle

Circular Cylinder  $R=2$

Legend

- $f = 10\% \alpha$
- △  $f = 12\% \alpha$
- $f = 14\% \alpha$
- $f = 16\% \alpha$
- $f = 18\% \alpha$
- ◻  $f = 20\% \alpha$
- $f = 25\% \alpha$
- △  $f = 30\% \alpha$
- x  $f = 40\% \alpha$

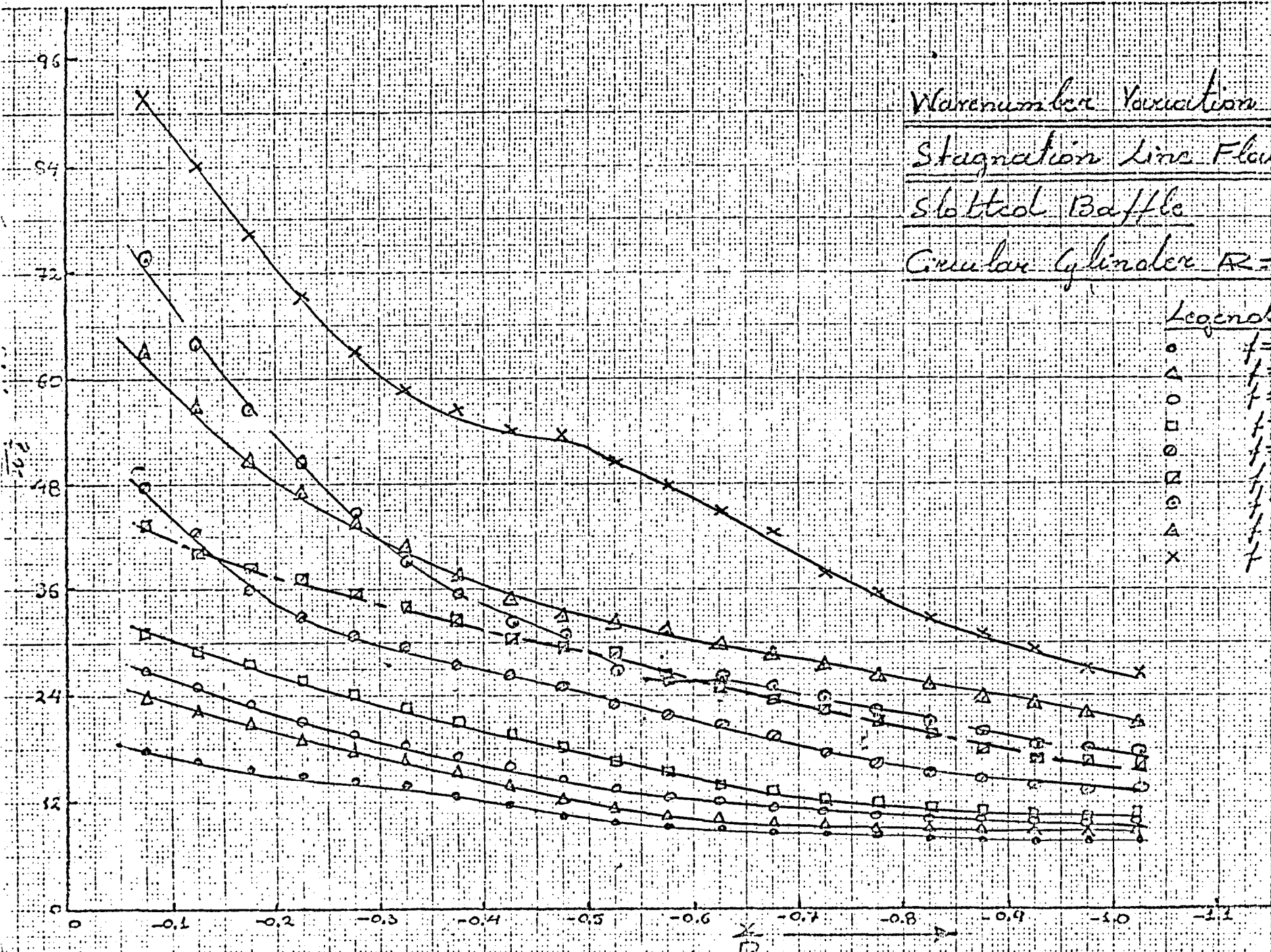


FIG:85



Wave number Variation  
Stagnation Line Flow  
Slotted Baffle  
Circular Cylinder  $AR=2$

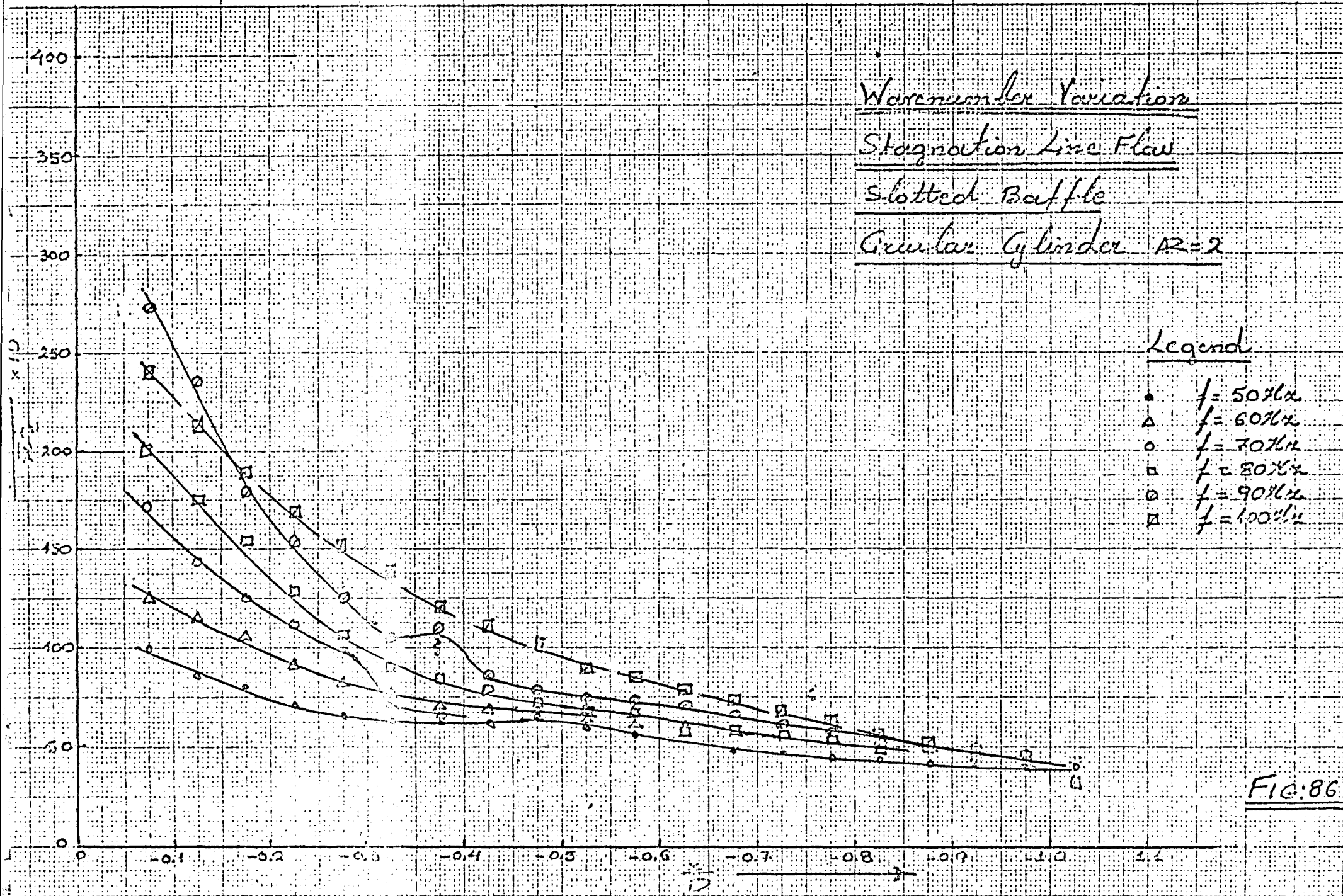


FIG. 86

# Wave number Variation

Flow at  $z=0$  m  $y=\pm 15$  mm

Slotted Baffle

Circular Cylinder  $R=2$

## Legend

- $f=2\%$
- △  $f=2.5\%$
- $f=3\%$
- $f=4\%$
- $f=5\%$
- $f=6\%$
- $f=7\%$
- △  $f=8\%$
- x  $f=9\%$

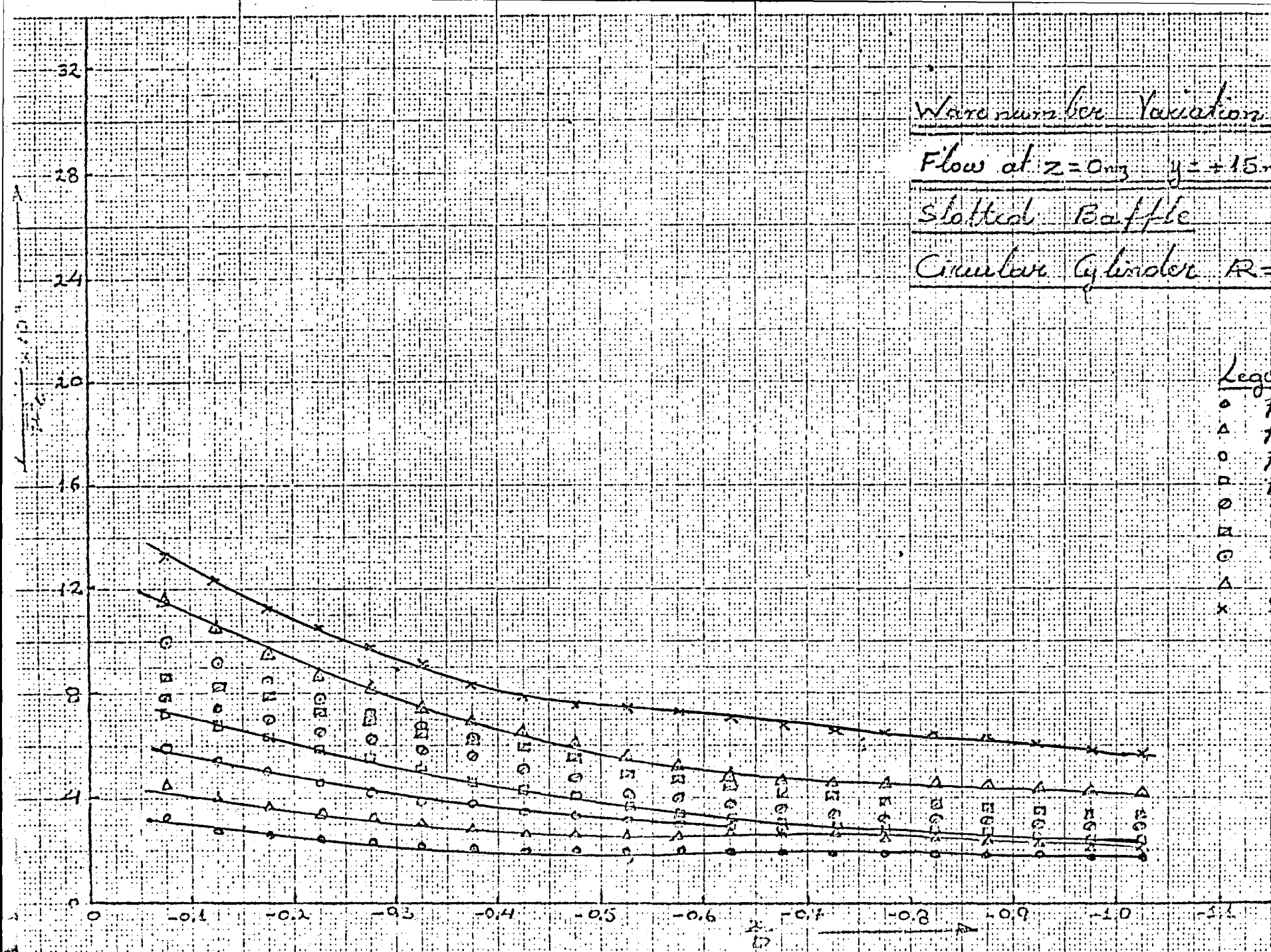


FIG: 87

Wavenumber Variation

Flow at  $z=0$  mm,  $y=+15$  mm

Slotted Raffle

Circular Cylinder  $R=2$

Legend

- $f=10\pi/\lambda$
- $\Delta$   $f=12\pi/\lambda$
- $f=14\pi/\lambda$
- $f=16\pi/\lambda$
- ◊  $f=18\pi/\lambda$
- ◻  $f=20\pi/\lambda$
- ⊙  $f=25\pi/\lambda$
- $\triangle$   $f=30\pi/\lambda$
- x  $f=40\pi/\lambda$

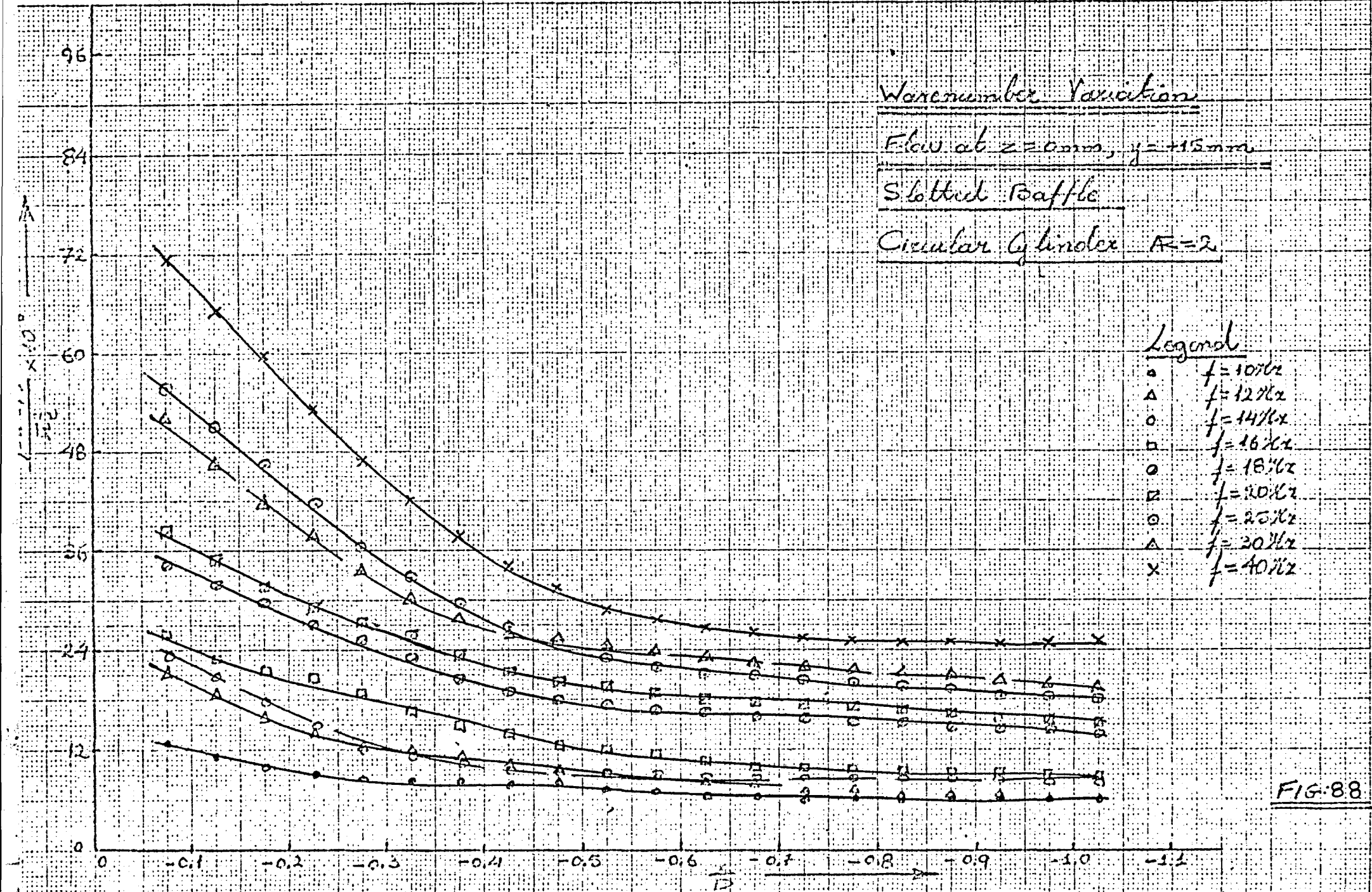


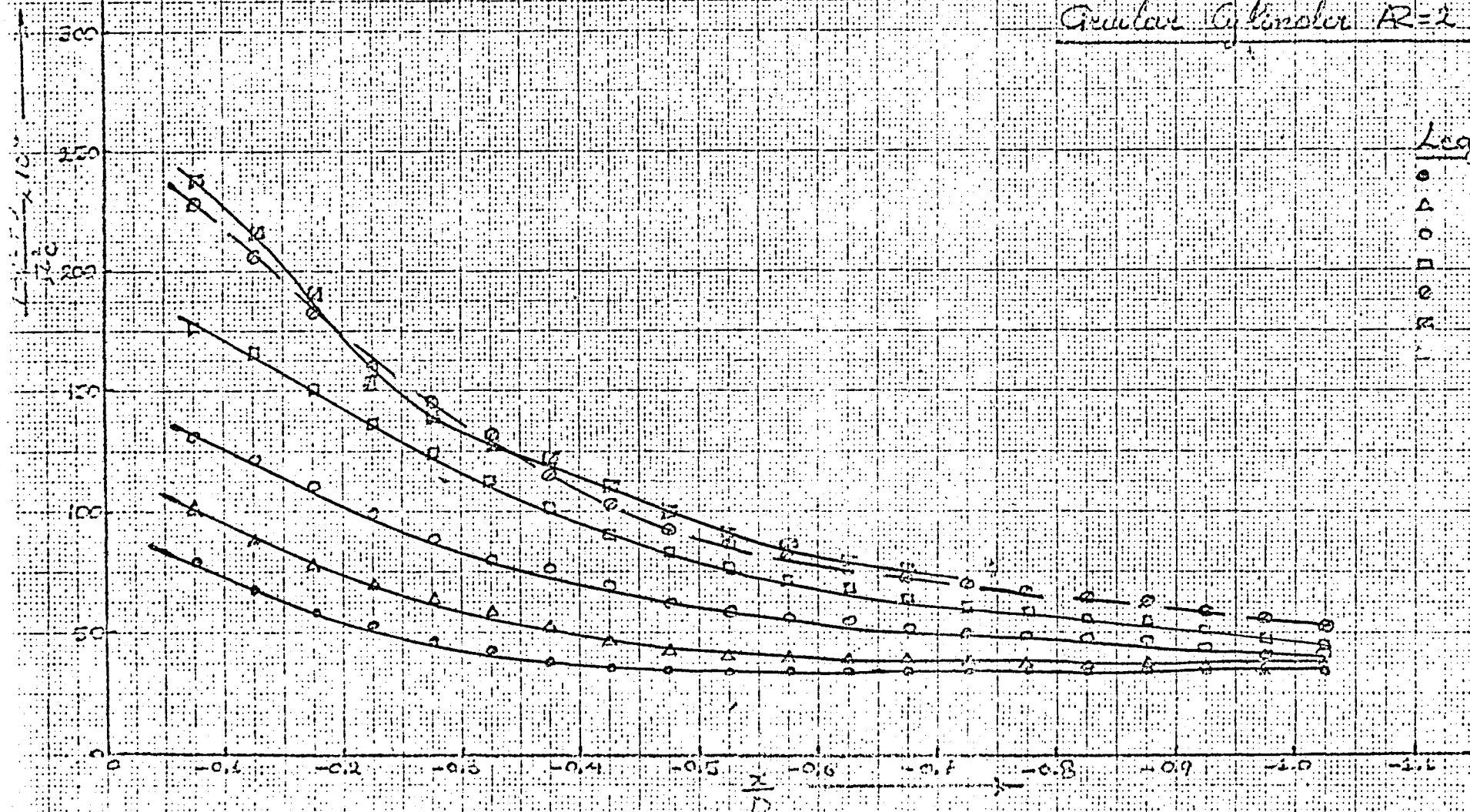
FIG:88

# Wave number Variation

Flow at  $z = 0$  mm,  $y = +15$  mm

Slotted Baffle

Circular Cylinder  $R=2$



## Legend

- $f = 50\%z$
- $f = 60\%z$
- $f = 70\%z$
- $f = 80\%z$
- $f = 90\%z$
- $f = 100\%z$

FIG: 89



# Wave number Variation

Flow at  $z=0$  mm,  $y=+30$  mm

Slotted Raffle

Circular Cylinder  $R=2$

## Legend

- $f=2\%2$
- $\Delta$   $f=2.5\%2$
- $f=3\%2$
- $f=4\%2$
- ⊙  $f=5\%2$
- ⊞  $f=6\%2$
- ⊕  $f=7\%2$
- $\Delta$   $f=8\%2$
- x  $f=9\%2$

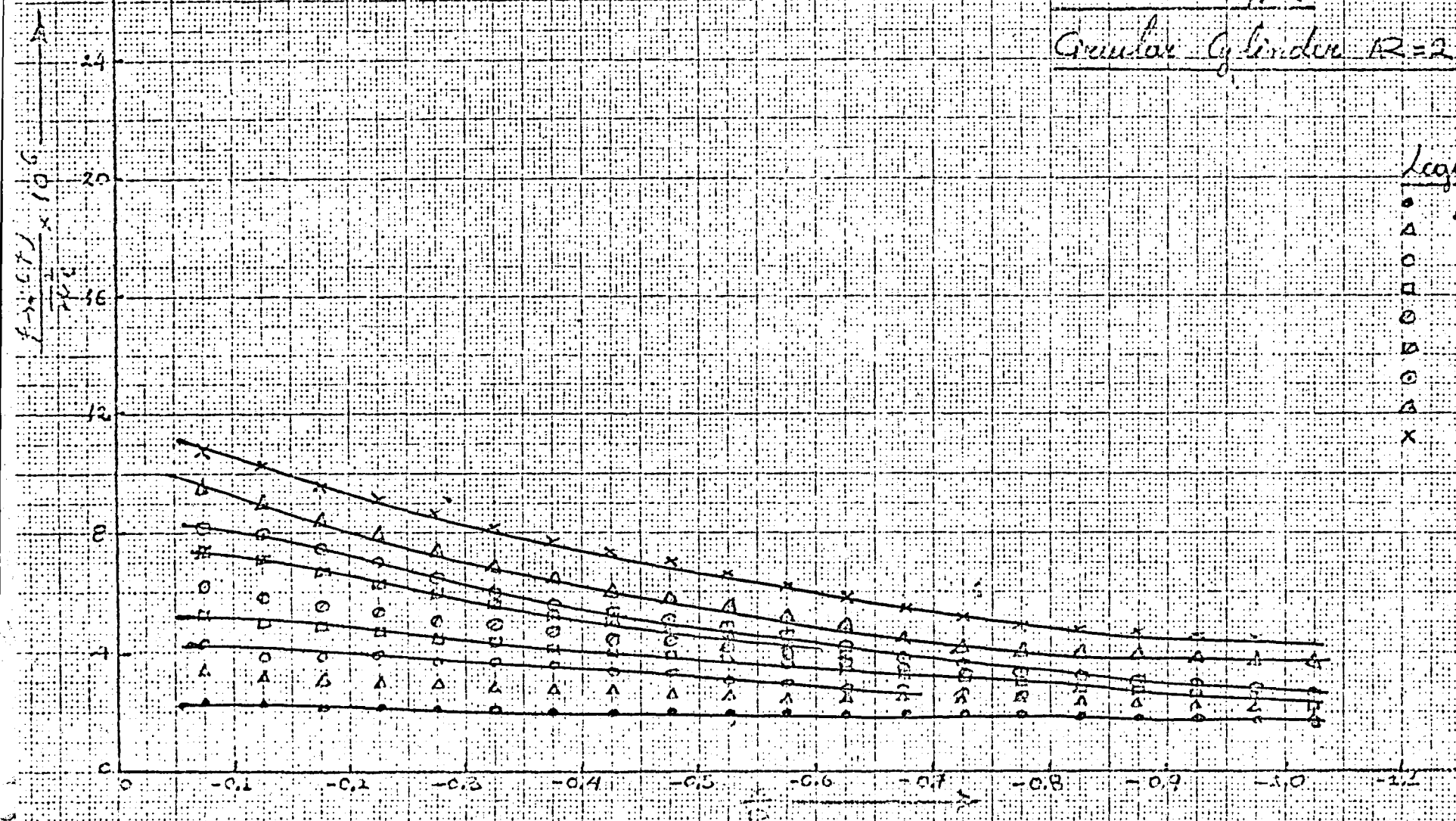


FIG. 90

# Wave number variation

Flow at  $x=0$  mm,  $y=+20$  mm

Slotted Baffle

Circular Cylinder  $R=2$

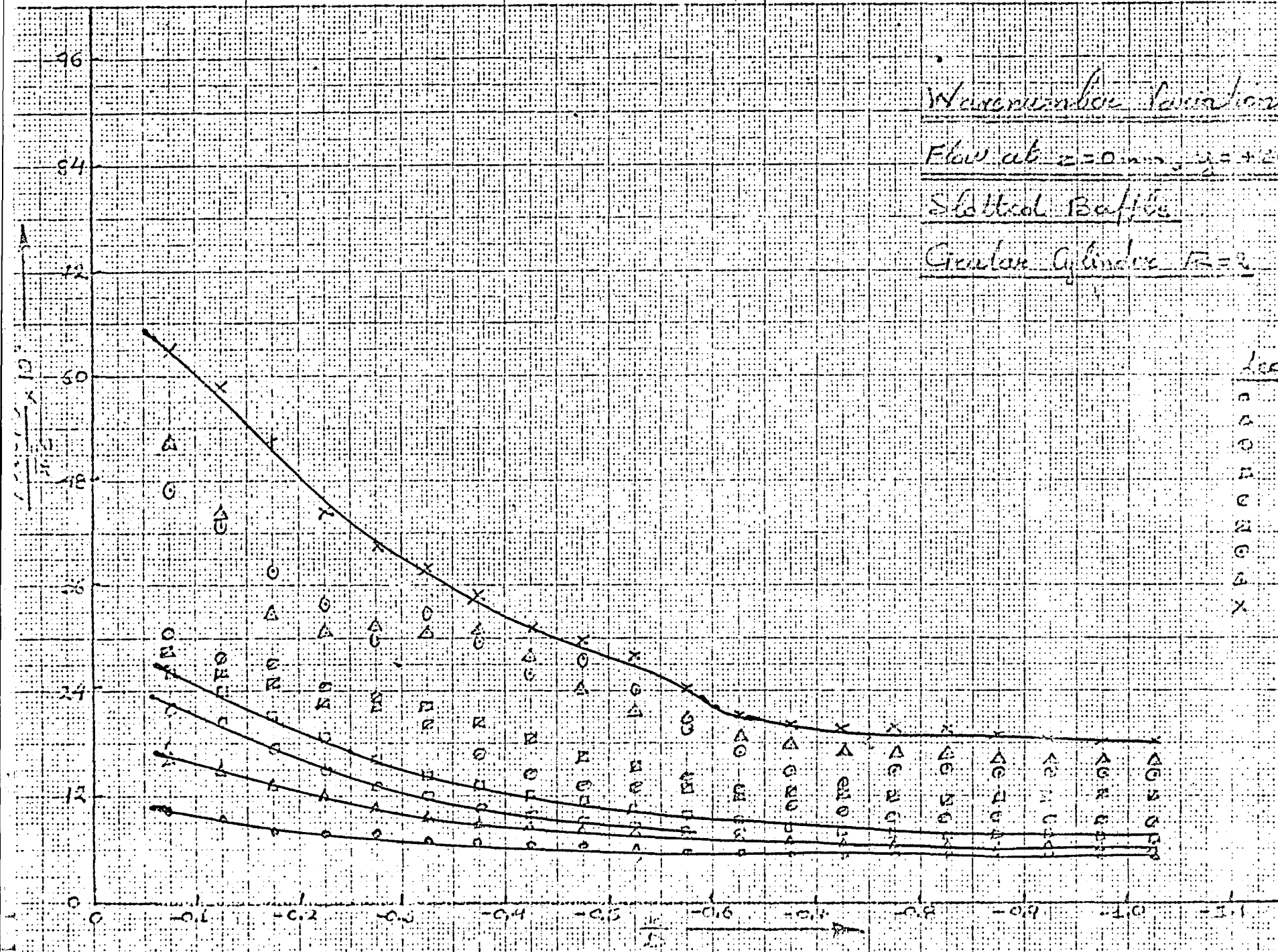


FIG. 91

Wave number Variation

Flow at  $z=0\text{ mm}$ ,  $y=+30\text{ mm}$

Slotted Baffle

Circular Cylinder  $AR=2$

Legend:  
○  $f=50\%$   
△  $f=60\%$   
□  $f=70\%$   
◇  $f=80\%$   
○  $f=90\%$   
□  $f=100\%$

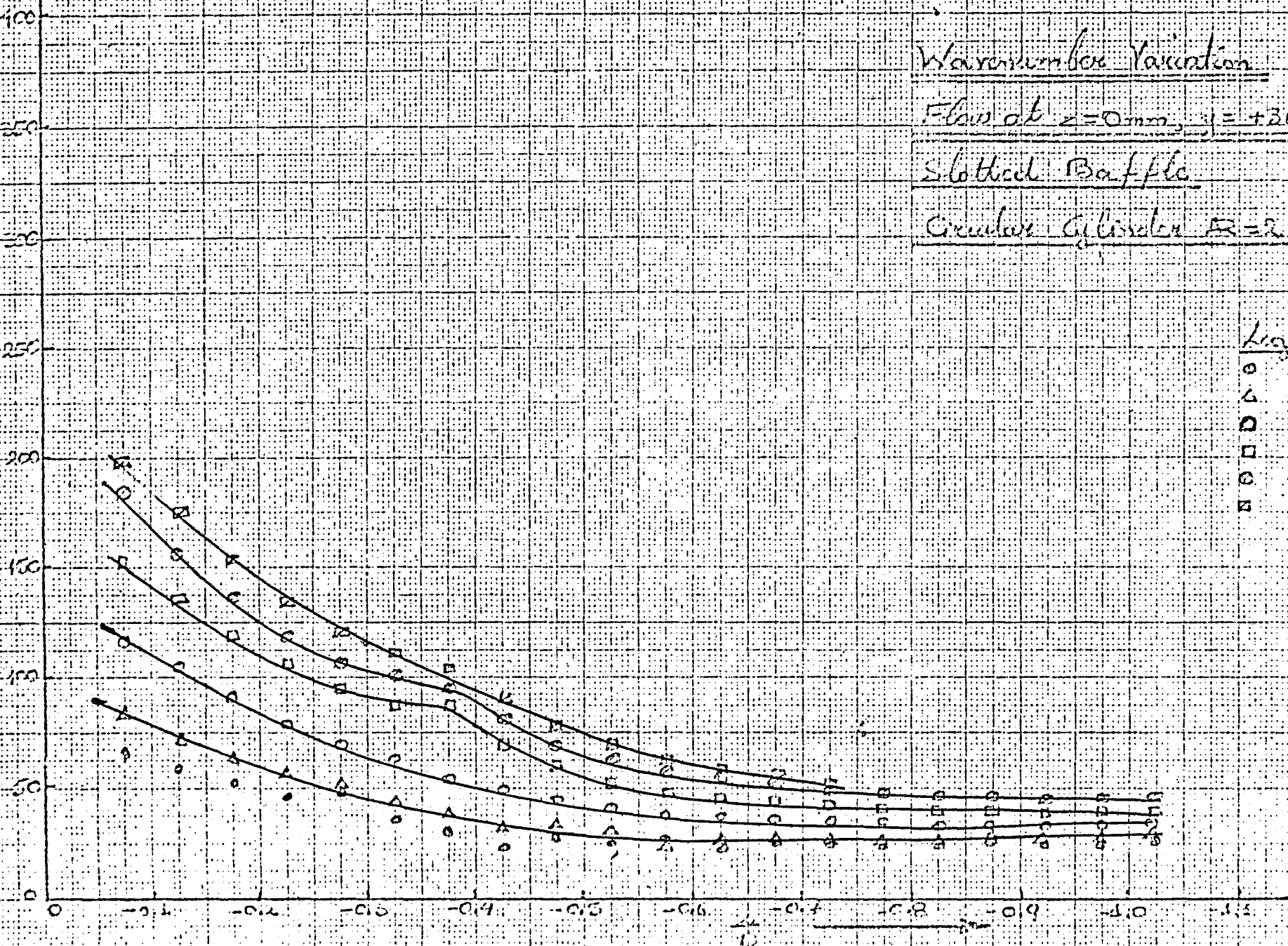


Fig: 92

Wave number Variation

Flow at  $z = 0 \text{ mm}$ ,  $y = \pm 40 \text{ mm}$

Slotted Baffle

Circular Cylinder  $R=2$

Legend

- $\circ$   $f = 2\% \epsilon$
- $\Delta$   $f = 2.5\% \epsilon$
- $\square$   $f = 3\% \epsilon$
- $\square$   $f = 4\% \epsilon$
- $\circ$   $f = 5\% \epsilon$
- $\square$   $f = 6\% \epsilon$
- $\square$   $f = 7\% \epsilon$
- $\Delta$   $f = 8\% \epsilon$
- $\times$   $f = 9\% \epsilon$

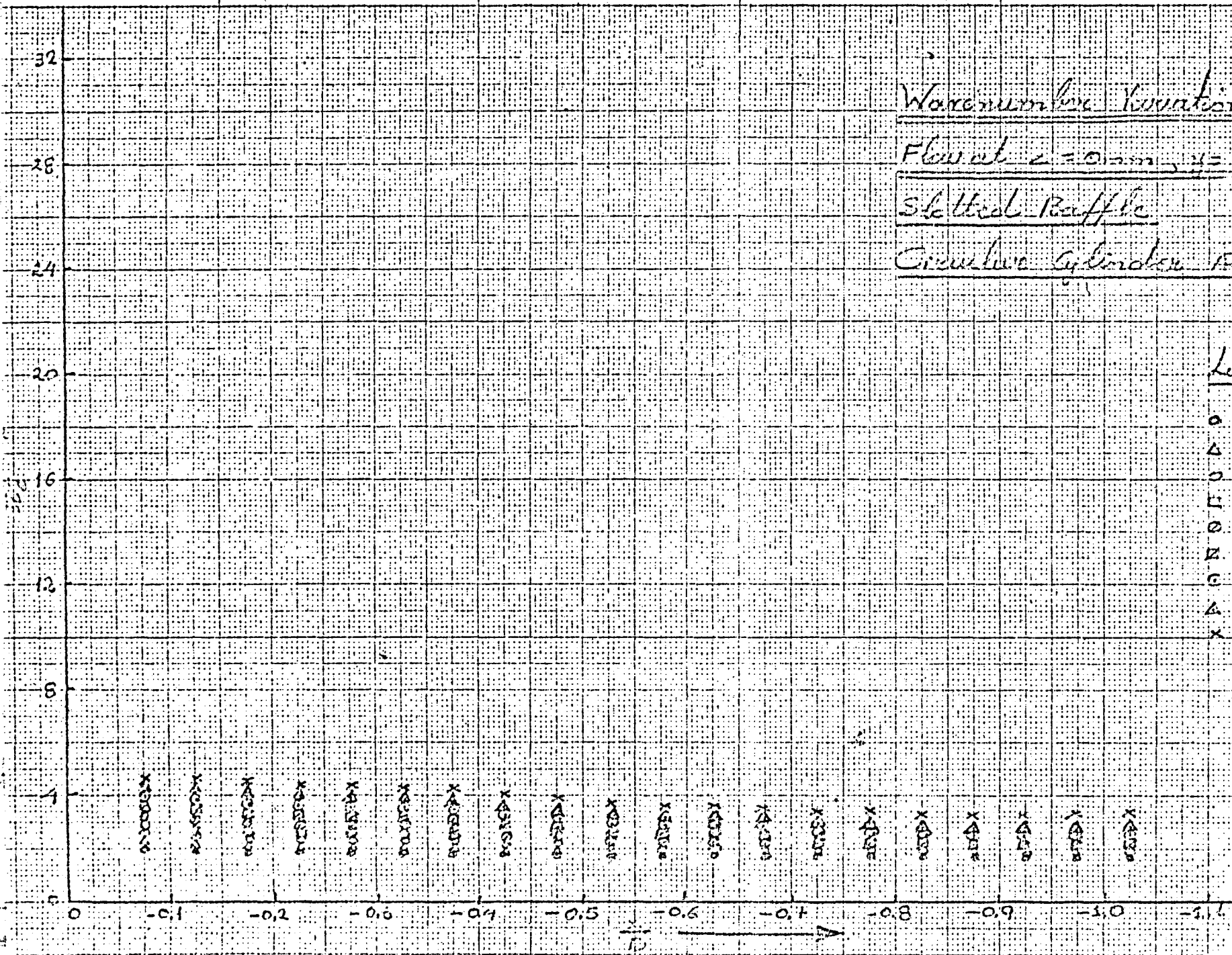
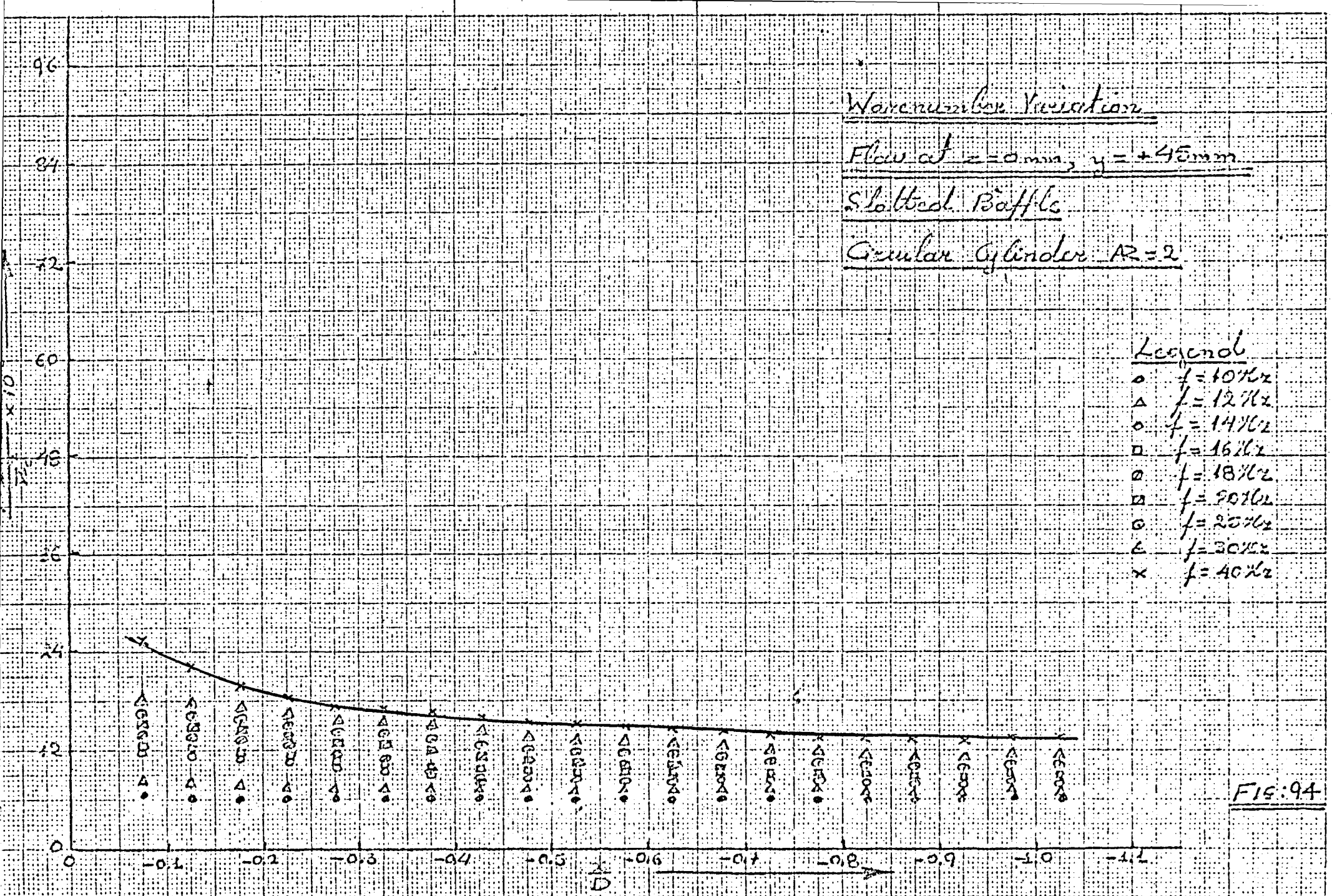


FIG: 93





Wave number Variation

Flow at  $z=0\text{mm}$ ,  $y=+45\text{mm}$

Slotted Baffle

Circular Cylinder  $R=2$

Legend

- $\circ$   $f=50\%$
- $\Delta$   $f=60\%$
- $\circ$   $f=70\%$
- $\square$   $f=80\%$
- $\diamond$   $f=90\%$
- $\times$   $f=100\%$

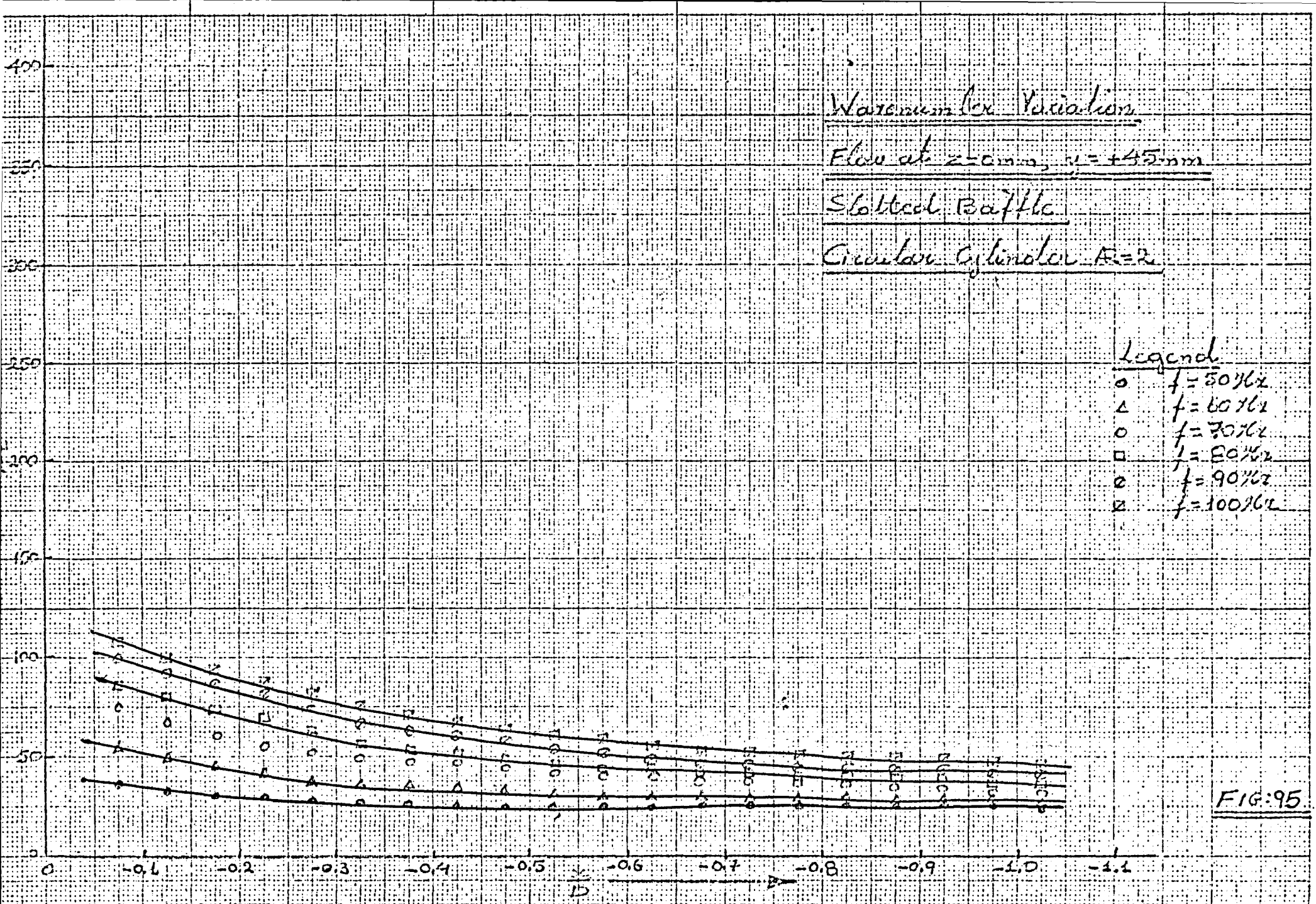


FIG:95

Wavenumber Variation

Flow at  $z = \pm 16\text{mm}$ ,  $y = 0\text{mm}$

Slotted Baffle

Circular Cylinder  $R=2$

Legend

- $\circ$   $f = 2\% \lambda$
- $\Delta$   $f = 2.5\% \lambda$
- $\square$   $f = 3\% \lambda$
- $\square$   $f = 4\% \lambda$
- $\square$   $f = 5\% \lambda$
- $\square$   $f = 6\% \lambda$
- $\square$   $f = 7\% \lambda$
- $\Delta$   $f = 8\% \lambda$
- $\times$   $f = 9\% \lambda$

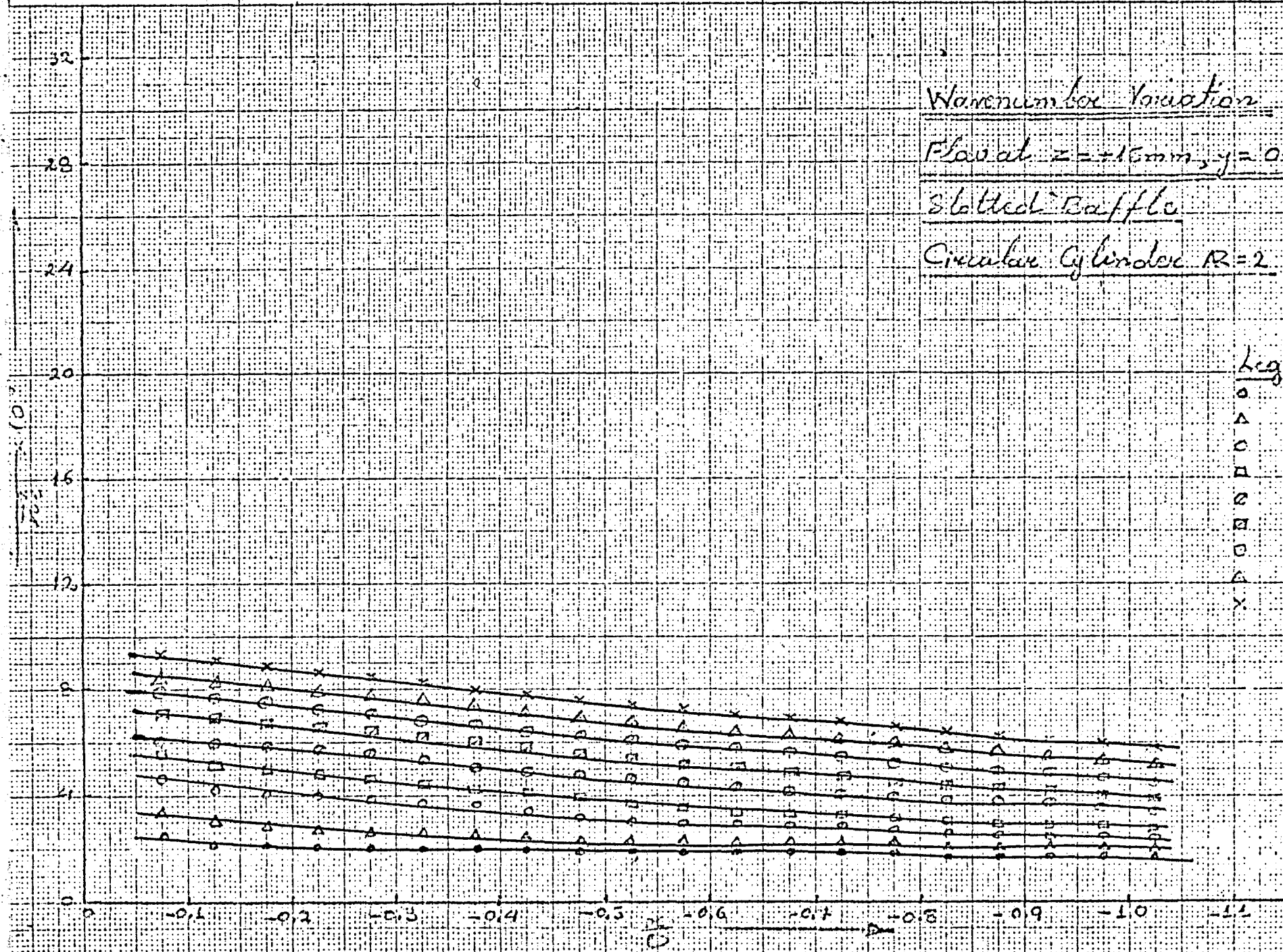


FIG: 96

Wave number Variation

Flow at  $x = x_{\text{down}}, y = 0.25x_{\text{up}}$

Slotted Baffle

Circular Cylinder  $Re = 2$

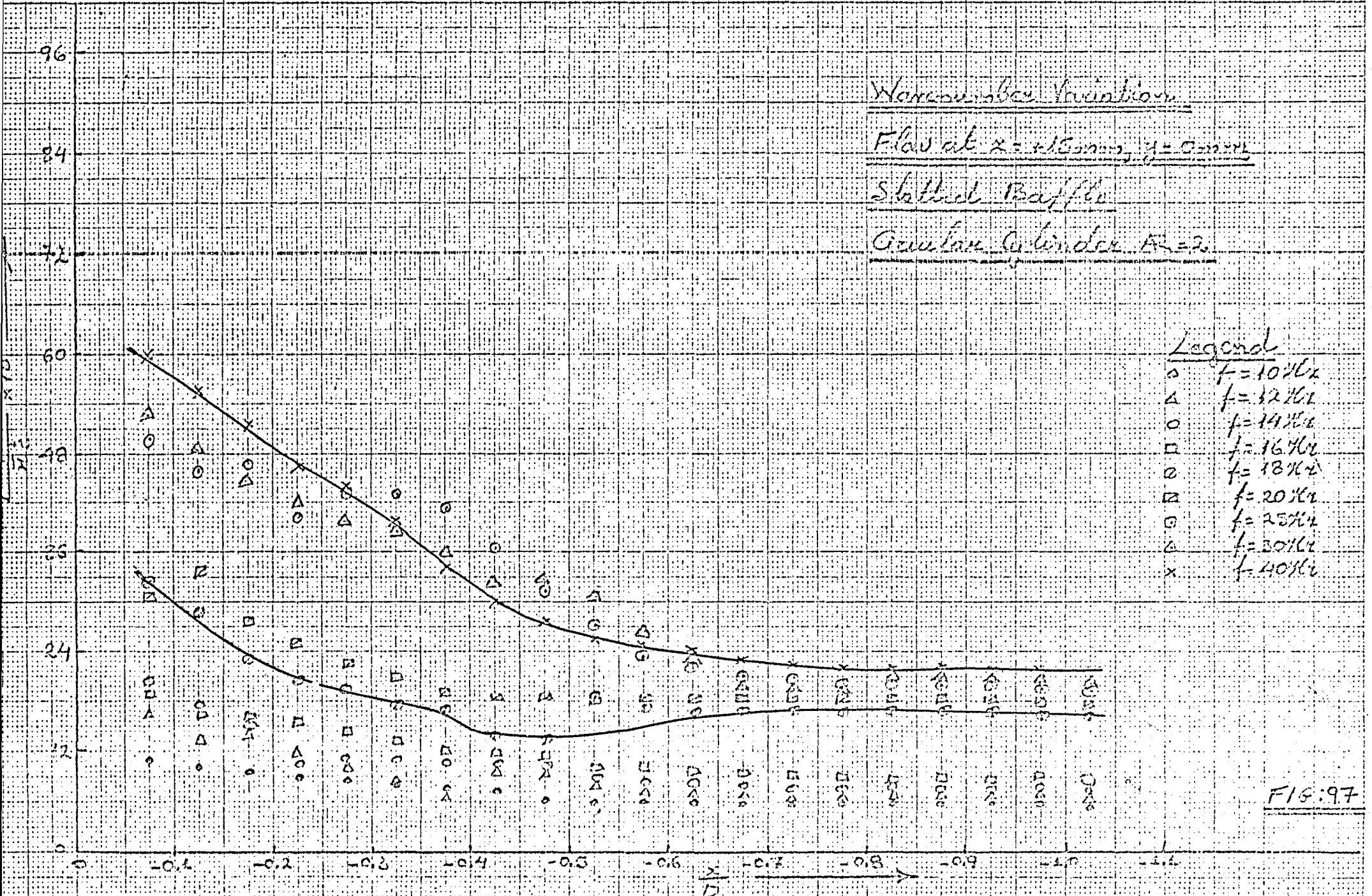


FIG: 97



# Wave number Variation

Flow at  $\lambda = 15 \text{ mm}$ ,  $\mu = 0.5 \text{ mm}$

Slotted Raffle

Granular Cylinder  $R=2$

### Legend

- $\circ$   $f = 50\% \lambda$
- $\Delta$   $f = 60\% \lambda$
- $\circ$   $f = 70\% \lambda$
- $\square$   $f = 80\% \lambda$
- $\circ$   $f = 90\% \lambda$
- $\square$   $f = 100\% \lambda$

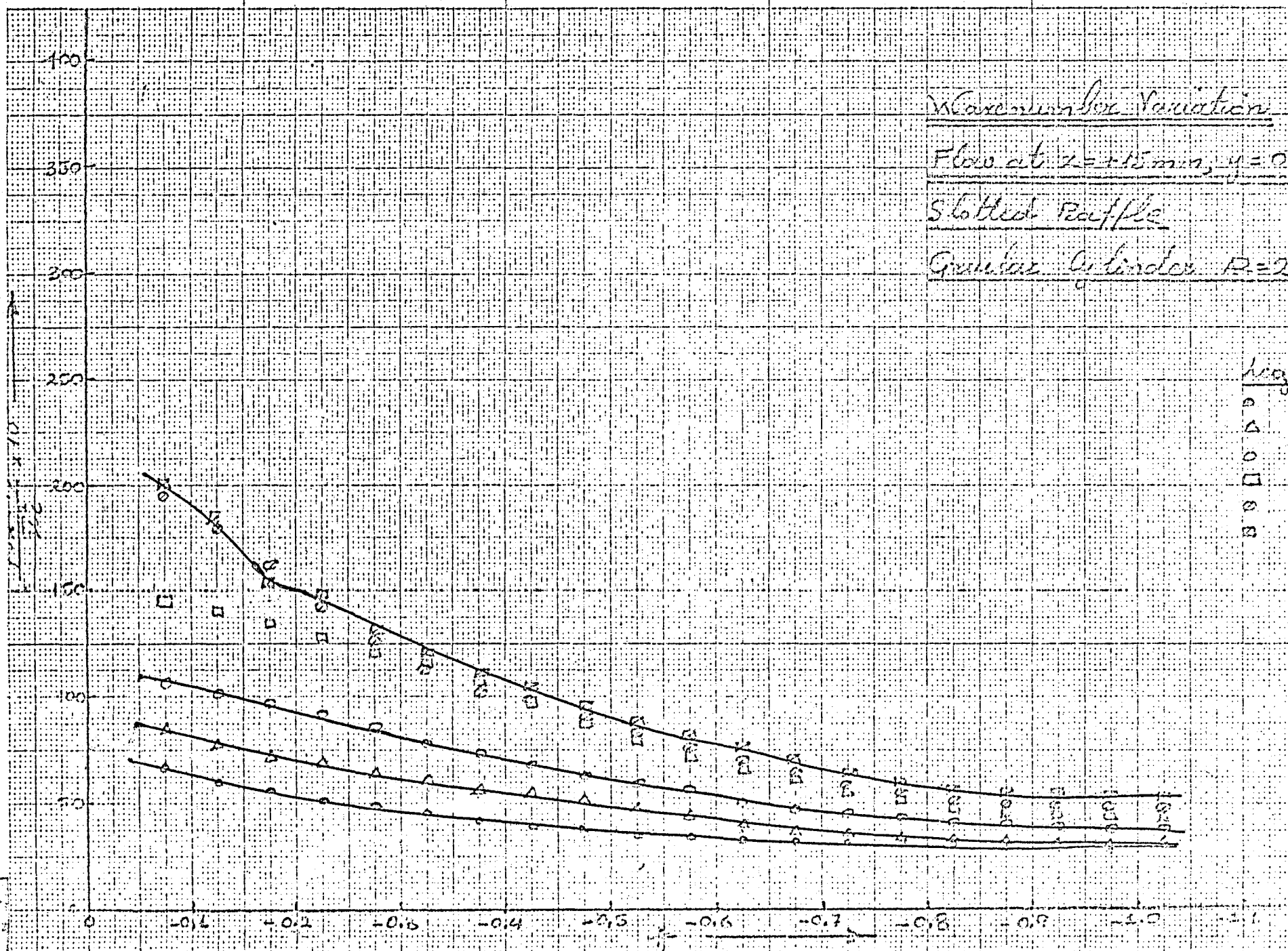


FIG. 98

# Wave number variation

Flow of  $y = 0$  mm,  $z = +30$  mm

Slotted Baffle

Circular cylinder  $R=2$

## Legend

- $\circ$   $f = 2\% \lambda$
- $\Delta$   $f = 2.5\% \lambda$
- $\circ$   $f = 3\% \lambda$
- $\square$   $f = 4\% \lambda$
- $\circ$   $f = 5\% \lambda$
- $\square$   $f = 6\% \lambda$
- $\circ$   $f = 7\% \lambda$
- $\Delta$   $f = 8\% \lambda$
- $\times$   $f = 9\% \lambda$

FIG: 99

# Wave number variation

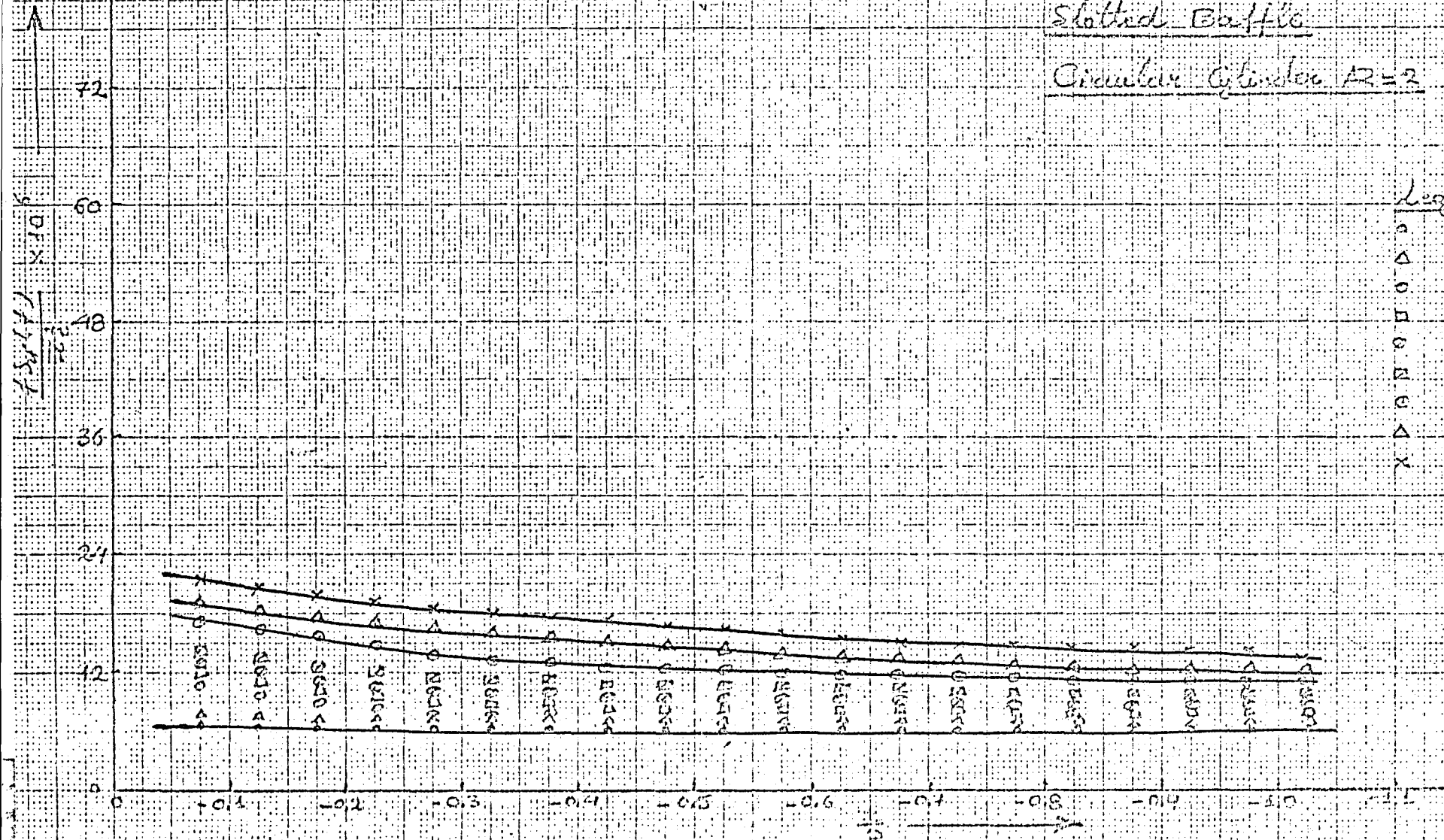
Flow at  $x=0$  mm,  $x_0 = +20$  mm

Slotted Baffle

Circular Cylinder  $AR=2$

## Legend

- $\circ$   $f=10\%$
- $\Delta$   $f=12\%$
- $\circ$   $f=14\%$
- $\square$   $f=16\%$
- $\circ$   $f=18\%$
- $\square$   $f=20\%$
- $\circ$   $f=25\%$
- $\Delta$   $f=30\%$
- $\times$   $f=40\%$



Wave number Variation

Flow at  $q = 0 \text{ mm}^2$ ,  $z = +20 \text{ mm}$

Slotted Baffle

Circular Cylinder  $AR = 2$

Legend

- $\circ$   $f = 50 \text{ Hz}$
- $\Delta$   $f = 60 \text{ Hz}$
- $\square$   $f = 70 \text{ Hz}$
- $\diamond$   $f = 80 \text{ Hz}$
- $\circ$   $f = 90 \text{ Hz}$
- $\times$   $f = 100 \text{ Hz}$

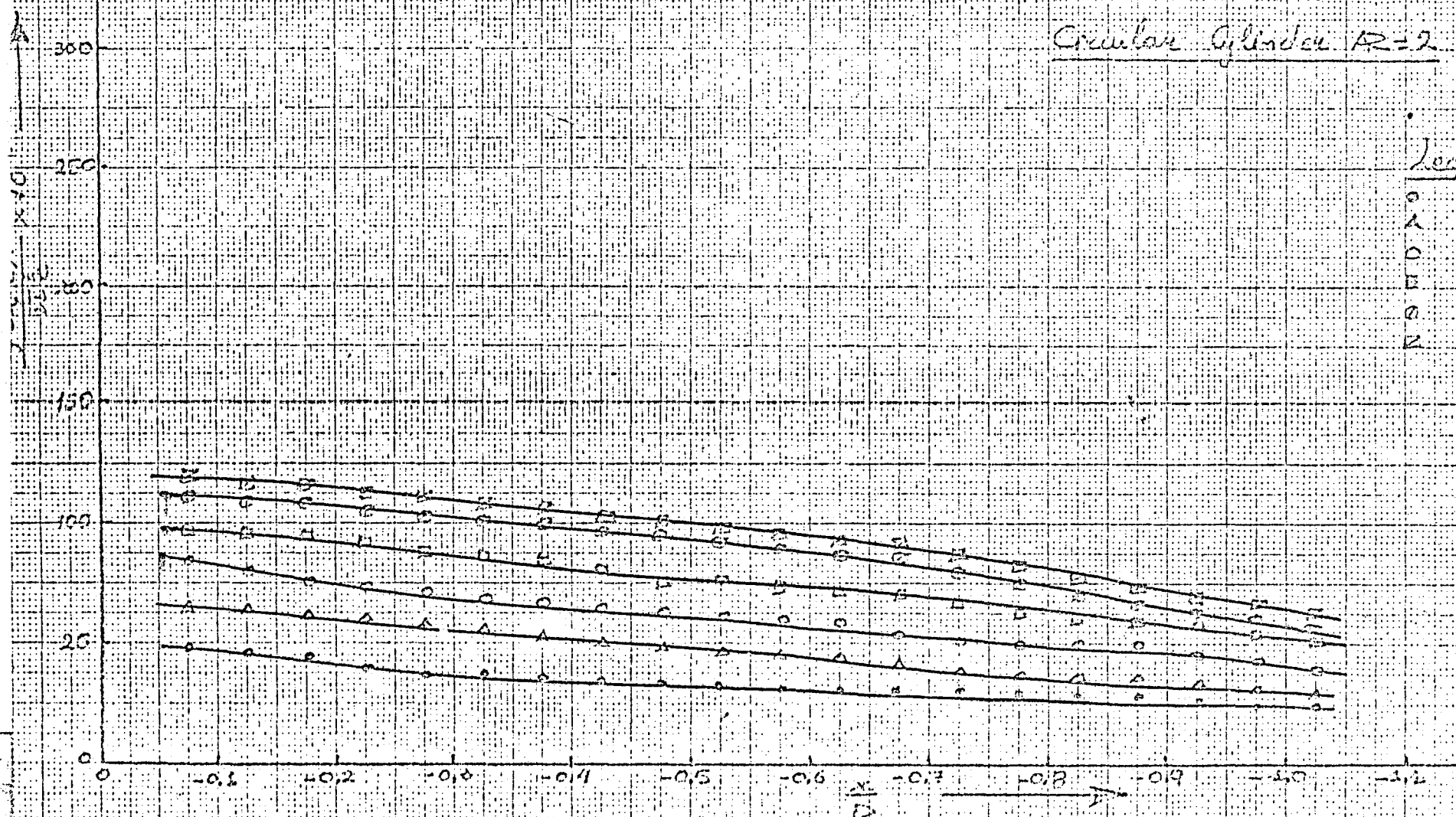


Fig: 101



Turbulence Level Variation  
in front of the  $R=2$  Circular  
Cylinder.  
Slotted Paddle



Legend

- 1 Flow at  $z=0$  mm,  $y=0$  mm
- 2 Flow at  $z=0$  mm,  $y=+15$  mm
- 3 Flow at  $z=0$  mm,  $y=+30$  mm
- 4 Flow at  $z=0$  mm,  $y=+45$  mm
- 5 Flow at  $z=+15$  mm,  $y=0$  mm
- 6 Flow at  $z=+30$  mm,  $y=0$  mm

FIG:102

Wavenumber Variation

Stagnation line Flow

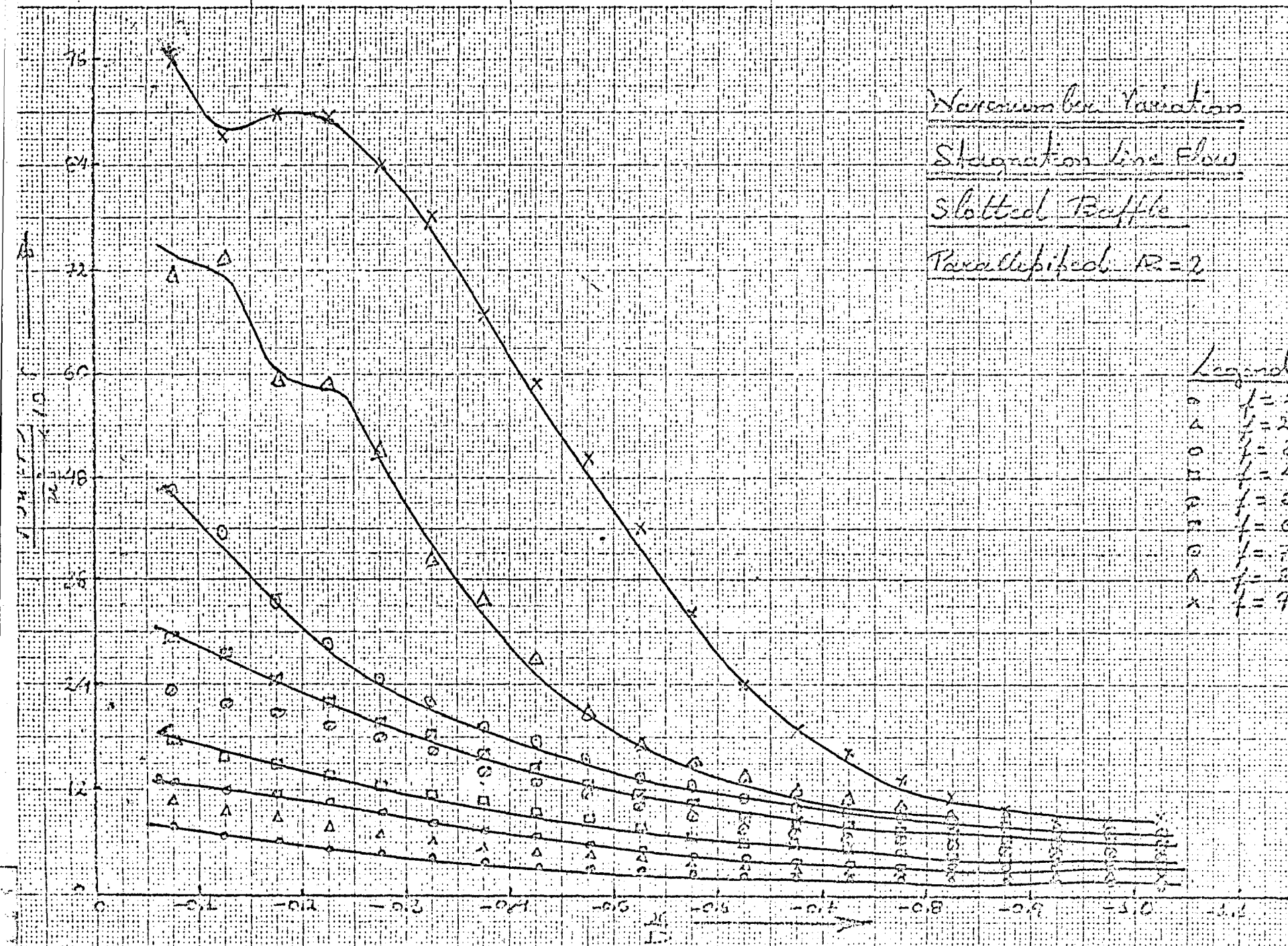
Slotted Baffle

Parallelized  $R_2 = 2$

Legend

- $\circ$   $f = 2\%$
- $\Delta$   $f = 2.5\%$
- $\circ$   $f = 3\%$
- $\square$   $f = 4\%$
- $\square$   $f = 5\%$
- $\square$   $f = 6\%$
- $\circ$   $f = 7\%$
- $\Delta$   $f = 8\%$
- $\times$   $f = 9\%$

FIG:103



Wave number Variation

Stagnation line Flow

Slotted Baffle

Parallelepiped  $R=2$

Legend

- $f = 10\% \alpha$
- △  $f = 12\% \alpha$
- $f = 14\% \alpha$
- $f = 16\% \alpha$
- $f = 18\% \alpha$
- $f = 20\% \alpha$
- $f = 25\% \alpha$
- △  $f = 30\% \alpha$
- x  $f = 40\% \alpha$

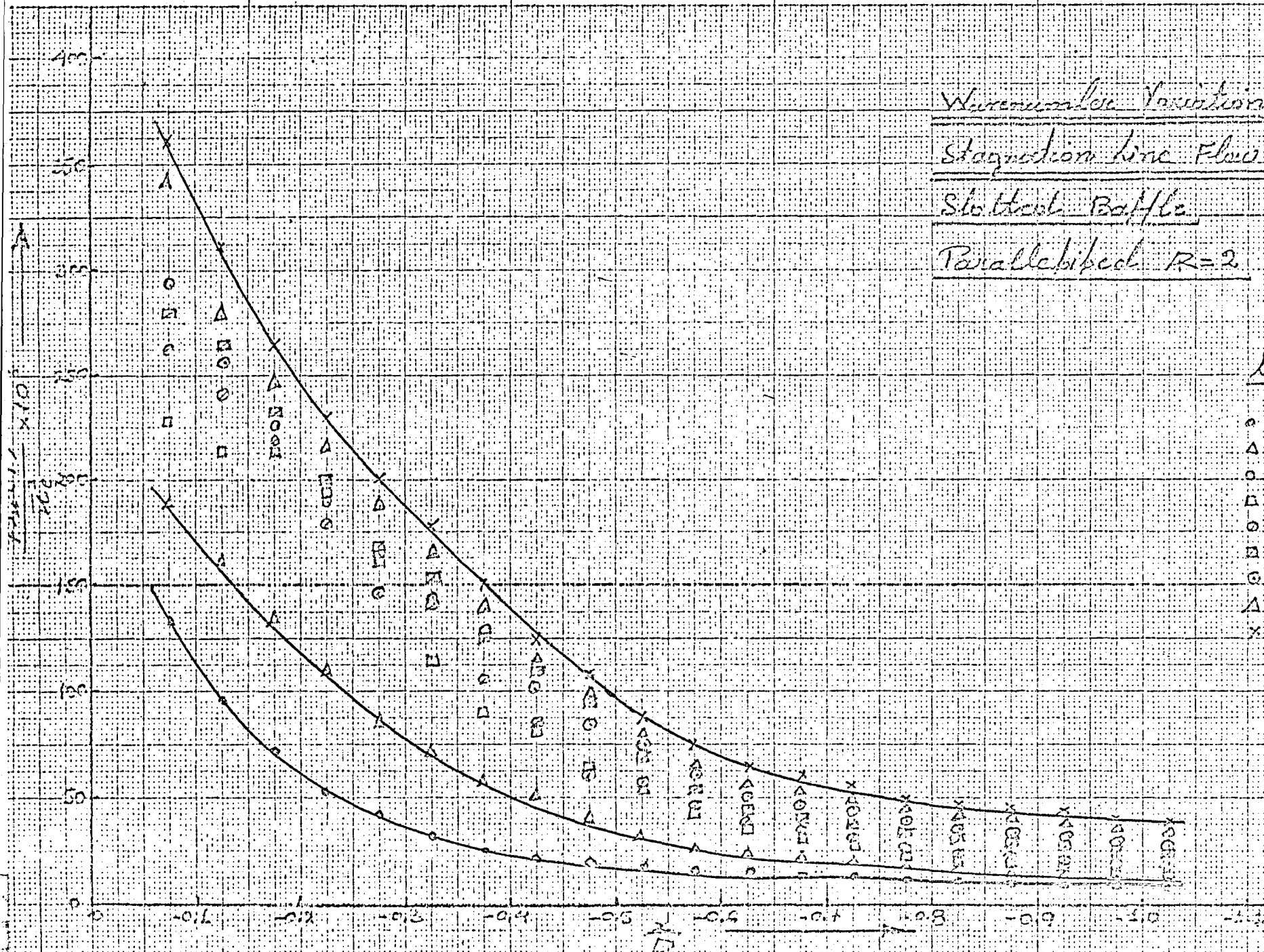


FIG:104



Wave number Variation

Stagnation line Flow

Slotted Baffle

Parallel bitted  $R=2$

Legend

- $\circ$   $f = 50\%$
- $\Delta$   $f = 60\%$
- $\square$   $f = 70\%$
- $\square$   $f = 80\%$
- $\circ$   $f = 90\%$
- $\square$   $f = 100\%$

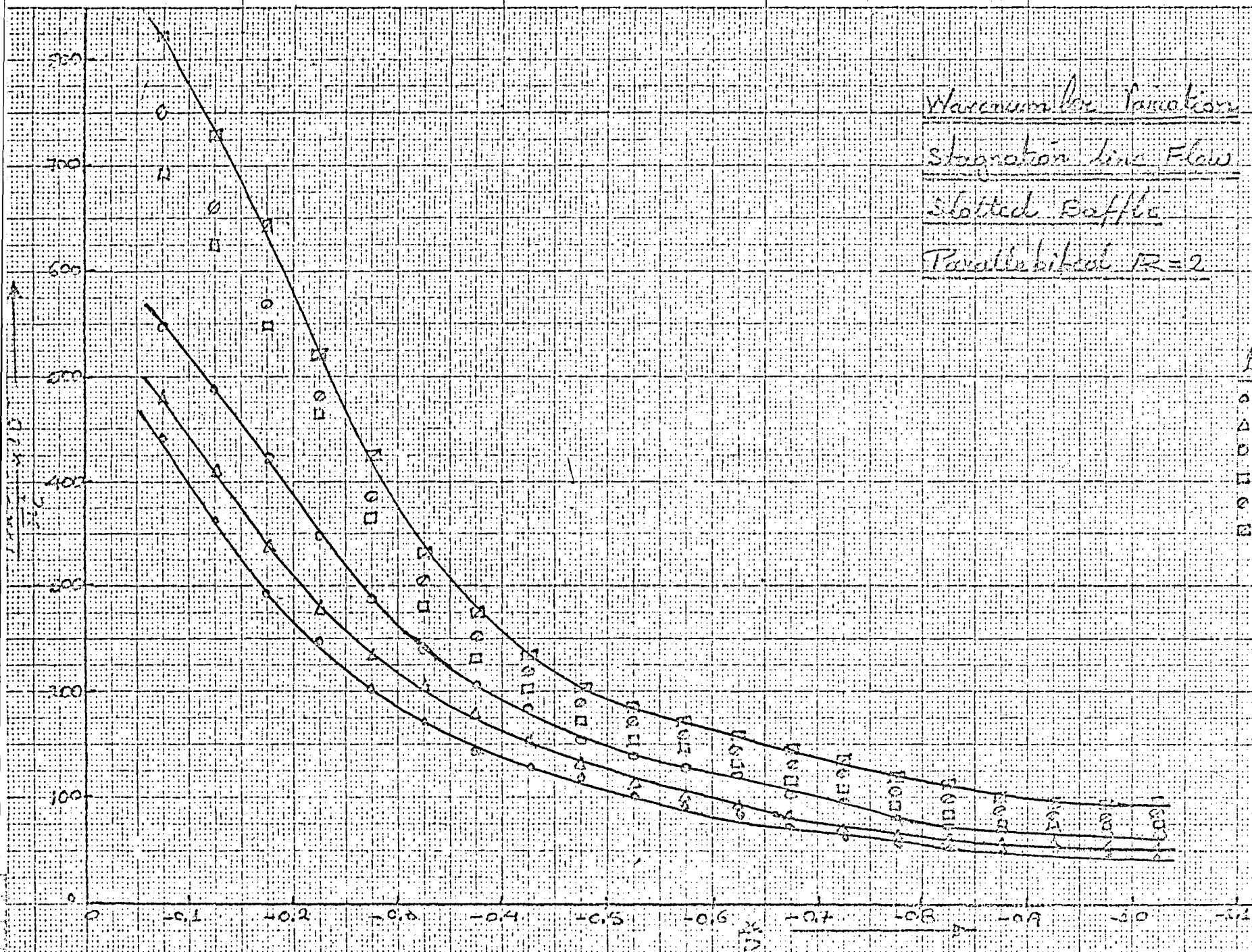
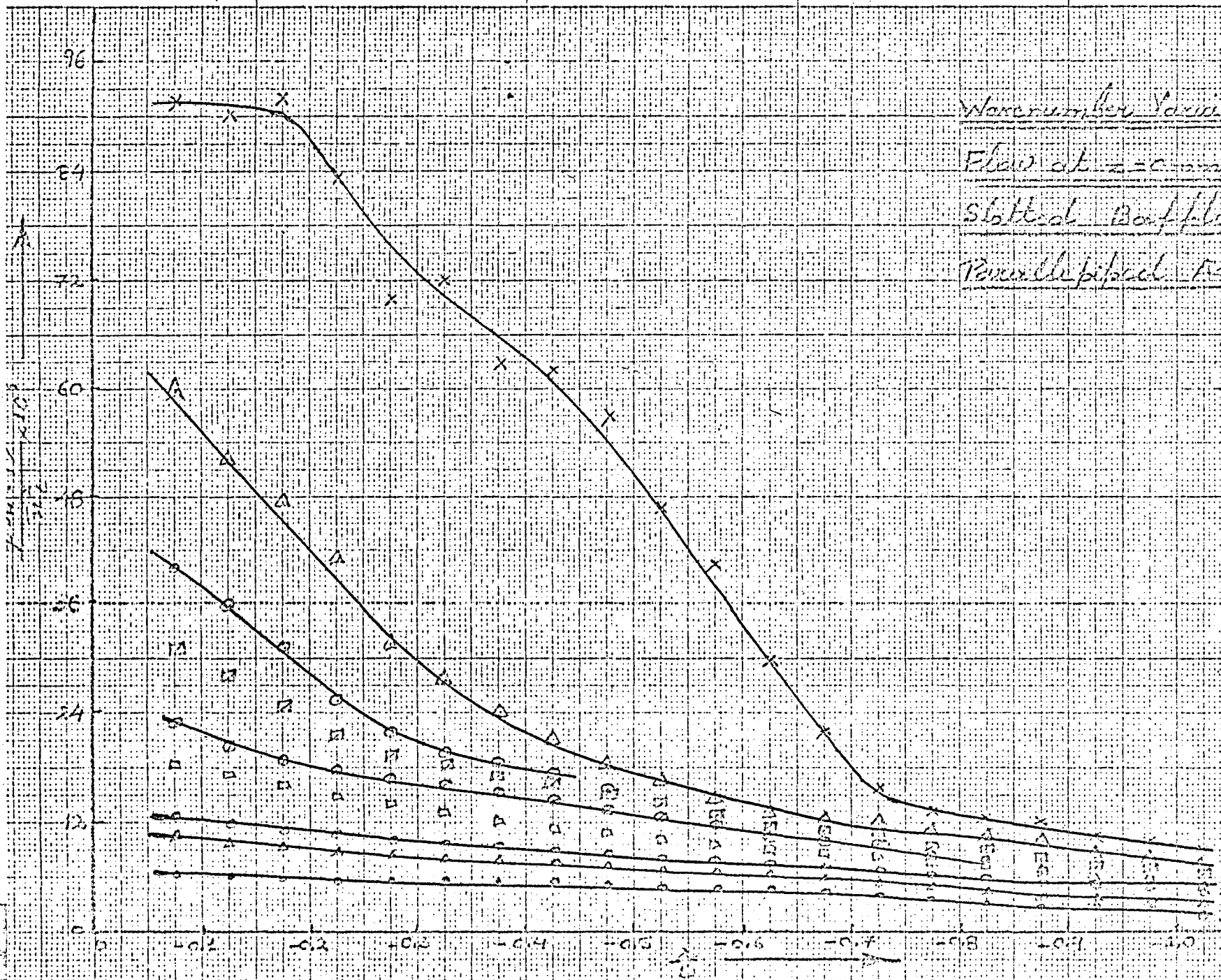


FIG: 105



Wave number Variations  
 Flow at  $z=0$  mm,  $x=15$  mm  
 Slotted Baffles  
 Parallel pipe  $R=2$

- Legend
- $f=2.5\%$
  - △  $f=3\%$
  - $f=4\%$
  - $f=5\%$
  - ◇  $f=6\%$
  - $f=7\%$
  - $f=8\%$
  - △  $f=9\%$

FIG. 106

Wave number variation

Flow at  $z = 0 \text{ mm}$ ,  $z = +15 \text{ mm}$

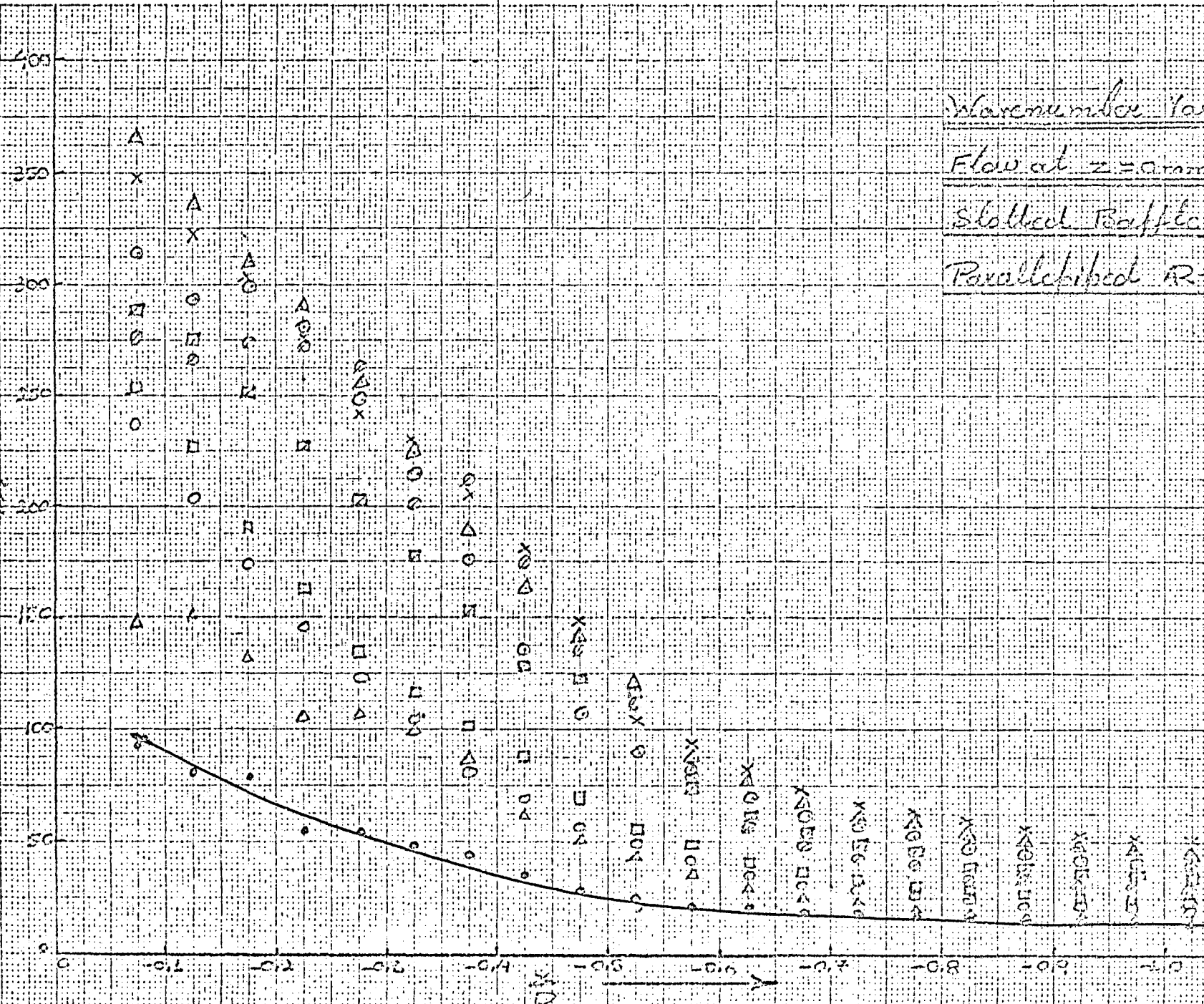
Slotted Baffle

Parallelised  $R=2$

Legend

- $\circ$   $f=10\%$
- $\Delta$   $f=12\%$
- $\square$   $f=14\%$
- $\square$   $f=16\%$
- $\square$   $f=18\%$
- $\square$   $f=20\%$
- $\square$   $f=25\%$
- $\Delta$   $f=30\%$
- $\times$   $f=40\%$

$\frac{F_{\text{max}}}{F_{\text{min}}} \times 100\%$



Wave number Variation

Flange  $a=0mm$ ,  $y=+15mm$

Slotted Baffle

Parallelized AR=2

Legend

- $\circ$   $f=50\%r$
- $\Delta$   $f=60\%r$
- $\circ$   $f=70\%r$
- $\square$   $f=80\%r$
- $\square$   $f=90\%r$
- $\square$   $f=100\%r$

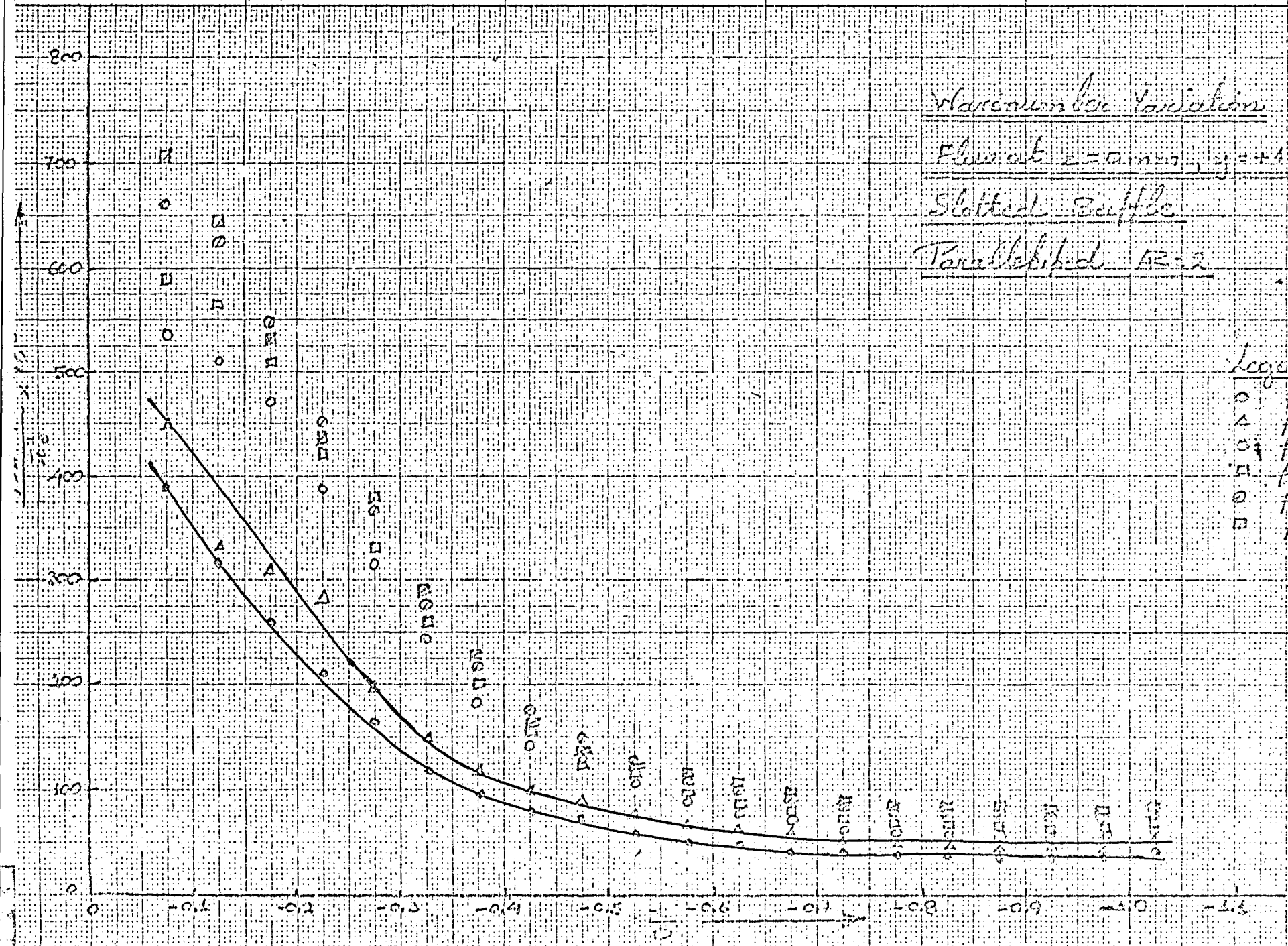


FIG:108



Wave number Variation

Flow at  $z=0$  mm,  $y=-30$  mm

Slotted Baffle

Parallelepiped  $AR=2$

Legend

- $f=2\%$
- △  $f=2.5\%$
- $f=3\%$
- $f=4\%$
- $f=5\%$
- $f=6\%$
- $f=7\%$
- △  $f=8\%$
- x  $f=9\%$

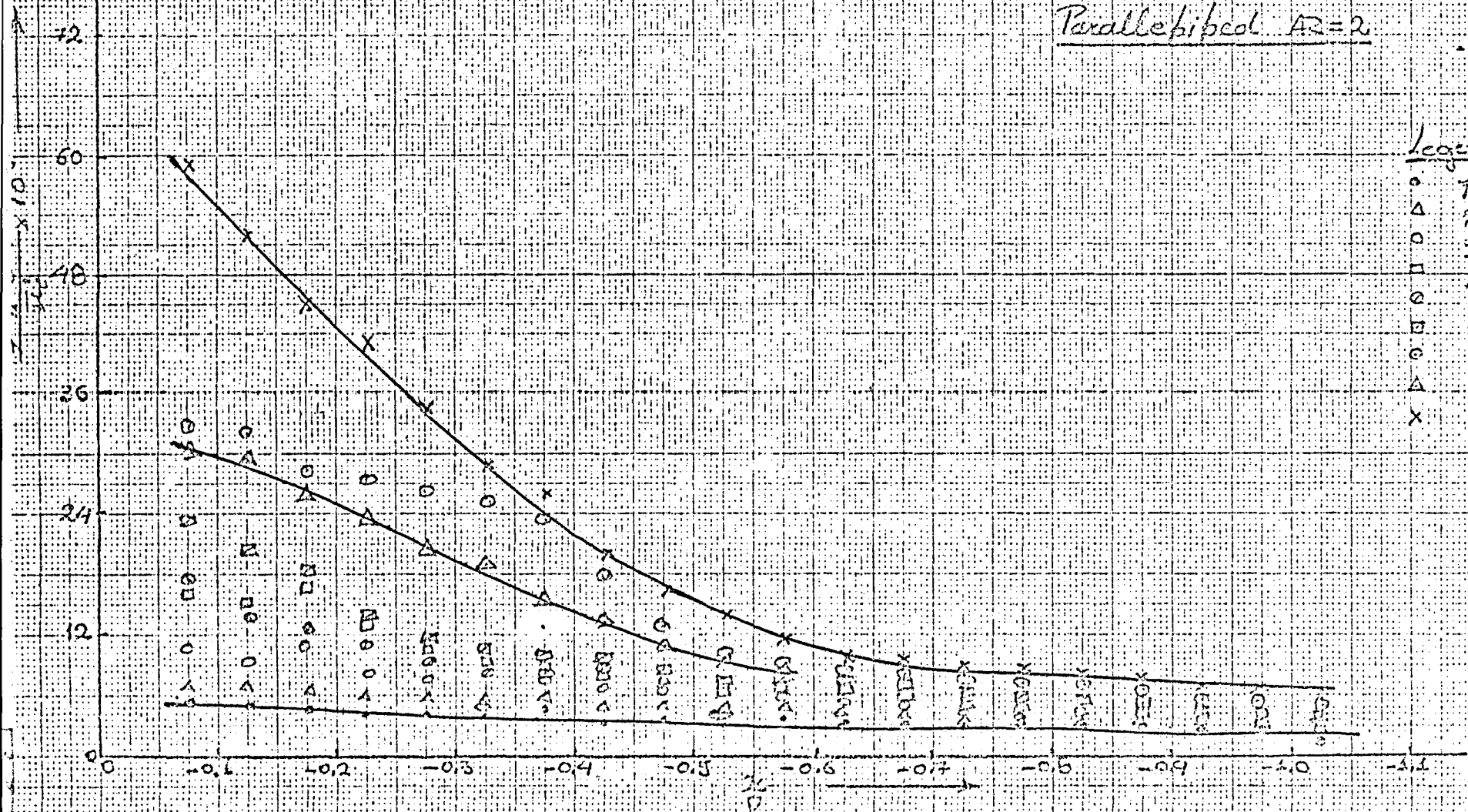


FIG: 109

Wave-number Variation

Flux at  $z=0$  mm,  $u=20$  mm

Slotted Baffle

Porocelphibol  $Re=2$

Legend

- $\circ$   $f=10\%$
- $\Delta$   $f=12\%$
- $\circ$   $f=14\%$
- $\square$   $f=16\%$
- $\circ$   $f=18\%$
- $\square$   $f=20\%$
- $\circ$   $f=25\%$
- $\Delta$   $f=30\%$
- $\times$   $f=40\%$

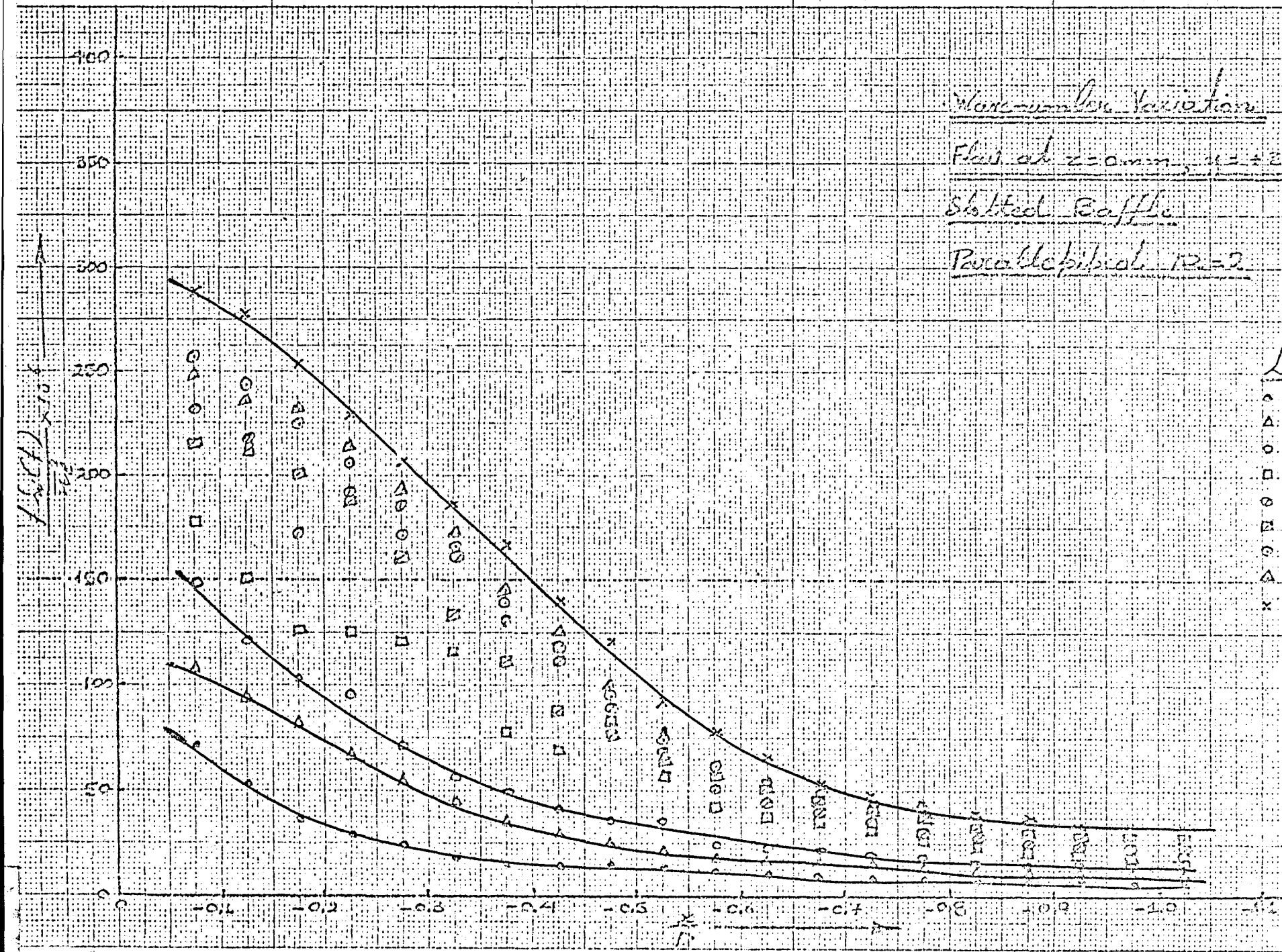


FIG. 110

Warcumbee Variation

Flow at  $z=0$  mm,  $y=20$  mm

Slatted Baffle

Parallelised  $A2=2$

Legend

- o  $f=50\%$
- $\Delta$   $f=60\%$
- o  $f=70\%$
- $\square$   $f=80\%$
- o  $f=90\%$
- $\square$   $f=100\%$

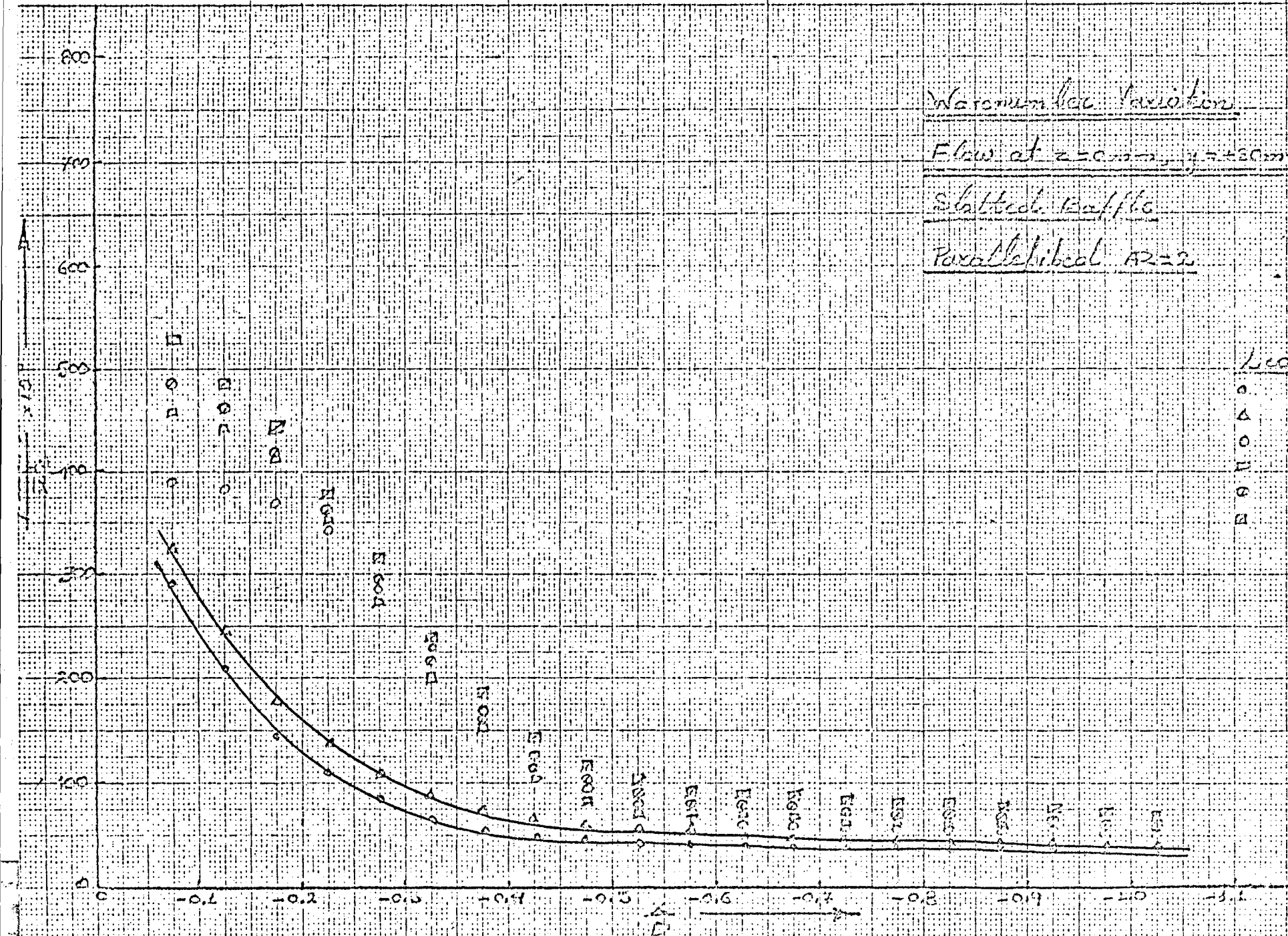


Fig: 111



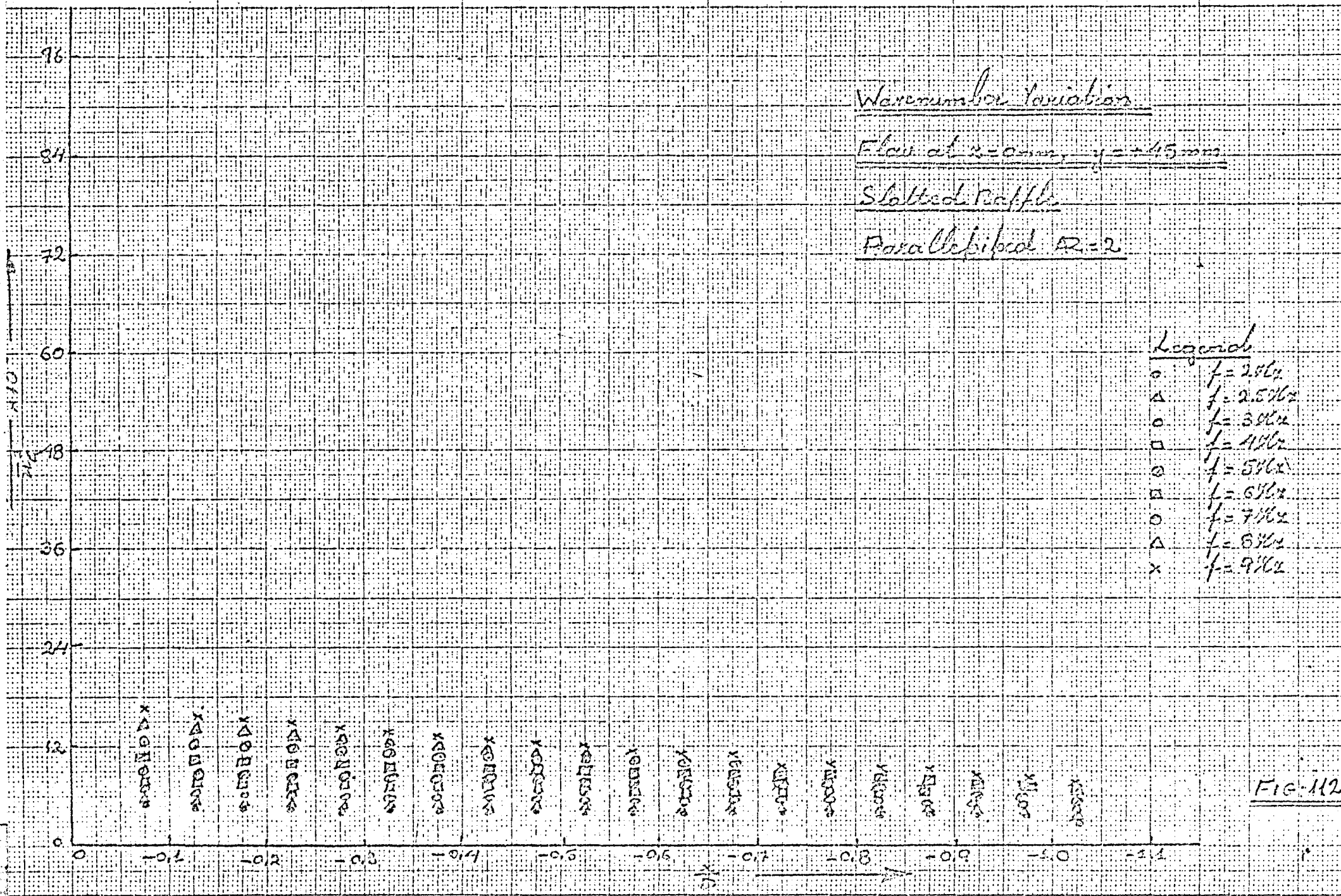
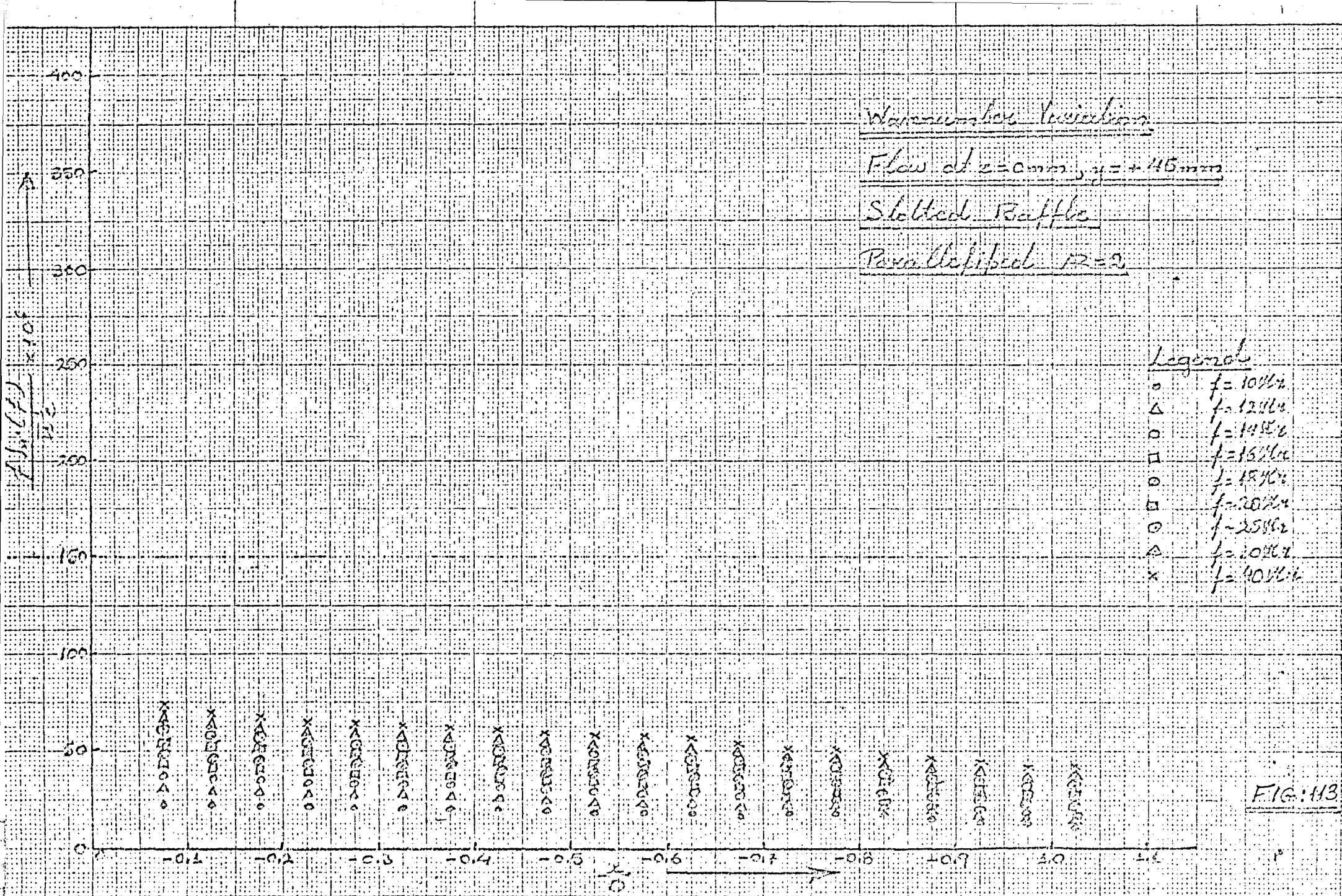
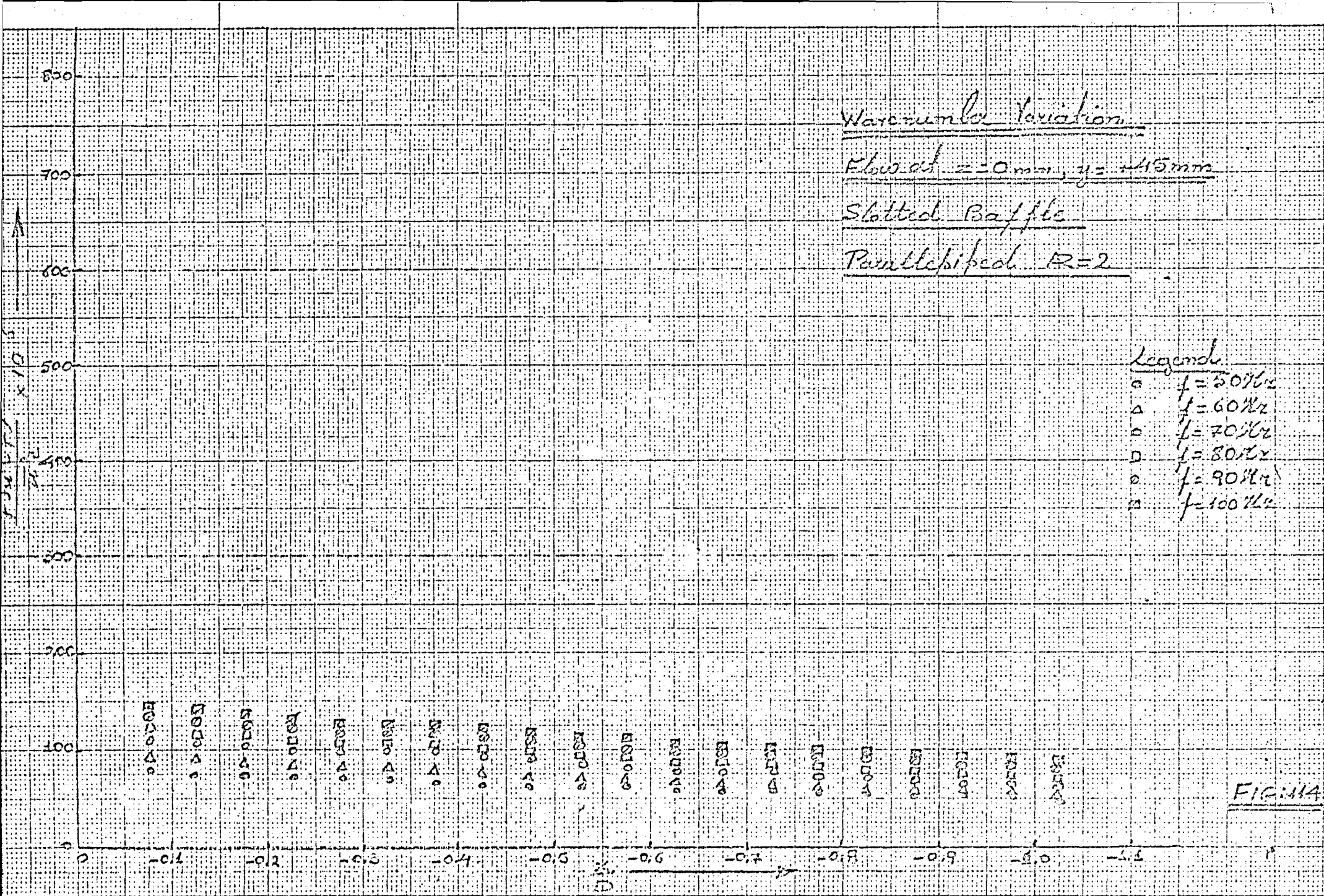


FIG-112





Wave number variation

Flow at  $z = +15\text{mm}$ ,  $\beta = 0\text{mm}$

Slatted Baffle

Parallelized  $BR=2$

Legend

- $\circ$   $f = 2\text{Hz}$
- $\Delta$   $f = 2.5\text{Hz}$
- $\circ$   $f = 3\text{Hz}$
- $\square$   $f = 4\text{Hz}$
- $\square$   $f = 5\text{Hz}$
- $\square$   $f = 6\text{Hz}$
- $\circ$   $f = 7\text{Hz}$
- $\Delta$   $f = 8\text{Hz}$
- $\times$   $f = 9\text{Hz}$

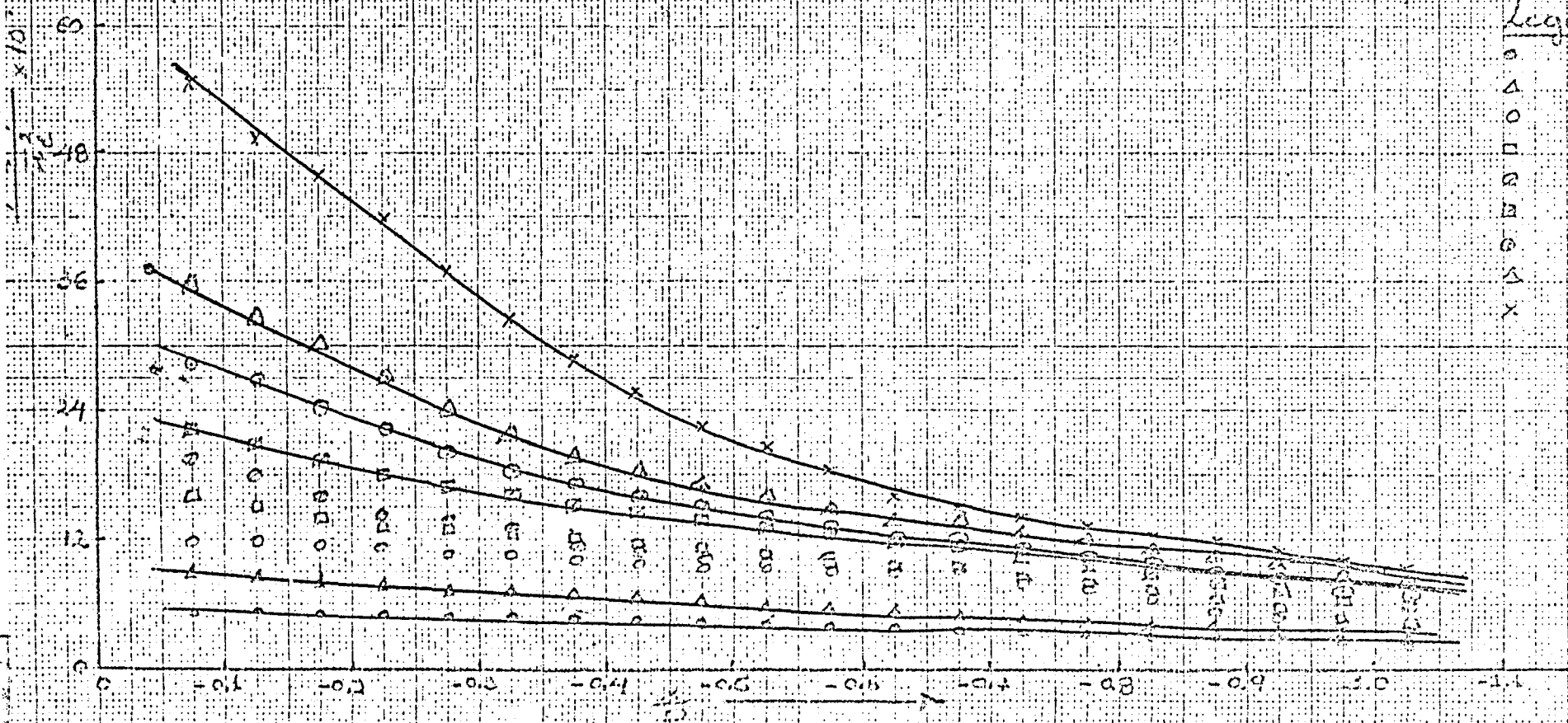


FIG. 115



Wavenumber Variation

Flow at  $z = +15 \text{ mm}$ ,  $z = 0 \text{ mm}$

Slothead Baffle

Parallelepiped  $AR=2$

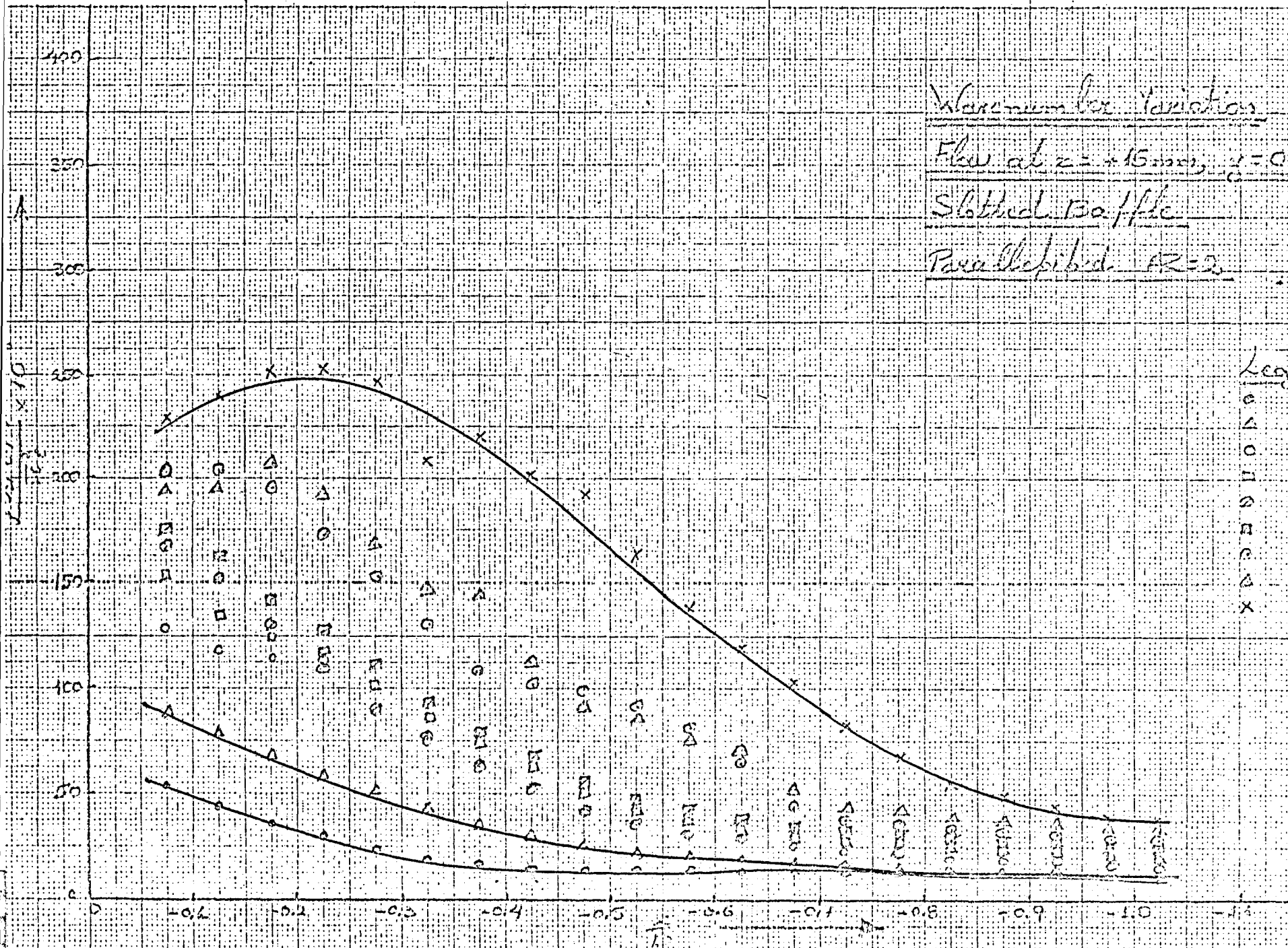


FIG. 116

# Wave number Variation

Flow at  $\infty$  - laminar,  $\nu = 0.5 \text{ cm}^2/\text{s}$

Slatbed Baffle

Para Elliptical  $R=2$

## Legend

- $\circ$   $f = 50\%$
- $\Delta$   $f = 60\%$
- $\square$   $f = 70\%$
- $\diamond$   $f = 80\%$
- $\circ$   $f = 90\%$
- $\square$   $f = 100\%$

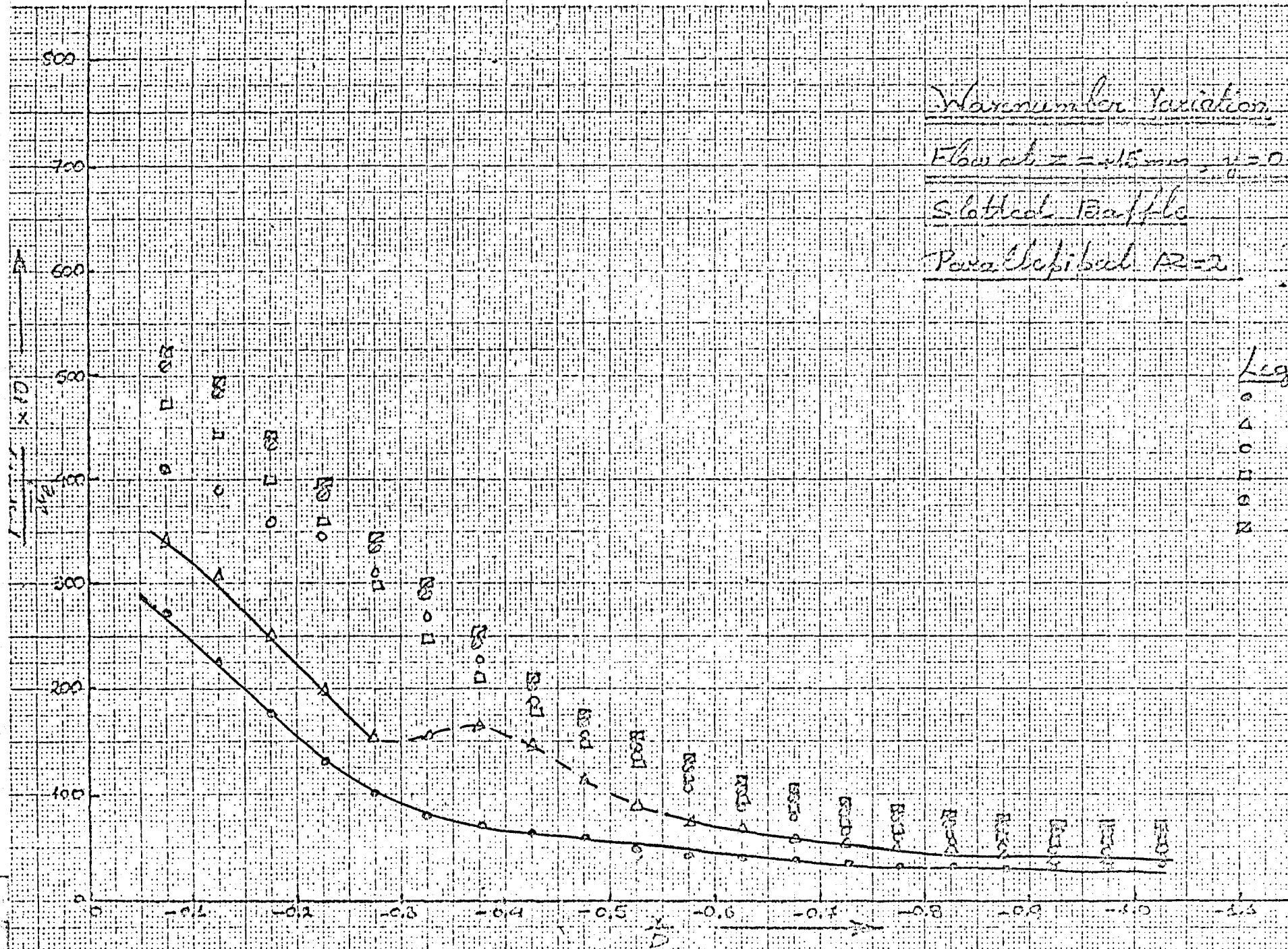


FIG: 117

Wave number function

Flange  $x = +20\text{ mm}$ ,  $y = 0\text{ mm}$

Slatted Baffle

Parallelepiped  $R=2$

Legend

- $\circ$   $f = 2\text{ KHz}$
- $\Delta$   $f = 2.5\text{ KHz}$
- $\circ$   $f = 3\text{ KHz}$
- $\square$   $f = 4\text{ KHz}$
- $\circ$   $f = 5\text{ KHz}$
- $\square$   $f = 6\text{ KHz}$
- $\circ$   $f = 7\text{ KHz}$
- $\Delta$   $f = 8\text{ KHz}$
- $\times$   $f = 9\text{ KHz}$

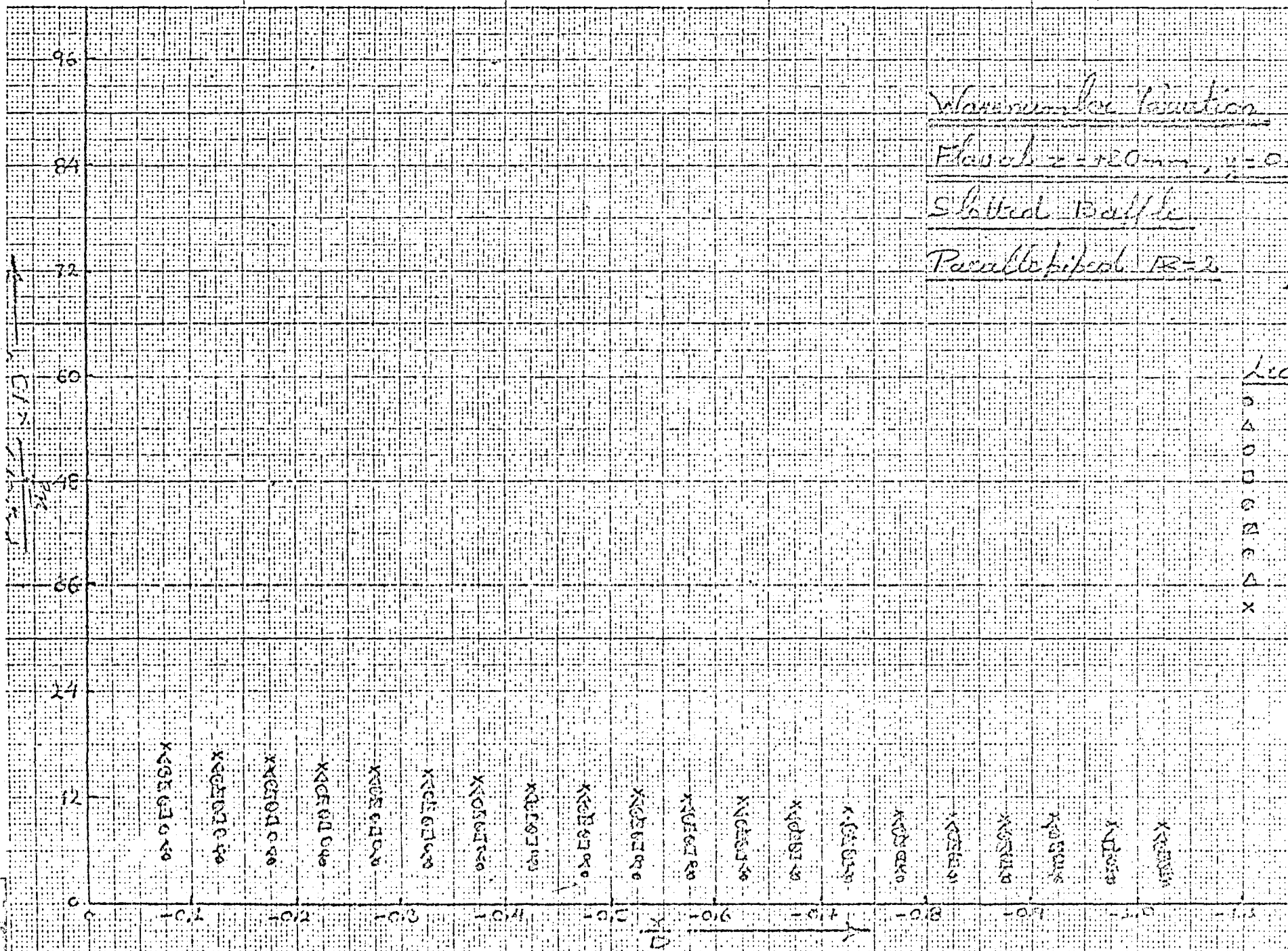
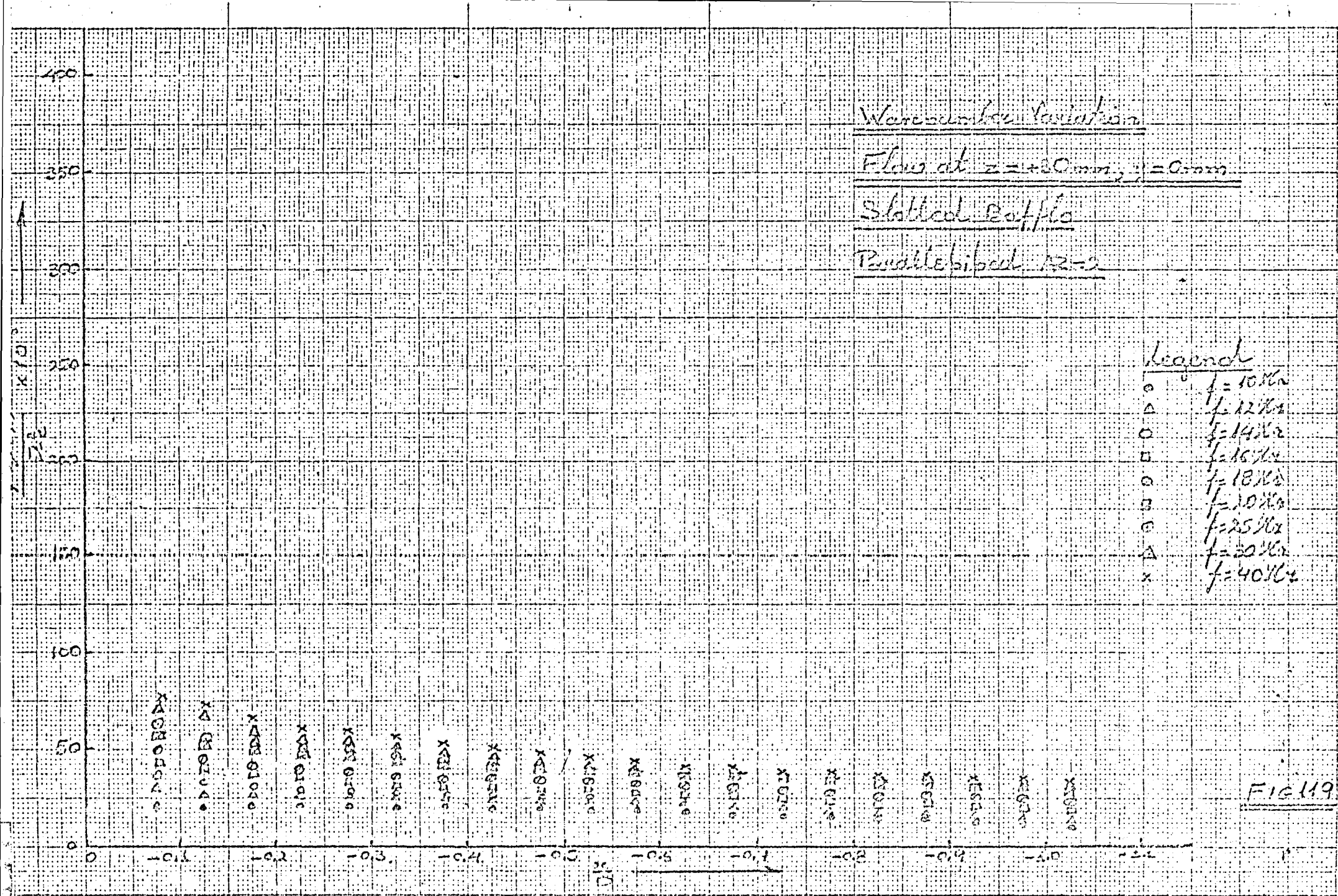
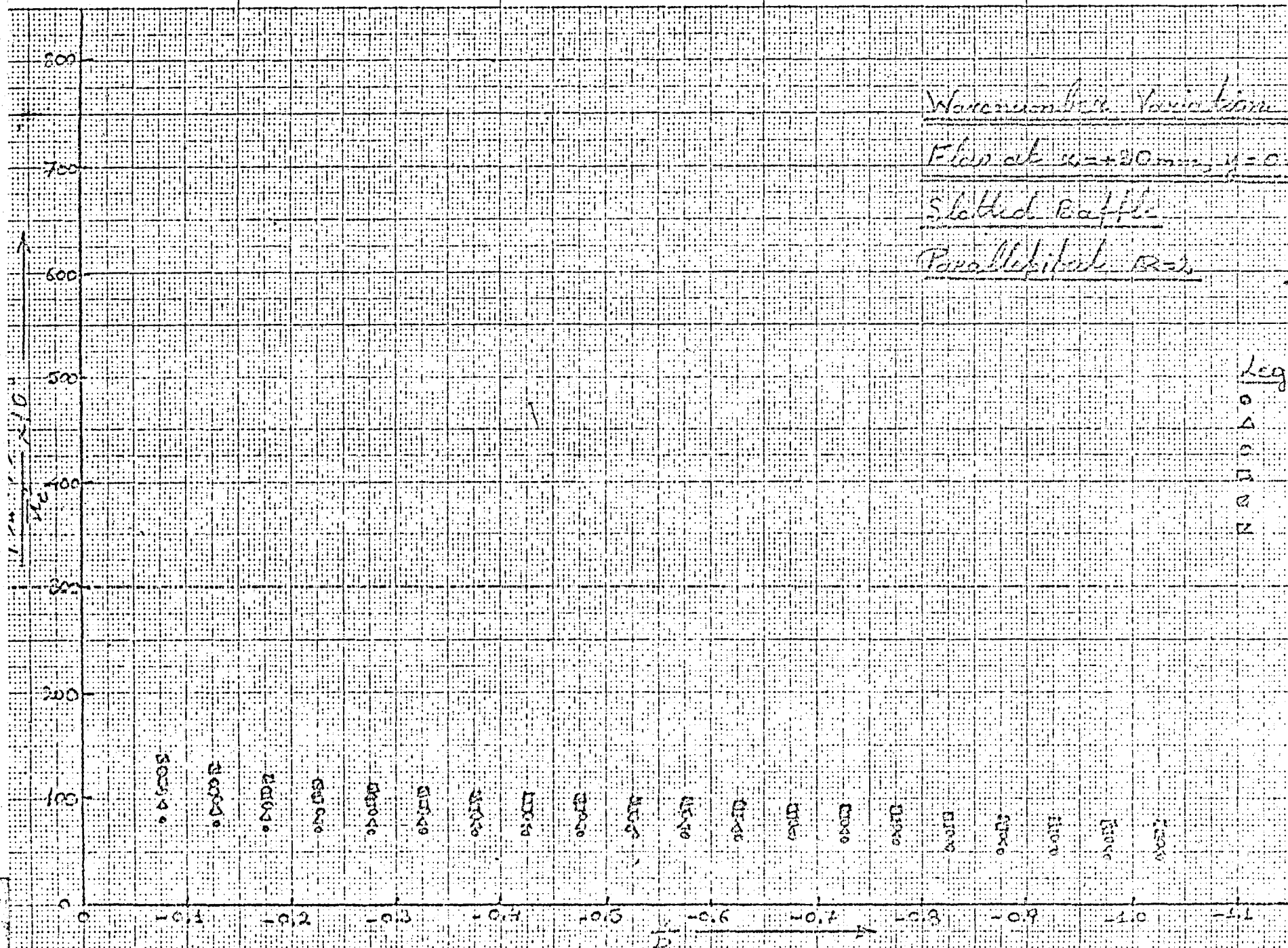


FIG. 118







Wave number Variation

Flow at  $u = +20 \text{ mm/s}$ ,  $\mu = 0.01 \text{ mm}$

Slatted Baffle

Parallelepiped Bars

- Legend
- $f = 50 \text{ Hz}$
  - △  $f = 60 \text{ Hz}$
  - $f = 70 \text{ Hz}$
  - ◇  $f = 80 \text{ Hz}$
  - ◊  $f = 90 \text{ Hz}$
  - ✕  $f = 100 \text{ Hz}$

FIG. 120

# Turbulence Level Variations

in front of the  $R=2$

Paved Slab

Slotted Baffle

## Legend

- Flow at  $z=0$ mm  
 $y=0$ mm
- △ Flow at  $z=0$ mm  
 $y=+15$ mm
- Flow at  $z=0$ mm  
 $y=+30$ mm
- x Flow at  $z=0$ mm  
 $y=+45$ mm
- Flow at  $z=+15$ mm  
 $y=0$ mm
- Flow at  $z=30$ mm  
 $y=0$ mm

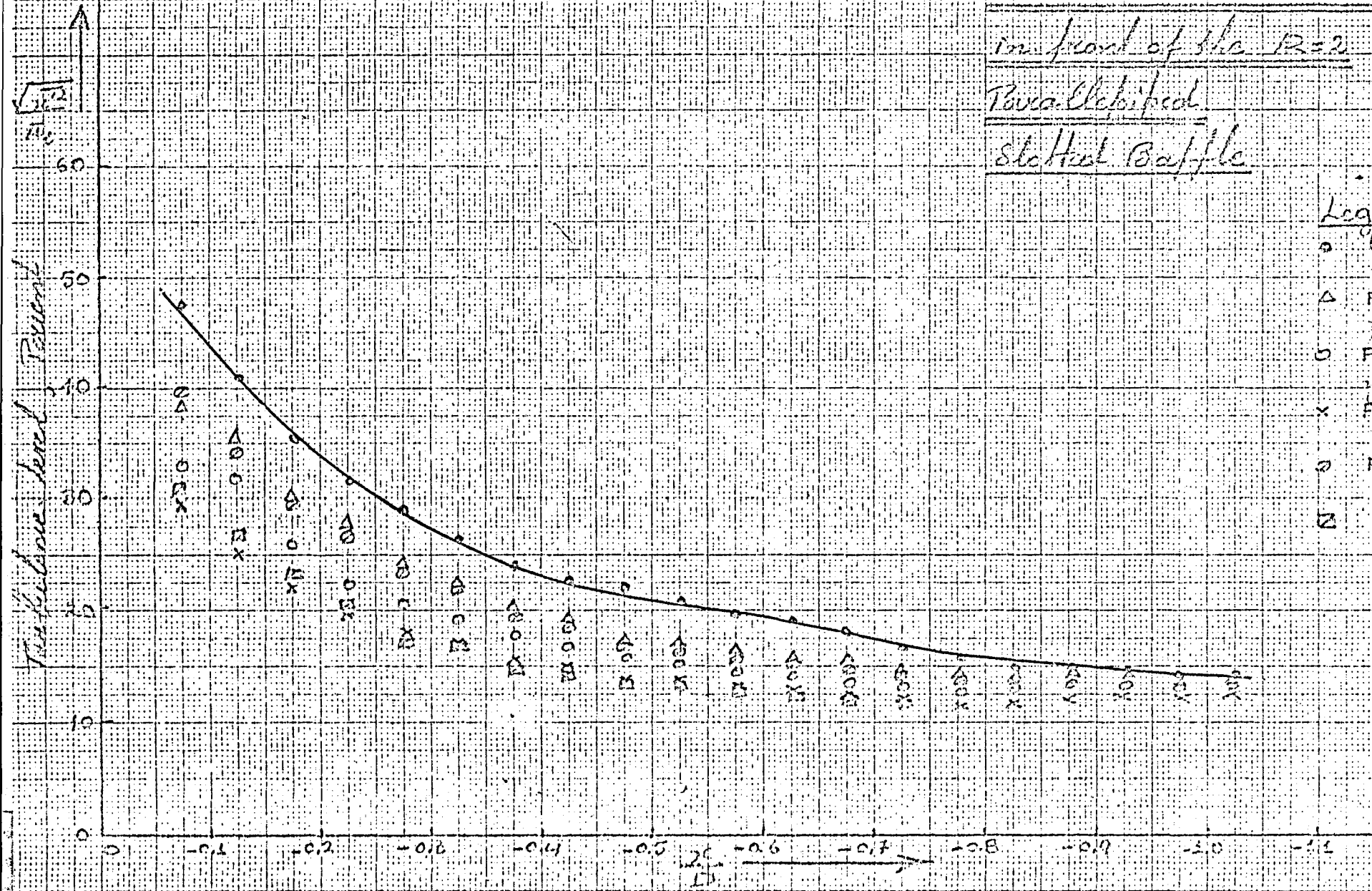


FIG. 12.1

VARIATION OF THE INTEGRAL SCALE OF TURBULENCE

IN FRONT OF THE MODELS

(Refer to Fig. 5m for definition sketch)

Variation of the Lateral Space Correlation  
(x-direction) in front of the AR=2 Circular Section Cylinder  
slotted Baffle. H.W. placed at  $\frac{x}{d_s} = -0.49$  from  
Centre of Oscillations  
Amplitude of Oscillations = 2mm

### Legend

- Wind Tunnel Empty
- x Model Held Rigidly
- o Model Free to Oscillate
- Oscil. Fr. = 3.9 Hz (Signal Unfil.)
- Oscil. Fr. = 3.9 Hz (Signal Fil.)
- △ Oscil. Fr. = 6.75 Hz (Signal Unfil.)
- ▲ Oscil. Fr. = 6.75 Hz (Signal Fil.)
- ▽ Oscil. Fr. = 7.84 Hz (Signal Unfil.)
- ▼ Oscil. Fr. = 7.84 Hz (Signal Fil.)

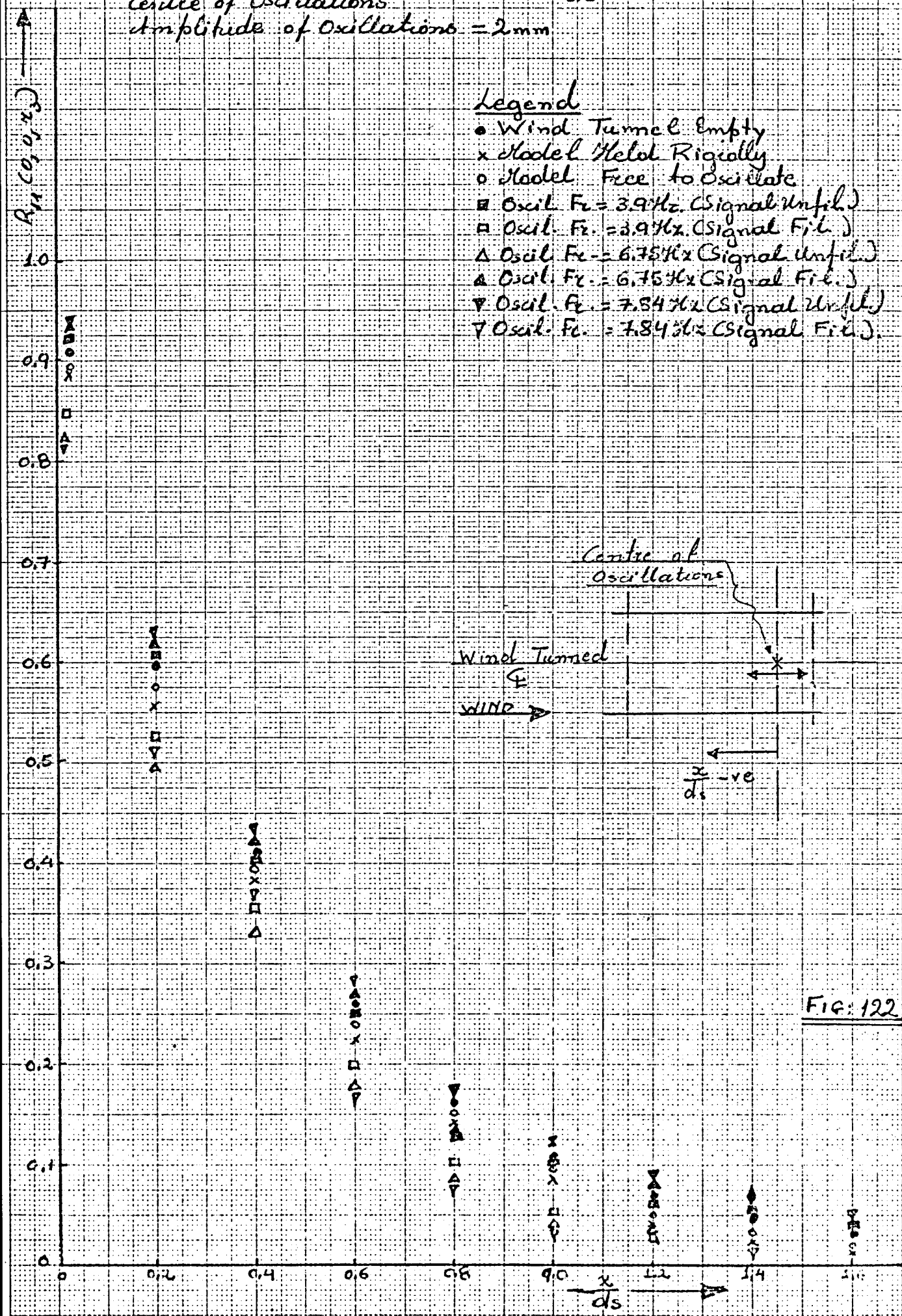


FIG: 122



Variation of the lateral space Correlation  
(x-direction) in front of the R=2 Circular Cylinder.  
Slotted Taffle. N.W. placed at  $\frac{x}{d_s} = -0.64$  from  
Centre of Oscillations  
Amplitude of Oscillations = 2mm

### Legend

- Wind Tunnel Empty
- x Model Held Rigidly
- Model Free to Oscillate
- Oscil. Fr. = 3.9% (Signal Unfil.)
- Oscil. Fr. = 3.9% (Signal Fil.)
- ▲ Oscil. Fr. = 6.75% (Signal Unfil.)
- △ Oscil. Fr. = 6.75% (Signal Fil.)
- ▽ Oscil. Fr. = 7.84% (Signal Unfil.)
- ∇ Oscil. Fr. = 7.84% (Signal Fil.)

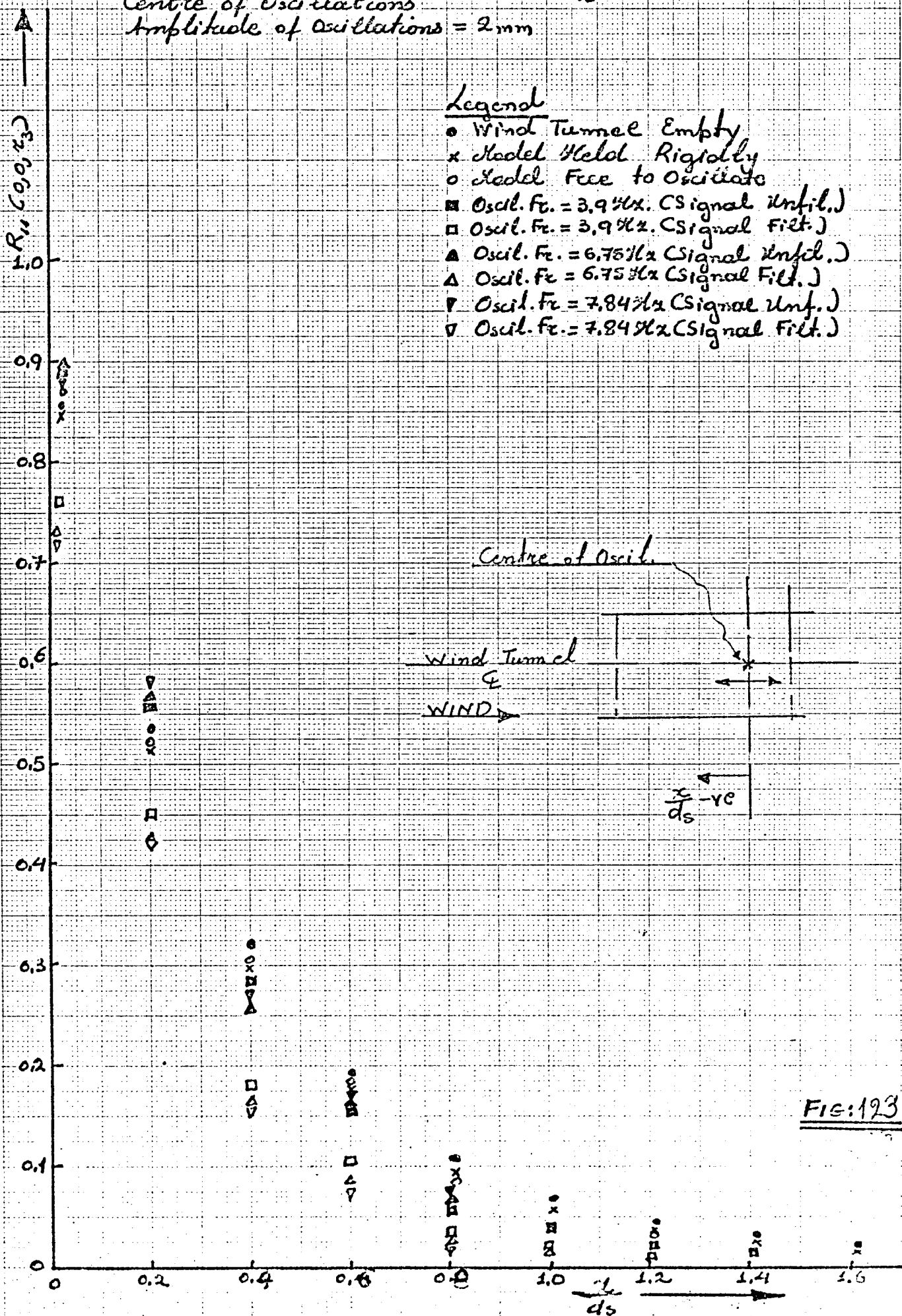


FIG: 123

Variation of the lateral Space Correlation  
(x-direction) in front of the AR=2 Circular Cylinder  
Slotted Raffle, H.W. placed at  $\frac{x}{d_s} = -0.95$  from  
Centre of Oscillations

Amplitude of Oscillations = 2 mm

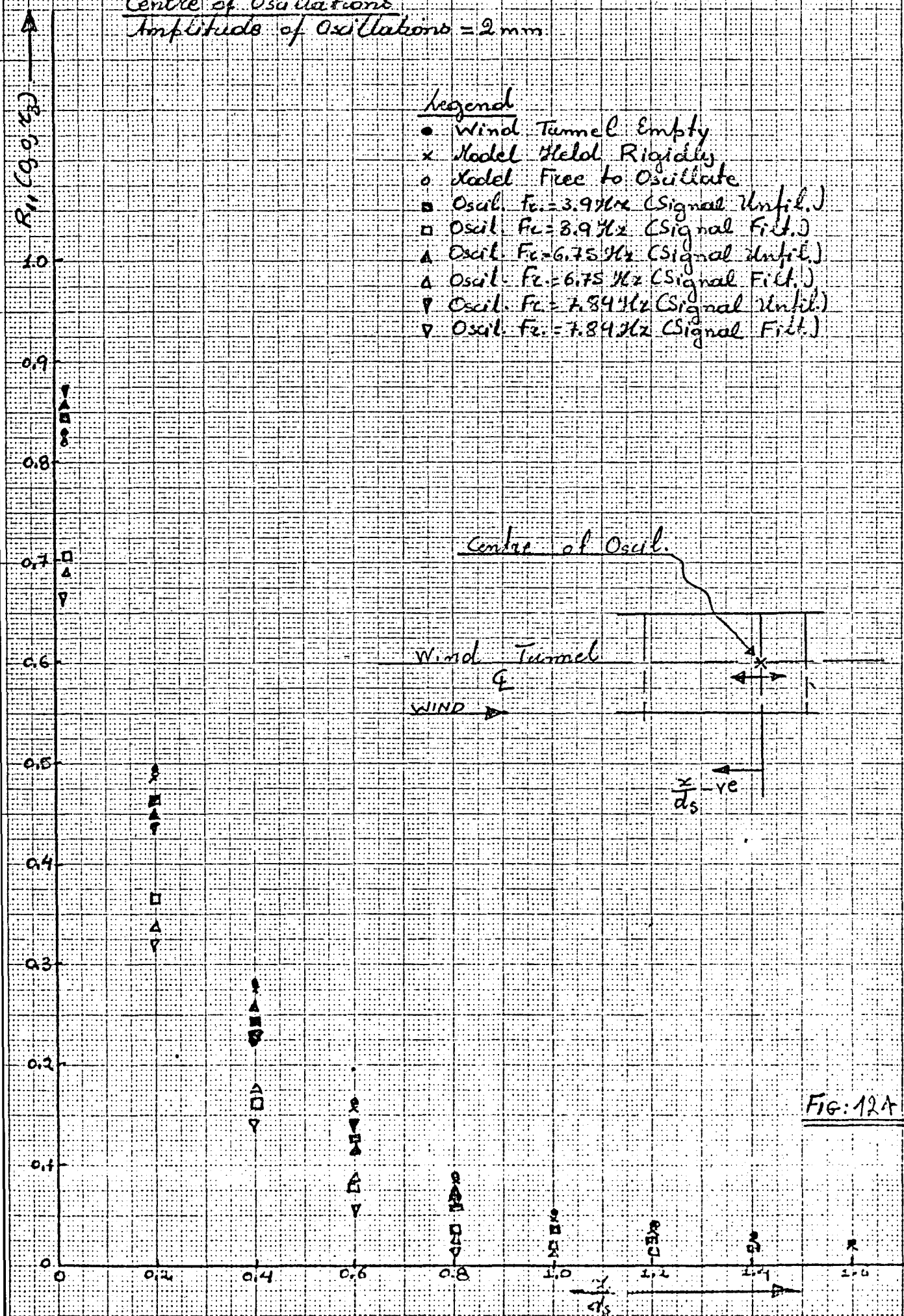


FIG: 12A



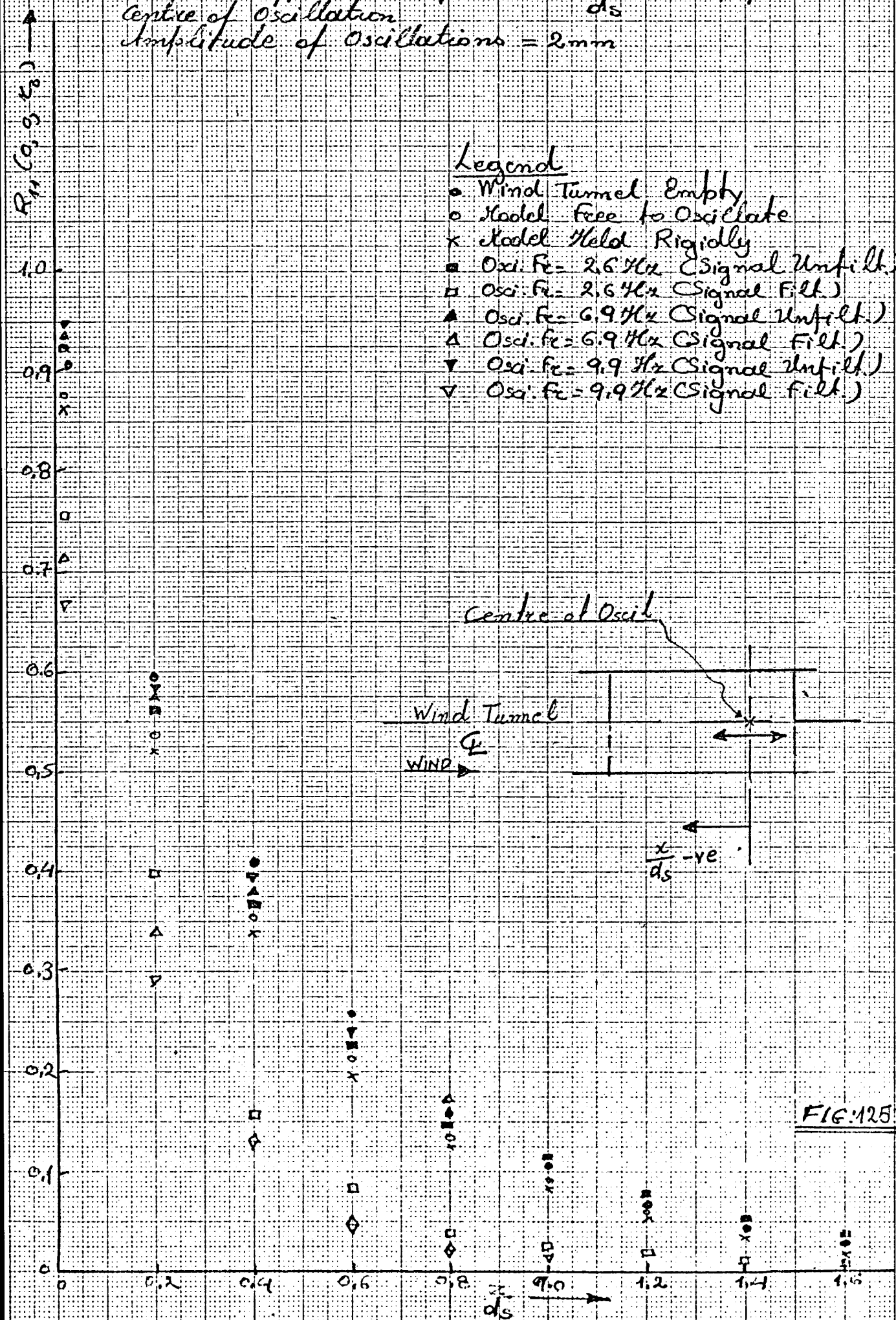
### Variation of the lateral space correlation ( $x$ -direction) in front of the $R=2$ plate,

Smallest Baffle. N.W. placed at  $\frac{x}{d_s} = -0.49$  from  
Centre of Oscillation

Amplitude of Oscillations = 2mm

### Legend

- o Wind Tunnel Empty
- o Model Free to Oscillate
- x Model Held Rigidly
- o Osci. Fc = 2.6 Hz (Signal Unfilt.)
- o Osci. Fc = 2.6 Hz (Signal Filt.)
- o Osci. Fc = 6.9 Hz (Signal Unfilt.)
- o Osci. Fc = 6.9 Hz (Signal Filt.)
- o Osci. Fc = 9.9 Hz (Signal Unfilt.)
- o Osci. Fc = 9.9 Hz (Signal Filt.)



Variation of the lateral space correlation  
(x-direction) in front of the  $AR=2$  plate  
Slotted Baffle. M.W. placed at  $\frac{x}{ds} = -0.64$  from  
Centre of Oscillations  
Amplitude of Oscillations = 2mm

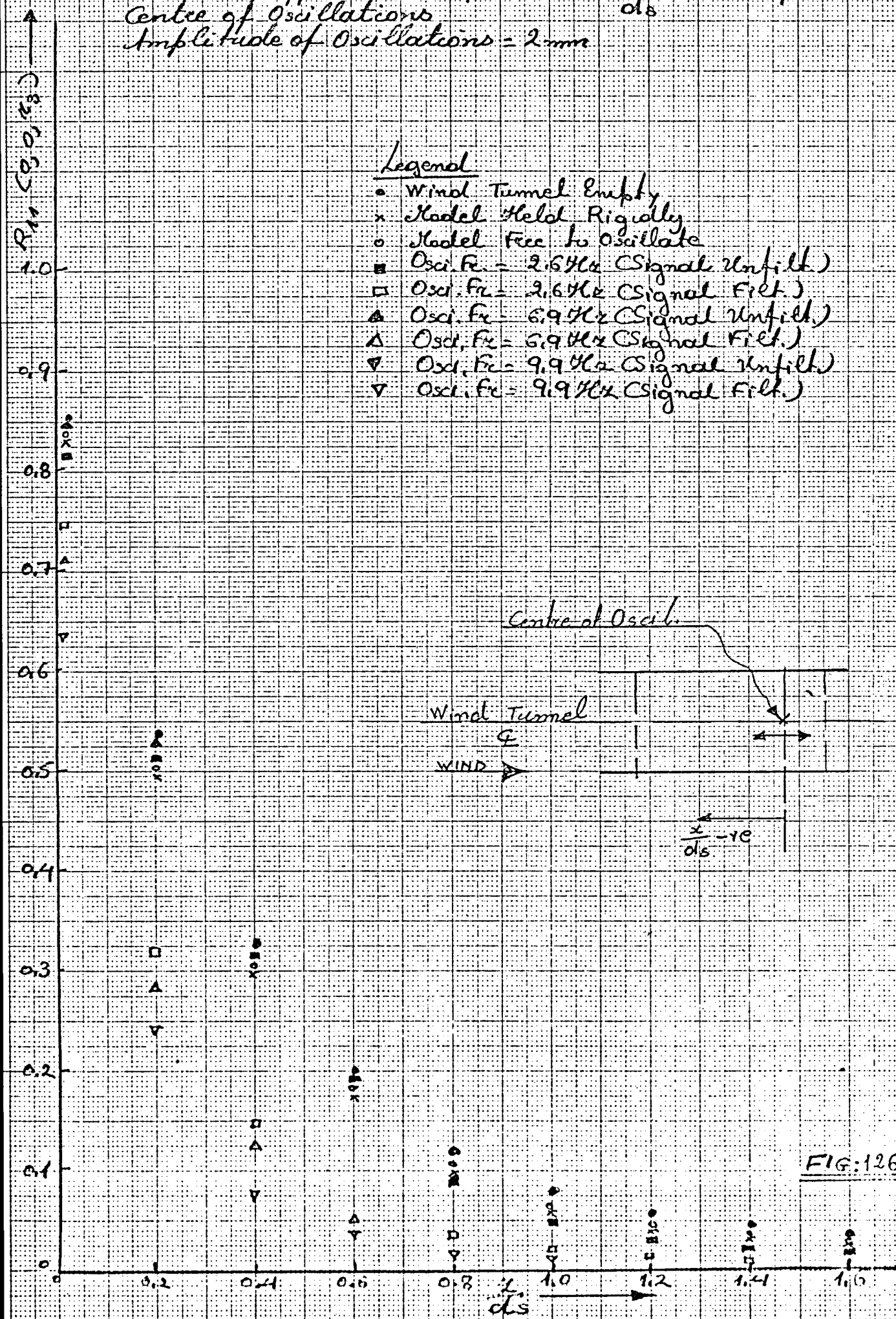
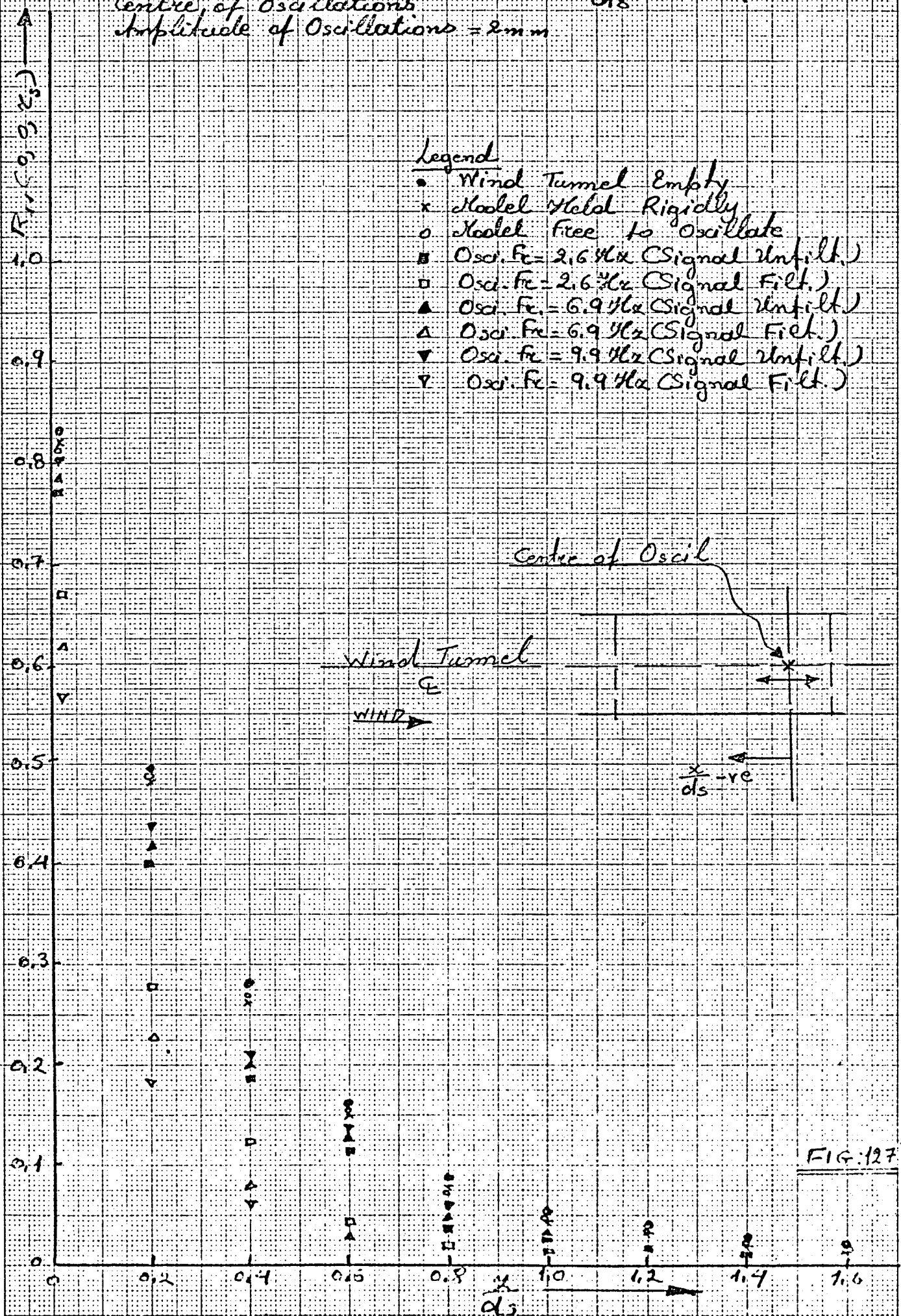


FIG:126

Variation of the Lateral Space Correlation  
(x-direction) in front of the  $R=2$  plate  
 Slotted Baffle, V.W. placed at  $\frac{x}{ds} = -0.96$  from  
 Centre of Oscillations  
 Amplitude of Oscillations = 2mm



	SLOTTED BAFFLE						30mm HOLES BAFFLE						50mm HOLES BAFFLE									
Scale	Position of Slot-wire Coincidence	Empty Tunnel	Model Free to Oscillate	Model Held Rigidly			Position of Slot-wire Coincidence	Empty Tunnel	Model Free to Oscillate	Model Held Rigidly			Position of Slot-wire Coincidence	Empty Tunnel	Model Free to Oscillate	Model Held Rigidly			Nature of Signal			
x (mm)	Oscil. Freq. $\rightarrow$						Oscil. Freq. $\rightarrow$						Oscil. Freq. $\rightarrow$									
	$\frac{x}{d_s} = -0.49$	26	18	12	$\frac{31}{16}$	$\frac{30}{13}$	$\frac{29}{10}$	$\frac{x}{d_{30}} = -0.59$	23	19	18	$\frac{22}{17}$	$\frac{24}{16}$	$\frac{27}{15}$	$\frac{x}{d_{50}} = -0.25$	23	20	19	$\frac{24}{17}$	$\frac{25}{15}$	$\frac{26}{14}$	Unfilled
	$\frac{x}{d_s} = -0.64$	25	23	23	$\frac{27}{15}$	$\frac{25}{13}$	$\frac{28}{12}$	$\frac{x}{d_{30}} = -0.77$	20	17	15	$\frac{21}{14}$	$\frac{18}{13}$	$\frac{23}{11}$	$\frac{x}{d_{50}} = -0.46$	20	19	18	$\frac{16}{14}$	$\frac{17}{15}$	$\frac{21}{13}$	Unfilled
	$\frac{x}{d_s} = -0.96$	20	19	19	$\frac{18}{16}$	$\frac{17}{13}$	$\frac{16}{12}$	$\frac{x}{d_{30}} = -1.14$	18	17	15	$\frac{15}{12}$	$\frac{19}{13}$	$\frac{20}{10}$	$\frac{x}{d_{50}} = -0.69$	18	17	17	$\frac{15}{13}$	$\frac{16}{14}$	$\frac{16}{11}$	Unfilled
y (mm)	Oscil. Freq. $\rightarrow$						Oscil. Freq. $\rightarrow$						Oscil. Freq. $\rightarrow$									
	$\frac{y}{d_s} = -0.49$	16	14	12	$\frac{11}{10}$	$\frac{15}{9}$	$\frac{13}{8}$	$\frac{y}{d_{30}} = -0.59$	13.5	12	11	$\frac{13}{9}$	$\frac{14}{8}$	$\frac{15}{7}$	$\frac{y}{d_{50}} = -0.35$	36.5	33	32	$\frac{37}{31}$	$\frac{38}{30}$	$\frac{39}{29}$	Unfilled
	$\frac{y}{d_s} = -0.64$	12	11	10	$\frac{10}{8}$	$\frac{8}{7}$	$\frac{8}{6}$	$\frac{y}{d_{30}} = -0.77$	11	9	9	$\frac{10}{7}$	$\frac{12}{6}$	$\frac{13}{4}$	$\frac{y}{d_{50}} = -0.46$	35	33	32	$\frac{36}{30}$	$\frac{34}{29}$	$\frac{37}{28}$	Unfilled
	$\frac{y}{d_s} = -0.96$	10	10	9	$\frac{8}{5}$	$\frac{7}{3}$	$\frac{6}{1}$	$\frac{y}{d_{30}} = -1.14$	9	9	8	$\frac{7}{5}$	$\frac{10}{4}$	$\frac{11}{3}$	$\frac{y}{d_{50}} = -0.69$	34	33	32	$\frac{30}{28}$	$\frac{31}{27}$	$\frac{35}{26}$	Unfilled
z (mm)	Oscil. Freq. $\rightarrow$						Oscil. Freq. $\rightarrow$						Oscil. Freq. $\rightarrow$									
	$\frac{z}{d_s} = -0.49$	14	11	10	$\frac{13}{9}$	$\frac{15}{8}$	$\frac{16}{6}$	$\frac{z}{d_{30}} = -0.59$	12.9	10	10	$\frac{14}{9}$	$\frac{15}{8}$	$\frac{16}{7}$	$\frac{z}{d_{50}} = -0.35$	26.5	25	24	$\frac{28}{24}$	$\frac{29}{23}$	$\frac{29}{22}$	Unfilled
	$\frac{z}{d_s} = -0.64$	10	9	8	$\frac{7}{5}$	$\frac{8}{3}$	$\frac{9}{2}$	$\frac{z}{d_{30}} = -0.77$	10	9	8	$\frac{7}{4}$	$\frac{9}{5}$	$\frac{11}{3}$	$\frac{z}{d_{50}} = -0.46$	24	23	22	$\frac{21}{20}$	$\frac{25}{19}$	$\frac{25}{18}$	Unfilled
	$\frac{z}{d_s} = -0.96$	8	8	7	$\frac{4}{3}$	$\frac{5}{3}$	$\frac{6}{2}$	$\frac{z}{d_{30}} = -1.14$	8	7	6	$\frac{4}{2}$	$\frac{5}{1}$	$\frac{7}{4}$	$\frac{z}{d_{50}} = -0.69$	23	22	21	$\frac{18}{16}$	$\frac{19}{17}$	$\frac{19}{15}$	Unfilled

Amplitude of Oscillations = 3.5 mm

FIG: 129

Scale	SLOTTED BAFFLE						30mm HOLES BAFFLE						50mm HOLES BAFFLE						Nature of Signal			
	Position of Hot-wire Coincidence	Empty Tunnel	Model Free to Oscillate	Model Held Rigidly			Position of Hot-wire Coincidence	Empty Tunnel	Model Free to Oscillate	Model Held Rigidly			Position of Hot-wire Coincidence	Empty Tunnel	Model Free to Oscillate	Model Held Rigidly						
x (mm)	Oscil. Freq. $\rightarrow$			3.63	6.72	11.3	Oscil. Freq. $\rightarrow$			5.26	7.61	9.83	Oscil. Freq. $\rightarrow$			3.72	8.64	10.6				
	$\frac{x}{d_s} = -0.55$	25	22	21	$\frac{23}{18}$	$\frac{26}{16}$	$\frac{26}{15}$	$\frac{x}{d_{50}} = -0.66$	22	20	19	$\frac{23}{16}$	$\frac{24}{14}$	$\frac{25}{13}$	$\frac{x}{d_{50}} = -0.75$	22	20	18	$\frac{23}{15}$	$\frac{24}{14}$	$\frac{24}{13}$	Unstable Filled
	$\frac{x}{d_s} = -0.83$	21	19	18	$\frac{15}{14}$	$\frac{16}{13}$	$\frac{17}{12}$	$\frac{x}{d_{50}} = -0.99$	19	18	16	$\frac{18}{13}$	$\frac{20}{11}$	$\frac{22}{10}$	$\frac{x}{d_{50}} = -0.6$	19	18	18	$\frac{20}{16}$	$\frac{20}{15}$	$\frac{21}{14}$	Unstable Filled
	$\frac{x}{d_s} = -0.99$	19	18	18	$\frac{16}{13}$	$\frac{16}{13}$	$\frac{17}{12}$	$\frac{x}{d_{50}} = -1.19$	17	16	16	$\frac{14}{12}$	$\frac{15}{11}$	$\frac{17}{10}$	$\frac{x}{d_{50}} = -0.75$	17	17	16	$\frac{14}{12}$	$\frac{15}{11}$	$\frac{16}{10}$	Unstable Filled
y (mm)	Oscil. Freq. $\rightarrow$			4.16	5.93	9.9	Oscil. Freq. $\rightarrow$			4.47	7.85	10.9	Oscil. Freq. $\rightarrow$			5.5	8.23	10.8				
	$\frac{x}{d_s} = -0.55$	16	15	15	$\frac{14}{13}$	$\frac{15}{12}$	$\frac{15}{12}$	$\frac{x}{d_{50}} = -0.66$	13	11	10	$\frac{9}{7}$	$\frac{12}{6}$	$\frac{14}{5}$	$\frac{x}{d_{50}} = -0.75$	36	33	31	$\frac{37}{28}$	$\frac{38}{26}$	$\frac{39}{25}$	Unstable Filled
	$\frac{x}{d_s} = -0.83$	11	11	10	$\frac{8}{6}$	$\frac{9}{6}$	$\frac{10}{5}$	$\frac{x}{d_{50}} = -0.99$	11	10	10	$\frac{8}{6}$	$\frac{9}{5}$	$\frac{10}{3}$	$\frac{x}{d_{50}} = -0.6$	34	32	30	$\frac{33}{28}$	$\frac{34}{27}$	$\frac{35}{27}$	Unstable Filled
	$\frac{x}{d_s} = -0.99$	9	8	7	$\frac{5}{3}$	$\frac{6}{4}$	$\frac{6}{2}$	$\frac{x}{d_{50}} = -1.19$	8	6	4	$\frac{3}{2}$	$\frac{4}{1}$	$\frac{3}{1}$	$\frac{x}{d_{50}} = -0.75$	33	32	31	$\frac{28}{26}$	$\frac{29}{24}$	$\frac{29}{22}$	Unstable Filled
z (mm)	Oscil. Freq. $\rightarrow$			3.86	7.53	11.9	Oscil. Freq. $\rightarrow$			3.35	6.73	8.89	Oscil. Freq. $\rightarrow$			6.1	7.36	9.79				
	$\frac{x}{d_s} = -0.55$	13	12	12	$\frac{11}{9}$	$\frac{12}{9}$	$\frac{12}{8}$	$\frac{x}{d_{50}} = -0.66$	12	10	10	$\frac{8}{6}$	$\frac{9}{6}$	$\frac{13}{5}$	$\frac{x}{d_{50}} = -0.75$	26	24	22	$\frac{27}{20}$	$\frac{28}{19}$	$\frac{28}{19}$	Unstable Filled
	$\frac{x}{d_s} = -0.83$	10	9	9	$\frac{8}{6}$	$\frac{7}{5}$	$\frac{9}{3}$	$\frac{x}{d_{50}} = -0.99$	9	7	6	$\frac{6}{4}$	$\frac{7}{8}$	$\frac{7}{2}$	$\frac{x}{d_{50}} = -0.6$	23	22	22	$\frac{20}{18}$	$\frac{21}{16}$	$\frac{22}{15}$	Unstable Filled
	$\frac{x}{d_s} = -0.99$	7	7	6	$\frac{4}{3}$	$\frac{3}{2}$	$\frac{5}{2}$	$\frac{x}{d_{50}} = -1.19$	8	8	7	$\frac{5}{3}$	$\frac{6}{2}$	$\frac{7}{1}$	$\frac{x}{d_{50}} = -0.75$	22	21	20	$\frac{18}{15}$	$\frac{19}{12}$	$\frac{19}{12}$	Unstable Filled



Amplitude of Oscillations = 5 mm

FIG: 130

Scale	S L O T T E D   B A F F L E						30mm HOLES   B A F F L E						50mm HOLES   B A F F L E						Nature of Sign			
	Position of Slot-wire Coincidence	Empty Tunnel	Model Free to Oscillate	Model Model Rigidity			Position of Slot-wire Coincidence	Empty Tunnel	Model Free to Oscillate	Model Model Rigidity			Position of Slot-wire Coincidence	Empty Tunnel	Model Free to Oscillate	Model Model Rigidity						
L <sub>x</sub> (mm)	Oscil., Freq. →						Oscil., Freq. →						Oscil., Freq. →									
	$\frac{x}{d_s} = -0.61$	23	21	20	$\frac{22}{17}$	$\frac{24}{15}$	$\frac{25}{14}$	$\frac{x}{d_{30}} = -0.73$	13	11	10	$\frac{11}{7}$	$\frac{12}{6}$	$\frac{12}{6}$	$\frac{x}{d_{50}} = -0.433$	21	19	18	$\frac{22}{16}$	$\frac{23}{15}$	$\frac{24}{15}$	Unit Fill
	$\frac{x}{d_s} = -0.915$	21	19	18	$\frac{20}{15}$	$\frac{20}{13}$	$\frac{22}{12}$	$\frac{x}{d_{30}} = -1.1$	12	10	9	$\frac{10}{5}$	$\frac{11}{4}$	$\frac{13}{3}$	$\frac{x}{d_{50}} = -0.66$	19	18	18	$\frac{20}{16}$	$\frac{21}{16}$	$\frac{21}{15}$	Unit Fill
	$\frac{x}{d_s} = -1.05$	20	19	18	$\frac{16}{13}$	$\frac{17}{12}$	$\frac{17}{11}$	$\frac{x}{d_{30}} = -1.26$	10	9	8	$\frac{9}{6}$	$\frac{11}{5}$	$\frac{11}{4}$	$\frac{x}{d_{50}} = -0.755$	17	16	16	$\frac{14}{12}$	$\frac{15}{11}$	$\frac{15}{11}$	Unit Fill
L <sub>y</sub> (mm)	Oscil., Freq. →						Oscil., Freq. →						Oscil., Freq. →									
	$\frac{x}{d_s} = -0.61$	15	14	13	$\frac{15}{11}$	$\frac{16}{10}$	$\frac{17}{9}$	$\frac{x}{d_{30}} = -0.73$	12	9	8	$\frac{10}{5}$	$\frac{11}{4}$	$\frac{12}{4}$	$\frac{x}{d_{50}} = -0.433$	35	33	31	$\frac{36}{29}$	$\frac{37}{28}$	$\frac{38}{28}$	Unit Fill
	$\frac{x}{d_s} = -0.915$	13	12	12	$\frac{13}{10}$	$\frac{14}{9}$	$\frac{15}{8}$	$\frac{x}{d_{30}} = -1.1$	11	9	8	$\frac{10}{6}$	$\frac{10}{5}$	$\frac{12}{5}$	$\frac{x}{d_{50}} = -0.66$	32	31	31	$\frac{33}{29}$	$\frac{34}{28}$	$\frac{35}{27}$	Unit Fill
	$\frac{x}{d_s} = -1.05$	11	10	10	$\frac{8}{6}$	$\frac{9}{5}$	$\frac{9}{4}$	$\frac{x}{d_{30}} = -1.26$	9	8	7	$\frac{5}{3}$	$\frac{6}{2}$	$\frac{8}{1}$	$\frac{x}{d_{50}} = -0.755$	31	30	30	$\frac{30}{28}$	$\frac{30}{27}$	$\frac{31}{26}$	Unit Fill
L <sub>z</sub> (mm)	Oscil., Freq. →						Oscil., Freq. →						Oscil., Freq. →									
	$\frac{x}{d_s} = -0.61$	12	10	9	$\frac{13}{8}$	$\frac{14}{7}$	$\frac{15}{7}$	$\frac{x}{d_{30}} = -0.73$	11	9	8	$\frac{10}{6}$	$\frac{12}{5}$	$\frac{13}{4}$	$\frac{x}{d_{50}} = -0.433$	25	25	24	$\frac{26}{22}$	$\frac{27}{20}$	$\frac{28}{20}$	Unit Fill
	$\frac{x}{d_s} = -0.915$	11	10	9	$\frac{11}{7}$	$\frac{12}{5}$	$\frac{13}{4}$	$\frac{x}{d_{30}} = -1.1$	9	8	7	$\frac{8}{4}$	$\frac{10}{3}$	$\frac{10}{1}$	$\frac{x}{d_{50}} = -0.66$	24	23	22	$\frac{21}{20}$	$\frac{22}{19}$	$\frac{23}{18}$	Unit Fill
	$\frac{x}{d_s} = -1.05$	8	7	7	$\frac{5}{3}$	$\frac{6}{2}$	$\frac{6}{1}$	$\frac{x}{d_{30}} = -1.26$	7	6	6	$\frac{4}{2}$	$\frac{5}{1}$	$\frac{6}{1}$	$\frac{x}{d_{50}} = -0.755$	23	22	21	$\frac{20}{19}$	$\frac{20}{19}$	$\frac{21}{18}$	Unit Fill

	SLOTTED BAFFLE						30mm HOLES BAFFLE						50mm HOLES BAFFLE									
Scale	Position of Slot-wire Coincidence	Empty Tunnel	Model Free to Oscillate	Model Held Rigidly			Position of Slot-wire Coincidence	Empty Tunnel	Model Free to Oscillate	Model Held Rigidly			Position of Slot-wire Coincidence	Empty Tunnel	Model Free to Oscillate	Model Held Rigidly		Nature of Signal				
L <sub>x</sub> (mm)	Oscil. Freq. $\rightarrow$						Oscil. Freq. $\rightarrow$						Oscil. Freq. $\rightarrow$									
					4.38	6.88	9.62					3.1	7.6	9.5				3.7	7.32	9.46		
	$\frac{x}{d_s} = -0.49$	26	17	10	$\frac{29}{12}$	$\frac{30}{9}$	$\frac{31}{9}$	$\frac{x}{d_{30}} = -0.59$	23	18	16	$\frac{20}{16}$	$\frac{21}{15}$	$\frac{24}{14}$	$\frac{x}{d_{50}} = -0.35$	23	19	18	$\frac{23}{16}$	$\frac{23}{15}$	$\frac{25}{13}$	Unfilled
	$\frac{x}{d_s} = -0.64$	25	21	20	$\frac{25}{13}$	$\frac{26}{12}$	$\frac{26}{12}$	$\frac{x}{d_{30}} = -0.77$	20	16	13	$\frac{20}{13}$	$\frac{21}{12}$	$\frac{21}{12}$	$\frac{x}{d_{50}} = -0.46$	20	19	17	$\frac{15}{14}$	$\frac{16}{12}$	$\frac{16}{12}$	Unfilled
	$\frac{x}{d_s} = -0.96$	20	18	17	$\frac{15}{14}$	$\frac{17}{11}$	$\frac{18}{11}$	$\frac{x}{d_{30}} = -1.14$	18	16	15	$\frac{16}{11}$	$\frac{17}{10}$	$\frac{18}{9}$	$\frac{x}{d_{50}} = -0.69$	18	16	15	$\frac{14}{12}$	$\frac{15}{11}$	$\frac{16}{10}$	Unfilled
L <sub>y</sub> (mm)	Oscil. Freq. $\rightarrow$						Oscil. Freq. $\rightarrow$						Oscil. Freq. $\rightarrow$									
					5.1	7.7	10.1					4.71	8.31	11.2				3.7	7.2	10.2		
	$\frac{x}{d_s} = -0.49$	16	13	11	$\frac{10}{9}$	$\frac{13}{8}$	$\frac{15}{6}$	$\frac{x}{d_{30}} = -0.59$	13.5	11	10	$\frac{11}{10}$	$\frac{13}{7}$	$\frac{14}{6}$	$\frac{x}{d_{50}} = -0.35$	36.5	32	30	$\frac{33}{30}$	$\frac{35}{28}$	$\frac{36}{26}$	Unfilled
	$\frac{x}{d_s} = -0.64$	12	10	9	$\frac{9}{8}$	$\frac{9}{6}$	$\frac{10}{5}$	$\frac{x}{d_{30}} = -0.77$	11	8	7	$\frac{10}{6}$	$\frac{10}{4}$	$\frac{11}{4}$	$\frac{x}{d_{50}} = -0.46$	35	31	30	$\frac{35}{28}$	$\frac{35}{27}$	$\frac{36}{26}$	Unfilled
	$\frac{x}{d_s} = -0.96$	10	9	9	$\frac{8}{7}$	$\frac{8}{4}$	$\frac{10}{2}$	$\frac{x}{d_{30}} = -1.14$	9	8	6	$\frac{7}{4}$	$\frac{8}{4}$	$\frac{10}{2}$	$\frac{x}{d_{50}} = -0.69$	34	32	29	$\frac{30}{27}$	$\frac{31}{26}$	$\frac{33}{25}$	Unfilled
L <sub>z</sub> (mm)	Oscil. Freq. $\rightarrow$						Oscil. Freq. $\rightarrow$						Oscil. Freq. $\rightarrow$									
					2.6	6.9	9.9					4.4	6.9	9.81				4.61	8.5	11.1		
	$\frac{x}{d_s} = -0.49$	14	11	11	$\frac{12}{8}$	$\frac{13}{7}$	$\frac{13}{6}$	$\frac{x}{d_{30}} = -0.59$	12.9	9	8	$\frac{13}{8}$	$\frac{13}{8}$	$\frac{14}{7}$	$\frac{x}{d_{50}} = -0.35$	26.5	24	23	$\frac{27}{24}$	$\frac{28}{22}$	$\frac{28}{20}$	Unfilled
	$\frac{x}{d_s} = -0.64$	10	8	7	$\frac{7}{6}$	$\frac{9}{4}$	$\frac{9}{1}$	$\frac{x}{d_{30}} = -0.77$	10	8	6	$\frac{7}{5}$	$\frac{8}{3}$	$\frac{9}{2}$	$\frac{x}{d_{50}} = -0.46$	24	22	21	$\frac{21}{20}$	$\frac{23}{18}$	$\frac{24}{17}$	Unfilled
	$\frac{x}{d_s} = -0.96$	8	7	7	$\frac{6}{4}$	$\frac{6}{3}$	$\frac{7}{1}$	$\frac{x}{d_{30}} = -1.14$	8	7	6	$\frac{4}{1}$	$\frac{5}{0.5}$	$\frac{5}{0.5}$	$\frac{x}{d_{50}} = -0.69$	23	21	20	$\frac{19}{15}$	$\frac{20}{14}$	$\frac{20}{13}$	Unfilled



Amplitude of Oscillations = 3.5 mm

FIG: 132

S L O T T E D   B A F F L E							30mm HOLES   B A F F L E							50mm HOLES   B A F F L E							Nature of Signu	
Scale	Position of Hot-wire Coincidence	Empty Tunnel	Model Free to Oscillate	Model Rigidly			Position of Hot-wire Coincidence	Empty Tunnel	Model Free to Oscillate	Model Rigidly			Position of Hot-wire Coincidence	Empty Tunnel	Model Free to Oscillate	Model Rigidly						
x mm)		Oscil. Free u. →			4.55	8.7	11.1		Oscil. Free u. →		3.2	6.8	9.4		Oscil. Free u. →		2.6	5.7	9.41			
	$\frac{x}{d_0} = -0.55$	25	21	20	$\frac{21}{17}$	$\frac{22}{15}$	$\frac{25}{14}$	$\frac{x}{d_0} = -0.66$	22	19	18	$\frac{20}{15}$	$\frac{21}{14}$	$\frac{22}{12}$	$\frac{x}{d_0} = -0.75$	22	19	17	$\frac{21}{14}$	$\frac{22}{12}$	$\frac{22}{11}$	Unst. Fill.
	$\frac{x}{d_0} = -0.83$	21	18	17	$\frac{15}{13}$	$\frac{15}{12}$	$\frac{16}{10}$	$\frac{x}{d_0} = -0.99$	19	17	16	$\frac{17}{12}$	$\frac{18}{10}$	$\frac{19}{9}$	$\frac{x}{d_0} = -0.6$	19	17	16	$\frac{17}{13}$	$\frac{17}{12}$	$\frac{18}{12}$	Unst. Fill.
	$\frac{x}{d_0} = -0.99$	19	17	16	$\frac{15}{12}$	$\frac{16}{11}$	$\frac{16}{10}$	$\frac{x}{d_0} = -1.19$	17	16	15	$\frac{15}{11}$	$\frac{16}{11}$	$\frac{17}{9}$	$\frac{x}{d_0} = -0.75$	17	15	14	$\frac{13}{11}$	$\frac{14}{11}$	$\frac{15}{9}$	Unst. Fill.
y mm)		Oscil. Free u. →			3.9	7.1	9.3		Oscil. Free u. →		4.13	7.82	10.4		Oscil. Free u. →		3.3	7.9	10.6			
	$\frac{x}{d_0} = -0.55$	16	14	12	$\frac{13}{12}$	$\frac{14}{11}$	$\frac{15}{10}$	$\frac{x}{d_0} = -0.66$	13	11	9	$\frac{9}{7}$	$\frac{11}{5}$	$\frac{12}{4}$	$\frac{x}{d_0} = -0.75$	36	32	29	$\frac{34}{27}$	$\frac{35}{25}$	$\frac{35}{23}$	Unst. Fill.
	$\frac{x}{d_0} = -0.83$	11	10	9	$\frac{8}{5}$	$\frac{8}{4}$	$\frac{10}{3}$	$\frac{x}{d_0} = -0.99$	11	9	8	$\frac{7}{7}$	$\frac{8}{5}$	$\frac{9}{3}$	$\frac{x}{d_0} = -0.6$	34	31	28	$\frac{32}{26}$	$\frac{33}{25}$	$\frac{35}{24}$	Unst. Fill.
	$\frac{x}{d_0} = -0.99$	9	7	6	$\frac{5}{4}$	$\frac{6}{3}$	$\frac{7}{1}$	$\frac{x}{d_0} = -1.19$	8	5	4	$\frac{4}{3}$	$\frac{4}{1}$	$\frac{5}{1}$	$\frac{x}{d_0} = -0.75$	33	30	29	$\frac{31}{25}$	$\frac{32}{23}$	$\frac{34}{21}$	Unst. Fill.
z mm)		Oscil. Free u. →			4.1	6.9	9.35		Oscil. Free u. →		5.2	7.8	9.76		Oscil. Free u. →		4.6	8.3	9.5			
	$\frac{x}{d_0} = -0.55$	13	11	10	$\frac{10}{9}$	$\frac{11}{8}$	$\frac{11}{7}$	$\frac{x}{d_0} = -0.66$	12	10	9	$\frac{8}{7}$	$\frac{8}{6}$	$\frac{10}{4}$	$\frac{x}{d_0} = -0.75$	26	23	21	$\frac{26}{19}$	$\frac{27}{17}$	$\frac{27}{17}$	Unst. Fill.
	$\frac{x}{d_0} = -0.83$	10	8	7	$\frac{7}{6}$	$\frac{8}{5}$	$\frac{9}{3}$	$\frac{x}{d_0} = -0.99$	9	7	5	$\frac{5}{3}$	$\frac{7}{1}$	$\frac{7}{1}$	$\frac{x}{d_0} = -0.6$	23	21	20	$\frac{20}{15}$	$\frac{20}{16}$	$\frac{21}{13}$	Unst. Fill.
	$\frac{x}{d_0} = -0.99$	7	6	5	$\frac{4}{3}$	$\frac{3}{3}$	$\frac{3}{1}$	$\frac{x}{d_0} = -1.19$	8	7	4	$\frac{5}{2}$	$\frac{5}{1}$	$\frac{7}{1}$	$\frac{x}{d_0} = -0.75$	22	19	18	$\frac{17}{14}$	$\frac{15}{12}$	$\frac{19}{11}$	Unst. Fill.

S L O T T E D   B A F F L E							30mm HOLES   B A F F L E							50mm HOLES   B A F F L E							Nature of Signal	
Position of Slot-wire Coincidence	Empty Tunnel	Model Free to Oscillate	Model Rigidly				Position of Slot-wire Coincidence	Empty Tunnel	Model Free to Oscillate	Model Rigidly				Position of Slot-wire Coincidence	Empty Tunnel	Model Free to Oscillate	Model Rigidly					
	Oscil. Freq. $\rightarrow$			3.7	6.9	9.82		Oscil. Freq. $\rightarrow$			5.2	8.2	10.3		Oscil. Freq. $\rightarrow$				3.1	7.2	9.9	
$\frac{x}{d_0} = -0.61$	23	20	19	$\frac{21}{16}$	$\frac{22}{14}$	$\frac{24}{13}$	$\frac{x}{d_0} = -0.73$	13	10	9	$\frac{10}{8}$	$\frac{11}{5}$	$\frac{11}{6}$	$\frac{x}{d_0} = -0.85$	21	18	17	$\frac{21}{14}$	$\frac{23}{16}$	$\frac{23}{11}$	Unst. Filt.	
$\frac{x}{d_0} = -0.915$	21	18	17	$\frac{20}{15}$	$\frac{19}{13}$	$\frac{21}{11}$	$\frac{x}{d_0} = -1.1$	12	9	7	$\frac{8}{6}$	$\frac{10}{5}$	$\frac{12}{3}$	$\frac{x}{d_0} = -0.95$	19	17	15	$\frac{19}{14}$	$\frac{20}{13}$	$\frac{20}{12}$	Unst. Filt.	
$\frac{x}{d_0} = -1.05$	20	18	17	$\frac{15}{12}$	$\frac{16}{10}$	$\frac{16}{10}$	$\frac{x}{d_0} = -1.26$	10	8	7	$\frac{4}{5}$	$\frac{8}{3}$	$\frac{9}{3}$	$\frac{x}{d_0} = -0.95$	17	15	13	$\frac{12}{10}$	$\frac{13}{9}$	$\frac{14}{9}$	Unst. Filt.	
	Oscil. Freq. $\rightarrow$			3.8	4.9	8.3		Oscil. Freq. $\rightarrow$			3.9	7.3	9.8		Oscil. Freq. $\rightarrow$				4.6	9.1	10.3	
$\frac{x}{d_0} = -0.61$	15	13	12	$\frac{14}{10}$	$\frac{16}{8}$	$\frac{16}{8}$	$\frac{x}{d_0} = -0.73$	12	8	7	$\frac{8}{6}$	$\frac{9}{4}$	$\frac{11}{3}$	$\frac{x}{d_0} = -0.85$	35	32	30	$\frac{33}{28}$	$\frac{35}{27}$	$\frac{36}{27}$	Unst. Filt.	
$\frac{x}{d_0} = -0.915$	13	11	10	$\frac{12}{9}$	$\frac{13}{7}$	$\frac{14}{7}$	$\frac{x}{d_0} = -1.1$	11	9	8	$\frac{10}{5}$	$\frac{11}{4}$	$\frac{11}{4}$	$\frac{x}{d_0} = -0.95$	32	30	28	$\frac{31}{28}$	$\frac{32}{27}$	$\frac{34}{26}$	Unst. Filt.	
$\frac{x}{d_0} = -1.05$	11	9	8	$\frac{7}{5}$	$\frac{8}{3}$	$\frac{8}{3}$	$\frac{x}{d_0} = -1.26$	9	7	6	$\frac{6}{2}$	$\frac{5}{1}$	$\frac{6}{1}$	$\frac{x}{d_0} = -0.95$	31	30	29	$\frac{29}{27}$	$\frac{30}{25}$	$\frac{32}{25}$	Unst. Filt.	
	Oscil. Freq. $\rightarrow$			5.1	7.6	9.9		Oscil. Freq. $\rightarrow$			2.1	7.6	9.1		Oscil. Freq. $\rightarrow$				3.12	7.5	9.2	
$\frac{x}{d_0} = -0.61$	12	9	8	$\frac{12}{7}$	$\frac{13}{6}$	$\frac{14}{5}$	$\frac{x}{d_0} = -0.73$	11	8	6	$\frac{11}{5}$	$\frac{12}{3}$	$\frac{13}{3}$	$\frac{x}{d_0} = -0.85$	25	23	22	$\frac{25}{21}$	$\frac{26}{19}$	$\frac{26}{17}$	Unst. Filt.	
$\frac{x}{d_0} = -0.915$	11	9	7	$\frac{10}{6}$	$\frac{10}{5}$	$\frac{11}{4}$	$\frac{x}{d_0} = -1.1$	9	7	5	$\frac{7}{4}$	$\frac{8}{3}$	$\frac{10}{2}$	$\frac{x}{d_0} = -0.95$	24	22	20	$\frac{20}{19}$	$\frac{21}{18}$	$\frac{21}{16}$	Unst. Filt.	
$\frac{x}{d_0} = -1.05$	8	7	6	$\frac{4}{2}$	$\frac{6}{1}$	$\frac{7}{1}$	$\frac{x}{d_0} = -1.26$	7	6	5	$\frac{5}{1}$	$\frac{5}{1}$	$\frac{6}{1}$	$\frac{x}{d_0} = -0.95$	23	21	19	$\frac{20}{18}$	$\frac{21}{17}$	$\frac{21}{16}$	Unst. Filt.	

PRESSURE VELOCITY CORRELATIONS

AND SPECTRA

(Refer to Fig.51 for definition  
sketch)

Pressure and Velocity

Spherical

Model Held Rigidly  
Plate  $R=2$

Slotted Baffle

Legend

x Velocity spectrum at  
stagnation line flow  
at  $\frac{x}{D} = -\frac{1}{10}$

o Pressure spectrum at  
stagnation point

$$\frac{f S_p(f)}{\bar{u}_c^2} \times 10^6$$

$$\frac{f S_p(f)}{\bar{p}^2} \times 10^6$$

FIG. 13A

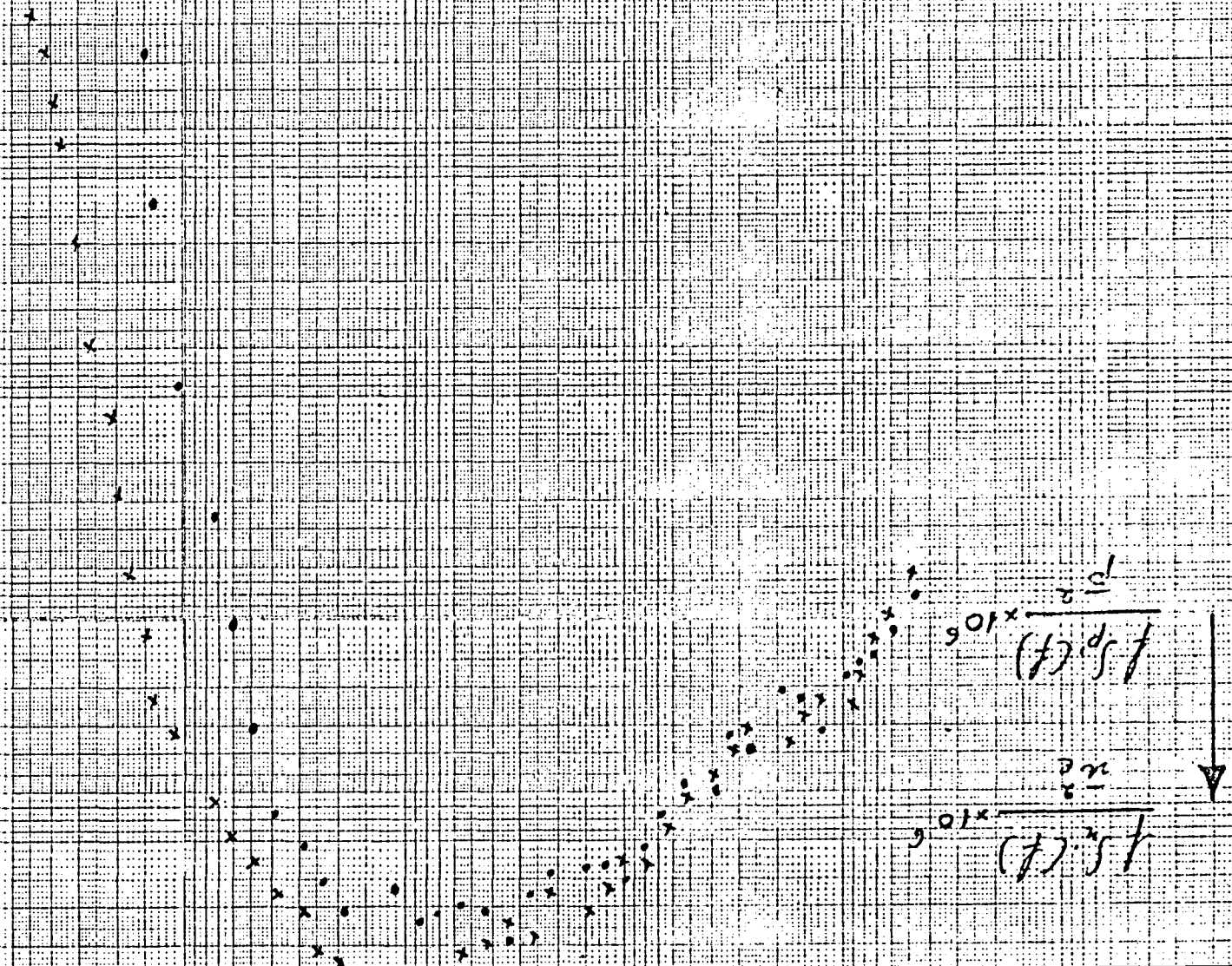
$$\frac{2\pi f}{u_c} \cdot L_x$$

Fig: 135

$\frac{2.07 \times 10^3}{10^3}$   
 $\rightarrow$

• Pressure spectrum at  
 stagnation point  
 and  $\frac{D}{x} = \frac{1}{10}$   
 x Velocity spectrum at  
 stagnation line flow  
 Legend

Steel Well Rigidity  
 Plate  $\mu = 2$   
 30 mm holes Baffle  
 Spectra  
 Pressure and Velocity





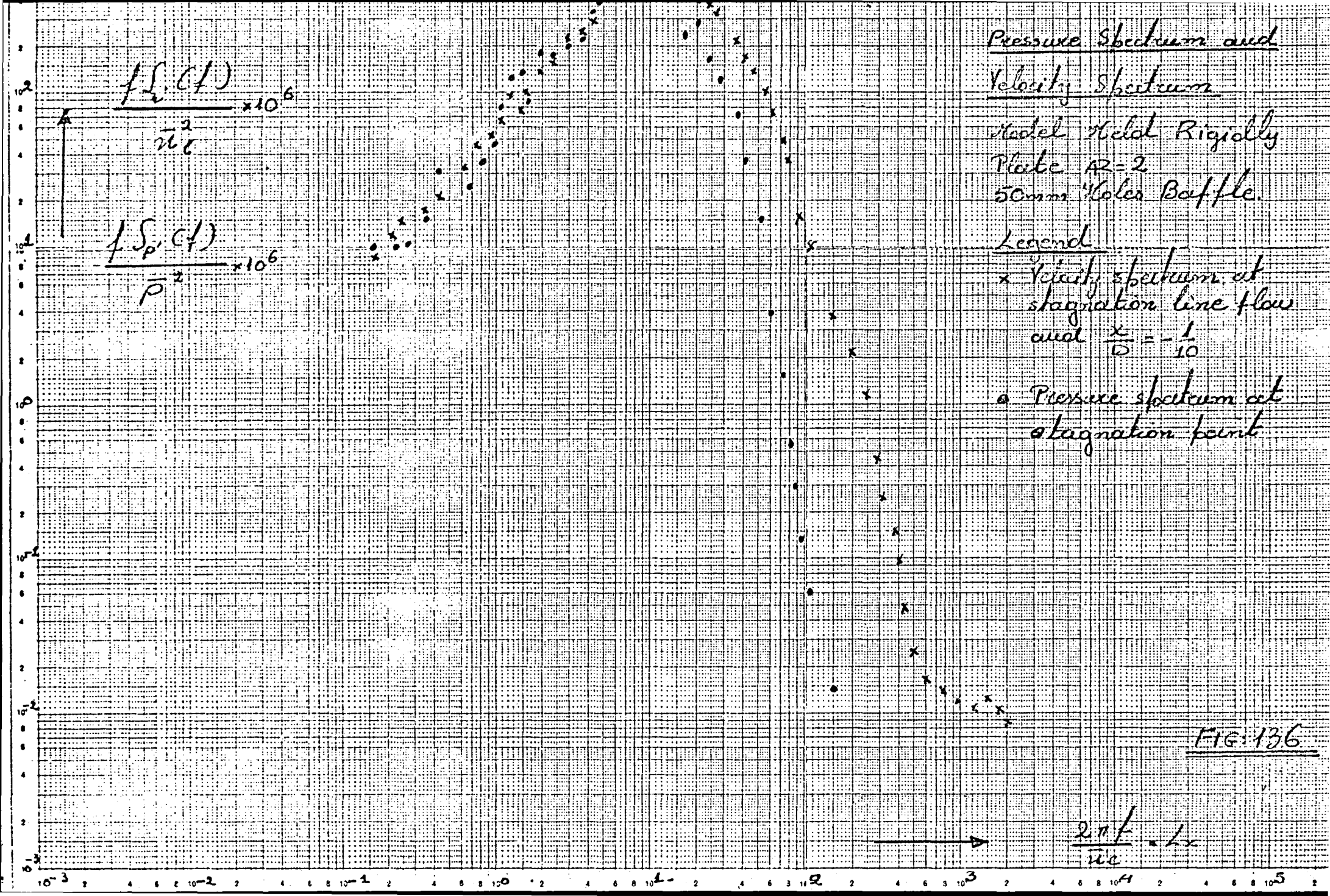
# Pressure Spectrum and Velocity Spectrum

Model Helix Rigolly  
Plate AR=2  
50mm Hole Baffle

## Legend

- x Velocity spectrum at  
stagnation line flow  
and  $\frac{x}{D} = -\frac{1}{10}$
- o Pressure spectrum at  
stagnation point

FIG: 136



# Velocity Pressure Correlation

slotted Baffle

Plate  $R=2$

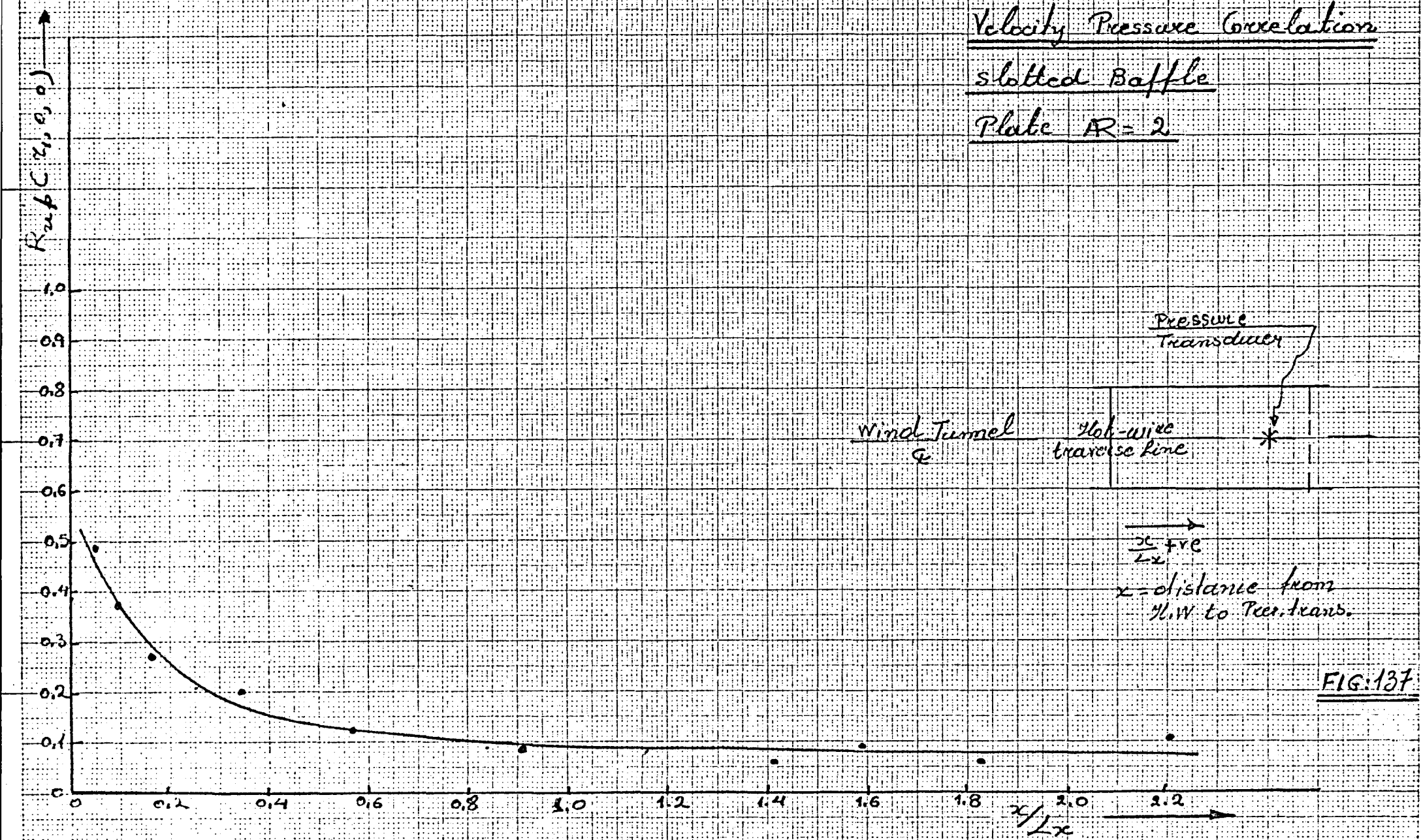


FIG:137



# Pressure Velocity Correlation

30 mm Gleser Baffle

Plate  $R=2$

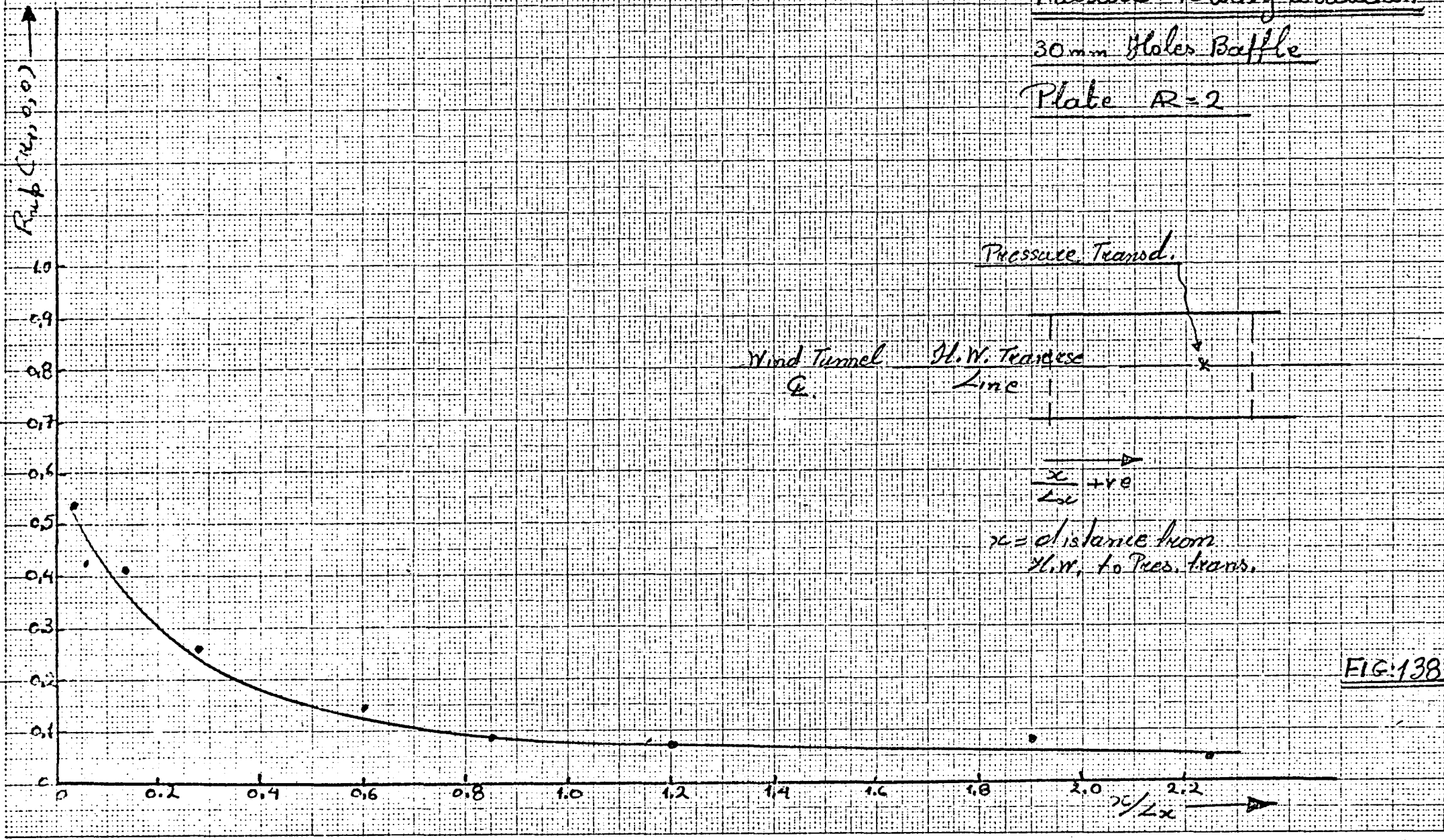


FIG:138

Pressure Velocity Correlation

50mm Holes Baffle

Plate  $R=2$

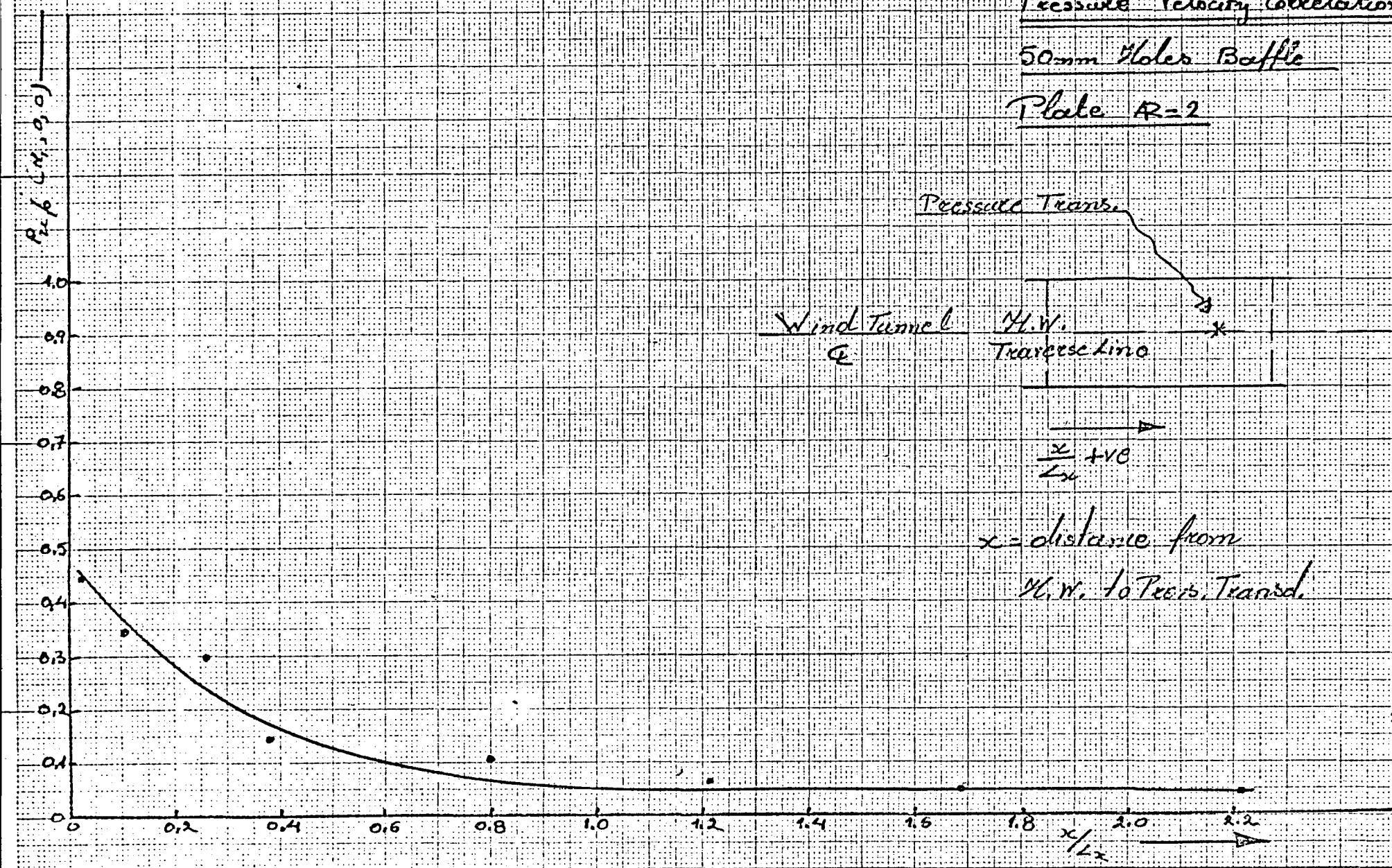


FIG: 139

